



**HAL**  
open science

# Damage and failure of heterogeneous materials and structures under complex loading

Darius Seyedi

► **To cite this version:**

Darius Seyedi. Damage and failure of heterogeneous materials and structures under complex loading. Engineering Sciences [physics]. Université Paris-Saclay, 2021. tel-04560033

**HAL Id: tel-04560033**

**<https://hal.science/tel-04560033>**

Submitted on 26 Apr 2024

**HAL** is a multi-disciplinary open access archive for the deposit and dissemination of scientific research documents, whether they are published or not. The documents may come from teaching and research institutions in France or abroad, or from public or private research centers.

L'archive ouverte pluridisciplinaire **HAL**, est destinée au dépôt et à la diffusion de documents scientifiques de niveau recherche, publiés ou non, émanant des établissements d'enseignement et de recherche français ou étrangers, des laboratoires publics ou privés.

Mémoire présenté en vue de l'obtention de  
l'Habilitation à Diriger des Recherches

Spécialité « Mécanique - Génie Mécanique - Génie civil »

*présenté par*

**Darius SEYEDI**

**Endommagement et rupture des matériaux et des structures  
hétérogènes soumis à des chargements complexes**

\* \* \*

**Damage and failure of heterogeneous materials and structures under  
complex loading**

HDR soutenue le 10 septembre 2021 devant le jury composé de :

<b>M. Djimédo Kondo</b> , Professeur, Sorbonne Université	Rapporteur
<b>M. Gilles Pijaudier-Cabot</b> , Professeur, Université de Pau et des Pays de l'Adour	Rapporteur
<b>M. Victor Saouma</b> , Professor, University of Colorado at Boulder	Rapporteur
<b>M. François Hild</b> , Directeur de recherches, LMT, CNRS/ENS Paris-Saclay	Examineur
<b>M. Habibou Maitournam</b> , Professeur, ENSTA Paris	Examineur
<b>M. Jean Sulem</b> , Directeur de recherches, Laboratoire Navier, Ecole des Ponts ParisTech	Examineur

**CEA Paris-Saclay**  
**Direction des Energies**  
**Institut des Sciences Appliquées et de la Simulation**  
**Département de Modélisation des Systèmes et Structures**  
**Service d'Etudes Mécaniques et Thermiques**  
**Laboratoire d'Etudes de Mécanique Sismique**



## **Remerciements**

Acknowledgment



## Abstract

This manuscript summarizes my research activities about damage and failure of heterogeneous materials and structures under complex loading. The work reported was undertaken as part of various projects and in collaboration with many researchers essentially at BRGM (French Geological Survey) from 2004 to 2012, and at Andra (French national agency for radioactive waste management) from 2012 to 2018. Three application domains are addressed in the present document, each one in a separate chapter.

First, thermo-hydromechanical (THM) behavior of Callovo-Oxfordian claystone (COx) is discussed as a potential host formation for an industrial radioactive waste repository. A synthesis of research conducted essentially within *Groupement de Laboratoires Comportement mécanique des ouvrages et des composants des stockages (GL Mouv)* at Andra is presented. GL Mouv activities consisted in laboratory experimental investigations, along with theoretical and numerical developments for characterization and modeling of the THM behavior of COx. Some *in situ* observations and THM experiments performed at Andra's Underground Research Laboratory are also presented to provide additional information on the COx behavior.

The second chapter concerns damage and fracturing of heterogeneous quasi-brittle materials. The main motivation for these developments has been the study of integrity of geological storage of  $CO_2$ . A non-local damage model accounting for the rock heterogeneities was developed. A Weibull model was used to account for the randomness of crack initiation(s) and then a fracture mechanics based threshold was considered to model crack propagation. The model was integrated in a finite element code via a nonlocal damage approach. A regularization operator based on a stress regularization was introduced. Both damage thresholds are checked using the "regularized" stress field to avoid mesh dependence. The model was then extended to account for hydromechanical couplings.

Seismic fragility of structures is addressed in the third chapter. Standard fragility functions represent the conditional probability for a structure to reach a certain damage level for a given earthquake represented by a single intensity measure. This standard procedure introduces epistemic uncertainties in the risk evaluation as such approach cannot fully represent the effect of an earthquake on the response of structures. A concept of vector-valued fragility functions (or fragility surfaces) is proposed enabling to represent earthquake shaking by two intensity measures. It is shown that an increase from one to two IMs leads to a significant reduction in the scatter in fragility functions. Moreover, the proposed methodology can be extended to multi-hazard risk assessment, and to account for initial damage of structures.

My resume and a short synthesis of my research activities in French are presented at the beginning of this manuscript. The document is concluded by some research perspectives.



# Contents

<b>Synthèse des activités de recherche et d'enseignement</b>	<b>xi</b>
S.1 Parcours professionnel et formation universitaire . . . . .	xi
S.2 Thématiques de recherche . . . . .	xii
S.2.1 Fatigue thermomécanique – thèse de doctorat et post-doctorat au LMT et EDF R&D . . . . .	xii
S.2.2 Vulnérabilité sismique des bâtis – travaux de recherche réalisés au BRGM et en cours au CEA . . . . .	xiii
S.2.3 Endommagement et fracturation de matériaux hétérogènes à comportement quasi-fragile : application à l'étude de l'intégrité du stockage géologique de CO <sub>2</sub> – travaux de recherche réalisés au BRGM . . . . .	xiv
S.2.4 Comportement THM de l'argilite du Callovo-Oxfordien : travaux de recherche réalisés à l'Andra . . . . .	xvi
S.2.5 Déchirure ductile des structures métalliques – travaux de recherche en cours au CEA . . . . .	xvii
S.3 Activités d'enseignement . . . . .	xviii
S.4 Encadrement d'étudiants et de post-doctorants . . . . .	xviii
S.5 Responsabilités académiques . . . . .	xix
S.6 Bilan de publications scientifiques . . . . .	xx
S.6.1 Publications scientifiques . . . . .	xx
S.6.2 Bibliométrie Google Scholar et Publon (WOS) . . . . .	xxi
S.7 Liste de publications . . . . .	xxii
S.7.1 Chapitres de livre . . . . .	xxii
S.7.2 Publications dans des revues internationales à comité de lecture . . . . .	xxii
S.7.3 Publication dans une revue française à comité de lecture . . . . .	xxiv
S.7.4 Communications dans des conférences internationales . . . . .	xxiv
<b>Introduction</b>	<b>1</b>
I.8 General context . . . . .	1
I.9 Document outline . . . . .	2
<b>1 Thermo-hydrromechanical behavior of the Callovo-Oxfordian calystone</b>	<b>5</b>
1.1 Introduction . . . . .	6
1.2 Callovo-Oxfordian calystone . . . . .	7
1.2.1 Callovo-Oxfordian microstructure . . . . .	7
1.2.2 Mechanical behavior . . . . .	9
1.2.3 Hydraulic behavior . . . . .	12
1.2.4 Thermal pressurization . . . . .	16

1.3	<i>In situ</i> observations . . . . .	19
1.3.1	<i>In situ</i> stress state . . . . .	19
1.3.2	Fracture networks around the drifts . . . . .	20
1.3.3	Hydromechanical response of COx to excavation operations . . . . .	21
1.3.4	Thermal tests . . . . .	26
1.4	Effect of anisotropy and hydromechanical couplings on pore pressure evolution . . . . .	32
1.5	Numerical modeling of the excavation operations within Callovo-Oxfordian claystone . . . . .	37
1.5.1	Calibration of model parameters . . . . .	38
1.5.2	Material point tests . . . . .	38
1.5.3	Excavation modeling test . . . . .	39
1.5.4	Concluding remarks . . . . .	44
1.5.5	Outlook . . . . .	45
1.6	Numerical modeling of COx response to thermal loading . . . . .	50
1.6.1	Numerical modeling of TED experiment - DECOVALEX-2019 international project . . . . .	50
1.6.2	Numerical modeling of a single cell - ALC experiment . . . . .	55
1.6.3	Numerical modeling of THM response at repository scale . . . . .	58
1.6.4	Influence of different THM parameters . . . . .	62
1.6.5	Sobol Indices . . . . .	63
1.6.6	Random Finite Element Method (RFEM) . . . . .	64
1.6.7	Benchmark exercise of an HLW repository . . . . .	65
1.6.8	Outlook . . . . .	72
<b>2</b>	<b>Damage and fracturing of quasi-brittle heterogeneous materials</b>	<b>73</b>
2.1	Introduction . . . . .	74
2.2	A non-local damage framework . . . . .	76
2.2.1	Crack initiation . . . . .	77
2.2.2	Crack propagation . . . . .	78
2.2.3	Threshold comparison . . . . .	78
2.2.4	Local constitutive law . . . . .	79
2.2.5	Numerical implementation . . . . .	80
2.2.6	Numerical validation . . . . .	80
2.2.7	Experimental verification . . . . .	86
2.3	Towards a hydromechanical fracturing model . . . . .	92
2.3.1	Hydromechanical coupling scheme . . . . .	93
2.3.2	Application example and results . . . . .	94
2.4	Outlook . . . . .	97
<b>3</b>	<b>Seismic fragility of structures</b>	<b>99</b>
3.1	Introduction . . . . .	100
3.2	Fragility surfaces . . . . .	102
3.2.1	Structural model and analysis . . . . .	103
3.2.2	Selection of input time-histories . . . . .	104
3.2.3	Selection of strong-motion parameters . . . . .	105
3.2.4	Construction of fragility surfaces . . . . .	106
3.3	Vector-valued fragility functions . . . . .	109
3.3.1	Test structure and numerical model . . . . .	110

3.3.2	Nonlinear dynamic analyses . . . . .	112
3.3.3	Studied IMs . . . . .	113
3.3.4	Vector-valued fragility functions . . . . .	115
3.3.5	Bivariate fragility functions . . . . .	116
3.4	Extension of the method to multi-hazard risk assessment and damaged structures . .	117
3.4.1	Fragility curves for masonry structures subjected to permanent ground dis- placements and earthquakes . . . . .	117
3.4.2	Fragility curves for damaged structures . . . . .	121
3.5	Outlook . . . . .	125
<b>4</b>	<b>Perspectives</b>	<b>127</b>
4.1	Concluding statement . . . . .	127
4.2	Some research perspectives . . . . .	127
4.2.1	Numerical modeling of ductile tearing . . . . .	128
4.2.2	Seismic fragility of structures . . . . .	129
	<b>References</b>	<b>131</b>
	<b>List of figures</b>	<b>143</b>
	<b>List of tables</b>	<b>149</b>



# Synthèse des activités de recherche et d'enseignement

## S.1 Parcours professionnel et formation universitaire

Je suis actuellement le responsable du laboratoire d'études de mécanique sismique (EMSI) à l'Institut des Sciences Appliquées et de Simulations pour des énergies bas-carbone (ISAS) au CEA Paris-Saclay. Le laboratoire EMSI comprend une équipe d'environ 25 personnes (ingénieurs-chercheurs, techniciens, doctorants et post-doctorants) spécialisés en mécanique sismique. Les activités de recherche de l'EMSI couvrent différentes thématiques de la mécanique sismique telles que l'étude de l'endommagement des structures sous chargement sismique, l'interaction sol-structure et la simulation numérique haute-performance. Le laboratoire bénéficie des moyens expérimentaux exceptionnels telle que la table vibrante Azalée avec 6 degrés de liberté, une surface de 6 m x 6 m, et une charge utile de 1000 kN.

Entre décembre 2018 et février 2021, j'ai été le responsable du Laboratoire d'Intégrité des Structures et de Normalisation (LISN) spécialisé en mécanique de la rupture et l'intégrité des structures.

Avant de rejoindre le CEA en décembre 2018, en tant qu'ingénieur-chercheur à la Direction de la recherche et développement de l'Agence nationale pour la gestion des déchets radioactifs (Andra), je coordonnais le Groupement de Laboratoires « Mécanique des ouvrages et des composants des stockages ». Je participais également à la réalisation de travaux de recherche notamment au sujet de la réponse thermo-hydomécanique des argilites aux chargements thermiques, et la modélisation du comportement hydromécanique des ouvrages de stockage.

Entre août 2004 et mars 2012, j'ai travaillé en tant qu'ingénieur-chercheur au service Risques du Bureau de Recherches Géologiques et Minières (BRGM). Auparavant, j'ai effectué une thèse de doctorat suivie par une recherche postdoctorale au LMT (ENS Cachan).

Avant de venir en France en 1999, j'ai obtenu un diplôme d'ingénieur et un Master en génie civil de l'Université de Téhéran. J'ai travaillé entre 1996 et 1999 en tant qu'ingénieur dans un bureau d'études, essentiellement sur la conception de barrages et de structures souterraines.

## **S.2 Thématiques de recherche**

L'investigation de la durabilité des matériaux et de l'intégrité des structures soumis à différents types de chargement lors de leur vie constitue le socle commun de mes travaux de recherche. Ainsi, j'ai travaillé sur la fatigue thermomécanique de tuyauteries métalliques, la vulnérabilité sismique de structures, la fracturation des formations géologiques sous chargement thermo-hydro-mécanique, le comportement thermo-hydro-mécanique des ouvrages souterrains et les grandes déchirures ductiles dans les structures métalliques. Mes travaux de recherche sont basés sur des méthodes probabilistes, des modélisations numériques et des traitements statistiques des simulations numériques. L'objectif est de mieux cerner les incertitudes et de prendre en compte l'effet de la nature hétérogène des matériaux sur le comportement des structures. La prise en compte des couplages multi-physiques (thermique, hydraulique, chimique et mécanique) et leurs impacts sur la durabilité des matériaux et des structures constitue une autre partie de mes travaux. La plupart de ces travaux de recherche ont été réalisés dans le cadre de différents types de collaboration (projets ANR, européens, collaborations de recherche. . .). J'ai également eu l'occasion de co-diriger plusieurs travaux de doctorat et de post-doctorat (cf. section S.4).

### **S.2.1 Fatigue thermomécanique – thèse de doctorat et post-doctorat au LMT et EDF R&D**

Des réseaux de fissures dues à la fatigue thermique à grand nombre de cycles ont été mis en évidence dans certains composants de centrales nucléaires lors de contrôles techniques. Ces fissures peuvent être tolérées tant qu'une analyse de rupture montre qu'elles ne se propagent pas considérablement pendant la durée de vie résiduelle du composant étudié. L'estimation de la durée de vie des composants endommagés est donc cruciale pour définir des programmes de surveillance et de maintenance des centrales nucléaires. L'objectif de ces travaux (thèse et post-doctorat) a été d'étudier la formation, la propagation et la coalescence de réseaux de fissures et de proposer des modèles capables d'analyser la durée de vie des composants soumis à des chargements thermomécaniques cycliques. Pour étudier l'amorçage des fissures sous fatigue thermomécanique à grand nombre de cycles, un modèle 3D d'endommagement à deux échelles a été développé :

- à l'échelle mésoscopique, le comportement est thermo-élastique, la limite d'élasticité du matériau n'étant pas atteinte lors de la fatigue à grand nombre de cycles.
- le comportement du matériau à l'échelle microscopique est considéré comme thermo-élasto-plastique endommageable. La limite d'élasticité à cette échelle est prise égale à la limite de fatigue du matériau.

Une loi de localisation (au sens de l'homogénéisation) permettant le changement d'échelle et donc le calcul des grandeurs « micro » a été développée [A29]. Ecrit en 3D, ce modèle rend compte du caractère multiaxial du chargement. Le modèle a été programmé sous forme d'un post-processeur de calcul d'endommagement.

Une fois les fissures amorcées, la durée de vie du composant fissuré dépend de leur propagation.

Deux principaux axes de travail ont été suivis. Dans un premier temps, un outil de simulation bidimensionnelle de la propagation d'un réseau de fissures de fatigue a été développé. Dans ce cadre, une stratégie de modélisation basée sur l'incrément de propagation et pas sur le nombre de cycles a été adoptée afin de pouvoir traiter un très grand nombre de cycles [A31]. Cet outil, basé sur une technique de remaillage automatique, a permis la réalisation d'une série de calculs paramétriques mettant en avant le rôle de différents paramètres sur la durée de vie des composants multi-fissurés. Toutefois, cette stratégie de modélisation ne peut pas représenter toutes les situations possibles de réseaux formés. Pour analyser le problème de formation des réseaux de fissures ou pour estimer la durée de vie de structures sans supposer l'existence d'un réseau de fissures prédéfini, d'autres moyens de calcul sont nécessaires. Une approche probabiliste basée sur le modèle de Weibull a été mise au point dans cette optique. L'interaction entre les fissures à l'amorçage et lors de la propagation a été prise en compte en définissant une zone d'écran autour de chaque fissure amorcée [A30]. Ce modèle permet d'évaluer l'influence du niveau de l'hétérogénéité du matériau sur sa durée de vie.

## **S.2.2 Vulnérabilité sismique des bâtis – travaux de recherche réalisés au BRGM et en cours au CEA**

Dans l'évaluation probabiliste du risque, deux sources principales d'incertitudes aléatoires sont généralement distinguées : la variabilité due au mouvement fort (sismique) et celle due aux propriétés mécaniques de la structure étudiée. Des méthodes modernes d'évaluation du risque sismique sont basées sur des courbes de fragilité représentant la probabilité conditionnelle pour une structure ou une typologie de construction d'atteindre ou de dépasser un niveau d'endommagement donné, en fonction d'un niveau d'aléa sismique caractérisé par une mesure d'intensité. Ainsi, en raison de l'emploi d'un seul paramètre scalaire pour décrire le mouvement sismique, les courbes de fragilité usuelles ont tendance à négliger la variabilité inhérente aux caractéristiques du signal non décrite par une unique mesure d'intensité.

Depuis l'année 2006, dans le cadre de deux projets ANR (VEDA et EVSIM) et d'un projet européen (PERPETUATE), nous avons développé une méthodologie stochastique pour définir d'abord des surfaces de fragilité où le mouvement sismique est représenté par deux paramètres du mouvement fort [A28] (au lieu d'un seul paramètre utilisé pour la construction des courbes de fragilité). Les surfaces de fragilité ont été développées en évaluant localement la probabilité d'atteindre un niveau de dommage. Les résultats obtenus mettent en évidence le rôle non négligeable d'un deuxième paramètre sur l'évaluation de la fragilité du bâtiment. La considération d'un seul paramètre permettrait la construction d'une courbe moyenne. Toutefois, une telle courbe moyenne ne peut pas prendre en compte l'effet de la variabilité du mouvement fort représentée par le deuxième paramètre. Grâce aux surfaces de fragilité, l'effet de cette variabilité peut être estimé et correctement propagé dans une chaîne d'évaluation du risque.

Puis, des courbes de fragilité vectorielles, pour lesquelles une combinaison de plusieurs paramètres du mouvement fort est considérée comme une mesure d'intensité, ont été introduites [A22]. Cette

méthodologie prend également en compte l'effet de la variabilité des propriétés mécaniques des matériaux de construction. Une procédure particulière a également été proposée afin de réduire le nombre de calculs numériques nécessaires pour construire ces surfaces/courbes. Ces travaux ont montré que le choix des paramètres les plus représentatifs dépend de la structure à étudier et que le passage d'un à deux paramètres de mouvement fort diminue l'incertitude de la procédure d'évaluation du risque.

Ce cadre a été étendu aux analyses multirisques et multi-aléas où plusieurs mesures d'intensité sont utilisées pour représenter l'effet d'aléas différents. Comme exemple d'application, dans le cadre du projet européen PERPETUATE, la combinaison d'un tassement permanent et d'une action sismique a été étudiée pour un bâtiment type représentant un monument historique. Des courbes de fragilité multi-aléas ont ainsi pu être développées pour ce bâtiment type [A19].

Enfin, l'impact du nombre de calculs réalisés pour la construction des courbes de fragilité a été étudié [A16]. Pour ce faire, les courbes de fragilité ont été construites à partir de nuages aléatoires des réponses dynamiques d'une structure en utilisant différentes méthodes de régression. Différentes mesures statistiques ont été utilisées pour vérifier la qualité des fonctions de fragilité obtenues et des recommandations ont été formulées pour le choix du nombre de calculs nécessaires.

### **S.2.3 Endommagement et fracturation de matériaux hétérogènes à comportement quasi-fragile : application à l'étude de l'intégrité du stockage géologique de $CO_2$ – travaux de recherche réalisés au BRGM**

Les géomatériaux en général et les roches en particulier présentent un comportement fragile en traction et quasi-fragile sous faible confinement. La rupture de la roche dans ces situations représente un caractère aléatoire et la contrainte de rupture diminue souvent avec la taille de l'échantillon.

Dans le cadre de la thèse de N. Guy réalisée au LMT et au BRGM, un modèle probabiliste a été développé pour prendre en compte l'effet de l'hétérogénéité du matériau sur son endommagement et sa fissuration [A24]. Deux seuils différents, tous les deux calculés avec une contrainte régularisée, ont été adoptés pour décrire l'amorçage et la propagation des fissures. Pour l'amorçage, un modèle de Weibull a été utilisé pour traduire l'effet de l'hétérogénéité de la roche sur sa probabilité de rupture. Une fois qu'une fissure est amorcée au sein d'un élément, sa propagation est vérifiée par une méthode faisant appel à la mécanique élastique linéaire de la rupture. De ce fait, une transition de la modélisation de l'amorçage des fissures par la mécanique de l'endommagement vers la modélisation de sa propagation par la mécanique de la rupture a été mise en place. En effet, l'opérateur de régularisation des contraintes choisi permet non seulement d'obtenir des résultats indépendants du maillage mais fournit aussi directement la valeur du facteur d'intensité des contraintes.

Ce modèle a été ensuite étendu pour prendre en compte des couplages hydromécaniques à travers le concept de la contrainte effective. Un schéma de chainage hydromécanique a été développé dans lequel les équations hydrauliques et mécaniques sont résolues séparément. Le couplage est ensuite assuré par le biais de l'influence de chaque phénomène sur les paramètres de contrôle de l'autre. Un

tel schéma nous permet : (i) d'avoir des modèles complexes pour chaque phénomène ; (ii) d'optimiser les développements numériques nécessaires. Dans ce cadre nous avons fait le choix de développer des schémas de chainage entre un simulateur thermohydraulique (TH) et un simulateur mécanique (M). Un tel schéma de couplage a été développé entre le code TOUGH2 pour la partie TH et le code-aster pour la partie M [A27], ainsi qu'entre les modules H et M du code-aster [B3].

L'évaluation de l'impact de l'endommagement et de la fracturation sur les propriétés hydrauliques d'un milieu poreux constitue une question centrale pour beaucoup d'applications. Ceci est d'autant plus difficile quand des réseaux de fissures denses se trouvent dans un milieu poreux où les échanges hydrauliques entre les fissures et le milieu ne sont pas négligeables. Dans le cadre de la thèse de M.N. Vu (Navier – BRGM) une méthode numérique visant à modéliser des écoulements dans des milieux poreux multi-fissurés, ainsi qu'à déterminer leur perméabilité effective, a été développée. Des solutions générales du potentiel sont proposées sous la forme d'une équation intégrale singulière décrivant l'écoulement dans et autour des fissures entourées par une matrice infinie soumise à un champ lointain. Des outils numériques ont été développés en se basant sur la méthode des éléments de frontières afin de résoudre les équations générales du potentiel [A23]. Cela permet, d'une part, de modéliser l'écoulement stationnaire dans un domaine poreux contenant un grand nombre de fissures et, d'autre part, de proposer une solution semi-analytique de l'infiltration dans une fissure isolée dépendant de la perméabilité de la matrice, de la conductivité hydraulique de la fissure et d'une variable géométrique de la fissure. Cette dernière est l'élément essentiel pour déterminer la perméabilité effective d'un milieu poreux fissuré en utilisant des schémas d'homogénéisation. L'approche par sous-structuration permet l'extension de la solution générale du potentiel, écrite pour un domaine infini, à celle d'un domaine fini [A20]. Le modèle de la perméabilité effective est appliqué dans le contexte du stockage géologique du  $CO_2$  en vue d'étudier le comportement d'une zone de faille constituée par un noyau argileux et de zones fissurées. La surpression engendrée par l'injection dans le réservoir peut affecter la perméabilité de zones fissurées et provoquer la réactivation de la faille si elle dépasse un seuil critique. Dans ce schéma, l'hétérogénéité de la zone de faille est prise en compte par un modèle spécifique à deux échelles [A15]. A l'échelle d'un VER de la zone de faille, les fractures sont modélisées par l'approche décrite précédemment. A l'échelle de la faille, un modèle basé sur le milieu continu équivalent est utilisé. Les résultats de simulations numériques permettent d'évaluer, d'une part, le risque de la remontée de saumure aux aquifères supérieurs, et d'autre part, le risque d'amorçage d'une rupture sismique sur le plan de la faille.

Concernant l'intégrité des puits, un modèle poromécanique est développé pour identifier comment les réactions chimiques de la carbonatation peuvent avoir un impact sur le comportement mécanique du ciment de puits dans le contexte du stockage du  $CO_2$  [A25]. Le modèle permet d'évaluer l'évolution de la surpression des pores, de la porosité et de la déformation du squelette solide au cours du processus de carbonatation. Les principales réactions chimiques qui se produisent dans le ciment et leurs conséquences sur les volumes de ciment dissous et de carbonate précipité sont identifiées. Ces informations sont importées dans un modèle poromécanique. Ce qui permet d'évaluer le risque de l'endommagement de ciment de puits soumis à l'intrusion de  $CO_2$  par le calcul de l'énergie libre

stockée dans la matrice solide.

#### **S.2.4 Comportement THM de l'argilite du Callovo-Oxfordien : travaux de recherche réalisés à l'Andra**

L'argilite du Callovo-Oxfordien (COx) est considérée comme une potentielle formation hôte pour le stockage profond des déchets radioactifs en France. L'Andra a commencé en 2000 la construction du Laboratoire Souterrain de Meuse/Haute-Marne (LS-M/HM) avec l'objectif principal de démontrer la faisabilité d'un stockage géologique dans cette argilite. Un réseau de galeries expérimentales a été excavé et instrumenté pour étudier le comportement de la roche. L'étude de la fracturation de la roche due au creusement des tunnels et l'évolution de la convergence des parois des tunnels au cours du temps est un sujet important pour le dimensionnement des ouvrages de stockage ainsi que pour l'évaluation de la sûreté de stockage à long-terme.

Une analyse approfondie de la convergence des galeries en lien avec la fracturation induite par leur excavation a été réalisée dans le cadre de la thèse de L.M. Guayacan-Carrillo (Navier/Andra). Cette analyse se base sur une loi semi-empirique et permet d'obtenir des prévisions fiables de la convergence à long terme, qui sont utiles pour le dimensionnement et la prévision de la performance du soutènement à long terme [A9, A13]. Ensuite, la réponse anisotrope du champ de pression interstitielle observé in situ a été étudiée en se basant sur une approche poroélastique anisotrope. Une analyse de l'apparition de la rupture montre le rôle clé que joue le couplage hydromécanique dans l'extension de la zone fracturée [A8].

Pour l'étude de la fracturation induite autour des ouvrages, une méthode numérique basée sur des éléments finis enrichis (E-FEM) a été mise en place dans le cadre de la thèse de P. Hauseux réalisée au Laboratoire de Mécanique de Lille en collaboration avec l'Andra [A12]. Un modèle Éléments Finis 3D (méthode E-FEM) a été développé pour représenter la fissuration. Plusieurs critères sont proposés pour caractériser l'amorçage des fissures avec une ouverture en mode I ou un glissement en mode II. L'influence de l'anisotropie des propriétés de la roche et du champ de contrainte in situ sur les réseaux de fractures et la convergence des galeries a été étudiée. Un modèle d'endommagement anisotrope a également été développés dans le cadre de la thèse d'E. Trivelatto (Navier/Andra).

Plusieurs modèles ont été développés dans le cadre du programme de recherche de l'Andra pour reproduire le comportement hydromécanique des argilites. Un exercice de benchmark a été organisé entre 2012 et 2015 afin d'obtenir un état des lieux factuel des modèles disponibles et d'investiguer l'influence de différentes hypothèses de base sur la réponse obtenue [A10]. Deux séries de cas tests de simulation ont été proposées dans ce cadre. Dans un premier temps, des chemins de contraintes représentatifs d'un chemin de chargement au voisinage de la paroi d'un tunnel ont été proposés. Les modélisations ont été effectuées à l'échelle d'un point matériel afin de s'affranchir des problèmes liés aux structures. Ensuite, des cas de simulations de creusement des tunnels avec différentes conditions aux limites et dans différents champs de contraintes initiales ont été proposés. Les résultats obtenus montrent que la prise en compte de l'anisotropie de l'argilite et l'utilisation d'une technique

de régularisation de la localisation des déformations peuvent fortement améliorer les résultats des modélisations par rapport aux observations in situ. Les résultats de cet exercice ont été publiés sous la forme d'un numéro spécial de la revue « Computers and Geotechnics » pour lequel j'ai été co-éditeur invité avec le Prof. Antonio Gens de l'Universitat Politècnica de Catalunya.

Une partie des déchets radioactifs sont des déchets exothermiques émettant de la chaleur pendant une longue période. L'augmentation de la température dans un milieu poreux peu perméable tel que le Callovo-Oxfordien engendre une surpression de fluide poral, essentiellement à cause de la différence de coefficient de dilatation thermique de l'eau porale ( $\sim 10^{-4} K^{-1}$ ) et du squelette solide des argilites ( $\sim 10^{-5} K^{-1}$ ). Cette augmentation de la pression interstitielle affecte l'état des contraintes effectives et dans certains cas peut provoquer des ruptures en cisaillement ou de la fracturation hydraulique. L'Andra a mené un vaste programme de recherche pour caractériser ce phénomène ainsi que pour le modéliser à différentes échelles (e.g., [A4, C2, C4]). Dans ce cadre, j'ai coordonné et participé à la Task E de projet international DECOVALEX au sujet de la modélisation numérique de la réponse THM du COx aux chargements thermiques à différentes échelles [A1, A2, A3]

### **S.2.5 Déchirure ductile des structures métalliques – travaux de recherche en cours au CEA**

Actuellement, les analyses de résistance à la déchirure ductile sont limitées à quelques mm de propagation. Cette limitation vient du critère utilisé et des méthodes d'obtention de la courbe  $J - \Delta a$  (essais sur éprouvettes CT). Cependant, les composants de grande dimension peuvent souvent tolérer de grandes déchirures ductiles, bien au-delà de cette limite. Ceci est particulièrement problématique lorsque l'on cherche à déterminer le chargement maximum que peut endurer le composant.

Une action pluriannuelle est actuellement en cours au Laboratoire d'Intégrité des Structures de Normalisation (LISN) afin d'améliorer les modèles décrivant la déchirure ductile à l'échelle des structures industrielles. Cette action comprend un volet expérimental et un autre de modélisation. Le volet expérimental vise à étudier la transférabilité des propriétés obtenues à partir d'échantillons de laboratoire (éprouvettes axisymétrique entaillées, éprouvettes CT) vers des structures industrielles. Dans le cadre de projet européen Atlas+, un essai de déchirure ductile sur une maquette soudée préparée spécifiquement pour cette étude vient d'être réalisé. L'objectif de l'essai est de déterminer la résistance à la déchirure ductile de liaisons soudées en acier inoxydable. Les caractéristiques mécaniques de la soudure en acier inoxydable vieillie ont été auparavant identifiées dans le cadre d'une campagne expérimentale.

Le volet de modélisation porte sur le développement de méthodes numériques pour la simulation de la déchirure ductile en cas de scénario accidentel. Ce type d'approche a pour but de prédire l'amorçage de fissures au sein d'une structure métallique, ainsi que leur propagation sur de grandes distances. L'objectif est de développer une approche de modélisation numérique applicable à l'échelle des structures industrielles. La modélisation de la déchirure ductile par des approches locales présente actuellement un certain nombre de difficultés. L'utilisation de ce type de modèle (Gurson, Rousselier,

GTN, ...) dans un code de calculs par éléments finis permet de réaliser des simulations avec de bons résultats pour décrire des phénomènes non-linéaires progressifs à l'échelle microscopique (germination, croissance et coalescence des cavités). En revanche, pour des cas où les phénomènes représentés vont atteindre une échelle supérieure à celle de discrétisation des phénomènes tels que la localisation de déformation ou la dépendance au maillage peuvent apparaître. Le travail en cours vise à développer un schéma de régularisation couplé à une méthode de remaillage automatique et de projection de champs afin d'alléger le temps de calcul et rendre des simulations tridimensionnelles des structures industrielles accessibles avec des lois de comportement avancées.

### S.3 Activités d'enseignement

- Depuis 2014, je suis le principal intervenant du cours de « énergies renouvelables » pour les élèves de M1 génie civil (14 heures de CM + 12 heures de TD) à l'Ecole normale supérieure Paris-Saclay. Le cours couvre différents aspects tels qu'un panorama général sur la production d'énergie et les défis associés, l'énergie éolienne, l'énergie hydroélectrique, la géothermie, la biomasse, le stockage d'énergie et le stockage géologique du  $CO_2$ .
- Depuis 2017, j'interviens dans le cours de « mécanique des roches » (6 heures de CM) pour les élèves de M2 au département des sciences de la terre, l'Université Paris-Saclay.
- Depuis 2018, j'interviens dans le cours de « Approfondissement en Géologie de l'ingénieur » (3 heures de CM) au département génie civil et construction de l'Ecole des Ponts ParisTech. L'intervention concerne le stockage profond des déchets radioactifs.
- Depuis 2020, j'interviens dans le cours de « Ouvrages, énergie et risques » (3 heures de CM) au département génie civil et construction de l'Ecole des Ponts ParisTech. L'intervention concerne les énergies marines.

### S.4 Encadrement d'étudiants et de post-doctorants

- **Chercheurs post-doctorants**
  - C. Plúa (2018) Up-scaling the thermo-hydro-mechanical behavior of the  $CO_x$  claystone, from in-situ experiments to repository scale. Taux d'encadrement 100%
  - M. Vitel (2016-2018) Modélisation thermo-hydro-mécanique des expérimentations thermiques in situ à grande échelle. Taux d'encadrement 100%.
  - S. Ghabezloo (2010) Modélisation probabiliste de l'endommagement des roches sous fortes contraintes de confinement. Taux d'encadrement 100%.
- **Doctorants**
  - E. Trivellato (2015-2018) Mécanismes de formation et modèle d'évolution de l'EDZ fracturée autour des ouvrages profonds dans les argilites, co-encadrée avec Dr. Amade Pouya et Dr. M.N. Vu. Taux d'encadrement 25% (Ecole des Ponts ParisTech/Andra).

- L.M. Guayacan Carrillo (2013-2016) Time-dependent behavior of underground drifts in Callovo-Oxfordien claystone: the role of mechanical anisotropy and hydromechanical couplings, co-encadrée avec Prof. Jean Sulem et Dr Siavash Ghabezloo. Taux d’encadrement 33% (Ecole des Ponts ParisTech/Andra)
- P. Hauseux (2012-2015) Modélisation numérique de la fissuration et propagation des incertitudes au travers de Méthodes Eléments Finis avec des approches non intrusives : Applications à des problèmes d’excavation, co-encadrée avec Prof. Jean-Baptiste Colliat. Taux d’encadrement 20% (Université Lille I/Andra)
- M.N. Vu (2009-2012) Modélisation des propriétés hydromécaniques des milieux poreux fractures par la méthode des éléments de frontières, co-encadrée avec Dr. Amade Pouya (ALERT PhD Prize 2013). Taux d’encadrement 50% (Ecole des Ponts ParisTech/BRGM).
- N. Guy (2006-2009) Modélisation probabiliste de l’endommagement des roches : application au stockage géologique du CO<sub>2</sub>, co-encadrée avec Dr. François Hild. Taux d’encadrement 50% (Ecole Normale Supérieure de Cachan/BRGM).

- **Etudiants de Master**

- R. Lemoine (2021) Etude de l’influence de l’historique des chargements mécanique et thermique sur la tenue de tuyauteries soumises à de forts séismes, co-encadré avec Dr. J.L. Fayard (CEA).
- R. Apperry (2021) Simulation numérique de la déchirure ductile par une approche locale couplée à une méthode de suppression d’éléments, co-encadré avec Dr. J. Bluthé (CEA).
- M. Anstett (2011) Une méthodologie stochastique pour la construction des surfaces de fragilité pour des bâtis courants (BRGM/IFMA).
- M. Chalmers (2008) The verification of fragility surfaces using a hybrid capacity spectrum method, co-encadré avec Dr John Douglas, Pierre Gehl et Prof. Tiziana Rossetto (BRGM/University College London).
- M. Khiar (2008) Construction des surfaces de fragilité pour l’évaluation de la vulnérabilité et risqué sismique des structures en béton armé, co-encadré avec Dr John Douglas et Pierre Gehl (BRGM/ENPC).
- N. Guy (2006) Modélisation probabiliste des réseaux de fissures dans les roches profondes, co-encadré avec Dr François Hild (BRGM/ENS Cachan).
- A. Mushtaq (2005) Un modèle probabiliste pour la formation et propagation des réseaux de fissures dans les roches hétérogènes, co-encadré avec Dr François Hild (BRGM/ENS Cachan).

## S.5 Responsabilités académiques

- **Fonction éditoriale dans des revues internationales**

- Computers and Geotechnics – “*Guest editor*” (avec Prof. Antonio Gens) du numéro spe-

cial “Numerical analysis of the hydromechanical response of Callovo-Oxfordian claystone in deep excavations” vol. 85, mai 2017

- **Organisation de workshops et de sessions dans les conférences internationales**
  - Avril 2018 : 5<sup>th</sup> Workshop of DECOVALEX2019 international project, Nancy, France
  - Avril 2018 : EGU2018 session ERE5.5 “Computational Methods for the Assessment of Barrier Integrity in Geological Repositories for Nuclear Waste Disposal and Contaminant Isolation”. Conveners: T. Nagel, I. Berre, J. Birkholzer, R. Blaheta, B. Graupner, H. Konietzky, J. Masmann, K-J Rölig, D. Seyedi
- **Comité scientifique de conférences**
  - 2021 : The Biot-Bazant Conference on Engineering Mechanics and Physics of Porous Materials, Northwestern University, USA.
  - 2019 : COGGUS2: Computational geomechanics and geoenvironment for underground and subsurface structures, Nancy, France.
  - 2017 : 6<sup>th</sup> Biot Conference on Poromechanics, Ecole des Ponts Paristech, Paris, France
  - 2017 : GeoProc2017: 6<sup>th</sup> International Conference on Coupled THMC Processes in Geosystems, Paris, France
  - 2016 : International Geotechnics Symposium cum International Meeting of CSRME & 14<sup>th</sup> Biennial National Congress HKU Main Campus, Hong Kong, China
  - 2015 : CIGOS 2015: 3<sup>rd</sup> French-Vietnamese conference on innovation in construction, Cachan, France
- **Rapporteur d’articles scientifiques pour les revues suivantes**
  - International Journal of Pressure Vessels and Piping, Rock Mechanics and Rock Engineering, Environmental Earth Sciences, International Journal of Rock Mechanics and Mining Engineering, Geomechanics for Energy and the Environment, Journal of Rock Mechanics and Geotechnical Engineering, International Journal of Greenhouse Gas Control, Engineering Structures, Earthquake Engineering and Structural Dynamics, Bulletin of Earthquake Engineering, Bulletin of Seismological Society of America

## S.6 Bilan de publications scientifiques

### S.6.1 Publications scientifiques

- 3 chapitres de livre
- 31 articles dans des revues internationales à comité de lecture
- 1 article dans une revue française à comité de lecture
- 38 communications dans des conférences nationales et internationales

## **S.6.2 Bibliométrie Google Scholar et Publon (WOS)**

Au 25 mai 2021 :

- 77 articles référencés dans Google Scholar. Le nombre total de citations est de 1207 avec un indice H de 20 : <https://scholar.google.ca/citations?user=7z4dJ50AAAAJ>
- 40 articles référencés dans Publon. Le nombre total de citations est de 635 avec un indice H de 16. Web of Science ResearcherID : A-1769-2012 (<http://www.researcherid.com/rid/A-1769-2012>)

## S.7 Liste de publications

### S.7.1 Chapitres de livre

- B1. Armand G., Bumbiler F., Conil N., Cararreto S., de la Vaissiere R., Noiret A., **Seyedi D.**, Talandier J., Vu M.N., Zghondi J. (2017) The Meuse/Haute-Marne Underground Research Laboratory: mechanical behavior of the Callovo-Oxfordian claystone. CH. 19, in *Rock Mechanics and Engineering*.
- B2. Armand G., **Seyedi D.** (2017) Les phénomènes thermo-hydromécaniques liés au stockage des déchets radioactifs : exemple du projet Cigéo, in *Manuel de Mécanique des Roches, Volume V – Thermodynamique des roches*, Berest P., Merrien-Soukatchoff V., Gasc M. Eds., Presse des Mines, pp. 235-261.
- B3. **Seyedi D.M.**, Guy N., Sy S., Granet S., Hild F. (2012) A non-local damage model for heterogeneous rocks – application to rock fracturing evaluation under gas injection conditions, in *Geomechanics in CO2 Storage Facilities*, Pijaudier-Cabot G., Pereira J.M., Eds., pp. 59-73, John Wiley & Sons, Inc., Hoboken, NJ USA.

### S.7.2 Publications dans des revues internationales à comité de lecture

- A1. Plúa C., Vu M.N., **Seyedi D.M.**, Armand G. (à paraître) Effects of inherent spatial variability of rock properties on the thermo-hydro-mechanical responses of a high-level radioactive waste geological disposal, *International Journal of Rock Mechanics & Mining Sciences*.
- A2. **Seyedi D.M.**, Plúa C., Vitel M., Armand G., Rutqvist J., Birkholzer J., Xu H., Guo R., Thatcher K.E., Bond A.E., Wang W., Nagel T., Shao H., Kolditz O. (2021) Upscaling THM modelling from small-scale to full-scale in-situ experiment in the Callovo-Oxfordian claystone, *International Journal of Rock Mechanics & Mining Sciences*, **144**, pp. 104-152.
- A3. Guo R., Thatcher K., **Seyedi D.M.**, Plúa C. (2020) Calibration of the thermo-hydro-mechanical parameters of the Callovo-Oxfordian claystone and the modelling of the ALC experiment, *International Journal of Rock Mechanics & Mining Sciences*, **132**, 104351.
- A4. Conil N., Vitel M., Plúa C., Vu M.N., **Seyedi D.**, Armand G. (2020) In situ investigation of the THM behavior of the Callovo Oxfordian claystone. *Rock Mechanics and Rock Engineering*, **53**, pp. 2747–2769.
- A5. Vu M.N., Pouya A., **Seyedi D.M.** (2018) Effective permeability of three-dimensional porous media containing anisotropic distributions of oriented elliptical disc-shaped fractures with uniform aperture, *Advances in Water Research*, **118**, pp. 1-11.
- A6. Guayacán-Carrillo L.M., Sulem J., **Seyedi D.M.**, Ghabezloo S., Armand G. (2018) Size effect on the time-dependent closure of drifts excavated in Callovo-Oxfordian claystone. *International Journal of Geomechanics*, **18**(10).
- A7. Guy N., **Seyedi D.M.**, Hild F. (2018) Characterizing fracturing of clay-rich Lower Watrous rock: From laboratory experiments to nonlocal damage-based simulations, *Rock Mechanics and Rock*

- Engineering*, **51**, pp. 1777-87.
- A8. Guayacán-Carrillo L.M., Ghabezloo S., Sulem J., **Seyedi D.M.**, Armand G. (2017). Tunnel excavation in low-permeability anisotropic ground: Effect of anisotropy and hydro-mechanical couplings on pore pressure evolution. *International Journal of Rock Mechanics and Mining Sciences*, **97**, pp. 1-14.
- A9. Guayacán-Carrillo L.M., Sulem J., **Seyedi D.M.**, Ghabezloo S., Noiret A., Armand G. (2017) Convergence analysis of an unsupported micro-tunnel at the Meuse/Haute-Marne underground research laboratory. In: *Radioactive Waste Confinement: Clays in Natural and Engineered Barriers*, Geological Society of London (GSL) Special Publication (SP), <https://doi.org/10.1144/SP443.24>
- A10. **Seyedi D.M.**, Armand G., Noiret A. (2017) “Transverse action - A model benchmark exercise for numerical analysis of the Callovo-Oxfordian claystone hydromechanical response to excavation operations”, *Computers and Geotechnics*, **85**, pp. 287-305.
- A11. Armand G., Conil N., Talandier J., **Seyedi D.M.** (2017) Fundamental aspects of the hydromechanical behaviour of Callovo-Oxfordian claystone: From experimental studies to model calibration and validation, *Computers and Geotechnics*, **85**, pp. 277-286.
- A12. Hauseux P., Roubin E., **Seyedi D.M.**, Colliat J.B. (2016) FE modelling with strong discontinuities for 3D tensile and shear fractures: application to underground excavation, *Computer Methods in Applied Mechanics and Engineering*, **309**, pp. 269-287.
- A13. Guayacán-Carrillo L.M., Sulem J., **Seyedi D.M.**, Ghabezloo S., Noiret A., Armand G. (2016) Long-term anisotropic convergence in drifts excavated in Callovo-Oxfordian claystone, *Rock Mechanics and Rock Engineering*, **49**, pp. 97-114.
- A14. Paroen B., **Seyedi D.M.**, Collin F. (2015) Shear banding modelling in cross-anisotropic rocks, *International Journal of Solids & Structures*, **72**, pp. 63-87.
- A15. **Seyedi D.M.**, Vu M.N., Pouya A. (2015) A two-scale hydromechanical model for fault zones accounting for their heterogeneous structure, *Computers and Geotechnics*, **68**, pp. 8-16.
- A16. Gehl P., Douglas J., **Seyedi D.M.** (2015) Influence of the number of dynamic analyses on the accuracy of structural response estimates, *Earthquake Spectra*, **31**, pp. 97-113.
- A17. Karatzetzou A., Negulescu C., Manakou M., François B., **Seyedi D.M.**, Ptilakis D., Ptilakis K. (2015) Microtremor measurements for the seismic hazard and the structural identification of historical buildings in Rhodes, *Bulletin of Earthquake Engineering*, **13**, pp. 331-345.
- A18. Douglas J., **Seyedi D.M.**, Ulrich T., Modaressi H., Foerster E., Ptilakis K., Ptilakis D., Karatzetzou A., Gazetas G., Garini E., Loli M. (2015) Evaluation of seismic hazard for assessment of historical elements at risk: description of input and selection of intensity measures, *Bulletin of Earthquake Engineering*, **13**, pp. 49-65.
- A19. Negulescu C., Ulrich T., Baills A., **Seyedi D.M.** (2014) Fragility curves for masonry structures submitted to permanent ground displacements and earthquakes, *Natural Hazards*, **74**, pp. 1461-1474.
- A20. Vu M.N., Pouya A., **Seyedi D.M.** (2014) Theoretical and numerical study of the steady-state flow through finite fractured porous media, *International Journal for Numerical and Analytical*

*Methods in Geomechanics*, **38**, pp 221-235.

- A21. Armand G., Noiret A., Zghondi J., **Seyedi D.M.** (2013) Short and long term behaviors of drifts in the Callovo-Oxfordian claystone at the Meuse Haute-Marne Underground Research Laboratory, *Journal of Rock Mechanics and Geotechnical Engineering*, **5**, pp. 221-230.
- A22. Gehl P., **Seyedi D.M.**, Douglas J. (2013) Vector-valued fragility functions for seismic risk evaluation, *Bulletin of Earthquake Engineering*, **11**, pp 365-384.
- A23. Vu M.N., Pouya A., **Seyedi D.M.** (2013) Modelling of steady-state fluid flow in 3D fractured isotropic porous media: Application to effective permeability calculation, *International Journal for Numerical and Analytical Methods in Geomechanics*, **37**, pp 2257–2277.
- A24. Guy N., **Seyedi D.M.**, Hild F. (2012) A probabilistic nonlocal model for crack initiation and propagation in heterogeneous brittle materials, *International Journal of Numerical Methods in Engineering*, **90**, pp 1053-1072.
- A25. Fabbri A., Jacquemet N., **Seyedi D.M.** (2012) A chemo-poromechanical model of oilwell cement carbonation under CO<sub>2</sub> geological storage conditions, *Cement and Concrete Research*, **42**, pp 8-19.
- A26. Guy N., **Seyedi D.M.**, Hild F. (2010) Hydro-mechanical modeling of geological CO<sub>2</sub> storage and the study of possible caprock fracture mechanisms, *Georisk*, **4**, pp 110-117.
- A27. Rohmer J., **Seyedi D.M.** (2010) Coupled large scale hydromechanical modelling for caprock failure risk assessment of CO<sub>2</sub> storage in deep saline aquifers, *Oil & Gas Science and Technology – Rev. IFP*, **65**, pp 503-517.
- A28. **Seyedi D.M.**, Gehl P., Douglas J., Davenne L., Mezher N., Ghavamian S. (2010) Development of seismic fragility surfaces for reinforced concrete buildings by means of nonlinear time-history analysis, *Earthquake Engineering and Structural Dynamics*, **39**, pp 91-108.
- A29 Desmorat R., Khan A., **Seyedi M.**, Sermage J.F. (2007) Two scale damage model and related numerical issues for thermo-mechanical High Cycle Fatigue, *European Journal of Mechanics - A/Solids*, **26**, pp 909-935.
- A30. Malyésys N., **Seyedi M.**, Vincent L., Hild, F. (2006) On the formation of crack networks in high cycle fatigue, *Comptes Rendus Mécanique*, **334**, pp 419-424.
- A31. **Seyedi M.**, Taheri S., Hild F. (2006) Numerical modeling of crack propagation and shielding effect in a striping network, *Nuclear Engineering and Design*, **236**, pp 954-964.

### S.7.3 Publication dans une revue française à comité de lecture

- F1. **Seyedi M.**, Hild F. (2007) Towards a probabilistic model for the formation of crack networks in rocks (In French), *Revue Française de Géotechnique*, **119**, pp. 73-82.

### S.7.4 Communications dans des conférences internationales

- C1. **Seyedi D.**, Vitel M., Vu M.N., Armand G. (2018) Key parameters controlling thermo-hydro-mechanical pressurization in Callovo-Oxfordian claystone, *International Symposium on Energy*

- Geotechnics (SEG-2018). Lausanne, Switzerland
- C2. **Seyedi D.**, Armand G., Conil N., Vitel M., Vu M.N. (2017) On the thermo-hydro-mechanical pressurization in Callovo-Oxfordian claystone under thermal loading, 6<sup>th</sup> Biot Conference on Poromechanics, July 9-13, Paris, France.
- C3. Guayacán-Carrillo L.M., Ghabezloo S., Sulem J., **Seyedi D.**, Armand G. (2017) Tunnel excavation in low-permeability anisotropic ground: Effect of anisotropy and hydro-mechanical couplings on pore pressure evolution, 6<sup>th</sup> Biot Conference on Poromechanics, July 9-13, Paris, France.
- C4. Vitel M., **Seyedi D.**, Armand G., Conil N. (2017) Thermo-hydro-mechanical modeling of an in situ heating test in the Callovo-Oxfordian claystone, July 5-7, 6<sup>th</sup> International Conference on Coupled THMC Processes in Geosystems, Paris, France.
- C5. Guayacán-Carrillo L.M., Sulem J., Ghabezloo S., **Seyedi D.M.**, Armand G. (2016) Tunnel excavations in low-permeability anisotropic ground: hydromechanical couplings. EMI International Conference, Metz, October 2016.
- C6. Guayacán-Carrillo L.M., Sulem J., Noiret A., **Seyedi D.M.**, Ghabezloo S., Armand G. (2016) The effect of over excavation on the time-dependent convergence of a drift in Callovo-Oxfordian claystone. In: Ulusay et al. (eds), Rock Mechanics and Rock Engineering: From the Past to the Future. Proc. ISRM International Symposium and EUROCK 2016, August 2016, pp 945-950. ISBN 978-1-138-03265-1.
- C7. Guayacán-Carrillo L.M., Ghabezloo S., Sulem J., **Seyedi D.M.**, Noiret A., Armand G (2016). Tunnel excavation in low permeability ground: effect of anisotropy on excess pore pressure. In: Ulusay et al. (eds), Rock Mechanics and Rock Engineering: From the Past to the Future. Proc. ISRM International Symposium and EUROCK 2016, August 2016, pp 463-467. ISBN 978-1-138-03265-1.
- C8. **Seyedi D.**, Vu M.N., Armand G, Noiret A. (2015) Numerical modeling of damage patterns around drifts in the Mesu/Haute-Marne Underground Research Laboratory. The 13<sup>th</sup> Int. ISRM Congress, May 10 to 13, Montreal, Canada.
- C9. Guayacán-Carrillo L.M., Sulem J., **Seyedi D.**, Ghabezloo S., Noiret A., Gilles A. (2015) Anisotropic closure of a drift in Callovo-Oxfordian Claystone based on in-situ convergence data. The 13<sup>th</sup> Int. ISRM Congress, May 10 to 13, Montreal, Canada.
- C10. Armand G., Noiret A., Morel J., **Seyedi D.** (2015) Pore pressure change during the excavation of deep tunnels in the Callovo-Oxfordian Claystone. The 13<sup>th</sup> Int. ISRM Congress, May 10 to 13, Montreal, Canada.
- C11. Souley M., Ghoreychi M., Kazmierczak J.B., Armand G., **Seyedi D.** (2015) An anisotropic elastoplastic model for geomaterials and numerical implementation. The 13<sup>th</sup> Int. ISRM Congress, May 10 to 13, Montreal, Canada.
- C12. Hauseux P., Colliat J.B., **Seyedi D.** (2015) 3D Numerical modeling with E-FEM method of induced fractures around drifts after an excavation. 13<sup>th</sup> U.S. National Congress of Computational Mechanics, July 26-30, San Diego, CA, USA.

- C13. Guayacán-Carrillo L.M., Sulem J., **Seyedi D.**, Ghabezloo S., Noiret A., Gilles A. (2014) Analysis of convergence measurements in drifts in Callovo-Oxfordian Claystone. 25<sup>th</sup> ALERT Workshop, 29 Sep. – 2<sup>nd</sup> Oct., Aussois, France.
- C14. Hauseux P., Colliat J.B., Shao J., **Seyedi D.** (2014) Probabilistic Finite Element Analysis of nonlinear systems: Application to tunnel excavation. 11<sup>th</sup> World Congress on Computational Mechanics (WCCM XI), 20-25 July, Barcelona, Spain.
- C15. **Seyedi D.**, Armand G. (2013) Numerical modeling of fracture patterns around deep underground drifts. The 3<sup>rd</sup> International Symposium on Computational Geomechanics (ComGeo III), 21-23 August, Krakow, Poland.
- C16. Réveillère A., Gehl P., **Seyedi D.**, Modaressi H. (2012) Development of seismic fragility curves for mainshock-damaged reinforced-concrete structures. 15<sup>th</sup> World Conference on Earthquake Engineering, Lisbon, Portugal.
- C17. **Seyedi D.**, Ducellier A., Vu M.N., Pouya A. (2011) A two-scale model for simulating the hydromechanical behavior of faults during  $CO_2$  geological storage operation. 45<sup>th</sup> US Rock Mechanics Symposium, 27-29 June, San Francisco, USA.
- C18. Gehl P., Sy S., **Seyedi D.** (2011) Developing fragility surfaces for more accurate seismic vulnerability assessment of masonry buildings. Computational Methods in Structural Dynamics and Earthquake Engineering (COMPDYN 2011), 22-24 June, Corfu, Greece.
- C19. Gravaud I., Sochala P., Fabbri A., **Seyedi D.** (2011) Numerical Chemo-hydro-mechanical Coupling Method for Well Cement Integrity in a  $CO_2$  Storage Context. 1<sup>st</sup> Sustainable Earth Sciences Conference Exhibition – Technologies for Sustainable Use of the Deep Sub-surface, 8-11 November 2011, Valencia, Spain.
- C20. Pouya A., Vu M. N., **Seyedi D.** (2001) Modelling of effective permeability of fracture networks in permeable rock formation by singular integral equations method. In Proceedings of Multiphase Flow - 6<sup>th</sup> International Conference on Computational and Experimental Methods in Multiphase and Complex Flow, Kos, Greece.
- C21. Ducellier A., **Seyedi D.**, Foerster E. (2010) A coupled hydromechanical fault model for the study of the integrity and safety of geological storage of  $CO_2$ . GHGT10, 19-23 Sept., Amsterdam, Netherlands.
- C22. Sy S., Fabbri A., Jacquemet N., Garaffa L.-H., **Seyedi D.** (2010) Evaluation of the  $CO_2$  leakage risk along the abandoned wells in the French context. GHGT10, 19-23 Sept., Amsterdam, Netherlands.
- C23. **Seyedi D.**, Guy N., Hild F., Granet S. (2010) A coupled hydromechanical damage model for heterogeneous rocks. 9<sup>th</sup> World Congress on Computational Mechanics, 19-23 July, Sydney, Australia.
- C24. **Seyedi D.**, Guy N., Granet S., Chavant C. (2009) Probabilistic modeling of induced damage around an underground gallery due to gas injection. 4<sup>th</sup> International Biot Conference on Poromechanics, pp. 177-182, 8-10 June, NY, USA.
- C25. Fabbri A., Jacquemet N., **Seyedi D.** (2009) Modelling of the chemio-mechanical behaviour of

- a wellbore cement plug in a context of  $CO_2$  storage. 4<sup>th</sup> International Biot Conference on Poromechanics, pp. 189-195, 8-10 June, NY, USA.
- C26. **Seyedi D.**, Negulescu C., Mohammadi-Nasr M. (2009) A set of vulnerability curves for seismic risk assessment of current buildings in urban zones of Iran. Computational Methods in Structural Dynamics and Earthquake Engineering (COMPDYN 2009), 22-24 June Rhodes, Greece.
- C27. Gehl P., **Seyedi D.**, Douglas J., Khiar M. (2009) Introduction of fragility surfaces for a more accurate modeling of the seismic vulnerability of RC structures. Computational Methods in Structural Dynamics and Earthquake Engineering (COMPDYN 2009), 22-24 June, Rhodes, Greece.
- C28. Sy S., Douglas J., **Seyedi D.** (2009) Estimating peak dynamic strains at ground surface and at depth during earthquake shaking: application to the safety study of geological storage of  $CO_2$ . European Geosciences Union General Assembly 2007, Vienna, Austria, 19 – 24 April.
- C29. Guy N., **Seyedi D.M.**, Hild F. (2008) Hydro-mechanical modelling of underground  $CO_2$  storage and risk evaluation through a probabilistic fracturing model. The 12<sup>th</sup> International Conference of IACMAG, 1-6 October, Goa, India.
- C30. Guy N., **Seyedi M.**, Hild F. (2007) A probabilistic model for the formation and propagation of crack networks applied to the study of caprock seal capacity for  $CO_2$  storage. In Proceeding of 18<sup>th</sup> Engineering Mechanics Division Conference of the American Society of Civil Engineers, Blacksburg, VA, USA.
- C31. **Seyedi M.**, Guy N., Rohmer J., Hild F. (2007) Coupled hydromechanical modeling of the integrity and safety of geological storage of  $CO_2$ . European Geosciences Union General Assembly 2007, Vienna, Austria, 15 – 20 April.
- C32. **Seyedi M.**, Mushtaq A., Hild F. (2006) A probabilistic model for the formation of crack networks in rocks under  $CO_2$  injection” In Proceeding of EUROCK06, pp. 99-104, Liege, Belgium.
- C33. Aochi H., **Seyedi M.**, Douglas J., Foerster E., Modaresi H. (2005) A complete BIEM-FDM-FEM simulation of an earthquake scenario - dynamic rupture process seismic wave propagation and site effects. European Geosciences Union General Assembly 2005, Vienna, Austria, 24 – 29 April.
- C34. **Seyedi M.**, Taheri S., Hild F., Stephan, J.-M. (2003) Study of crack propagation in a multicroaked structure in thermal fatigue. SMiRT 17, 17 - 22 August 2003, Prague, Czech Republic
- C35. **Seyedi M.**, Hild F. (2003) Probabilistic aspects in the formation and propagation of crack networks in thermomechanical fatigue. In Proceeding of 5<sup>th</sup> International Conference of the Engineering Integrity Society FATIGUE2003, EMAS Publishing, pp. 495-502, 7-9th April 2003, Cambridge, UK.
- C36. **Seyedi M.**, Hild F., Taheri S. (2002), Propagation and shielding effects in a multicroaked structure in thermal fatigue. In Proceeding of 8<sup>th</sup> International Congress of Fatigue FATIGUE2002, EMAS Publishing, Vol. 3, pp. 1735-1742, Stockholm, Sweden.
- C37. Gatmiri B., **Seyedi M.** (2001) Thermohydromechanical behaviour of non linear inelastic saturated porous media. In Proceeding of 6th International workshop on key issues in waste isolation

research, pp. 423-462, ENPC, Paris, France.

- C38. Gatmiri B., **Seyedi M.**, Delage P., Fry J.J. (1997) A new suction based mathematical model for thermohydromechanical behavior of unsaturated porous media. In Proceeding of NUMOGIV, Canada.

# Introduction

## I.8 General context

I am currently the head of the laboratory of Seismic Mechanics Studies (EMSI Lab) at CEA Paris-Saclay. The EMSI Lab comprises a team of around 30 people (research engineers, technicians, PhD students and post-docs) specialized in seismic mechanics. EMSI research activities cover different themes of seismic mechanics such as the study of damage of structures under seismic loading, soil-structure interaction and high-performance computing. The laboratory benefits from exceptional experimental facilities such as the Azalée shaking table with 6 DOF, 6 m x 6 m, and a payload of 1000 kN.

Between December 2018 and February 2021, I was the head of the laboratory of structural integrity and standards (LISN) at CEA Paris-Saclay. LISN research activities cover different aspects of fracture mechanics such as brittle fracture, large tearing in the ductile domain, study of the ductile - brittle transition, and the initiation and propagation of fatigue cracks.

Before joining CEA in December 2018, as a research engineer at the Research and Development Division of the National Agency for the Management of Radioactive Waste (Andra), I coordinated the Group of Laboratories "Mechanics of structures and storage components". I also coordinated activities related to the numerical modeling of *in situ* experiments carried out at the Underground Laboratory of Meuse/Haute-Marne of Andra.

Between August 2004 and March 2012, I worked as a research engineer in the Risks department of BRGM (French geological survey). Previously, I performed a PhD followed by a postdoctoral research at LMT (ENS Paris-Saclay) on initiation and propagation of cracks in high-cycle thermal fatigue.

Before coming to France in 1999, I obtained a Civil engineering and a Master degree from the University of Tehran in 1996. I was working between 1996 and 1999 as a civil engineer essentially on dam and underground structures design.

The production of energy has been a major concern for human being since antiquity. Assuming the energy supply and preserving the environment became a principal preoccupation of engineers during recent years. Civil and mechanical engineers play an essential role in this view. Materials and structures used in the construction of components of energy production/transfer/storage facilities are subjected to complex multi-physical solicitations during their service life. Developing technologies to reduce the negative effects of anthropogenic activities on climate change raise similar questions

regarding their lifetime.

The investigation of the durability of materials and the integrity of structures subjected to different types of loading during their lifetime has formed the common basis of my research work over the past twenty years. The targeted applications concern energy production and environment protection.

Thus, I had the opportunity of working on the thermomechanical fatigue of metal pipes, the seismic vulnerability of structures, the fracturing of geological formations under thermo-hydro-mechanical loading, the thermo-hydro-mechanical behavior of underground structures and large ductile tears in metal structures. My research work is based on probabilistic methods, numerical modeling and statistical processing of numerical simulations. The main goal is to better understand the uncertainties and to take into account the effect of the heterogeneous nature of materials and variable character of loading on the behavior of structures. Accounting for multi-physical couplings (thermal, hydraulic, chemical and mechanical) and their impact on the durability of materials and structures constitutes another part of my work.

Most of these research works were carried out within different types of collaborations (ANR and Europeans funded projects, industry-academia research collaborations. . . ). I also had the opportunity to co-supervise five doctoral and three post-doctoral works.

## I.9 Document outline

The document is organized in four chapters to present my research activities. An overview of the thermo-hydro-mechanical behavior of the Callovo-Oxfordian claystone (COx) is presented in Chapter 1. COx is considered as a potential host for the high- and intermediate-level long-lived radioactive waste in France. COx can be considered as a low-permeability porous medium with heterogeneous microstructure. Its specific mineralogy and micro-structure, very low permeability as well as different perturbations induced by the construction of an underground repository and emplacement of waste packages render COx behavior complex in the context of the radioactive waste disposal. I will focus on the work performed within the framework of the "*Groupement de laboratoires comportement mécanique des ouvrages et des composants de stockage*" at Andra R&D Division that I coordinated between 2012 and 2018.

Chapter 2 focuses on the numerical modeling of damage initiation and propagation within semi-brittle heterogeneous materials like concrete and rocks. Different challenges arise in this view, among them strain localization and mesh dependency of the results, the heterogeneous character of brittle failure and handling the transition between damage initiation and fracture propagation. When dealing with fracture initiation and propagation within porous media and under thermo-hydrmechanical loading other issues and complexities (e.g., the role of pore pressure/temperature on fracture initiation, flux exchange between fracture and porous medium, permeability of fractured porous medium, ...) will also arise. The feasibility of using the developed model within this context is also presented.

Chapter 3 is dedicated to the seismic vulnerability of structures. Modern methods of seismic risk assessment are based on fragility curves representing the conditional probability for a structure or a

type of construction of reaching or exceeding a given level of damage, depending on a level of seismic hazard characterized by an intensity measurement. Due to the use of a single scalar parameter to describe the seismic motion, the usual fragility curves tend to neglect the inherent variability of signal characteristics, which cannot be described by a single intensity measurement. A methodological framework has been developed between 2006 and 2012 when I was working at BRGM to represent the strong motion by more than one parameter resulting to fragility surfaces and vector-valued fragility curves. This framework is then extended to multi-hazard risk estimations.

I finish this document with some concluding remarks and perspectives. Some miscellaneous works on chemo-poromechanical modeling of oilwell cement carbonation under  $CO_2$  geological storage conditions, calculation of the equivalent permeability of fractured porous media as well as the work performed during my PhD and post-doc on thermomechanical fatigue and my current works on numerical modeling of large ductile tearing are not detailed in the present document.



## Chapter 1

# Thermo-hydromechanical behavior of the Callovo-Oxfordian calystone

Most of the works presented in this chapter have been performed within the framework of the GL Mouv research program (*Groupement de Laboratoires Comportement mécanique des ouvrages et des composants des stockages*) that I coordinated between 2012-2018. GL Mouv activities consisted in laboratory experimental investigations, along with theoretical and numerical developments for characterization and modeling of the thermo-hydromechanical (THM) behavior of Callovo-Oxfordian claystone (COx). Some *in situ* observations and THM experiments performed at Andra's Underground Research Laboratory (MHM URL) are also presented to provide additional information on the COx behavior. The semi-analytical model for analyzing drift convergences, and numerical analyses of the influence of hydromechanical couplings on fracture initiation around drifts were developed during PhD of L.M. Guayacain-Carrillo (co-supervised with Prof. J. Sulem and Dr S. Ghabezloo). The THM simulations of *in situ* heating tests have been performed during 2 post-doc researches that I supervised (M. Vitel and C. Plúa) within DECOVALEX international project.

## List of abbreviations

BSEi	Backscattered Electron imaging
EDZ	Excavation Damaged Zone
EFZ	Excavation Fractured Zone
FIB	Focused Ion Beam
GSA	Global Sensitivity Analysis
HLW	High Level waste
ILLW	Intermediate Level Long Lived waste
IUPAC	International Union of Pure and Applied Chemistry
MIP	Mercury Intrusion Porosimetry
RFEM	Random Finite Element Method
SEM	Scanning Electron Microscope
SMR	Reinforced Measurement Station
UA	Clay Rich Unit
URL	Underground Research Laboratory
USC	Silty carbonate-rich Unit
Zira	Zone of interest for in-deep investigation

### 1.1 Introduction

In their natural state, clay formations exhibit very favorable conditions for use as radioactive waste repositories. Various countries such as Belgium, Switzerland and France are currently studying clay or claystone as potential host rocks for radioactive waste repositories. In France, the National Radioactive Waste Management Agency (Andra) is responsible for investigating and designing sustainable waste management solutions. Current investigations focus on reversible deep geological disposal solutions for high- and intermediate-level long-lived radioactive waste (HL and IL-LL projects). In the 1990s, Andra began to study Callovo-Oxfordian (COx) claystone as a potential host rock for radioactive waste repository. COx has been selected thanks to its very low hydraulic conductivity, low molecular diffusion and significant radionuclide retention capacity. Preliminary investigations consisted of borehole-drilling and geophysical survey work covering an area of over one hundred square kilometers near the village of Bure (Northeast of France) for identification of geological sequences and characterization of physical, chemical, mechanical and transport properties via samples. The surface reconnaissance program conducted to identify the site location of the Meuse Haute-Marne Underground Research Laboratory (MHM URL) also provided an impressive amount of data covering a broad range of geoscience disciplines, including hydrogeology [Distinguin and Lavanchy, 2007], structural geology, mineralogy [Gaucher *et al.*, 2009], geochemistry and rock mechanics [Lebon and Ghoreychi, 2000]. In 2000, Andra initiated the construction of MHM URL by sinking two shafts to study COx claystone located at a depth between 420 and 550 m below the ground surface. Boreholes drilling operations from both surface and underground sites provided numerous samples for

characterization of COx claystone properties through laboratory tests.

Detailed knowledge of the thermo-hydro-mechanical (THM) behavior of COx claystone is crucial for designing repository structures and performing associated safety calculations. In the following, a very brief description of the THM behavior of COx is first presented. *In situ* observations are then provided to complete this description. Finally, numerical modeling of THM response of COx to excavation operations and thermal loads are addressed. The associated challenges and some results are presented and discussed.

## 1.2 Callovo-Oxfordian calystone

Callovo-Oxfordian sediments comprise a dominant clay fraction rich in carbonates, quartz, minor feldspars and accessory minerals. The Callovo-Oxfordian geological layer is vertically divided into three lithostratigraphic units (listed in order from the base) [Armand *et al.*, 2017]

- Clay unit (UA): Approximately two-thirds of total layer thickness. Highest clay mineral content (over 40% on average). Weak and gradual mineralogical variations. Clay minerals consist of illites, ordered illite/smectite mixed-layer minerals, kaolinite, trioctahedral iron-rich chlorite and minor biotite
- Transition unit (UT): Transition between clay unit (UA) and silty carbonate-rich unit (USC). Highest carbonate content (40 to 60%)
- Silty carbonate-rich unit (USC): 20 to 30 m thick. Significant vertical variability of petro-physical parameters due to lithological alterations (marl and carbonate siltstone). More varied and heterogenous mineral composition, with progressive carbonate enrichment marking the initiation of the Upper Oxfordian carbonate platform.

### 1.2.1 Callovo-Oxfordian microstructure

At the main level of MHM URL, Callovo-Oxfordian claystone can be considered as a clay matrix (clay content ranging from 40 to 60%) with carbonate and tectosilicate grain inclusions (Figure 1.1(b)). The non-porous inclusions considered as rigid with respect to the clay matrix, with grain sizes ranging from of 0.1 to 100  $\mu\text{m}$ . As a result, most of the porosity is located within the clay matrix [Robinet *et al.*, 2015], and there is a strong correlation between clay content and porosity values at the scale of the Callovo-Oxfordian geological layer. Porosity characterization studies indicate that the pore network is mainly composed of meso/micro pores (as per IUPAC classification). Figure 1.1(a) shows a typical unimodal pore size distribution curve obtained from Mercury Intrusion Porosimetry (MIP) tests, with a well-defined peak at approximately 10 to 30 nm [Song *et al.*, 2015].

Various imaging techniques such as electron microscopy (alone or coupled with focus ion beam systems) and X-ray microtomography have been used to determine the spatial distribution of pore size and mineral content. 3D reconstructions of the pore network show very low connectivity (Figure 1.2-right) for pores larger than 40 nm [Song *et al.*, 2015], which is consistent with pore size distribution

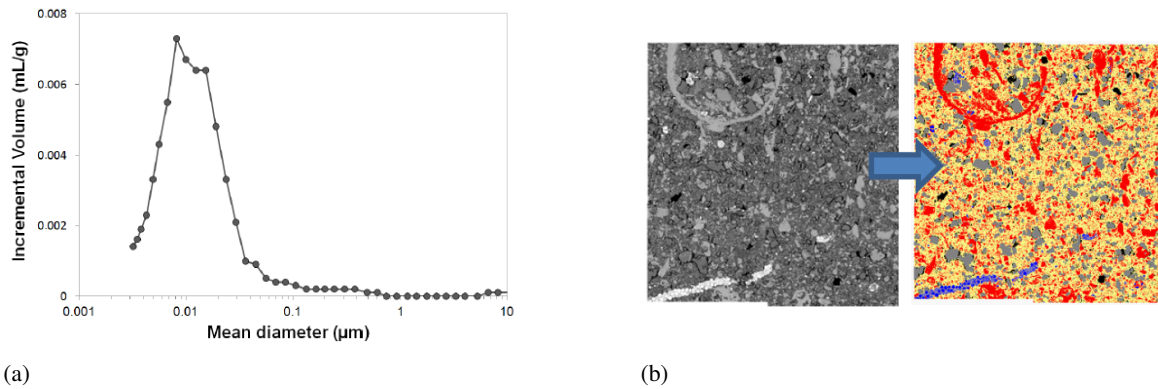


Figure 1.1: Pore size distribution curves for COx claystone [Armand *et al.*, 2017] (a) and, Spatial distribution of mineral content visualized by SEM BSEi after image segmentation (b) [Robinet *et al.*, 2012] (Clay matrix shown in Yellow).

curves obtained by MIP. Mineral distribution maps [Robinet *et al.*, 2012] show a preferential orientation of carbonate and tectosilicate inclusions parallel to the bedding plane (Figure 1.2(a)). However, the orientation of clay particles and aggregates with respect to the bedding plane is not so as marked as in the case of other indurated clays such as Opalinus Clay in Switzerland [Wenk *et al.*, 2008]. This leads to a slight anisotropy of most rock properties, particularly in terms of solute diffusion, water permeability and mechanical parameters.

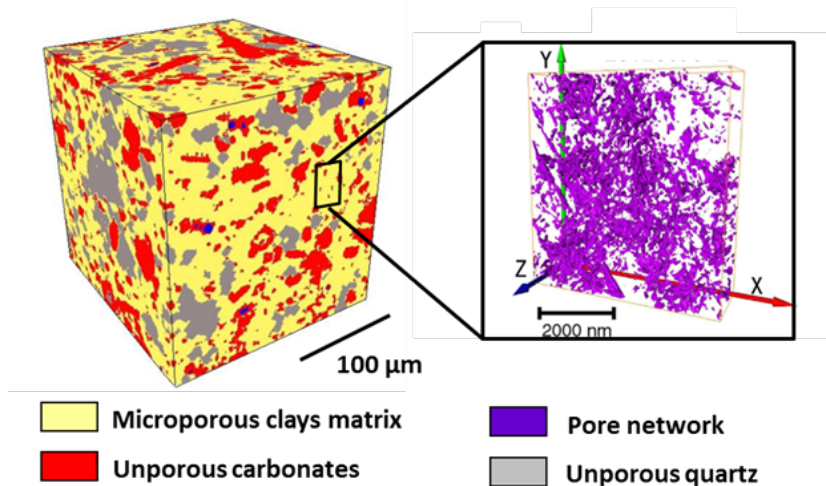


Figure 1.2: COx claystone microstructure at different scales: (right) Clay matrix with carbonate and quartz inclusions, viewed using synchrotron X-ray microtomography [Robinet *et al.*, 2012], (left) 3D reconstruction of pore network from segmented images obtained by FIB/SEM [Song *et al.*, 2015])

## 1.2.2 Mechanical behavior

The mechanical behavior of COx claystone is first controlled by its mineralogical composition. So a distinct behavior can be observed between clay-rich unit (UA) and silty carbonate one (USC). As many claystones, Callovo-Oxfordian claystone is sensitive to variations in air and water content. In fact, drilling/cutting/shaping processes necessary for sample preparation prior to testing always induce a limited desaturation of the sample. The resaturation (like the desaturation) generates a gradient of water content inside the sample. This gradient induces a kinematic incompatibility of swelling or shrinkage strain leading to creation of local tensile stresses. Such tensile stresses may become significant in large samples and then responsible for microcrack initiation during resaturation or desaturation processes. Consequently, the claystone samples can be damaged even cracked before mechanical loading. Ewy [2015] presented the results of investigations performed to quantify the impact of exposure to air, and to different liquids on different shales and claystones. These investigations show that the water content of such rocks is controlled by the relative humidity of the surrounding air. Most shales/claystones will lose water, shrink and desaturate if exposed to air, causing desiccation damage. While exposure to water (even if water has the same chemistry of pore fluid) will prevent desiccation, but will result in water uptake and swelling, and a different type of alteration and damage.

Concerning COx, most samples have been extracted from a large number of air drilled boreholes in the URL. Core samples are subjected to a complex hydromechanical loading path before testing, due to drilling, conditioning and preparation. Within the framework of GL Mouv, some procedures for core extraction and packaging as well as a systematic sample preparation protocol have been proposed in order to minimize the uncertainties on test results [Conil *et al.*, 2018].

A review of the THM behavior of COx can be found in [Armand *et al.*, 2017]. In the following a brief description of the mechanical (short and long term) behavior of COx is first presented. Some major aspects of the THM couplings within COx claystone are summarized in the next section.

### 1.2.2.1 Short-term behavior

Figure 1.3 presents the results of a series of triaxial compression tests performed on COx samples under different confining pressures (2, 6 and 12 MPa). By neglecting the nonlinear part in the beginning of the stress-strain curves induced by closure of initial microcracks, the main features of the short-term mechanical behavior are summarized as:

1. a short linear elastic part in the beginning of the stress-strain curves;
2. rather diffuse damage before the peak stress illustrated with a slight stiffness decrease;
3. strain softening characterizing the post-peak behavior where cracks are generally observed on the samples;
4. the residual domain where the rock behaves as a cohesion-less completely frictional material corresponding to the behavior of the formed macrocracks.

As for other quasi-brittle materials, the confining pressure has an important influence on the COx mechanical behavior. Under low confining stresses a quasi-brittle failure followed by a sharp decrease

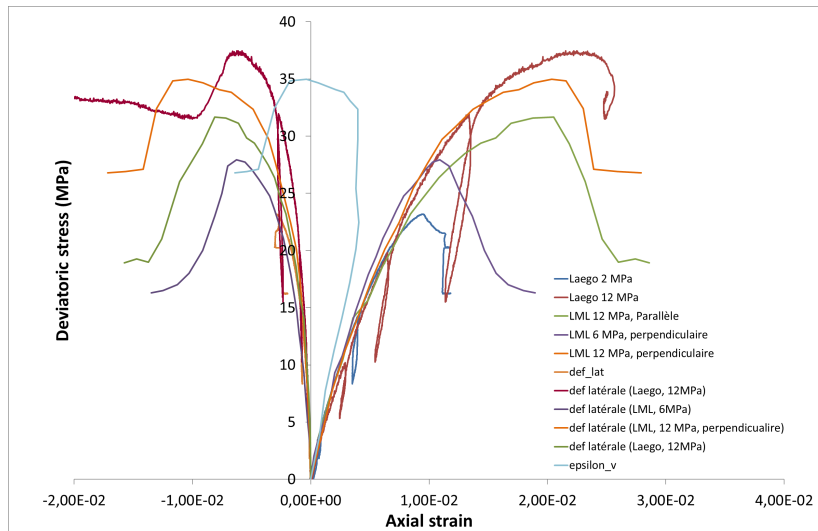


Figure 1.3: Stress-strain curves of triaxial compression tests under different confining pressures on COx claystone [Armand *et al.*, 2017]

of the stress level occurs. By increasing the confining stress, the failure type changes towards a ductile-like response with a softening post-peak behavior. Under triaxial conditions, the transition confining stress corresponding to a completely ductile failure is estimated of about 20 MPa. The post-peak behavior leads to a residual behavior where the rock behaves as a cohesion-less completely frictional material corresponding to the behavior of the formed macro-cracks. COx presents a brittle behavior under tensile loading. Tensile strength of COx depends on its mineralogy and increases with the carbonate ratio [Armand *et al.*, 2017].

During the excavation of underground structures, points located at the vicinity of the tunnel wall follow rather an extensional load path than a compressive one. The hoop stress increases close to the tunnel wall while the radial stress decreases. This stress path is quite different from the classical compressive triaxial stress path, which usually is used to characterize the mechanical behavior of rocks. Moreover, around the gallery the axial stress (the one parallel to the galleri's axis) is almost constant and tends to maintain a part of initial confinement. To study the influence of the loading path on the mechanical response of COx other tests called extension triaxial tests under constant mean stress were also performed. Figure 1.4 presents the results of two tests performed under constant mean stress. Two mean stresses, namely; 12 and 13 MPa are used. It can be seen that the failure has occurred under lower values of deviatoric stresses.

### 1.2.2.2 Long-term behavior

Long-term behavior of COx claystone has been studied through creep tests. Figure 1.5 presents the typical creep strain-time curves on five COx samples under multi-step uniaxial loads over 6 years. Zhang *et al.* [2010] showed that the creep behavior under increasing load is characterized by two phases. First, a transient one with decreasing rates governed by strain hardening is observed. This

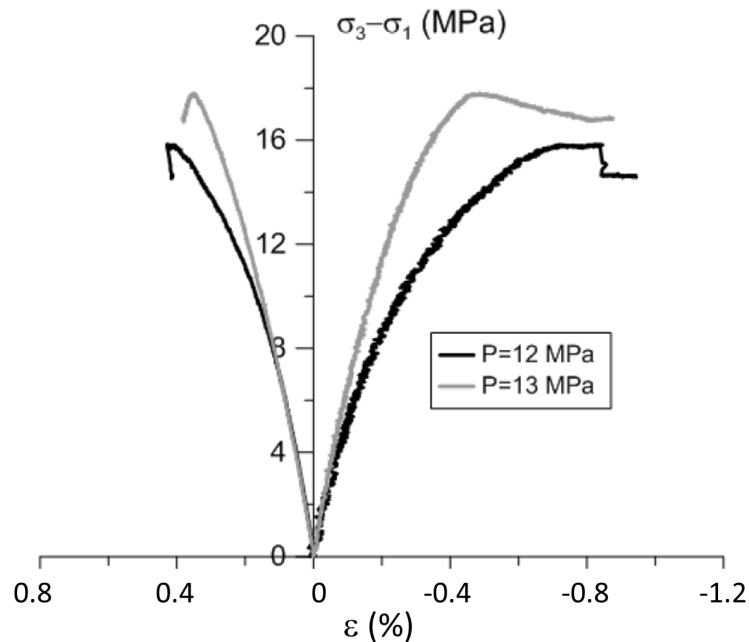


Figure 1.4: Stress-strain curves of triaxial extension tests at two different mean pressures, with HR = 90% [Armand *et al.*, 2017]

phase is followed by a second one with an asymptotically constant rate after strain recovery. The creep test under decreasing load contrary evolves firstly backwards with negative rates and then inversely returns with time to a steady-state creep at a positive rate. The creep rates of  $2 \times 10^{-11} \text{ s}^{-1}$  to  $6 \times 10^{-11} \text{ s}^{-1}$ , obtained on five samples after uploading, are relatively higher than those obtained after downloading ( $10^{-11} \text{ s}^{-1}$  to  $2 \times 10^{-11} \text{ s}^{-1}$ ). The creep behavior thus depends on the loading path. Zhang *et al.* [2010] also pointed out that in uniaxial creep tests, the creep rate varies very slowly and linearly with stress at low stresses (below 13 to 15 MPa). Above that level, the creep rate increases and deviates from a linear form. The acceleration of creep seems to be linked with damage onset and growth.

The performed tests did not demonstrate the existence of a viscoplastic threshold beyond which the creep phenomenon is active. Multi-stage creep tests highlighted the existence of a stress threshold below which creep strains stabilized [Armand *et al.*, 2017]. However, the experimental conditions and the low number of tests do not permit to draw final conclusions. Moreover, the measurement campaigns of the natural stress state performed at the Meuse/Haute-Marne URL show an anisotropic natural stress state. This anisotropy is lower than what is observed in the surrounding carbonate formations. The absence of measurable creep threshold would mean that COx creeps in its initial state before excavation, which is unlikely from a physical point of view.

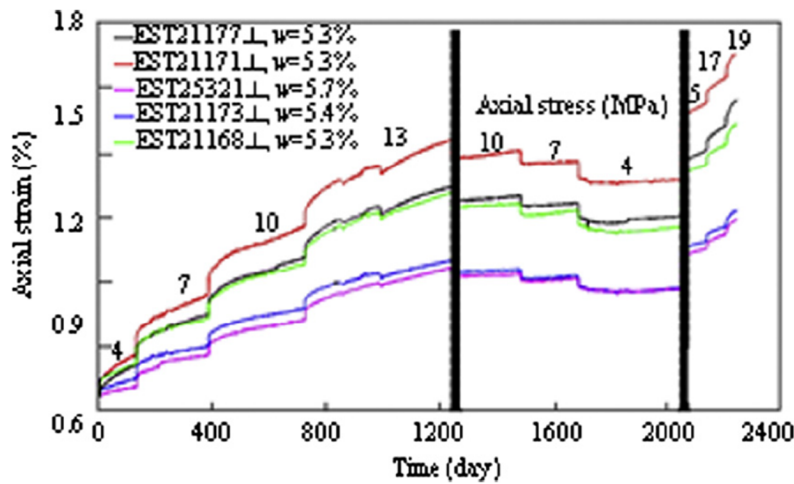


Figure 1.5: Strain evolution with time during uniaxial creep tests [Zhang *et al.*, 2010]

### 1.2.3 Hydraulic behavior

In clay-rich rocks, given the structure of the water molecule, which allows for electrostatic interactions with the surface of minerals, interstitial water is found in different states: (i) absorbed in the clay sheets (immobile under the effect of a hydraulic gradient), (ii) adsorbed on the surface of clay minerals (not very mobile under the effect of a hydraulic gradient) and (iii) free between clay minerals and aggregates [Michot *et al.*, 2002].

Given the very small size of pores, and strong interactions between pore water and clay minerals, validity of Darcy's law in this type of material is questionable. If the pore size is less than 4-6 nm, the structuring of water molecules, in the double layer zone developing from the surface of the clay minerals, annihilates advection [Horseman *et al.*, 1996]. In the case of COx claystone, the part of porosity greater than this threshold corresponds to more than half of the total porosity according to the whole available porosimetry measurements. Moreover, the results of the *in situ* tests and measurements seem to show that Darcy's law can represent the hydraulic behavior of COx at the scale of structures [e.g. Distinguin and Lavanchy, 2007].

#### 1.2.3.1 Hydromechanical coupling

Hydromechanical couplings have been observed during a wide range of tests performed on samples. These couplings are revealed also through changes in pore pressure levels around the structures, due to excavation [Armand *et al.*, 2015, Guayacan-Carrillo *et al.*, 2017] and in *in situ* thermal tests [Armand *et al.*, 2017b]. Within the elastic behavior range, it is currently considered that Biot's theory of porous mechanics [Biot, 1941] may represent the macroscopic behavior of the Callovo-Oxfordian for practical applications.

Biot theory offers the advantage of a solid thermodynamic foundation and a micromechanics interpretation of processes, based on many experimental observations at different scales. However, it

is based on a representation of the porous medium by one or more "free" fluid phases (water, gas) and a solid phase, which itself may be composed of various solids organized in a matrix arrangement (clay minerals), inclusions (quartz) or in a more or less connected/continuous skeleton (case of calcite in the silty-carbonated unit). This representation implies the existence of a purely mechanical interaction between the two phases in such a way that the deformation of the solid phase results from external mechanical actions applied to the solid phase, and from internal mechanical actions applied to the solid phase by pressure from interstitial fluid(s). In addition, it implies that the solid phase is inert with respect to the fluid saturating the porous network, which is not the case for COx. When dealing with fully saturated porous materials containing pores of manometer size, aside from the fluid pressure acting on the pore walls, additional effects due to adsorption and confinement of the fluid molecules in the smallest pores must be accounted for [Pijaudier-Cabot *et al.*, 2011]. In nanometer-scale pores, the molecules of fluid are confined inducing fluid-fluid and fluid-solid interactions at the pore scale. If adsorption in nanopores induces instantaneous deformation at a higher scale, matrix swelling may close the transport porosity, reducing the global permeability of the porous system [Perrier *et al.*, 2018].

Concerning COx claystone, a significant portion of the interstitial water is in a bound state ( $\sim 50\%$ ) and will therefore not participate in free water-solid interactions. However, no experimental data currently exists showing that there is no free connected water in COx. In the current state of knowledge, Biot's theory is therefore used to model the macroscopic hydromechanical behavior of COx. However, this theory cannot explain detailed behavior of COx at smaller scales. In particular, to understand correctly the mechanisms controlling the volumetric behavior, particularly swelling of COx needs the use of more detailed theories.

Considering Biot's theory in saturated conditions, the equation of state that establishes the link between the stress tensor  $\sigma$ , the strain tensor  $\varepsilon$  and the pressure  $p$  of the interstitial fluid is expressed as

$$\sigma = \mathbf{C} : \varepsilon - bp\mathbf{I} \quad (1.1)$$

where  $\mathbf{C}$  is the Hooke's tensor,  $b$  Biot's coefficient (scalar for an isotropic medium) and  $\mathbf{I}$  the identity tensor.

Different experimental investigations have been performed to measure the poroelastic parameters of COx claystone. Considering a poroelastic behavior, a hydraulic compressive modulus  $H$  is also defined, resulting from the variation in volume of a porous medium under the effects of an interstitial pressure variation

$$H = \frac{\Delta p}{\Delta \varepsilon_v} = \frac{K_d}{b} \quad (1.2)$$

where  $K_d$  is the drained compressive modulus. So, with keeping constant the confining stress while the applied pore pressure varies, the measurement of volumetric strains provides a relationship between the drained modulus and the Biot's coefficient (Equation (1.2)).

An isotropic compression test without membrane corresponds to a load pathway for which the

pressure and confinement increments are applied simultaneously ( $\Delta\sigma = \Delta p$ ). The "differential" stress ( $\sigma_d$ ) therefore remains constant under these conditions. The measured volumetric strain values are used to express a modulus with no membrane,  $K_s$

$$\frac{1}{K_s} = -\frac{1}{V_0} \left( \frac{dV}{dp} \right) \quad (1.3)$$

An important set of experimental works has been performed to determine the value of Biot's coefficient in COx. Among them, hydrostatic loading tests, gaz injection tests and unjacketed copression teats can be mentioned. During hydrostatic loading tests,  $K_d$  and H coefficients (Equation 1.2) can be determined by varying the pore pressure and thus provide an estimation of Biot's coefficient. During gas tests, gas is injected through the sample, while the degree of saturation is kept constant. The pore pressure variation will be equal to the injected gas pressure [Cariou *et al.*, 2012]. The comparison of the strains induced by confinement change and those due to pore pressure changes permits to calculate Biot's coefficient. A series of tests have been performed using helium as the injected gas [Yuan *et al.*, 2017]. Cylindrical samples 20 mm in diameter and 40 mm in height were used for the tests. The samples were cured under different conditions. First, they have been dried at 60°C and then stabilized at different relative humidity (RH) equal to 11%, 59%, 73%, 85%, 92% and 98%. Figure 1.6 shows the obtained values. It should be noted that the experimental protocol, based on the drying and humidification of samples, may induce irreversible microstructural degradation. This may explain Biot's coefficient very close to 1 obtained in this experimental program.

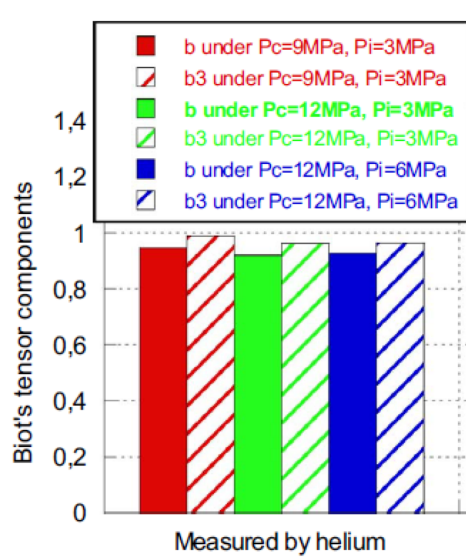


Figure 1.6: Biot's tensor components obtained by gas test using argon and helium (modified from [Yuan *et al.*, 2017])

Complementary experimental studies have been launched within "GL Mouv" to reduce, if possible, the remaining uncertainty on the values of hydromechanical coupling parameters. In this framework, an experimental study was carried out following several isotropic loading paths allowing

to independently measure several poromechanical parameters, namelyunjacketed modulus, drained bulk modulus, Biot's modulus, undrained bulk modulus and Skempton coefficient [Belmokhtar *et al.*, 2017, Braun *et al.*, 2019]. A transversely isotropic elastic behavior was considered. A first series of tests have been performed during the PhD thesis of M. Belmokhtar [Belmokhtar *et al.*, 2017]. This study shows a very weak anisotropy of the Biot coefficients obtained in both directions ( $b_1 = 0.85$  and  $b_2 = 0.9$  under an effective confinement of 10 MPa).

An experimental procedure based on three stages (Fig. 1.7) has been developed more recently as part of P. Braun's doctoral thesis [Braun *et al.*, 2019]. This protocol made it possible to identify four poromechanical parameters as well as a measure of the permeability of the sample. The three stages are [Braun *et al.*, 2019]:

- Stage 1: Application of rapid mechanical or thermal loading, while the drainage system is closed
- Stage 2: Confining stress and temperature are held constant with closed drainage system, until measured strains and pore pressure stabilize
- Stage 3: The drainage system is opened and the initial pore pressure is prescribed until the measured strains stabilize.

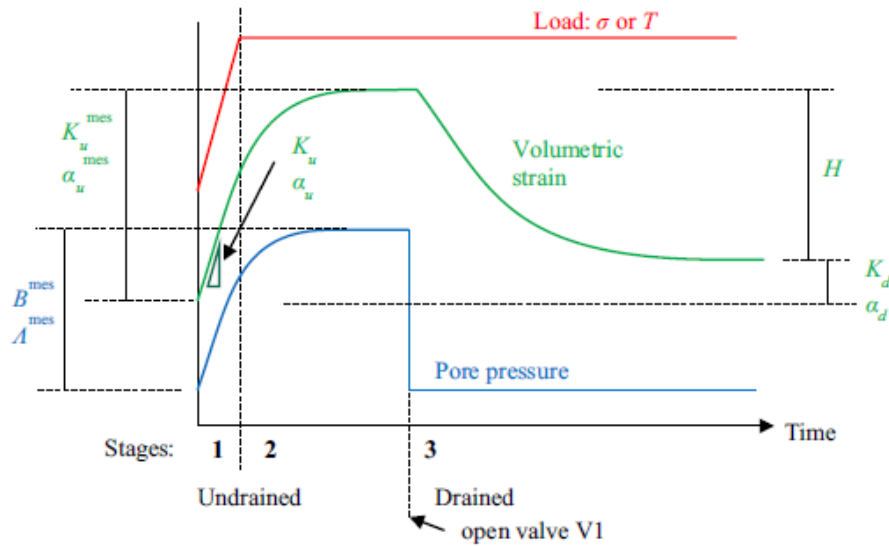


Figure 1.7: Three-stage loading protocol and schematic volumetric response for mechanical or thermal tests [Braun *et al.*, 2019]

The fast loading of the first step makes it possible to correctly measure the undrained modulus  $K_u$  and the undrained expansion coefficient  $\alpha_u$  of the sample. Stage 2 corresponds to an almost undrained state. The difference between the quasi-undrained (stage 2) and drained (stage 3) strains makes it possible to calculate Biot's modulus,  $M$  while the difference between the initial state and the drained strains informs us about the value of the drained parameters. The determination of these four parameters,  $K_d$ ,  $K_u$ ,  $B$  and  $M$  allows us to calculate Biot's coefficient  $b$ . The value of the Biot's

coefficient obtained, after correction, is equal to 0.83 for an undrained modulus  $K_u = 10.7GPa$  and a drained modulus  $K_d = 2.2GPa$ .

More recent work seems to reduce uncertainty about the value of Biot's coefficient of COx claystone. It is however important to note that in all cases, the results are very sensitive to the hydraulic and mechanical state of the samples. Core sampling, sample preparation, and (re)saturation may cause pre-test damage, which may partly explain the scatter of experimental values. The nature of this type of material with very small pore sizes, the combined presence of free and bound water and the impact of desaturation (induced by sampling and sample preparation) make experimental characterization difficult. Characterization research continues to improve methods and interpretation.

Important complementary information can be obtained from back-analysis of *in situ* experiments (see section 1.3). In fact, *in situ* experiments, like those performed at Andra's MHM URL in Bure allow to bypass the sampling stage and to be closer to real "*in situ*" behavior. However, *in situ* data are often indirect calculated ones. Moreover, borehole drilling and instrumentation operation induce also some disturbance in the hydromechanical response of rock mass. An integrated characterization approach combining sample and *in situ* experiments may thus improve the confidence level of the obtained results.

#### 1.2.4 Thermal pressurization

Following the current concept (see Figure 1.8), High-Level Waste (HLW) packages will be placed in a set of parallel micro-tunnels of 0.80 m to 0.90 m in diameter and 80 m to 150 m in length (see Figure 1.9). HLW are characterized by radioactivity concentrations that make them highly irradiating and generating more heat than Intermediate Level Long Lived Waste (ILLW). The heat emitted from the waste leads to an increase of temperature within the host formation (limited to about 90°C). The temperature rise in a low permeability porous medium such as COx claystone induces a pore pressure increase essentially due to the difference between the thermal expansion of pore water and the solid skeleton. The thermal expansion coefficient of bulk water at 20°C, is about  $210^{-4}K^{-1}$ , while the thermal expansion coefficient of COx is about 1.2 to  $1.5 \cdot 10^{-5}K^{-1}$ .

Pressure build-up due to the temperature increase is observed in many fine-grained geomaterials. Beyond nuclear waste repository applications, thermal pressurization is also investigated in the petroleum engineering where the reservoir rock at the vicinity of wellbores may be subjected to rapid thermal variations. This phenomenon is also important in the study of the nucleation of seismic failure on faults when shear heating tends to increase the pore pressure and to decrease effective compressive stress and shearing resistance of the fault material [Rice, 2006, Sulem *et al.*, 2007].

Experimental investigations show that the amplitude of the induced over-pressure may be related to that of temperature change through a thermal pressurization coefficient  $\Lambda$  defined as the pore pressure increase due to a unit temperature increase in undrained condition. In undrained condition, the pore pressure change due to a thermomechanical loading reads

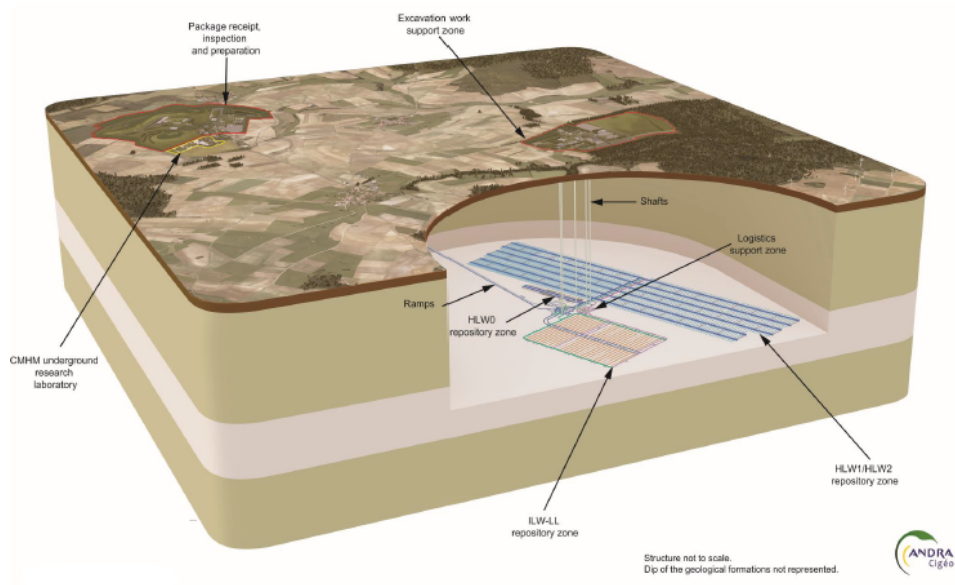


Figure 1.8: Schematic representation of the Cigéo facilities [Levard *et al.*, 2017]

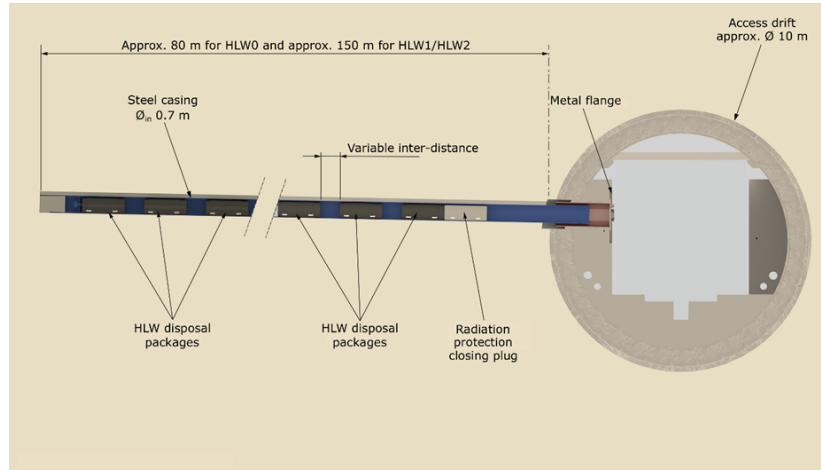


Figure 1.9: Schematic representation of HLW micro-tunnels [Seyedi *et al.*, 2021]

$$\Delta P = B\Delta\sigma_m + \Lambda\Delta T \quad (1.4)$$

where B is Skempton's coefficient, which reads

$$B = \frac{\frac{1}{K} - \frac{1}{K_s}}{\phi_0 \left( \frac{1}{K_f} - \frac{1}{K_s} \right) + \frac{1}{K} - \frac{1}{K_s}} \quad (1.5)$$

and  $\Lambda$  the thermal pressurization coefficient

$$\Lambda = \frac{\phi_0(\alpha_f - \alpha)}{\phi_0 \left( \frac{1}{K_f} - \frac{1}{K_s} \right) + \frac{1}{K} - \frac{1}{K_s}} \quad (1.6)$$

where  $K, K_f, K_s$  are respectively the bulk modulus of drained porous medium, fluid and solid skeleton;  $\alpha_f$  and  $\alpha$  the coefficients of thermal expansion of fluid and of porous medium;  $\phi_0$  the initial porosity; and  $\sigma_m$  the mean total stress.

The values of the undrained thermal pressurization coefficient depends on several factors as the nature of the material, the state of stress, the range of temperature change, and induced damage. Ghabezloo and Sulem [2008] gathered typical values of the thermal pressurization coefficient for some geomaterials. Table 1.1 presents these values completed by some more recent experimental results. An important scatter is observed in existing values for the thermal pressurization.

Table 1.1: Typical values of thermal pressurization coefficient of some geomaterials

Geomaterial	$\Lambda$	Reference
Clay	0.01	Campanella and Mitchell [1968]
Sandstone	0.05	
Kayenta sandstone	0.59	Palciauskas and Domenico [1982]
Boom clay	0.06	Vardoulakis [2002]
Clayey fault gouge	0.1	Sulem <i>et al.</i> [2007]
Intact rock at great depth	1.5	Lachenbruch [1980]
Opalinus clay	0.445 to 0.659	Monfared <i>et al.</i> [2011]
Callovo-Oxfordian claystone	0.12	Mohajerani <i>et al.</i> [2012]
Callovo-Oxfordian claystone	0.23	Braun <i>et al.</i> [2019]

A specific isotropic compression cell was designed by Mohajerani *et al.* [2012] to measure the undrained thermal pressurization coefficient of COx. A sample confined to *in situ* stress conditions is subjected to temperature rise in undrained conditions. The excess pore pressure is monitored by a pressure transducer. Two COx samples obtained from a core drilled at the MHM URL main level have been tested. Regarding the measured water content (6.4%) and porosity of the samples (22%), it is concluded that the samples have been desaturated and probably damaged during sampling and preparation operations. The measured values of water content at the main level of the M/HM URL show that the *in situ* value ranges between 7 and 8.5%. COx porosity varies between 14 and 20% with a mean value about 18% at the main level [Armand *et al.*, 2017]. It has been shown through experimental investigations that natural COx claystone saturation is no reversible [Conil *et al.*, 2018]. The effect of this initial state may tend to an underestimation of  $\Lambda$  as initial damage results a decrease of the sample bulk modulus.

The obtained results showed that  $\Lambda$  varies between 0.065 and 0.145 MPa/°C for two tested samples (Figure 1.10). Moreover, it can be noted that the value of  $\Lambda$  does not increase with temperature. However, the thermal expansion coefficient of bulk water is multiplied by three and that of claystone by two between 20°C and 80°C. Keeping Equation (1.4) in mind, such evolution of thermal expansion coefficients had to induce a significant increase of  $\Lambda$  with temperature. The authors interpreted this observation based on the combined effect of the change of the thermal expansion of pore water with temperature and the stress dependency of compressibility of claystone.

In a recent work, some improvements have been made to the experimental device mainly in the

measurement of local strains [Braun *et al.*, 2019]. A new experimental protocol is also developed. The specimen was initially subjected to isotropic stresses close to the *in situ* Terzaghi effective mean stress, i.e., an isotropic stress of 10 MPa. The specimen was compressed at constant water. Once the specimens were brought to the desired effective stress state, they were saturated with synthetic pore water having a salinity comparable to the natural one. The measured thermal pressurization coefficient was 0.23 MPa/°C.

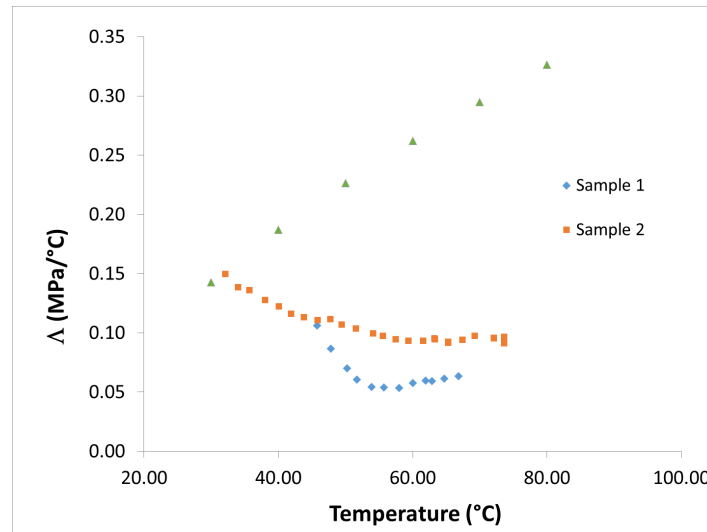


Figure 1.10: Measured thermal pressurization coefficient on two COx samples (modified from [Mohajerani *et al.*, 2012]).

### 1.3 *In situ* observations

The construction of the Meuse/Haute-Marne URL (Figure 1.11) has been launched in 2000 at Bure located about 300 km North-East of Paris by Andra to demonstrate the feasibility of a radioactive waste repository in a COx claystone formation. An important experimental program is planned to characterize different properties of the host rock and to study its response to different shaft and drift excavation. Numerous experiments and direct measurements have been performed in laboratory drifts excavated at  $-445$  m (short experimental drift in Figure 1.11) and then at the main level located at  $-490$  m. Extensive surveys have been conducted to investigate the fractured zone around excavated drifts. These studies provided fruitful insights on the effect of drift geometry, *in situ* stress state and rock properties on the pattern and extent of induced fracture networks.

#### 1.3.1 *In situ* stress state

An anisotropic *in situ* initial stress is observed at MHM-URL. The largest principal stress is horizontal ( $\sigma_H$ ) and the vertical ( $\sigma_v$ ) and the smallest horizontal ( $\sigma_h$ ) stresses are close to each other [Wileveau *et al.*, 2007]. At the main level of the URL (i.e., at  $-490$  m)  $\sigma_H \simeq 16$  MPa and  $\sigma_v \simeq \sigma_h \simeq 12$  MPa.

Most of the drifts are excavated following the horizontal principal stresses at the main level of URL (Figure 1.11). Several drifts are instrumented to measure drift convergence, the displacement induced in rock mass around drifts due to the excavation and pore pressure change [Armand *et al.*, 2017b]. The *in situ* observations show that the extent of the fractured zone follows a similar pattern in relation to the drift diameter for drifts with different sizes. Based on the observed results a conceptual fracturing model is proposed for drifts parallel to each principal stress direction [Armand *et al.*, 2014].

### 1.3.2 Fracture networks around the drifts

The experimental drift excavated at  $-445$  m in the silty-carbonate-rich unit layer (USC) does not exhibit significant induced fracture networks due to excavation. In contrast, all drifts excavated at the main level (i.e.,  $-490$  m) within the clay-rich layer (UA) show induced fracture networks. Different techniques have been employed for characterizing induced damage around drifts. The main investigation techniques are [Armand *et al.*, 2014]

- Structural analysis of the core samples drilled from drifts
- Geological survey of the drift face and sidewalls
- Seismic measurements (measuring the evolution of P and S wave velocities due to damage)
- Permeability measurements
- Overcoring of resin-filled fractures

The performed analyses showed that the fracture patterns and the extent of the fractured zone around drifts depend essentially on drift orientation, i.e., on the *in situ* stress state. The extent of the fractured

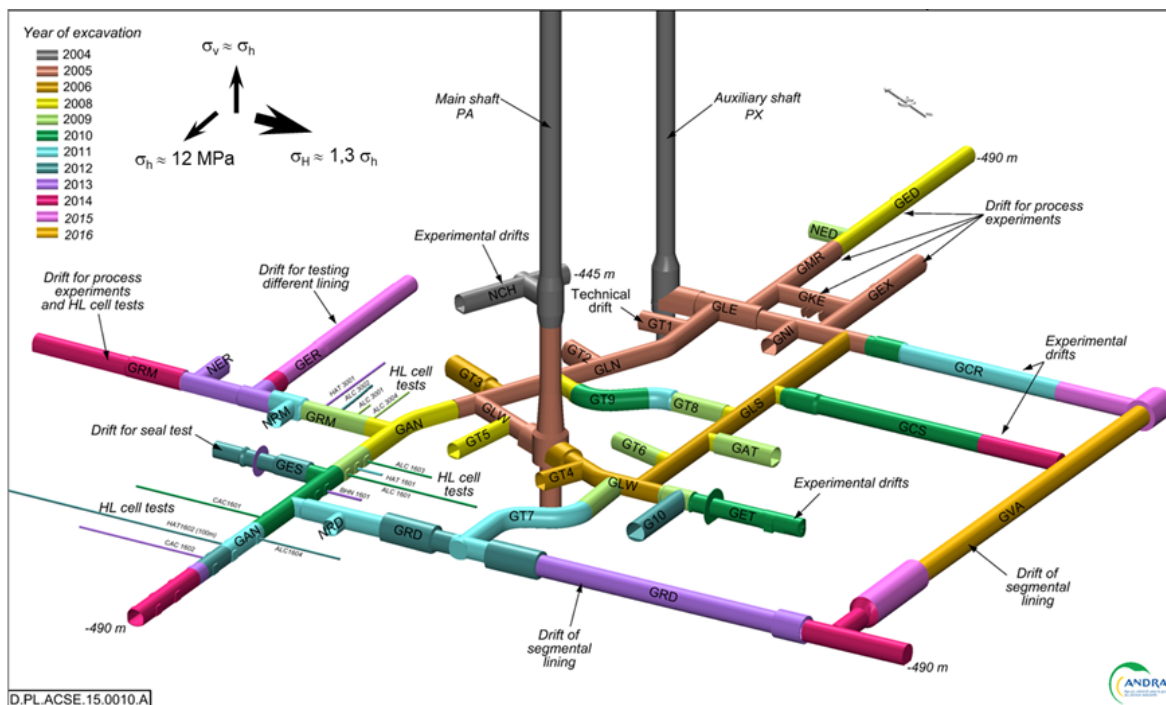


Figure 1.11: Meuse/Haute-Marne URL layout and principal stress directions. [Seyedi *et al.*, 2017].

zone was determined taking into account all available data in different directions [Armand *et al.*, 2014]. Two kinds of fractures are distinguished namely; shear fractures (mode II) and "tensile/extension" fractures (mode I).

An anisotropic extent of the fractured zone is observed in both directions. For drifts parallel to  $\sigma_H$  the vertical extent of the fractured zone is not significant while the lateral extent reaches one diameter. Drifts excavated parallel to  $\sigma_h$  show an important extent in the vertical direction while the lateral extent of the fractured zone is limited.

The results exhibit a large variability showing that the extent of fractured zones varies along the drifts. However, it is seen that the support system has not a significant influence on the extent of the induced fracture network. Based on the observed results, conceptual fracturing models are proposed for drifts [Armand *et al.*, 2014]. Shear fractures constitute the majority of the observed fractures (Figures 1.12 and 1.13). They are longer and expand deeper in the rock. Mode I fractures are concentrated near the drift wall with a more heterogeneous dip and strike.

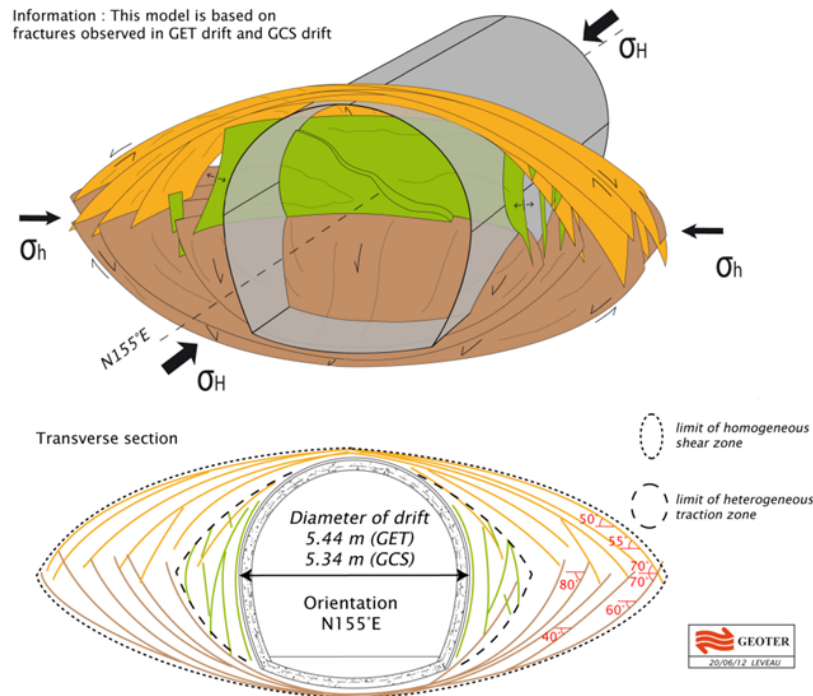


Figure 1.12: Conceptual model of induced fracture networks around drifts parallel to  $\sigma_H$ . Dark and light brown surfaces show shear fractures and green ones extension fractures [Armand *et al.*, 2014].

### 1.3.3 Hydromechanical response of COx to excavation operations

Rock mechanics experiments performed in URL provide a deep understanding of the hydromechanical response of COx to excavation operations including rock and structure interaction. These experiments will give important input to design (and to optimize the design) of different elements of the repository like support systems. Since 2006, a step-by-step approach is carried out by Andra based on compar-

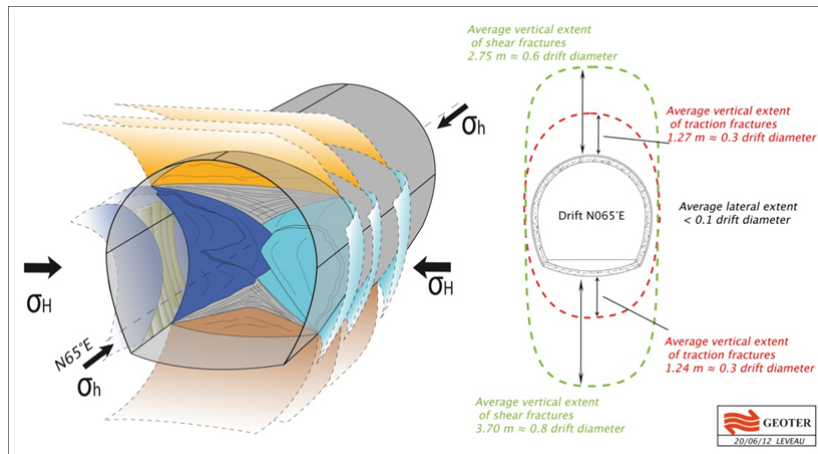


Figure 1.13: Conceptual model of induced fracture networks around drifts parallel to  $\sigma_h$  [Armand *et al.*, 2014].

isons of the hydromechanical behavior of parallel drifts excavated/supported by different construction methods (Figure 1.11). The hydraulic hammer technique was first used for excavation. Bolts, sliding arches and 10 cm-thick layer of shotcrete were set in place immediately after a two-meter maximum advancement. Other excavation and construction techniques have been and will be used, like road-header, stiff and flexible support. A tunnel boring machine has also been operated (GRD drift - see Figure 1.11) to test segments (concrete wedges) emplacement technique with different gap filling materials. All new experimental drifts are instrumented in order to measure the short and long term hydromechanical behavior. These various configurations give insight into the influence of construction method on the Excavation Fractured Zone (EFZ) extent and evolution, and on the progressive loading of the support, which are key issues to design disposal drifts.

In 2010, a new drift called GCS (Soft Conception Drift) was excavated parallel to the major horizontal stress. Drift is instrumented to monitor displacement and pore pressure in the rock mass due to the excavation as well as long-term behavior. An important number of boreholes has been drilled to analyze the extent of EFZ and its properties (hydraulic conductivity).

GCS drift has been excavated from the south drift (GLS) and 30 m away from GAT drift (Figure 1.11) in order to restrict hydromechanical interference between them (at short time). GCS has a circular section 2.6 m in radius. The excavation was performed with a road header machine, which allowed getting an average over excavation less than 0.1 m, except at the floor where it could reach 0.4 m. The spans of excavation are mainly 1.2 m long and are immediately covered with a 3 to 5 cm thick fiber-reinforced shotcrete. The support is ensured by 18 cm thick fiber reinforced shotcrete shell, interrupted by 12 yieldable concrete wedges; completed by a crown of 12 HA25 radial bolts 3 m in length and 1 m spacing. Eleven 12 m long rock bolts are placed at the front face every 6 m. The yieldable concrete wedges composed by a high strength concrete matrix with porous aggregates have a compressive strength of 40.5 MPa and can be strained up to 40% before failure. In parallel, shotcrete has a compressive strength of about 25 MPa. This difference in strength allows for the concentration

of deformation in the wedges. A complete description of the work can be found in [Bonnet-Eymard *et al.*, 2011].

### 1.3.3.1 Convergence measurements

Along the drifts, convergence measurements have been carried out in several sections. Six monitoring points located in a plane normal to the drift axis have been installed in each section. Measurements of wall movements are recorded along five different strings, which connect these points as shown in figure 1.14. The distribution of these strings permits the global deformation of the drift to be monitored in vertical, horizontal and transverse directions. In general, these monitoring points are installed at an initial distance of about  $2m$  from the tunnel face. A detailed analysis of convergence measurements can be found in [Guayacan-Carrillo *et al.*, 2016]. The radial displacements of the ground around the drifts have been followed by the installation of borehole extensometers, as a complement to convergence measurements. The extensometers provide useful information about the deformation distribution inside the rock mass and its evolution with time. Two groups of borehole extensometers can be distinguished. One group has been installed along the drifts during the excavation progress in sections called "Reinforced Measurement Sections (SMR)", and the other group has been installed before the beginning of drift excavation as part of mine-by tests. Six convergence sections were placed in the CGS drift. The convergence sections give a global view of the drift behavior. Figure 1.15(a) shows the horizontal and vertical convergences measured at different sections of the GCS drift as a function of time. The horizontal convergences are higher than the vertical ones (ratio of about 2), even if the state of stress is nearly isotropic. However, the evolution of horizontal and vertical convergences is similar.

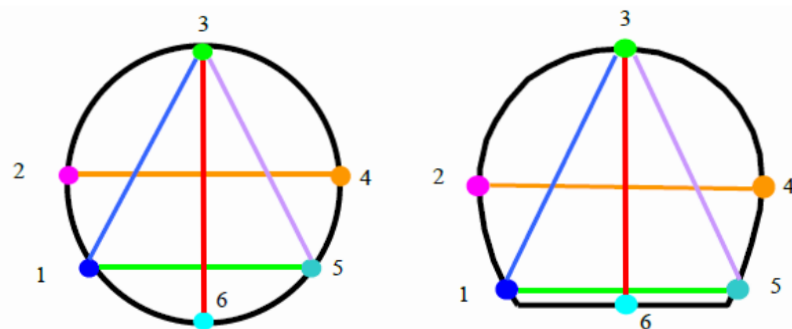


Figure 1.14: Convergence measurement sections for two different drift geometries [Guayacan-Carrillo *et al.*, 2016]

GED drift is excavated following  $\sigma_h$  by a pneumatic hammer machine. It has a horse-shoe section with an average diameter of  $4.6m$  and a length of  $71.2m$ . The initial *in situ* stress state is anisotropic in the section of the drift. The major principal stress to the vertical principal stress ratio is about 1.3. In this case, vertical convergence is about four times larger than horizontal convergence. As in perpendicular drifts, high convergence rates are observed during the first hundred days. After that, the

horizontal convergence stabilizes (Figure 1.15(b)).

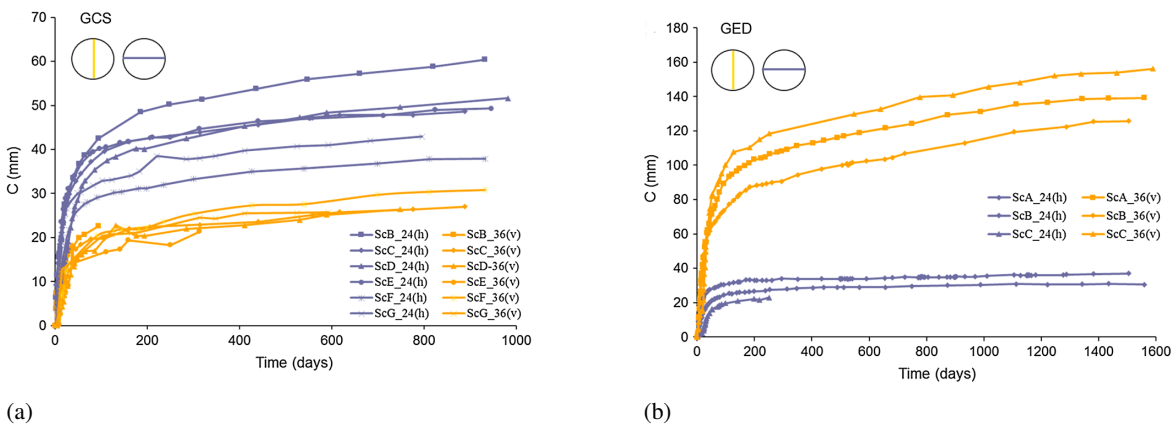


Figure 1.15: Horizontal and vertical convergences measured at GCS (a) and GED (b) drift [Guayacan-Carrillo *et al.*, 2016].

A semi-analytical model is developed during PhD of L.M. Guayacan-Carrillo to analyze the convergence measurements. The anisotropic character of the deformation was taken into account by assuming that the drifts section evolves following an elliptical shape. The characteristics of the deformed elliptical section are evaluated following the methodology proposed by Vu *et al.* [2013]. Then, using the semi-empirical law proposed by Sulem *et al.* [1987], the convergence evolution is fitted independently for each axis of the ellipse [Guayacan-Carrillo *et al.*, 2016]. This method allows to distinguish two effects: the face advance and the time-dependent behavior of the ground. The results for two drift orientations (along the major horizontal stress and perpendicular to it) show very close values for the parameters describing the time-dependent properties of the ground, the distance of influence of the face, and the extent of the decompressed zone around the drift. Finally, the model was validated by keeping these parameters as constants and by simulating the convergence data on a new drift. It was shown that with a period of about 40 days of convergence monitoring, the model can provide valuable insights for predictions of the convergence evolution in the long-term (Figure 1.16).

### 1.3.3.2 Mine-by test

A mine-by experiment is a state-of-the-art *in situ* test to characterize the hydromechanical response of rock mass around an underground opening during excavation and to determine the induced damage [Martin *et al.*, 2002, Armand *et al.*, 2011]. Different types of instrumentation are used to characterize the strain and stress fields of rock during excavation. The displacement field is recorded by extensometers, inclinometer and convergence measurement sections. The pore pressure field is recorded by multi-packer systems in the pressure measurement boreholes. Figure 1.17 shows location of boreholes, which have been implemented before excavation of GCS drift (at least two months in advance in order to achieve equilibrium in pore pressure measurements).

In order to point out the extent of hydromechanical impact of the excavation, a large pore pressure

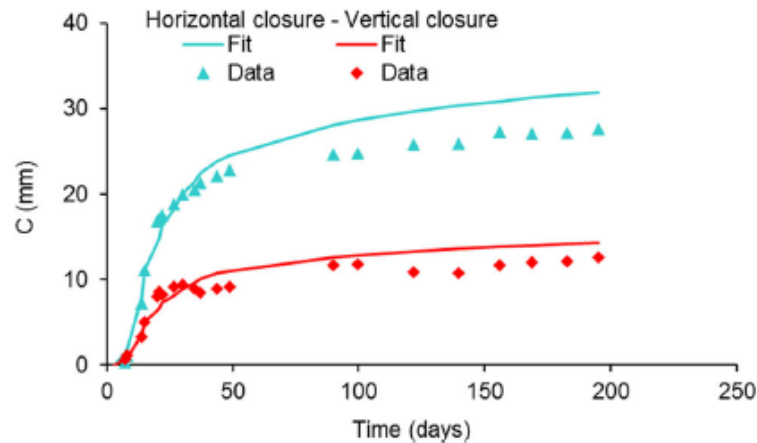


Figure 1.16: Comparison between predicted convergence (solid lines) and measurements (points) as a function of time for a drift parallel  $\sigma_H$  (GCR). Model parameters are fitted on the 40 first days of data [Guayacan-Carrillo *et al.*, 2016].

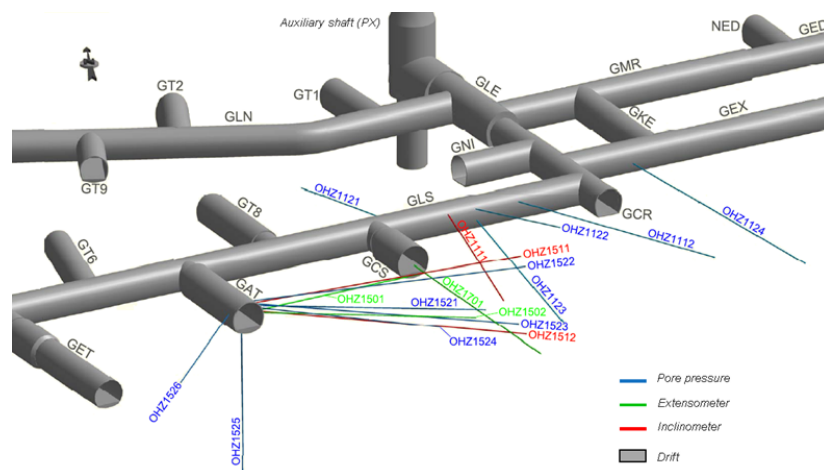


Figure 1.17: Concept of the mine-by test at GCS drift [Seyedi *et al.*, 2017]

monitoring has been set up. In total, 15 instrumented long boreholes (30 to 50 m long) were drilled from the surrounding drifts (GAT & GLS). Nine boreholes (5 chambers) are devoted to measurement of pore pressure and cover an area from the GCS wall up to 50m away. Three extensometers measure radial and axial displacements in the horizontal plane, and 3 inclinometers vertical displacements.

Figure 1.18 shows the radial displacement measured by an extensometer, which has been drilled horizontally from the GAT drift towards GCS. The end of the borehole is located nearly at the side wall of the GCS. The main advantage of this measurement compared to convergence measurements or to classically installed extensometers is that it records displacements before the front face reaches each section. Radial deformations measured have been reanalyzed in order to separate instantaneous and time-dependent responses to excavation operations [Armand *et al.*, 2013]. To do so, it has been supposed that all displacement occurring during the front advancement time corresponds to the

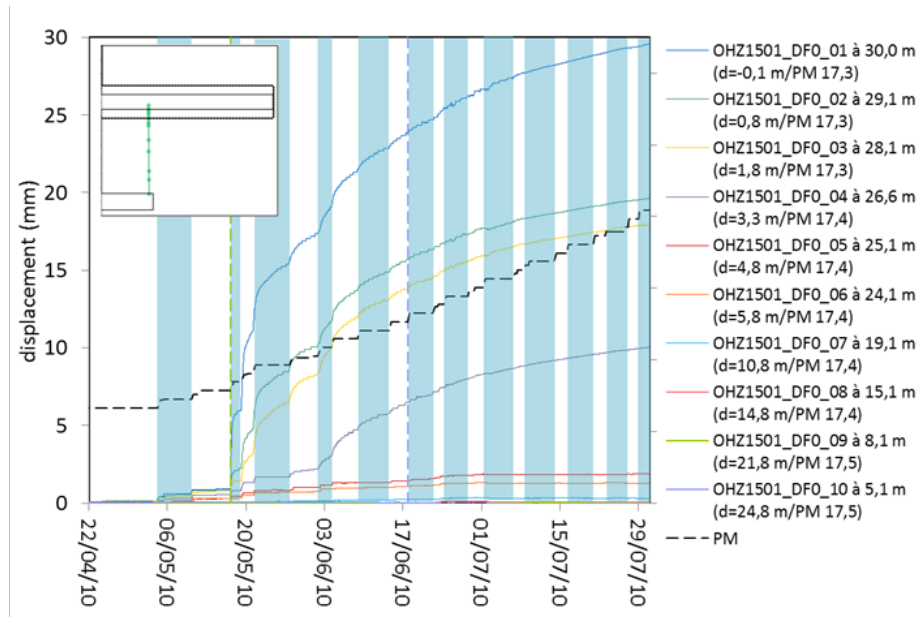
instantaneous behavior of the rock. The displacement occurred between the excavation steps of 1.2m (the delay between two steps takes into account time to install the support and measurements, e.g., borehole, and week-end closure) corresponds to the time-dependent behavior. It is seen in Figure 1.18(b) that the front advancement does not provoke any additional instantaneous displacement when the drift front is sufficiently far from each section (about 2 diameters in this case). However, the time-dependent displacement continues to increase while its rate decreases with time.

Figure 1.19 shows the pore pressure evolution around the drift GCS. Despite the initial stress state being nearly isotropic around the GCS drift, the pore pressure response is anisotropic. An overpressure of several MPa in the horizontal direction is observed (1 order of magnitude difference with the vertical plane). A drop of pressure is observed near the front face and stabilization as a function of the pore pressure gradient. The distance of influence of the excavation is estimated at about 20 m. The mechanisms behind the pore water pressure response around an underground opening are twofold. The first type of mechanisms can be associated with nearly undrained behavior, due to the very low permeability of COx, and the related pore water pressure changes induced by the stress redistribution triggered by the tunnel excavation. This means in the short term the pore pressure changes are due to volumetric deformation of the rock mass. The presence of over pressure deep in the field (> 1 diameter) in a section with isotropic stress state emphasizes the role of the elastic anisotropy (the material is more stiff in the direction of bedding, i.e. horizontal). The second type of mechanism is related to drainage of excess pore water pressure governed by the atmospheric water pressure condition at the gallery wall and the water flow law.

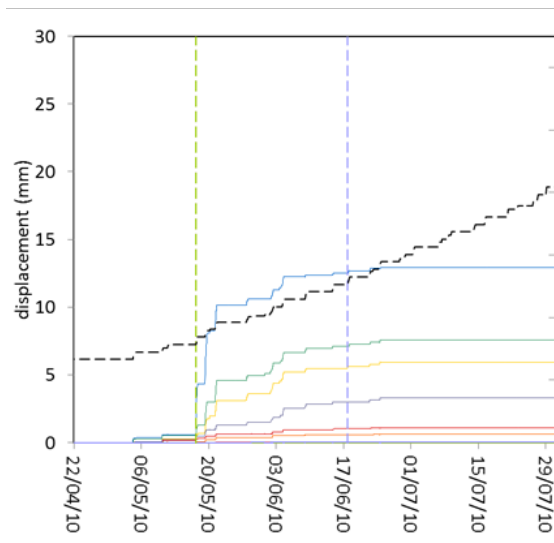
### 1.3.4 Thermal tests

An important research program has been conducted by Andra since 2005 in order to investigate the THM response of COx to thermal loading through *in situ* experiments [Armand *et al.*, 2017b]. The *in situ* experimental program consists of a step-by-step approach started by small scale heating boreholes (TER: one heating borehole, and TED: three heating boreholes) to full-scale experiments (ALC: a full-scale heating micro-tunnel). In the following, a brief description of the TED experiment is presented.

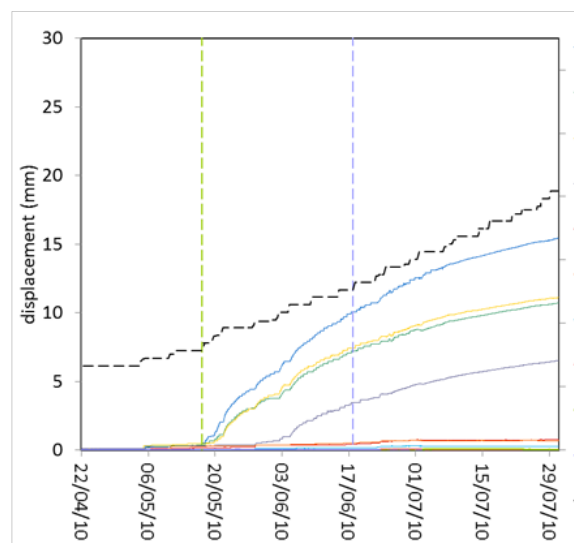
The TED experiment [Conil *et al.*, 2020] started in January 2010 and ended in July 2013 to characterize the thermal properties of intact COx, to improve the understanding of COx THM behavior and to estimate various THM parameters and comparison between *in situ* and laboratory measurements. The experiment involved three heaters in three parallel boreholes at a distance of about 2.7 m. This arrangement was intended to study the overpressure generated in a similar configuration to HLW cells with parallel microtunnels, but at a small-scale. The TED experiment is located in the GED drift (Figure 1.11), at the main level of the MHM URL (i.e., -490m). The three heaters are 4 m long and have been installed at the end of 160 mm in diameter and 16 m long boreholes in order to avoid the influence of temperature variations of the GED drift. The boreholes are drilled parallel to the maximum horizontal stress ( $\sigma_H$ ). The experiment is heavily instrumented in order to monitor



(a) OHZ1501 total response

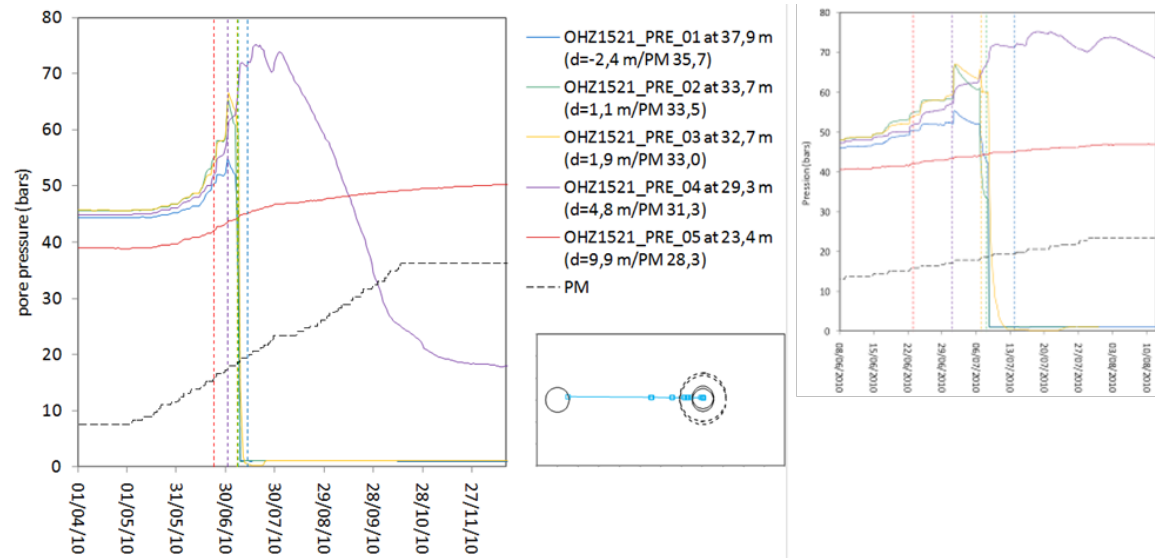


(b) instantaneous response

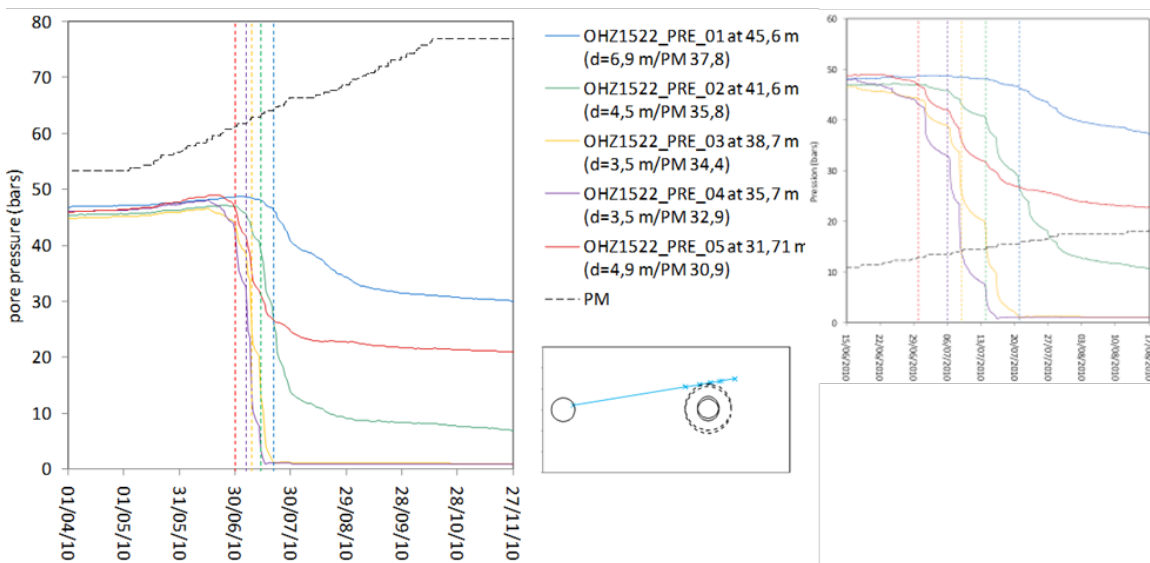


(c) time-dependent response

Figure 1.18: Rock mass displacement measured in the mine-by test: (a) Total response; (b) instantaneous response; and (c) time-dependent response of the extensometer OHZ1501. "PM" values represent the face advancement, "d" values show the distance of each point from the drift wall. Green dashed line shows the instance when the face reaches the extensometer location. Purple dashed line represents the instance beyond which, there is no face advancement effect on the section [Armand *et al.*, 2013].



(a) OHZ1521 horizontal response



(b) OHZ1522 vertical response

Figure 1.19: Pore pressure evolution during the digging in horizontal (a) and vertical (b) direction. "PM" values represent the face advancement, "d" values show the distance of each point from drift wall. Dashed vertical lines show the instance when the face reaches the measurement points [Seyedi *et al.*, 2017].

temperature, pore pressure and displacement induced in the surrounding rock during the heating and cooling phases. A particular attention has been paid towards reducing uncertainties in the sensors location in boreholes.

The temperature sensors in the rock mass recorded the temperature within the heated zone as well as in the non-heated zone. The monopacker boreholes were close to the heaters in such a way that they could be used to observe the impact of heating on the pore pressure. The multipacker boreholes were installed further from the heated zone and measured the pressure gradient from the drift wall. Most of the sensors lied at 14 m distance from the GED drift, in the plane coinciding with the mid-section of the heaters. The nominal power to be applied in each heater was designed to achieve a maximum temperature of 90°C on the rock-heater interface when the three heaters were switched on. The layout of the experiment platform is illustrated in figure 1.20. Figure 1.21 shows the location of all boreholes around the heating ones.

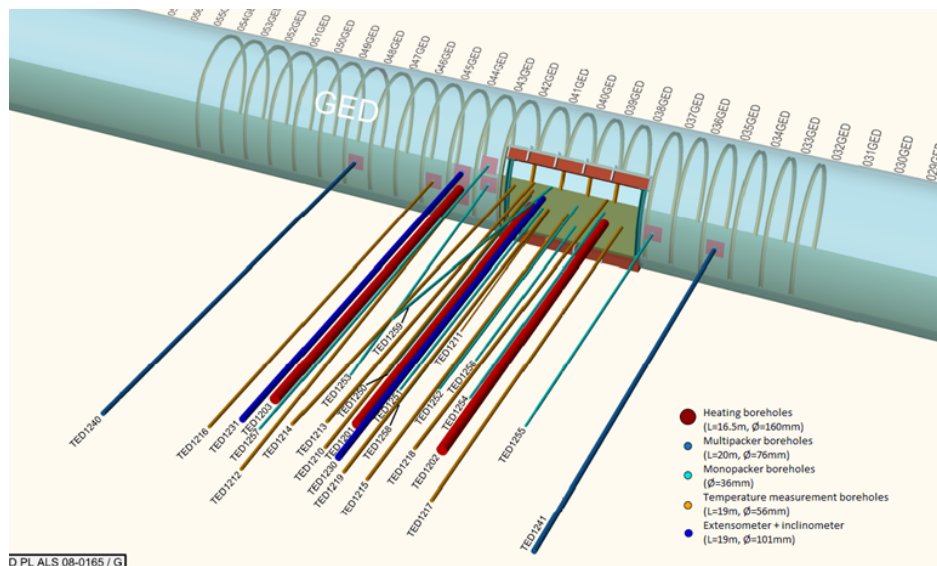


Figure 1.20: Three-dimensional layout of the TED experiment [Conil *et al.*, 2020].

The temperature measurements made during the TED experiment showed that the rock has an anisotropic thermal conductivity. The temperature increase is higher in the parallel to bedding direction than in the perpendicular direction (see Figure 1.22 with boreholes TED1219 and TED1210). At each distance, in the parallel direction the temperature increase is greater and faster than in the perpendicular direction. This is due to anisotropic heat conduction. The thermal conductivity is greater in the bedding plane than perpendicular to it. This anisotropy was also reported on samples [Armand *et al.*, 2017] and has been numerically confirmed through TED data analyses.

Concerning the pore pressure evolution, it is the result of the interplay of pore pressure generation by heating and pore pressure dissipation due to drainage (see Figure 1.23). When heating starts, the differential thermal expansion of water and solid skeleton causes a pore pressure increase (at a rate that depends on the temperature increase rate). Then, the pressure increase in the heated zone induces

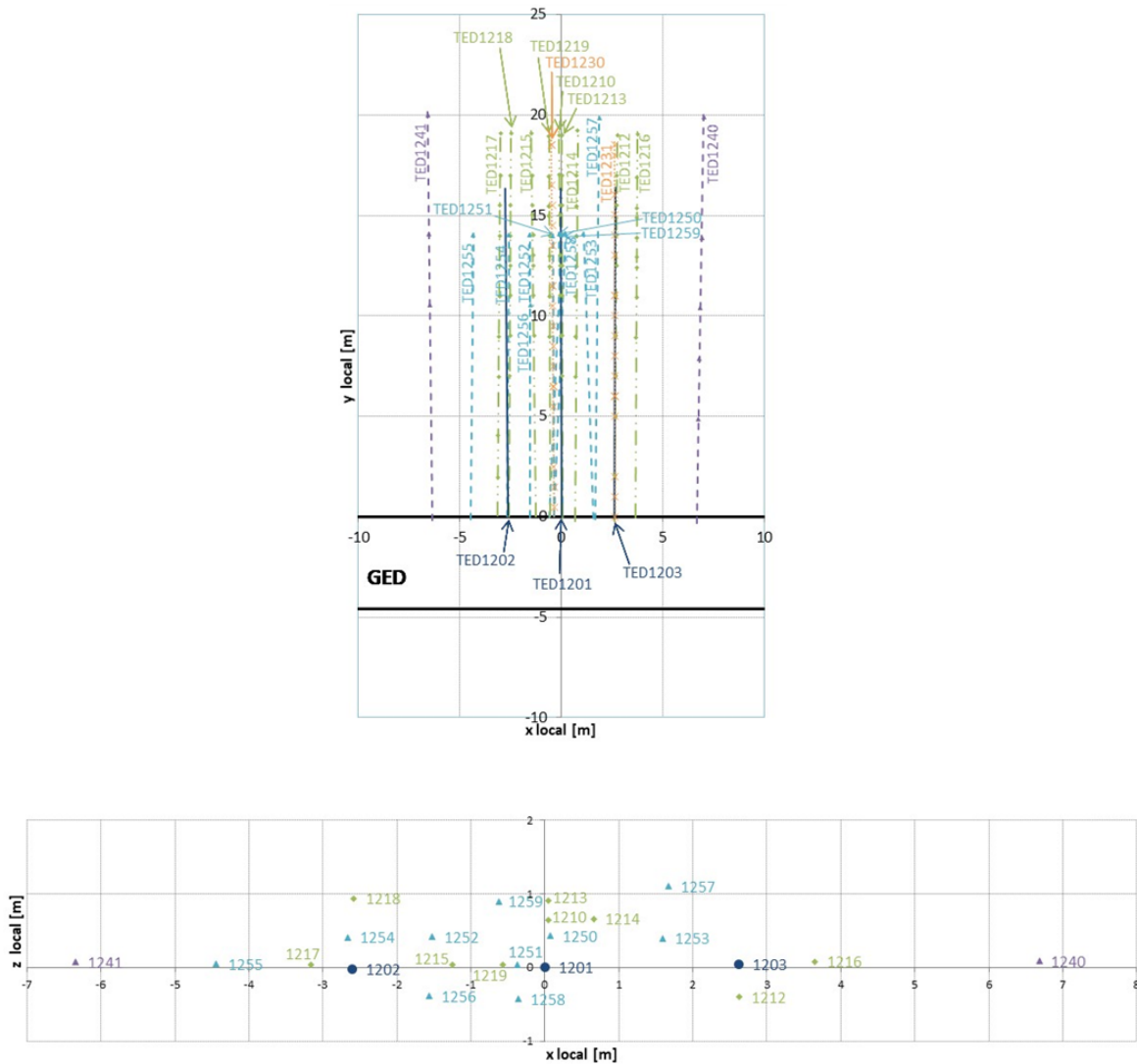


Figure 1.21: Plan view of the temperature (green diamonds), pressure (cyan triangles for monopackers and purple triangles for multipackers) and displacement (orange crosses) measurement boreholes and sensors in rock mass (top) and cross-section view at the 14 m plane of the temperature and pressure sensors (bottom) [Conil *et al.*, 2020].

a pressure gradient between the heated zone and the surrounding medium. As soon as this pressure gradient becomes sufficiently high, the pore pressure dissipates at a rate that depends on hydraulic conductivity of the sound rock. Observations of pore pressure also showed that its evolution depends on the location with respect to the bedding plane. Following a power increase, the pore pressure increases faster in the direction parallel to bedding than in perpendicular direction.

A thermal pressurization coefficient for COx was calculated as the slope of the pore pressure curve with temperature at its beginning, when the overall behavior is close to an undrained one. The obtained value ranges between 0.2 to 0.5 MPa/°C. It is worth noting that even if the drainage effects are very weak at the beginning of each heating phase, a completely undrained behavior cannot be achieved

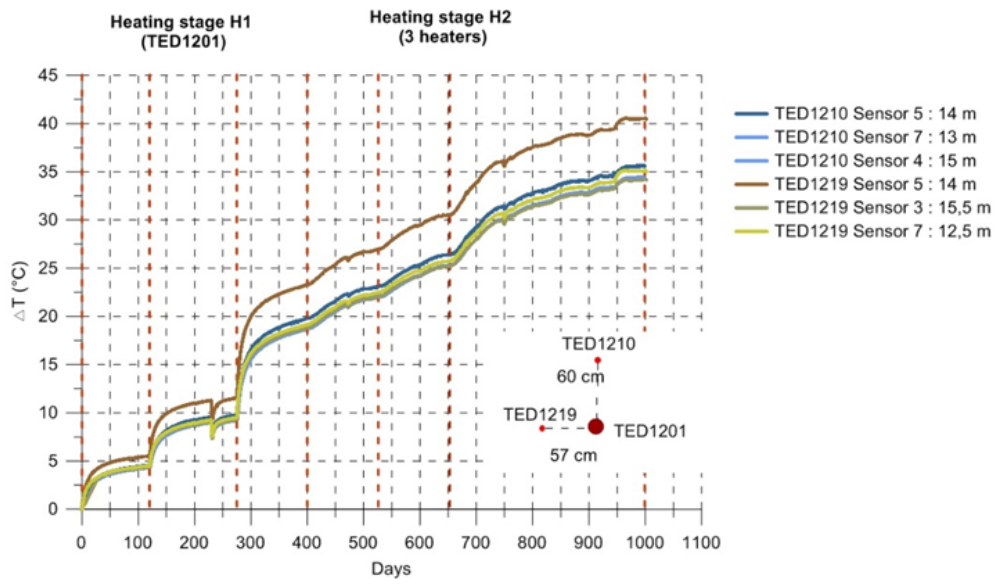


Figure 1.22: Temperature history in boreholes TED1210 (perpendicular to the bedding plane) and TED1219 (in the bedding plane) at three distances from the drift [Conil *et al.*, 2020].

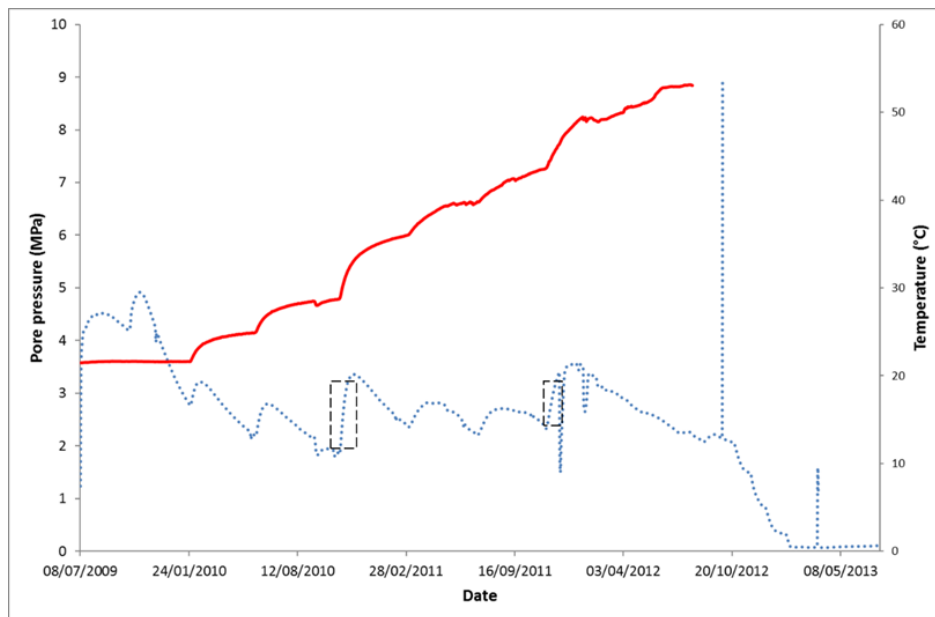


Figure 1.23: Temperature and pore pressure evolution at borehole TED1253. Modified from [Conil *et al.*, 2020].

under *in situ* conditions. Moreover, the steady state thermal regime is not established during the test. Total stress changes can also explain why the measured values of  $\Lambda$  are higher during *in situ* tests comparing those measured on samples where the mean total stress remains constant.

## 1.4 Effect of anisotropy and hydromechanical couplings on pore pressure evolution

A poroelastic analysis is performed using finite element method during PhD of L.M. Guyacan-Carrillo to simulate the pore pressure evolution induced by drift excavation. The main goal of this study is to understand the principal trends of the pore pressure evolution with a simple model taking into account the influence of elastic anisotropy of the material. It is assumed that the porous material is fully saturated and under isothermal conditions. The set of Equation (1.7) are implemented in the finite element code FreeFem++ [Hecht, 2012].

$$\begin{cases} \nabla \cdot (C_{ijkl}d\varepsilon_{kl} + b_{ij}dp_f) = 0 \\ b_{ij} \frac{d\varepsilon_{ij}}{dt} + \left( \frac{1}{N} + \frac{\phi}{K_f} \right) \frac{dp_f}{dt} - \frac{1}{\rho_f} \nabla \cdot \left( k \frac{\rho_f}{\mu_f} \nabla p_f \right) = 0 \end{cases} \quad (1.7)$$

where  $\mathbf{C}$  is the elasticity tensor,  $\varepsilon_{kl}$  the strain tensor,  $b_{ij}$  Biot's tensor,  $p_f$  pore pressure,  $N$  Biot's skeleton modulus,  $\phi$  porosity,  $K_f$  the unjacketed pore bulk modulus [Berryman, 1992],  $k$  the intrinsic permeability, and  $\mu_f$  the water dynamics viscosity.

As mentioned above, *in situ* measurements show that for drifts following the direction of  $\sigma_H$ , even if the initial stress state is quasi-isotropic in the plane of the drift section, the pore pressure evolution and the mechanical response are anisotropic. These observations indicate that the intrinsic anisotropy of the material plays a key role in the response of the rock formation. For the particular case of COx claystone, mineral distribution maps [Robinet *et al.*, 2012] show a preferential orientation of carbonate and tectosilicate inclusions parallel to the bedding plane, while clay particles and aggregates do not follow a clearly marked orientation. This leads to a slight anisotropy of most rock hydromechanical properties. Compressive and shear wave measurements on cubic samples and also triaxial tests have exhibited elastic anisotropy. The anisotropy ratio of the dynamic Young's modulus varies between 1.2 and 2.0 [Armand *et al.*, 2017]. Furthermore, it has also been observed that uniaxial compressive depends on the orientation of load with respect to bedding planes.

Using a 2D plain strain model, the influences of anisotropy of poromechanical parameters (Young's modulus, Biot's effective stress coefficient, permeability) and the *in situ* stress state (drifts following  $\sigma_h$  and  $\sigma_H$  direction) on the pore pressure evolution due to excavation have been analyzed. The size of the finite element model is 100 m x 100 m considering a radius ( $r$ ) of drift of 2.6 m. Figure 1.24 shows the model geometry, the finite element mesh, and the initial and boundary conditions. The initial stress state ( $\sigma_{x,0}$  and  $\sigma_{y,0}$ ) and the initial pore pressure ( $p_0$ ) are prescribed on the external boundaries, normal displacements and water flow are set to zero on the symmetry axes. A zero pore pressure is prescribed on the drift wall, in order to simulate drainage. The analysis is performed for each direction of excavation. Eight different cases have been analyzed by combining variations of various material and stress state parameters to investigate the effect of each parameter and phenomenon (Table 1.2).

Figure 1.25 presents the pore pressure response to instantaneous excavation for the different studied cases. The results showed the significant effect of elastic anisotropy and stress state anisotropy on the observed pore pressure field around the drift after excavation. For the drifts following the direction

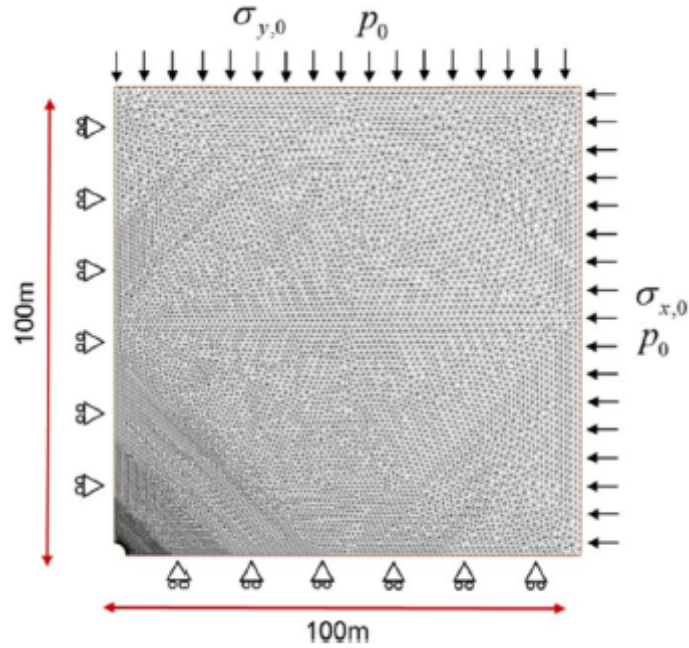


Figure 1.24: Initial conditions for two-dimensional numerical model ( $\sigma_{x,0}$  and  $\sigma_{y,0}$  are the initial stress state in horizontal and vertical direction of the drift cross section; and  $p_0$  the initial pore pressure) [Guayacan-Carrillo *et al.*, 2017].

Table 1.2: Material and stress state parameters for various studied cases in a 2D model for the excavation effect [Guayacan-Carrillo *et al.*, 2017].

	Direction	$\sigma_x$ (MPa)	$\sigma_y$ (MPa)	$E_x$ (MPa)	$E_y$ (MPa)	$\nu_{xz}$	$\nu_{yx}$	$G$ (MPa)	$b_x$	$b_y$	$k_x$ (m <sup>2</sup> )	$k_y$ (m <sup>2</sup> )
Case 1	$\sigma_H$ $\sigma_h$	12.4		4000		0.3		1540	0.6		$2.7 \times 10^{-20}$	
Case 2	$\sigma_H$ $\sigma_h$	12.4 16.1	12.7	4000		0.3		1540	0.6		$2.7 \times 10^{-20}$	
Case 3	$\sigma_H$ $\sigma_h$	12.4 16.1	12.7	4000		0.3		1540	0.6		$4 \times 10^{-20}$	$1.3 \times 10^{-20}$
Case 4	$\sigma_H$ $\sigma_h$	12.4 16.1	12.7	5200	4000	0.2	0.3	1700	0.6		$4 \times 10^{-20}$	$1.3 \times 10^{-20}$
Case 5	$\sigma_H$ $\sigma_h$	12.4 16.1	12.7	5200	4000	0.2	0.3	1700	0.85	0.85	$4 \times 10^{-20}$	$1.3 \times 10^{-20}$
Case 6	$\sigma_H$ $\sigma_h$	12.4 16.1	12.7	6400	4000	0.2	0.3	1800	0.75	0.79	$4 \times 10^{-20}$	$1.3 \times 10^{-20}$
Case 7	$\sigma_H$ $\sigma_h$	12.4 16.1	12.7	5600	4000	0.2	0.3	1750	0.8	0.82	$4 \times 10^{-20}$	$1.3 \times 10^{-20}$
Case 8	$\sigma_H$ $\sigma_h$	12.4 16.1	12.7	4800	4000	0.2	0.3	1650	0.84	0.84	$4 \times 10^{-20}$	$1.3 \times 10^{-20}$

of  $\sigma_H$ , the results obtained for cases 1, 2 and 3 are very close (Figure 1.25a). The initial stress state is quasi-isotropic and the difference with respect to the fully isotropic case (case 1) is not significant. Moreover, it was observed that considering the very low permeability of rock, the slight anisotropy of permeability (case 3) does not have a significant influence on the instantaneous rock response.

Conversely, it is observed that the anisotropy of elastic moduli (case 4) significantly influences the maximum pore pressure. In this case, an overpressure of 22% was observed in the horizontal direction of the cross-section, while in the vertical direction no overpressure was observed. For drifts following the direction of  $\sigma_h$ , it was observed that the anisotropy of the initial stress state is the main cause of the overpressures observed in the vertical direction (case 2). As explained above, the anisotropy of the permeability does not have a significant influence, thus the results obtained in cases 2 and 3 are very close (Figure 1.25(b)). However, taking into account elastic anisotropy (case 4) leads to a lower vertical overpressure compared to cases 2 and 3. These observations show that the anisotropy of elastic properties plays a key role on the pore pressure evolution for both directions of excavation. This anisotropic evolution of the pore pressure just before the tunnel front passes a section, affects

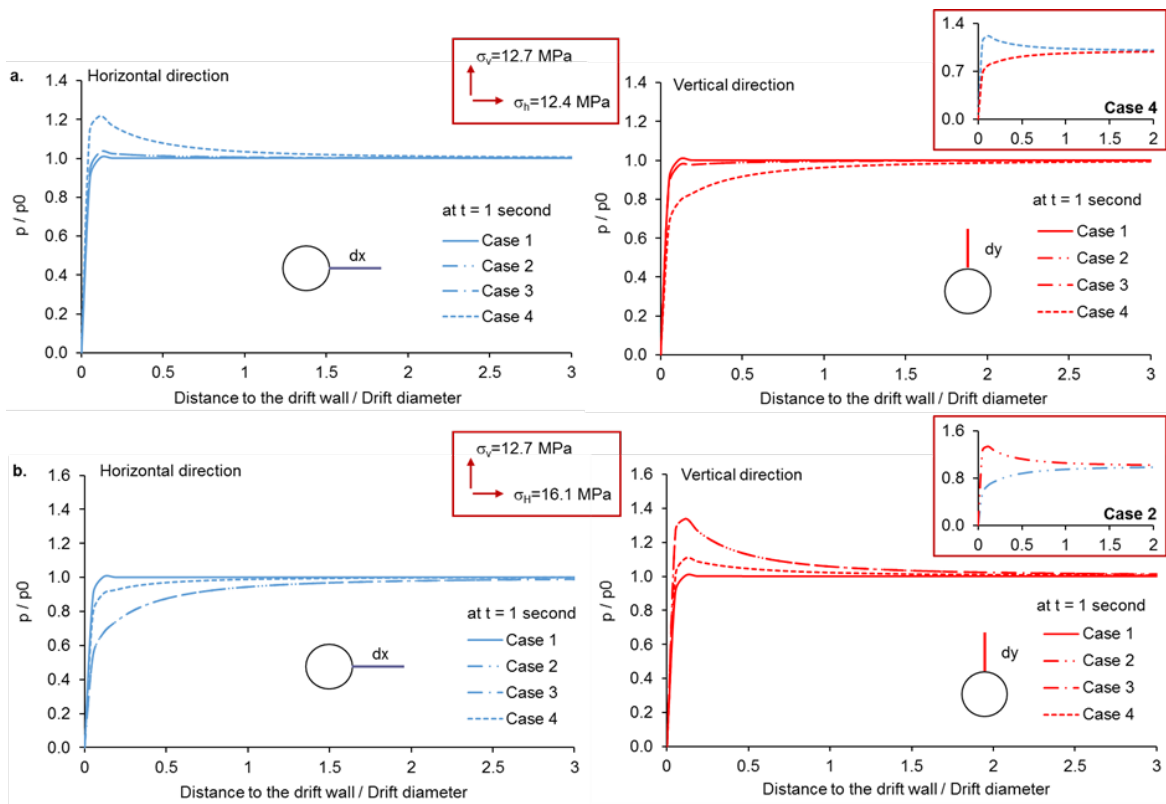


Figure 1.25: Instantaneous pore pressure change induced by instantaneous excavation with drained boundary conditions: (a) Drift following the direction of  $\sigma_H$ . (b) Drift following the direction of  $\sigma_h$ . Left: horizontal pore pressure evolution, right: vertical pore pressure evolution [Guayacan-Carrillo *et al.*, 2017].

the effective stress field around drifts. In deed, even for drifts parallel to  $\sigma_H$ , where the initial total stress is quasi-isotropic in the section of drift, the effective stress field becomes anisotropic due to the induced lateral overpressure.

In an attempt to highlight the influence of the hydro-mechanical couplings in the initiation of fractures around drifts, an analysis was performed based on the Terzaghi effective stress distribution ( $\sigma'_{ij} = \sigma_{ij} + p$ ) around excavations. Cases 6, 7 and 8 presented in Table 1.2 have been considered.

The principal stresses around the excavation ( $\sigma'_1$  and  $\sigma'_3$ ) were calculated in the case of instantaneous excavation by imposing a zero-flow boundary condition at the drift wall. The *in situ* observations show the presence of mode I and mode II fractures in the vicinity of drift walls. Failure initiation was thus assessed by using an interpolation between Fairhurst's generalized Griffith fracture criterion and the Mohr-Coulomb shear failure criterion. Fairhurst's generalized Griffith fracture criterion [Fairhurst, 1964], which is a generalization of Griffith criterion [Griffith, 1921], allows to analyze the tensile failure based on the ratio of compressive to tensile strength  $n = \sigma_c/|\sigma_t|$ . For  $n \geq 3$ , which is the case for almost all geomaterials, the failure criterion is given by

$$\sigma'_1 = \frac{1}{2} \left[ (2\sigma'_3 + A|\sigma_t|) + \sqrt{(2\sigma'_3 + A|\sigma_t|)^2 - 4(\sigma_3'^2 - A|\sigma_t|\sigma'_3 + 2AB\sigma_t^2)} \right] \quad (1.8)$$

$$A = 2 \left( \sqrt{\sigma_c/|\sigma_t| + 1} - 1 \right)^2; \quad B = \frac{1}{8}A - 1$$

The Mohr-Coulomb failure criterion, describes shear failure initiation

$$\sigma'_1 = \frac{1+\sin\phi}{1-\sin\phi}\sigma'_3 + \frac{2C\cos\phi}{1-\sin\phi} \quad (1.9)$$

where,  $C$  is the cohesion and  $\phi$  the friction angle of rock mass formation. The combination of Fairhurst and Mohr-Coulomb failure criteria permits to distinguish between zones around the excavation that exhibit extension/tensile failure and, those exhibiting shear failure. The continuity between the two criteria was assumed by imposing the same tangent at their intersection. It should be noted that the tensile strength and the cohesion were considered to be anisotropic and vary with the angle between the normal to bedding planes and the direction of loading. Based on available experimental data  $\sigma_t$  was taken equal to  $-1.5$ ,  $-1.2$  and  $-1.3$  MPa respectively for directions parallel, perpendicular and diagonal with respect to the bedding plane. The cohesion  $C$  was taken equal to  $6.6$ ,  $5.9$  and  $5.6$  MPa respectively for the aforementioned directions. The friction angle  $\phi$  was taken constant and equal to  $23^\circ$ .

As an example, Figure 1.26 presents the failure criteria for case 6 ( $E_x/E_y = 1.6$ ), as well as the principal stresses in the three orientations analyzed for drifts following the direction of  $\sigma_H$  and  $\sigma_h$  respectively. The results showed that for both orientations of drift and for all studied cases, tensile failure occurs in the horizontal direction of the drift cross section ( $0^\circ$ ). In the diagonal and vertical directions ( $45^\circ$  and  $90^\circ$ ) the failure mode depends on the degree of elastic anisotropy and on the orientation of drifts.

The effect of elastic anisotropy on the shape of the fracture initiation zone is illustrated in Figure 1.27 for drifts following the orientation of  $\sigma_H$ . In this direction, the highest extension of the failure initiation zone was obtained in the horizontal direction and the lowest in the vertical direction, as observed *in situ*. The anisotropy of the failure zone is more pronounced for a higher degree of elastic anisotropy. On the contrary, for drifts following the orientation of  $\sigma_h$  the highest extension of the failure zone was observed in the vertical direction and the lowest one in the horizontal direction, as observed *in situ*. In this direction, the increase of elastic anisotropy implies a more isotropic extension

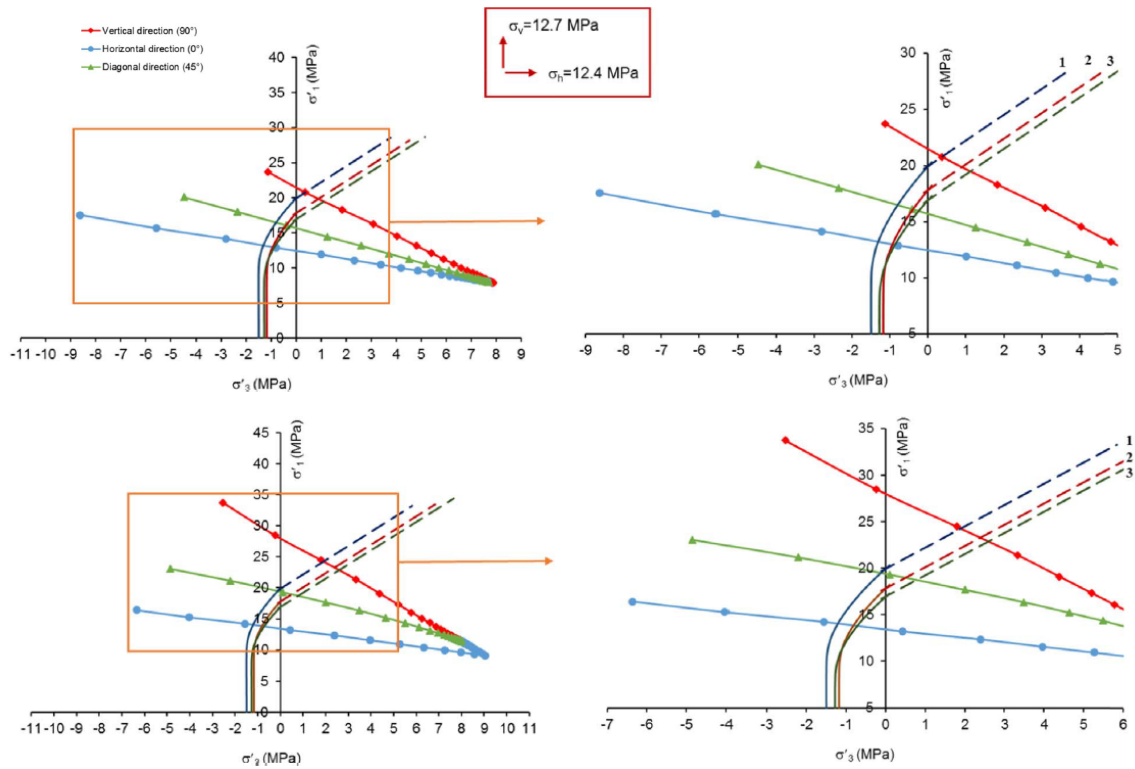


Figure 1.26: Major and minor principal effective stresses ( $\sigma'_1$  and  $\sigma'_3$ ) in the horizontal, vertical and diagonal directions of drift cross-section for a drift following the orientation of  $\sigma_H$  (top) and  $\sigma_h$  (bottom) for Case 6 ( $E_x/E_y = 1.6$ ). Fairhurst's criterion is represented with solid lines and Mohr-Coulomb criterion with dashed lines [Guayacan-Carrillo *et al.*, 2017].

of the failure initiation zone around the drift (Figure 1.28).

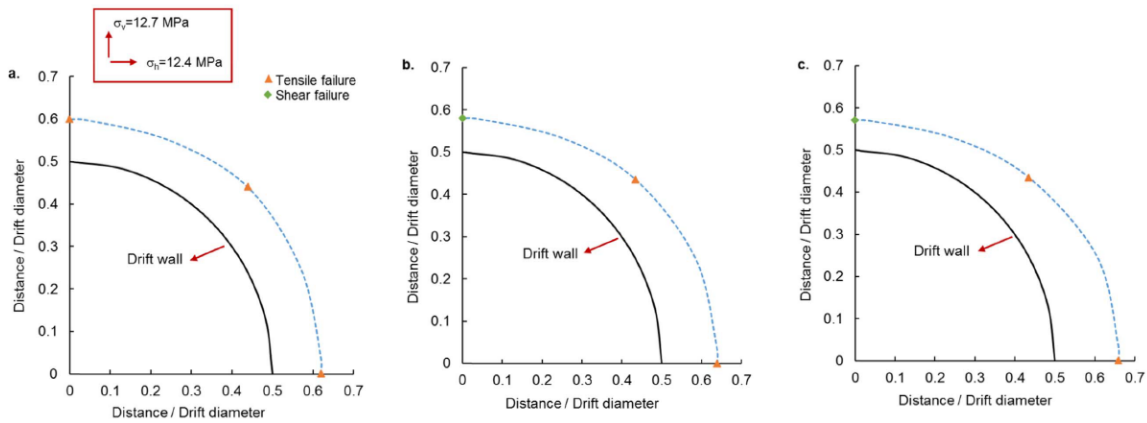


Figure 1.27: Extension of the failure zone around a drift parallel to  $\sigma_H$ . (a) Case 8, (b) Case 7, (c) Case 6 [Guayacan-Carrillo *et al.*, 2017].

In summary, it is seen that the elastic anisotropy of rock plays an important role on failure initiation around drifts through hydromechanical couplings. It is worth noting that the analysis presented in

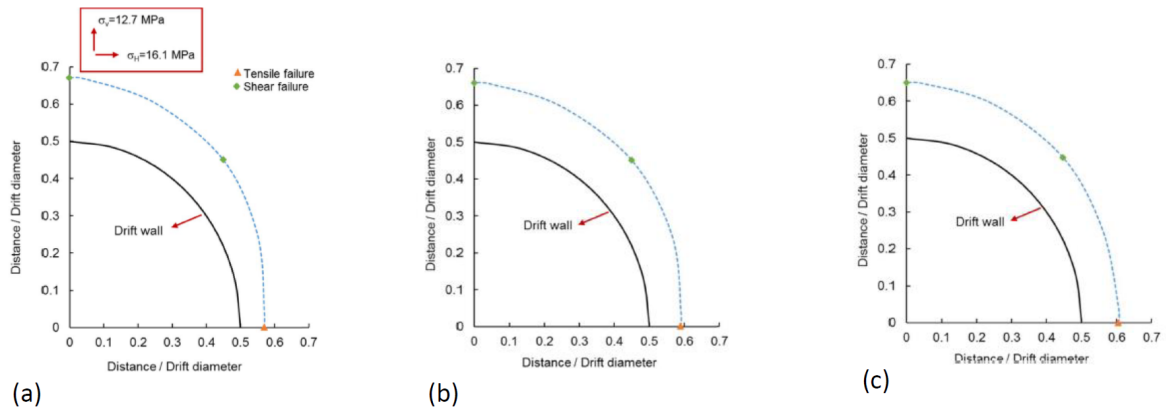


Figure 1.28: Extension of the failure zone around a drift parallel to  $\sigma_h$ . (a) Case 8, (b) Case 7, (c) Case 6 [Guayacan-Carrillo *et al.*, 2017].

this section provides only qualitative estimations of fracture initiation patterns. The degradation of rock properties and increase of the permeability in zones where a failure initiated may affect the final fracture patterns. Quantitative investigations must account for the onset and propagation of different fracture modes around drifts, considering the non-linear behavior of the porous material. The initiation and propagation of fractures and/or dilatant localized shear zones may significantly affect the local pore pressure field. In the next section, a set of numerical models developed within Andra's research program to reproduce the hydromechanical response of COx to excavation operations will be briefly introduced, followed by a short discussion on their performance.

## 1.5 Numerical modeling of the excavation operations within Callovo-Oxfordian claystone

The formation of damaged zones around underground facilities is one of the main features to be investigated in the context of geological radioactive waste repositories. The excavation of underground openings induces fracture networks in the surrounding rock. Understanding damage mechanisms and the possible pattern and extent of induced fracture zones around repository structures constitute an important issue. The impact of fractures on hydraulic permeability of fractured rock mass depends on the fractures' conductivity and density. Moreover, the extent and nature of the fractured zone has a direct impact on the loading transferred to the drifts lining and thus affects the support system design.

Several constitutive models have been developed/used in the framework of the R&D and simulation programs of Andra. These models aim to reproduce the THM behavior of COx under different repository situations and for different structures. A model benchmark exercise has been launched in 2012 [Seyedi and Gens, 2017, Seyedi *et al.*, 2017] to provide an overall view of the developed models, their basic assumptions, their mathematical descriptions, variables and parameters, and to investigate the consequences of these basic assumptions on the calculated results with regard

to the experimental observations. Four main constitutive model families are considered; namely, visco-elasto-plastic models, damage-mechanics based, rigid block spring method and computational homogenized (CHM) ones. Nine teams using different models participated in this benchmark exercise namely, GeoRessources Lab (Université de Lorraine), PRISME Lab (Université d'Orléans), LML Lab (Université de Lille), S3R Lab (Université de Grenoble), Liège Université (ULg), Universitat Politècnica de Catalunya (UPC), EDF R&D, INERIS and EGC.

Two series of test cases are defined. In the first one, simple stress paths close to those that can be produced during excavation of underground facilities are proposed. The stress paths are applied to material points to avoid any structural effects on the response obtained by different models. The second series of the test cases consist in the numerical modeling of underground drifts oriented in two principal directions.

### 1.5.1 Calibration of model parameters

A series of experimental results has been provided by Andra for parameter calibration. It has been decided to consider a recent experimental campaign with a limited number of tests performed on samples taken all from the same geological horizon. In this manner, we aimed to minimize the variability of the results due to mineralogical variability of the rock and to reduce scatter in parameter identification. The experimental results contain triaxial compression tests under different confinement stresses, triaxial extension tests under constant mean stress condition and triaxial creep tests under different deviatoric stresses and different confinement stresses [Armand *et al.*, 2017]. All involved teams have been working with Andra for several years and possess detailed knowledge of the mechanical behavior of COx claystone. The specific experimental data have been provided to the teams to calibrate their models in order to make easier the comparison of results. *In situ* observations could be also used to recalibrate model parameters especially for the last test case (case 2.3).

### 1.5.2 Material point tests

Most of rock mechanics models are designed to reproduce rock response following compression stress paths (e.g., triaxial compression path). In this exercise, simple stress paths are defined to be as close as possible to those that can be produced during the excavation of underground facilities. Extension/compression paths with or without constant mean stress and torsional stress cases are proposed in this step. The stress paths are applied to material points to avoid any structural effects on the response obtained by different models. The main goal of this first part was to investigate the effects of basic assumptions on the simulated response.

Results of this first stage showed that most of the models provide similar results before the peak. For most of the models, the predicted behavior is close regardless if the material point is loaded in contraction or in extension. An important scatter is observed concerning the calculated peak and post-peak behavior [Seyedi *et al.*, 2017]. It is worth noting that the theoretical character of the proposed stress paths prevents a comparison with an "exact" behavior.

### 1.5.3 Excavation modeling test

The second series of test cases consisted of the numerical modeling of underground drifts oriented in two principal directions. As mentioned before, most of the excavated drifts at the main level (i.e.,  $-490\text{m}$ ) of the MHM URL follow directions of the *in situ* principal horizontal stresses. Both directions, i.e., parallel to  $\sigma_h$  and parallel to  $\sigma_H$  were considered.

When drifts are excavated parallel to  $\sigma_h$ , the initial stress at the section of the drift is anisotropic. The horizontal stress is about 30% higher than the vertical one. Two different configurations were considered, namely with and without hydromechanical couplings. A 2D plane strain configuration was considered. The geometry of the model and prescribed boundary conditions are illustrated in Figure 1.29. A homogeneous initial stress state was considered by neglecting gravity effects. When hydromechanical couplings were considered the initial pore pressure was assumed to be equal 4.7 MPa everywhere in the model.

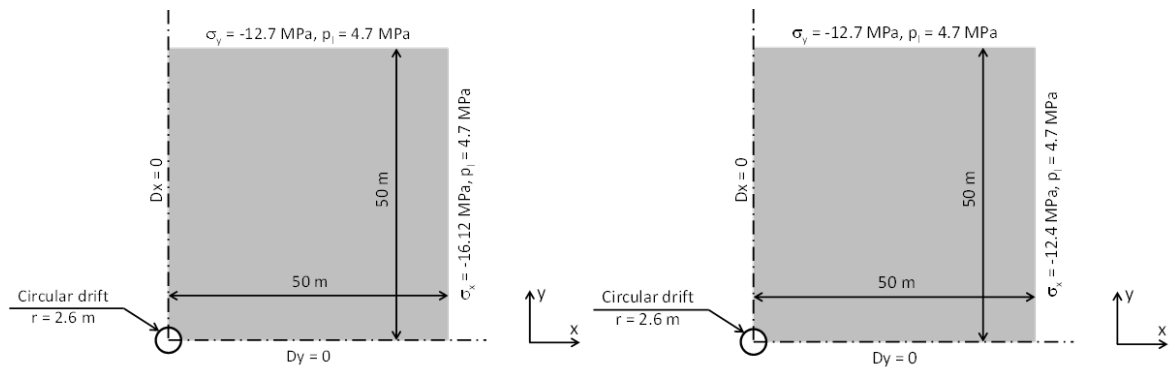


Figure 1.29: Geometry and boundary conditions, drift parallel to  $\sigma_h$  (left), drifts parallel  $\sigma_H$  (right) [Seyedi *et al.*, 2017].

For drift excavated parallel to  $\sigma_H$ , the initial stress state is quasi-isotropic in the section of the drift. The main goal of this type of tests was rather to obtain a modeling strategy that can reproduce as close as possible the *in situ* observations, than an inter-comparison between different modeling results. In this view, each modeling team was able to recalibrate model parameters based on *in situ* observations, taking into account hydromechanical couplings, or mechanical/hydraulic anisotropies to improve the modeling results. The only condition was to use the same model.

The excavation operation was modeled following the convergence-confinement method [Panet, 1995]. In this setting the three-dimensional effects of the tunnel face advancement is simulated by a 2D model where a fictitious inner pressure is applied on the tunnel wall. The applied pressure is decreased following a deconfinement curve representing the mechanical response of the rock mass to the excavation progress. An experimental deconfinement curve based on *in situ* observations of the MHM URL is proposed for the present benchmark [Seyedi *et al.*, 2017].

When hydromechanical couplings were considered (e.g., test case 2.2), a rather rapid pore pressure decrease on the tunnel wall was considered jointly with mechanical deconfinement. The observed

lateral pressure increase just before the front was not applied as boundary condition on the tunnel wall. A progressive decrease of the pore pressure on the tunnel wall was considered to avoid numerical instabilities (Figure 1.30).

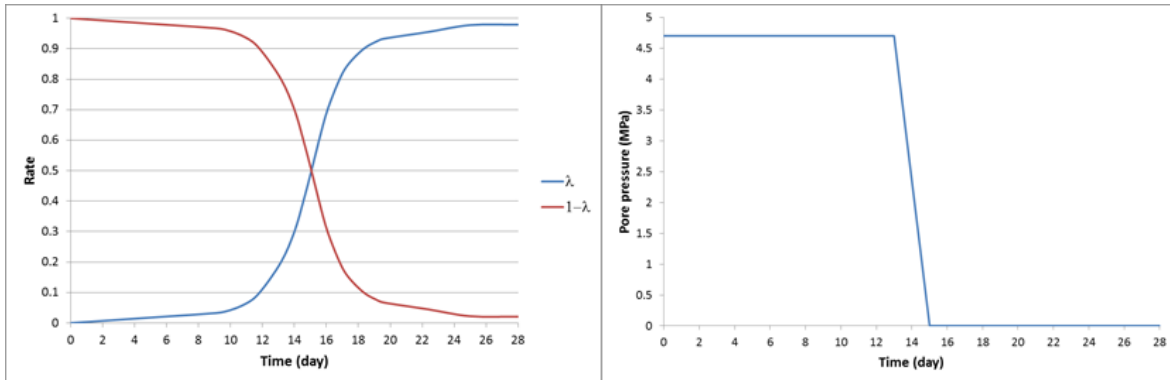


Figure 1.30: Mechanical (left) and hydraulic (right) deconfinement curves. [Seyedi *et al.*, 2017]

### 1.5.3.1 Extent of the damage zone

When an elastoplastic constitutive law is used, the model can provide the extent of the plastic zone (e.g., [Souley *et al.*, 2017, Cuvilleza *et al.*, 2017]). As a first order approximation, the extent of the plastic zone can be compared to the global extent of the damaged zone. However, any information cannot be provided on the detailed behavior of the fractured zone, density of fractures and their possible opening. As for any softening constitutive law, using an elastoplastic model to simulate the behavior beyond the strength peak yields to mesh dependent results associated with strain localization [e.g. Aubry and Modaressi, 1992]. A regularization treatment method is thus necessary to obtain mesh-objective results. When a localization treatment method is used, the formation of localization bands can be considered as precursors of fracture initiation. As an example, a second gradient approach was used by Pardoen and Collin [2017] to avoid mesh dependency. The followed approach considers a constitutive stress-strain relationship between the kinematics and the stress at the microscale. In this manner, the physical microstructure of the material is represented by introducing an internal length scale to regularize the post-localization material behavior [Chambon *et al.*, 1998]. Combining this approach with an anisotropic mechanical constitutive law [Pardoen and Collin, 2017] and taking into account hydromechanical couplings allowed for a good reproduction of the extent of the fractured zones even for test case 2.3 (Figure 1.31).

Discrete element based methods represent another way to model induced fractures around underground structures. An extended Rigid Block Spring Method (RBSM) was developed and used within the present benchmark exercise by Yao *et al.* [2017]. Rock mass is characterized by an assembly of rigid blocks linked together with interface laws representing the macroscopic mechanical behavior of rock. The mechanical behavior of each interface is described by a uniform distribution of normal and tangential springs, which together define the deformation and failure process of the interface.

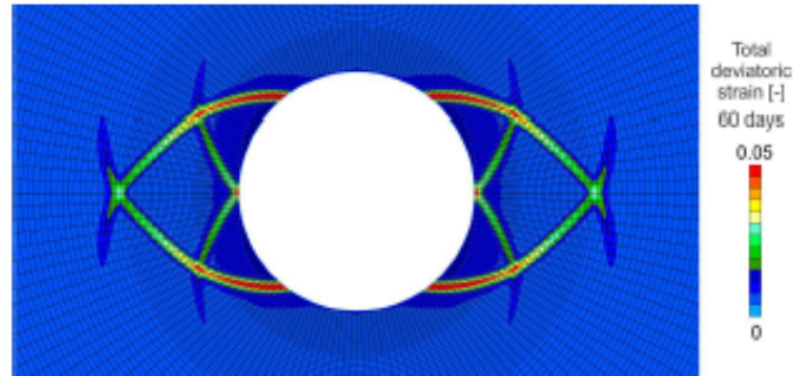


Figure 1.31: Shear banding around a drift parallel to  $\sigma_H$  (test case 2.3) representing the overall extent of the fractured zone [Pardoen and Collin, 2017].

The local failure process of an interface is controlled by both normal and shear stresses with tensile and shear failures mechanisms. Considering a transversely isotropic behavior for COx, the failure parameters of interfaces are assumed to vary with their orientation regarding to the isotropic plane (bedding planes). In addition, in order to describe overall anisotropic elastic properties, it is assumed that both normal and tangential stiffnesses of an interface vary with its orientation. Modeling results showed that taking into account mechanical anisotropy significantly improves the calculated fracture patterns in both directions (Figure 1.32).

A two-scale computational homogenized model (CHM) was developed and used by van den Eijnden *et al.* [2017]. Rock is modeled at the microscale through representative elementary volumes (REVs), taking into account the interaction of different mechanical constituents and its interaction with pore fluid. The micromechanical behavior is coupled to the macroscale boundary value problem of a poromechanical continuum with local second gradient paradigm within the framework of computational homogenization. The explicit modeling of the material microstructure is used to introduce material anisotropy. The effect of anisotropy in initiation and growth of strain localization around excavated drifts was studied and the influence on gallery convergence was investigated. Despite encouraging results, it seems that more efforts are still necessary for a more realistic microstructural representation and to improve the efficiency of the model to be used at large-scales.

### 1.5.3.2 Calculated convergence

Figure 1.33 shows the results in terms of drift convergence. It is seen that most models could not correctly reproduce anisotropic convergences observed at the URL drifts. Taking into account mechanical anisotropy seems to improve significantly calculated convergences. Another important factor comes from accounting for the accelerating effect of damage on time-dependent strains.

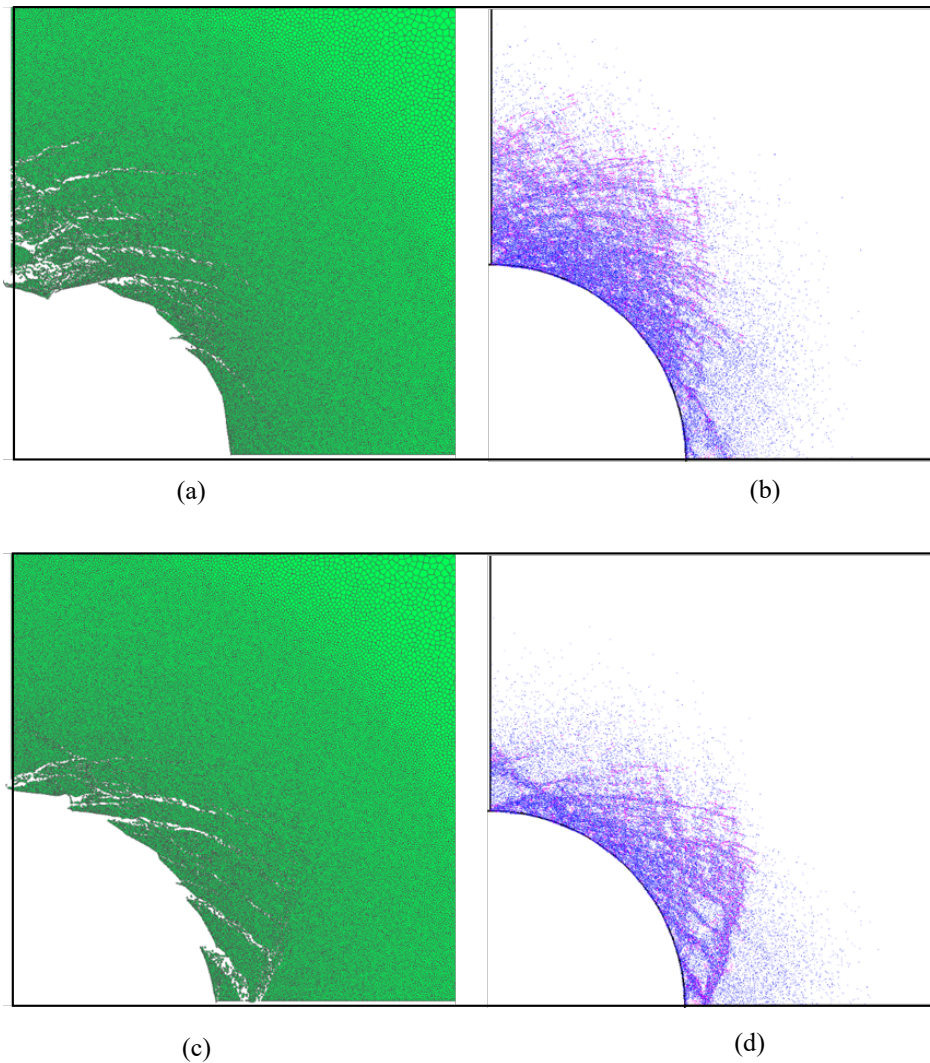


Figure 1.32: Fracture patterns for test case 2.1 ( $//\sigma_h$ ) (a) Displacement magnified by 5; (b) blue color for tensile cracks and pink for shear cracks. Test case 2.3 ( $//\sigma_H$ ). (c) Displacement magnified by 5; (d) blue color for tensile cracks and pink for shear cracks [Yao *et al.*, 2017]

### 1.5.3.3 Pore pressure evolution

As mentioned in the previous section, the hydromechanical couplings seem to play a key role on the pore pressure history around drifts. The stiffness anisotropy of COx seems to affect significantly the excess pore pressure observed especially around drifts parallel to  $\sigma_H$  just before face passage [Guayacan-Carrillo *et al.*, 2017]. Most of the models used within the benchmark could not reproduce the anisotropic evolution of pore pressure around drifts parallel to  $\sigma_H$ , mainly when elastic anisotropy is not considered.

The closest response to the measurements were obtained by an anisotropic time-dependent model developed by Manica *et al.* [2017]. The short-term response of rock is described within the framework of elasto-plasticity. Under low deviatoric stresses the response is assumed transversely isotropic elastic,

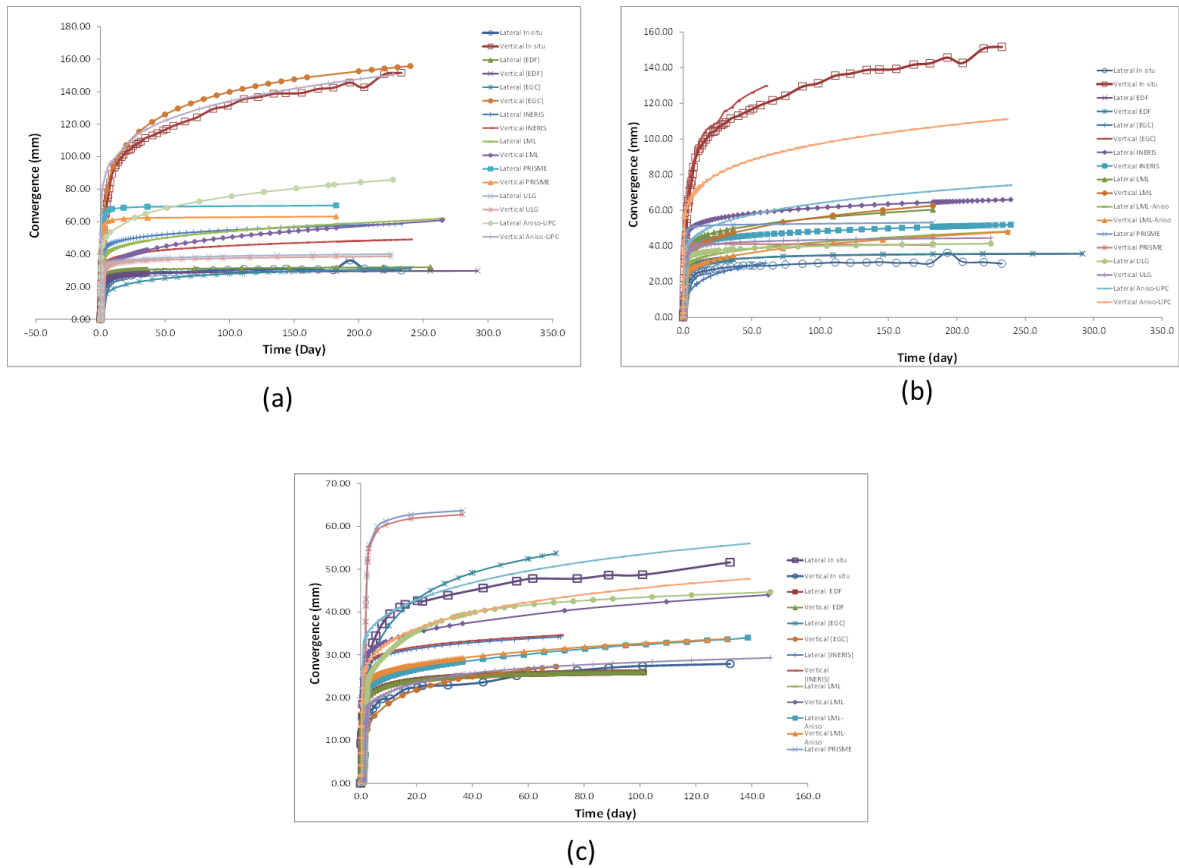


Figure 1.33: Computed convergence. (a) Test case 2.1: drift parallel  $\sigma_h$  with a soft support system. (b) Test case 2.2: drift parallel  $\sigma_h$  with a soft support system. (c) Test case 2.3: drift parallel  $\sigma_h$  with a soft support system and hydromechanical coupling [Seyedi *et al.*, 2017]

with a vertical symmetry axis. In addition, vertical and horizontal Young's moduli depend on the effective mean stress. At higher deviatoric stresses, plastic deformations develop. Transverse isotropy is taken into account through a non-uniform scaling of the stress tensor. The model is able to reproduce the liquid pressure drop in the horizontal direction near the tunnel wall just after face passage due to increased permeability in the damaged zone. The increase of pore pressure before crossing of excavation is also well reproduced, although the observed maximum peak value was not quite reached (Figure 1.34). Even though the field data show that this peak is maintained for some time, in the model the liquid pressure begins to fall off just after the front passes but it should be remembered that three dimensional effects of tunnel excavation are modeled here in a very approximate manner. However, the model could not reproduce the sharp drop of pore pressure in the vertical direction after face passage (Figure 1.34).

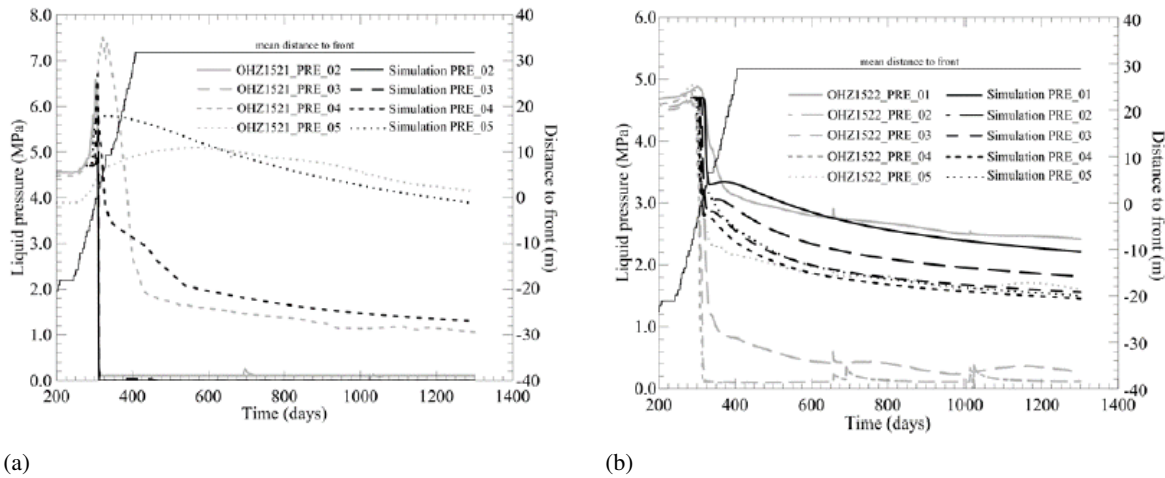


Figure 1.34: Calculated (dashed lines) and measured (solid lines) pore pressure evolution in measurement points of borehole OHZ1521 (horizontal response) (a), and in measurement points of borehole OHZ1522 (vertical response) (b) [Manica *et al.*, 2017].

#### 1.5.4 Concluding remarks

The mechanical response of COx claystone to excavation works is complex and is governed by different phenomena. *In situ* observations at MHM URL provide valuable insights regarding the impact of excavation techniques, support types and excavation rate on the rock behavior characterized mainly by asymmetrical fracture patterns, anisotropic evolution of pore pressure and time-dependent convergences around underground structures. Among others, it seems that the drift orientation regarding *in situ* principal directions (i.e., direction of initial principal stresses) affects in a significant manner the response of rock mass. Asymmetrical induced fracture patterns even around drifts, for which the initial stress state at the section of excavation is close to an isotropic state, may be considered as evidence of the inherent anisotropy of hydromechanical properties of COx.

Detailed reproduction of all observed phenomena through numerical simulations remains an open and challenging area despite important progress that has been achieved during recent years. Andra has been following an important research program aimed at providing constitutive and numerical models, which be able to reproduce as accurately as possible the observed phenomena and to be used as predictive tools for future repository structures. In this framework, different approaches have been followed based on phenomenological assumptions or micromechanical hypotheses.

The majority of the models used within the “Transverse Action” benchmark are based on the elasto-visco-plastic concept. The simulation results show that elasto-visco-plastic models provide some overall information about the global behavior of rock mass around drifts. Accounting for strain localization and considering an initial mechanical anisotropy can improve in a significant manner the obtained results especially for drifts excavated parallel to  $\sigma_H$ . The formed shear bands can be considered as precursors of shear fractures observed *in situ*. However, these models cannot provide any information on the fracture density and detailed behavior of the fractured zones. Moreover, these

models are more suitable for reproducing shear fractures (mode II) than mode I fractures. Even if about 70% of the observed events around MHM URL structures are shear fractures, mode I fractures induced near drift walls play an important role on the hydromechanical properties of the dense fractured zone.

Continuum damage mechanics models may be considered as a complementary approach to elasto-visco-plastic models. More effort is necessary for development of robust damage models especially regarding damage evolution laws and the treatment of the damage localization phenomena. Discrete element models used at micro-scales replacing a phenomenological constitutive law at macro-scale show their ability on providing interesting insights into the fracture network formations. Additional effort is necessary to improve their efficiency and also for taking into account hydromechanical coupling, time-dependent behavior and hydromechanical anisotropy. A next step will also be to perform such calculations in 3D configurations.

Taking into account hydromechanical couplings in an accurate manner remains a challenge. Most of the deployed models at the present exercise could not reproduce correctly the anisotropic pore pressure evolution observed *in situ*, particularly the pore pressure increase in the horizontal direction around drifts parallel to  $\sigma_H$ . Inherent and induced hydromechanical anisotropy of rock mass seems to play an important role and induces the observed changes. Three-dimensional effects must also be considered. Research efforts are currently ongoing at Andra and its partners to improve the consideration of hydromechanical couplings in the modeling process.

### 1.5.5 Outlook

An important point to take into account is the the role of COx's microstructure on its mechanical behavior. A series of homogenization based models has been developed within the framework of the GL Mouv to derive micro-macro models. As an example, a three-scale model was developed by [Shen et al. \[2013\]](#). The morphology of COx at the meso-scale was considered as a matrix-inclusion system. At the microscopic scale, the clay matrix was composed of an assembly of clay particles (solid phase) and inter-particle pores. The choice of such morphology was justified by the fact that the average pore size is significantly smaller than that of mineral inclusions. In order to account for the dependence of mechanical properties on the mineral compositions and porosity, a micro-macro mechanical model was proposed. The effective inclusion was characterized by a linear isotropic elastic model. The solid phase of the porous clay matrix was modeled as an isotropic elastoplastic medium, and the pores were assumed spherical. The representative volume element (RVE) is represented in Figure 1.35.

By means of a two step homogenization procedure, a macroscopic plastic criterion was formulated to estimate the nonlinear behavior of clayey rock taking into account influences of pores and mineral inclusions. Both associated and non-associated macroscopic plastic flow rules depending whether the solid phase is associated or not, have been considered. The mechanical behavior of clayey rock in conventional triaxial compression tests was studied with the proposed micro-macro model. It was shown that the non-associated plastic flow rule of the solid phase is an essential mechanism for the description of the macroscopic plastic deformation of clayey rock. This result is consistent with

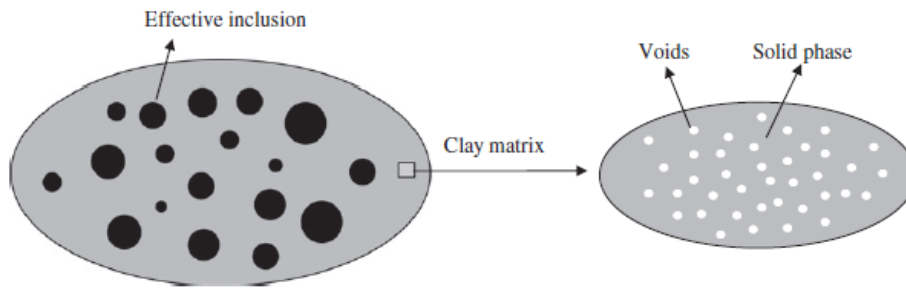


Figure 1.35: Representative volume element (RVE) of COx modeled as a matrix-inclusion system at meso-scale and an assembly of clay particles and inter-particle pores at micro-scale [Shen *et al.*, 2013].

almost all studies performed on COx. Comparisons between the predicted results and experimental data showed that the proposed model is able to capture the main features of the mechanical behavior of the studied material.

A multiscale model to simulate damage and time-dependent behavior of COx was also developed based on micro-macro approaches by Guéry *et al.* [2009]. COx was considered to be composed of three constituents: an elastoviscoplastic clay matrix, elastic quartz minerals, and elastic damaged calcite grains. The macroscopic constitutive law was obtained by adapting the incremental method proposed by Hill [1965]. To describe damage, an isotropic model, which accounts for unilateral effects due to microcracks' closure was developed for the calcite phase. The damage state was represented by a positive scalar variable, which corresponds to the density of microcracks in calcite grains. A Perzyna type elastoviscoplastic formulation was used to describe the local time-dependent behavior of the clay matrix. Thus, the local model for the long-term behavior was obtained as an extension of the short-term model.

Such models can be implemented in finite element calculation codes and used to estimate the influence of mineralogical variation within a repository area on the mechanical behavior of the host rock. They also can be extended to account for hydromechanical couplings and time-dependent behavior. It is expected that using ellipsoidal inclusions instead of spherical ones may introduce elastic anisotropy to the model. The introduction of oriented interface properties between inclusions and the clay matrix may be considered as a potential piste to account for plastic anisotropy.

Elastoplastic models can provide an overall view of disturbed zones around structures and the resulting convergence. However, any information on the density of fractures and their opening cannot be obtained using this kind of approach. Furthermore, predicting the long-term behavior of fractured zones especially after casting of rigid linings cannot be provided. Taking into account fractures as explicit discontinuities within such models is necessary.

Using fracture mechanics based models to evaluate initiation and propagation of fractures seems to be an interesting pathway to explore. Moreover, Discret Element Method (DEM) and continuum damage mechanics models seem to be interesting alternatives for plasticity based models.

Beyond the RSBM used within the Transverse benchmark, a discrete approach is proposed to study damage and failure processes by [Dinç and Scholtès \[2018\]](#). An important achievement of this work is to account for inherent anisotropy of rock. Material anisotropy is taken into account in the numerical model by introducing weakness planes distributed at the interparticle scale following predefined orientations and intensity. Similar to other DEM models, the rock material is represented by dense polydisperse assemblies of rigid and spherical particles bonded together following predefined contact laws.

The weakness planes are defined as contacts oriented according to the direction of bedding plane. Their behavior allows also introducing a load delatancy, when sliding occurs between interacting particles. Figure 1.36 shows the evolution of stiffness and uniaxial compressive strength (UCS) by the model for COx for different orientation of loading regarding the isotropy plane ( $\Theta$ ).

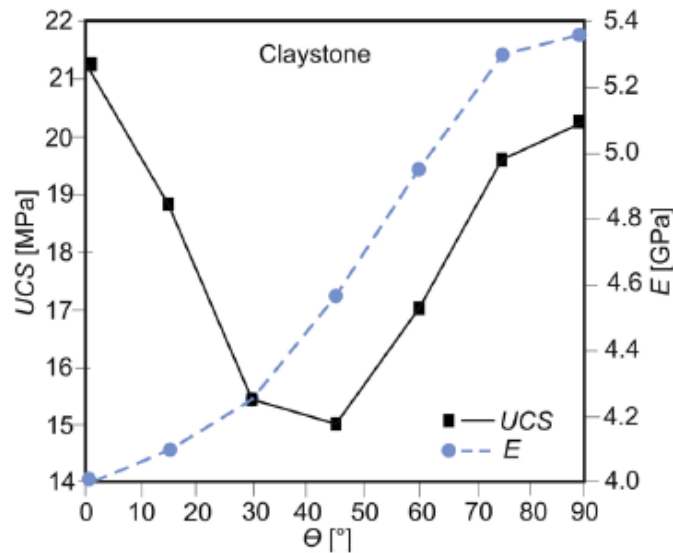


Figure 1.36: Influence of the direction of loading with respect to the material orientation on the uniaxial compressive strength (UCS) and axial elastic modulus (E) of the calibrated anisotropic DEM model [[Dinç and Scholtès, 2018](#)]

Using the calibrated model, [Dinç and Scholtès \[2018\]](#) investigated the origins of damage and shear banding processes developing in argillaceous rocks by modeling plane-strain tests performed on COx samples. Plane strain compressive tests have been performed on COx samples under a true triaxial device [[Bésuelle and Hall, 2011](#)]. Digital image correlation techniques have been used to follow the displacement and the strain field during the experiments. Figure 1.37 shows sequential evolution of the microcracking and deviatoric strain field. Different stages of the response observed experimentally have been successfully reproduced by the model.

Even if the model shows good capacity to reproduce most of the micromechanisms involved in the development of shear banding in argillaceous rocks and therefore constitutes a good basis for further studies aiming at understanding macroscopic processes, its application to large-scale simulations of excavation operation needs more developments.

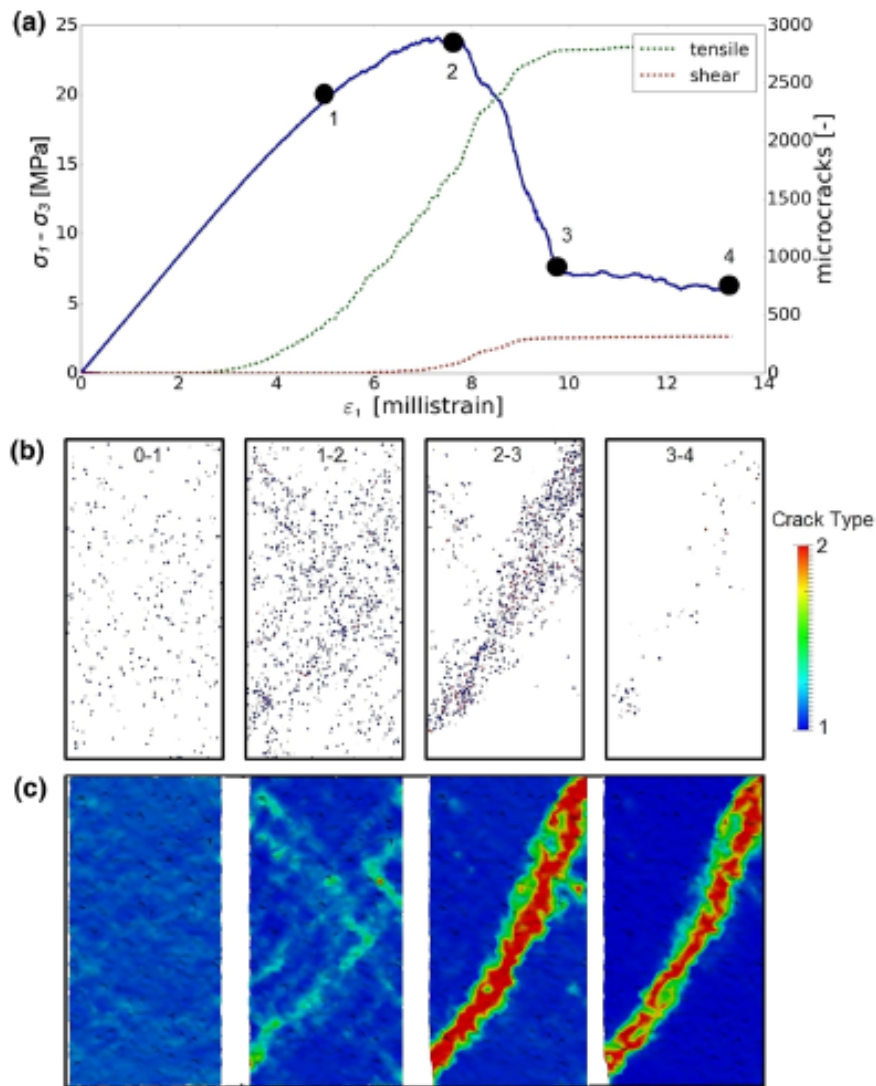


Figure 1.37: Micromechanical description of damage and failure during a biaxial compression test ( $\sigma_3 = 2$  MPa). (a) Stress–strain response and cumulative number of microcracks, (b) spatiotemporal distribution of microcracks [tensile cracks are classified as type 1 (blue), whereas shear cracks are classified as type 2 (red)], and (c) deviatoric strain fields [Dinç and Scholtès, 2018]

Continuum damage mechanics and fracture mechanics based models are two other families of models that can bring valuable insights into understanding and simulating the complex fracture patterns around underground structures built within CO<sub>2</sub>.

A 3D numerical model with strong discontinuities implemented within the Enhanced Finite Element Method (E-FEM) was developed during the PhD of P. Hauseux [Hauseux *et al.*, 2016] to address multi-cracking problems. Two failure criteria were proposed for two (tensile and shear) fracture modes; namely an anisotropic Mohr–Coulomb criterion with sliding and an anisotropic principal strain criterion with pure opening. This model was used to reproduce induced fracture networks around drifts after an underground excavation. A transversely isotropic behavior was considered for the host

rock. The influence of anisotropy of rock properties and *in situ* stress field on induced fractures and convergence of drifts were also studied.

A theoretical framework has been developed during the PhD of T. Carlioz to model crack nucleation within anisotropic media [Carlioz, 2017]. First, an idealized geometric model for cracks was justified. By specifying the notion of stable nucleation length and based on the classical tools of linear fracture mechanics, a nucleation criterion was proposed. In this view, the usual thermodynamics framework was revisited within adiabatic framework from a micromechanics point of view in order to be more in line with the brutality of crack nucleation. A purely energetic criterion was finally proposed for crack nucleation. Different methods to compute the key quantity, which is the incremental energy released rate were then built. Finally, the criterion was applied to give some justifications to the anisotropic geometry of excavation-induced fractures.

To go beyond these first attempts, it is necessary to conduct a rigorous experimental study to investigate COx fracture properties (e.g., fracture toughness) and its variation in different directions. A very first study is performed within the PhD of Mohamad Abdulmajid [Abdulmajid, 2020]. Tapered Double Cantilever Beam tests (TDCB) have been performed on COx samples machined in different directions to obtain its fracture toughness (Figure 1.38). The use of Sandwiched-beam tests is another alternative to obtain stable crack propagation for quasi-brittle materials and measure their fracture properties (see Chapter 2). Another point to consider is the role of elastic anisotropy on crack

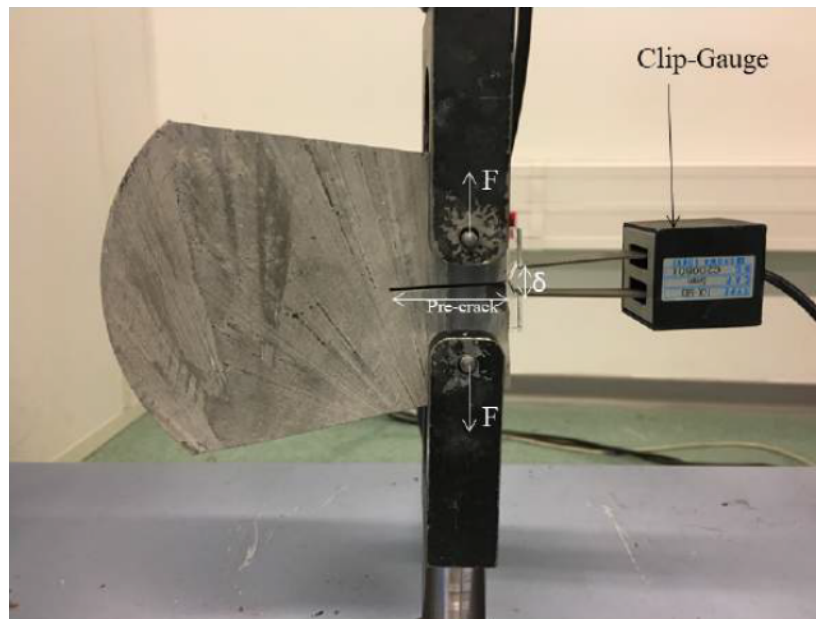


Figure 1.38: Experimental test setup used to perform quasi-static fracture tests. The electromechanical machine is equipped with a load cell sensor of 10kN, and a clip gauge with 5 mm maximum opening to measure the applied force and the crack opening displacement, respectively [Abdulmajid, 2020].

propagation in one hand and on the pore pressure evolution on the other hand. A review of experimental investigation, *in situ* observations and simulation results suggest that the anisotropic patterns of induced

fractures around MHM URL structures are the results of a combination of different factors such as anisotropic initial stress state, elastic and failure anisotropy of COx and hydromechanical couplings.

## 1.6 Numerical modeling of COx response to thermal loading

In the following, some issues of numerical modeling of the COx behavior under thermal loads are addressed. A step-by-step approach is followed. First, a numerical modeling of a small-scale *in situ* test (TED) performed within the DECOVALEX international project is presented. Then, THM simulations of a full scale demonstrator HLW cell tested at Andra's URL is presented. Finally, a THM modeling at the repository scale and accounting for spatial variability of COx parameters is discussed.

### 1.6.1 Numerical modeling of TED experiment - DECOVALEX-2019 international project

In the framework of the DECOVALEX-2019 international project (<https://decovallex.org/>), a model benchmark is proposed and coordinated by Andra for numerical modeling of the THM response of COx to thermal loadings. The main purpose of the exercise was upscaling THM models from small size experiments (some cubic meters) to real scale cell (some ten cubic meters) and to the scale of waste repository (cubic kilometers). In the first step, the models have been benchmarked to validate the correctness of their implementation considering THM processes. The second step consisted in an interpretative modeling of a small-scale *in situ* heating experiment (TED). The simulation of a full scale heating experiment (ALC experiment) on the basis of model calibrations performed at a smaller scale (TED experiment) has been done in the third step. Extending the behavior of one single cell to the repository scale (several parallel cells) approached in a last step. The results of the second step; the modeling of TED experiment are presented shortly in this subsection.

Five modeling teams participated in the exercise namely, Andra, LBNL, Quintessa, NWMO and UFZ/BGR. Three dimensional realistic THM models taking into account the experimental set-up including the main drift and different boreholes (Figure 1.20) were considered by all the teams. The models include the GED drift (radius = 2.3 m) and the heater boreholes (TED1201, TED1202 and TED1203). The hydraulic effects of the extensometer boreholes (TED1230 and TED1231) that have been shown to be draining, and to locally affect the pore water pressure field has been also considered. The considered geometry consists of a cube with a side length of 50 m (a distance set to represent far field regarding diameter of boreholes) centered in height at  $z = 0$ , i.e. almost exactly the GED drift center at the depth of 490 m. By far field, we mean a distance sufficiently far from boreholes, where COx response is not affected by the borehole damage zone.

A complete determination of the initial state before the heating phase and after GED drift excavation and borehole drilling would need in itself a whole study and would require sophisticated models. The excavation of GED drift affects the temperature, pore pressure and stress fields in its vicinity. It has also been observed that the pore pressure field is significantly affected near some of the boreholes that

have been shown to be draining: the heater boreholes and the extensometer ones.

Therefore, it has been asked to the teams to concentrate on the heating phase and not to spend too much time on excavation and drilling modeling. The determination of accurate initial pore pressure state is not necessarily essential. Since the heating part of the boreholes is located relatively far from the drift wall (i.e., between 12 and 16 m), it was assumed that the pressure and stress fields are not much affected by the presence of the excavation damaged zone around GED. It is worth noting that the fractured zone around GED drift represents an important vertical extent (up to 1 diameter) and a limited horizontal extent [Armand *et al.*, 2014].

The whole domain represented by a cube was assumed to be a homogeneous anisotropic material. The teams were asked to calibrate their models against experimental data by adjusting the different THM parameters from reference values or reference range of values provided by Andra, depending on the uncertainty about the parameters.

Regarding the mechanical properties, no parameter has been given since the teams may use different mechanical models to reproduce CO<sub>x</sub> behavior. Thus, results of a set of laboratory tests performed on samples obtained from the same location in order to minimize scatter due to mineralogical variabilities were proposed. They were meant to be calibrated by each team to determine the reference values for the mechanical parameters of their model.

The hydraulic properties were calibrated by comparing the numerical results with the measurements acquired at one pair of pressure sensors located 14 m from the drift wall, one sensor perpendicular and another one parallel to the bedding plane, in monopacker boreholes TED1253 and TED1258. The study of the pore water pressure gradient towards the drift wall is based on the pressure measured in a multipacker borehole at far field from the experiment, the TED1240 borehole, which contains 5 sensors.

Despite the existence of two strain measurement boreholes in the experiment, their results are not reliable and they cannot be used. Therefore, for displacements and stresses no comparison with field data was possible. An intercomparison study was conducted with the numerical results of the modeling teams.

#### **1.6.1.1 Modeling strategies**

All teams calibrated the thermal conductivity parameters by carrying out a thermal analysis of the heating phase with a 95% of the total heating power emitted from the boreholes; it should be noted that the heaters are emitting less heat than the designed heater output according to the observed temperature measurements. The influence of hydraulic and mechanical responses on the thermal response can be considered negligible since the dominant heat transfer mechanism is conduction. The hydraulic parameters were obtained by running coupled THM and/or TH simulations of the heating phase and considering only pore pressure increments. The main goal of these preliminary simulations was to calibrate appropriate values of the permeability in the perpendicular and parallel directions with respect to the bedding. Once the THM parameters of CO<sub>x</sub> were calibrated, a complete THM

simulation was carried out by taking the results of a previous stage to set the initial conditions (i.e., pore pressure distribution around the drift and stress state). This stage consisted mainly in the excavation of the GED drift.

COx was assumed to behave as an elastic homogeneous and anisotropic material. Therefore, the THM coupling is based on thermo-poroelasticity [e.g., Coussy, 2004]. However, each team introduces their own particularities in their respective models; especially, in hydraulic parameters in order to achieve more adequate and realistic properties of COx. Moreover, some teams partially modified the boundary conditions. The approach to obtain the pore pressure distribution and stress state after GED drift excavation also varies from one team to another. A detailed description of the specific approach followed by each team can be found in [Seyedi *et al.*, 2021]. All teams considered that the use of realistic hydraulic properties such as density, dynamic viscosity and thermal expansion plays an important role in the description of the THM behavior of COx.

Parameters such as the initial porosity  $\phi_0$ , the equivalent heat capacity  $C_{p,eq}$ , the volumetric coefficient of the thermal expansion of solid grains remained unchanged during the calibration process. The calibrated thermal parameters show a low scatter compared to the calibrated mechanical parameters (Young's modulus) and these differences become even more marked for the hydraulic parameters (intrinsic permeability). This trend is a consequence of the fact that each team follows different approaches [Seyedi *et al.*, 2021], in addition to the uncertainty introduced by parameters such as the intrinsic permeability.

In the following, the thermal, hydraulics and mechanical results will be discussed separately, highlighting similarities and differences between the different teams. Special attention is paid to the pore pressure due to the particularities in the modeling approaches followed by each team in setting the initial and boundary conditions (i.e. excavation of GED drift, draining boreholes). All teams obtained good approximations of the temperature evolution as well as the thermal anisotropic properties of COx. Different thermal conductivity coefficients were calibrated by the different teams. It should be noted that a 15% variability is observed in the field.

Figure 1.39 shows the temperature history of TED1210 and TED1219 during the heating phase. The computed temperature is in good agreement with the measurements for these two sensors. The results in TED1210 (perpendicular to bedding) and TED1219 (parallel to bedding) show that the anisotropy was also well captured by the calibrated parameters. The maximum discrepancy found between temperature data and numerical simulations for these two sensors is  $\pm 1^\circ\text{C}$ . This is in accordance with the low scatter of calibrated thermal parameters.

One of the main difficulties was to correctly reproduce the pore pressure distribution due to the excavation of the GED drift. The evolution of the pore pressure for two representative points located perpendicular and parallel to bedding (TED1253 and TED1258, respectively) were considered to compare experimental and numerical results. The other complexity comes from the choice of accurate hydraulic boundary conditions for the heater boreholes.

The most efficient changes that improved the results were:

- Decrease the intrinsic permeability of the undamaged COx,

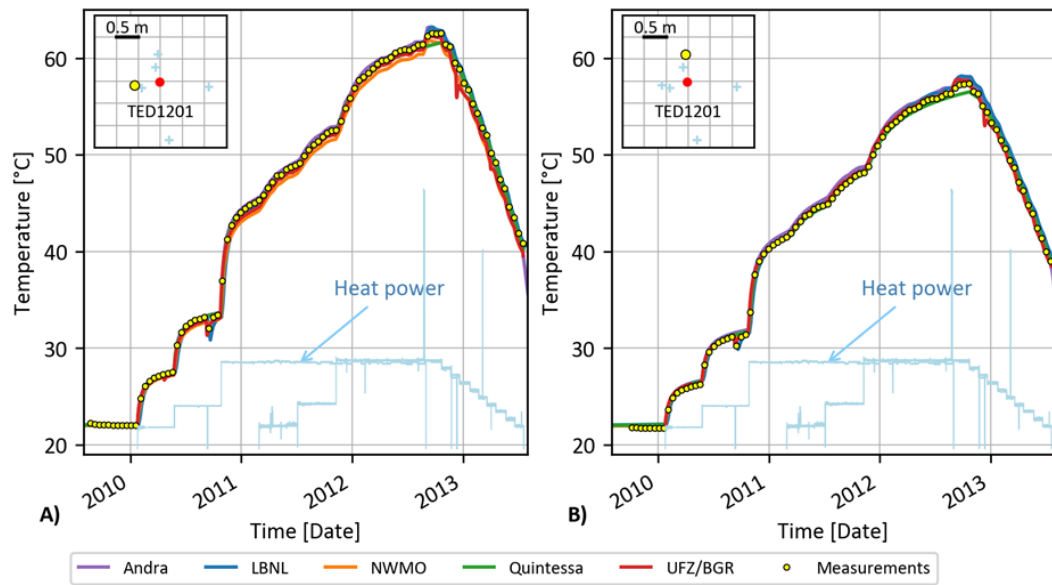


Figure 1.39: Temperature evolution at sensors: (A) TED1219\_05, located parallel to bedding and (B) TED1210\_05, located perpendicular to bedding. The heat power history is plotted in light blue [Seyedi *et al.*, 2021].

- Add an EDZ of 1 m around the drift GED with a higher permeability,
- Choose appropriate pore compressibility for boundary elements to make the draining condition between fully drain and impermeable condition,
- Modeling the boreholes with a porous material with a tuned intermediate permeability

These modifications led to major improvements on the approximation of the pore pressure evolution.

Observations of the pore pressure also show an anisotropic response due to anisotropic properties of CO<sub>x</sub>. Figure 1.40 shows the pore pressure evolution for two sensors located perpendicular and parallel to the bedding, respectively. The numerical results show that the anisotropy was well captured by the teams. There is a lower level of agreement in the pressure results than the thermal ones. This is likely due to the fact that the pressure response is a coupled one, depending on more processes and parameters in the models than the thermal response. The teams experienced difficulties in achieving a correct reproduction of the pore pressure due to the excavation of the GED drift, but this was not the main focus of the task.

The pore pressure build-up is consistent with the heating stages and the scatter of the results is more limited in the horizontal direction (TED1253\_01). The anisotropy of the pressure response is also captured and agrees with the measurements. However, the pressure peaks are either globally underestimated (TED1258\_01) or overestimated (TED1253\_01).

Figure 1.41 shows the pore pressure histories for two sensors located relatively far from the heating boreholes. The numerical comparison against the measurements shows that all teams underestimate the pressure change due to heating for sensor TED1240\_02. This may be due to spatial variability in CO<sub>x</sub> properties and representing the temperature evolution at these measuring points would help to

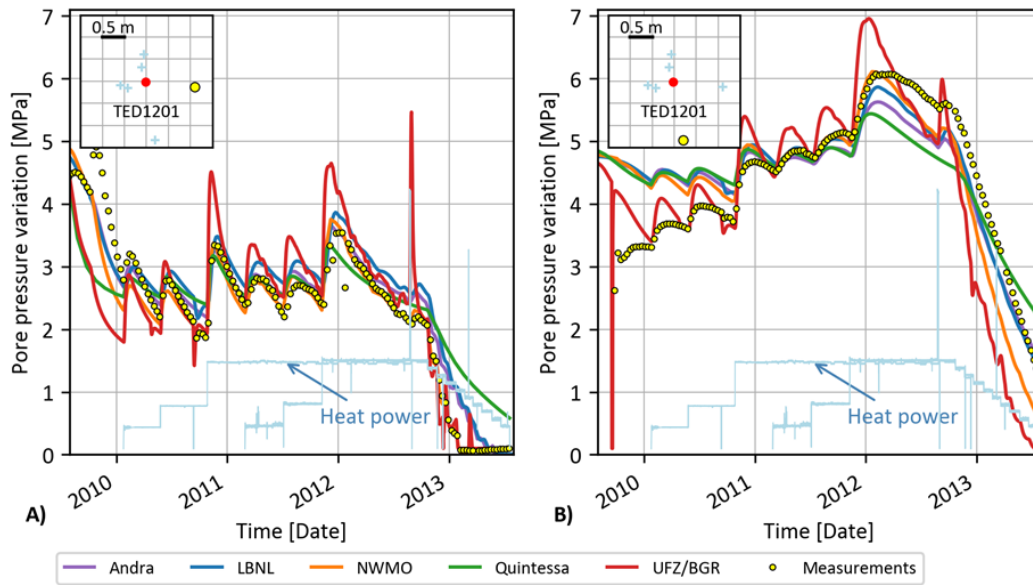


Figure 1.40: Pressure evolution at sensors: (A) TED1258\_01, located parallel to bedding, (B) TED1258\_01, located perpendicular to bedding. The heat power history is plotted in light blue [Seyedi *et al.*, 2021].

understand these differences. Unfortunately, temperature measurements were not provided for these points. The numerical results of the total stresses show that heat emitted from boreholes induces

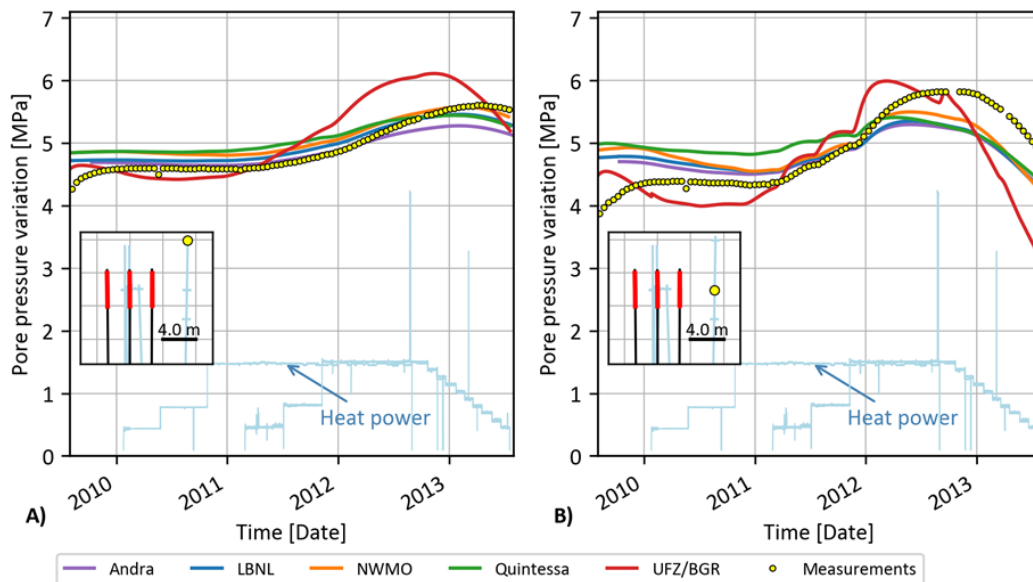


Figure 1.41: Pressure evolution at sensors (A) TED1240\_01 and (B) TED1240\_02. The heat power history is plotted in light blue [Seyedi *et al.*, 2021].

compressive total stresses far from the boreholes. It is due to the fact that the heated rock (i.e. the

near field) cannot expand freely due to the fact that the surrounding rock mass, i.e., the far field, has a lower temperature. Greater compressive stresses are induced in the horizontal direction due to elastic anisotropy of CO<sub>x</sub>. The cooling phase leads to a relaxation of these compressive stresses.

These results have shown that the thermal models work correctly and consistently for all teams (e.g., absolute values are well reproduced, the anisotropy of temperature evolution is captured). According to the observed temperature measurements, the heaters emit less heat than the designed output. Therefore, all the modeling teams agreed to use a correction coefficient of 95% to account for power loss within heaters, which were then used for the ALC experiment. The general trend of the pressure build-up due to temperature increase is well reproduced. The anisotropy of the pressure response is also captured. According to the results, the two major factors in the pore pressure description are the permeability, the Young's modulus, and their anisotropy ratios.

### 1.6.2 Numerical modeling of a single cell - ALC experiment

The ALC experiment is a full-scale demonstrator of the 2009 French concept for one single HLW disposal cell (no filling material is considered in the gap between the casing and the rock). The main objectives were [Bumbieler *et al.*, 2021] (1) to test the feasibility of such disposal, (2) to study the thermomechanical behavior of the cell and its interface with the host rock, and (3) to study the THM behavior of the host rock as previously conducted in TED experiments. Unlike the TED configuration, the ALC experiment was at its heating stage at the time of this work, thus no cooling phase was considered.

The experiment consists of a micro-tunnel (ALC1604), drilled from the GAN drift parallel to the maximum horizontal stress; it has a total length of 25 m. The ALC1604 micro-tunnel is divided into two parts: a head part 6 m in length with an excavated diameter of 0.791 m and a 19 m long usable part with an excavated diameter of 0.75 m. The head part has a steel insert, with 0.767 m external diameter and 21 mm thick, and the usable part has a casing, with 0.70 m external diameter and 20 mm in thickness. There is an overlapping zone of 1 m width between the casing and the insert (i.e., between 5 and 6 m from the GAN drift wall). The heated zone is located in the usable part between 10 and 25 m in depth and is made up of five 3 m long heating devices. An overview of the ALC1604 micro-tunnel and the instrumentation boreholes is shown in Figure 1.42. A heating test at low power (33 W/m) was first conducted between 31<sup>st</sup> January and 15<sup>th</sup> February 2013. The main heating phase started on 18<sup>th</sup> April 2013, at a constant nominal power of 220 W/m.

A blind prediction has been performed by all participating teams within "DECOVALEX" Task E. The initial conditions were obtained in the same manner as for TED experiment. CO<sub>x</sub> THM parameters are the same as the values calibrated in the TED experiment. The proper way of representing this architecture was one of the main issues of this task. The teams were free to choose their own approach. In this way, the real geometry could be simplified (including or not the casing, applying a homogeneous thermal load on the rock wall or not, modeling the annular space).

The modeling teams kept their respective models along with the calibrated parameters in the TED

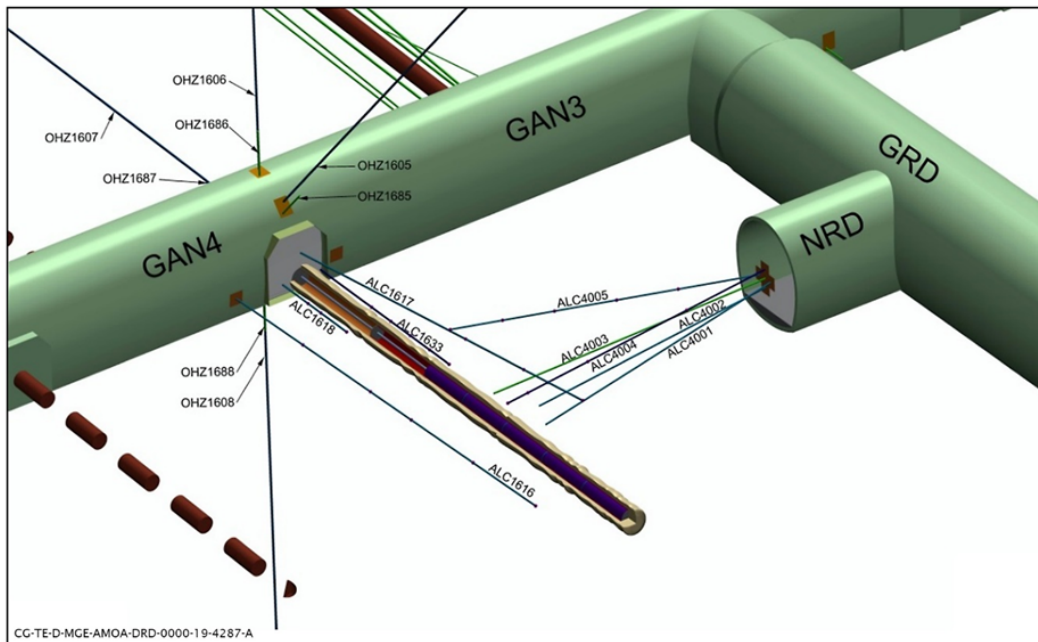


Figure 1.42: Three-dimensional layout of the ALC experiment [Bumbieler *et al.*, 2021].

experiment. Following the approach in the TED experiment, the thermal model was used to predict the temperature, which was then compared to the provided measurements in the field. The heat input was reduced to 95% to account heat losses. The fully coupled THM formulation was used to predict pore pressure and be compared against the pore pressure measurements and as a first approach, no EDZ around the micro-tunnel was considered.

The results of the blind prediction of the temperature and the pore pressure are presented from the beginning of the main heating phase until 1000 days after the beginning of the cell excavation (Figure 1.43 and Figure 1.44).

The numerical results of all modeling teams for the blind prediction show a good agreement with the measured temperature evolution (Figure 1.43). The good prediction of the temperature for sensors located in the parallel and perpendicular directions to bedding shows that the thermal conductivity coefficient and its anisotropic ratio were well calibrated.

The numerical results of the predicted pore pressure by the modeling teams are shown in Figure 1.44. The pore pressure before the beginning of the main heating phase was not well captured in most cases and is not been shown. However, some modeling teams not only captured the pore pressure evolution near the GAN drift wall due to seasonal temperature variations but also globally, meaning that the modeling of the EDZ around the GAN drift was well approximated. In general, pore pressure build-up due to heating was well represented in the direction parallel to the bedding (i.e., ALC1616\_02) as well as ALC4005\_04. On the contrary, the measured pore pressure for the sensors located in the direction perpendicular to the bedding (i.e., ALC1617\_01 and ALC1617\_02) shows a lower dissipation, which was not captured by any of the teams. This remains an open question

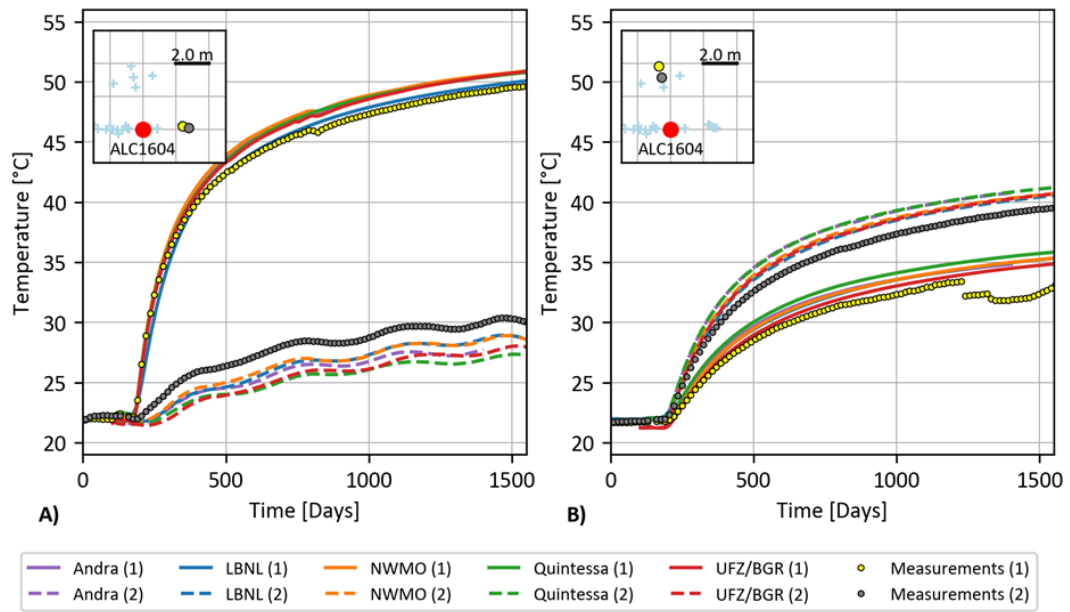


Figure 1.43: Comparison of numerical prediction and measurements of temperature for sensors (A) ALC1616\_02 (1) and ALC1616\_05 (2), parallel to bedding and (B) ALC1617\_01 (1) and ALC1617\_02 (2), perpendicular to bedding [Seyedi *et al.*, 2021].

and needs to be tackled again in future works as it could not be resolved currently even after intense discussion and various attempts as discussed in the following paragraph.

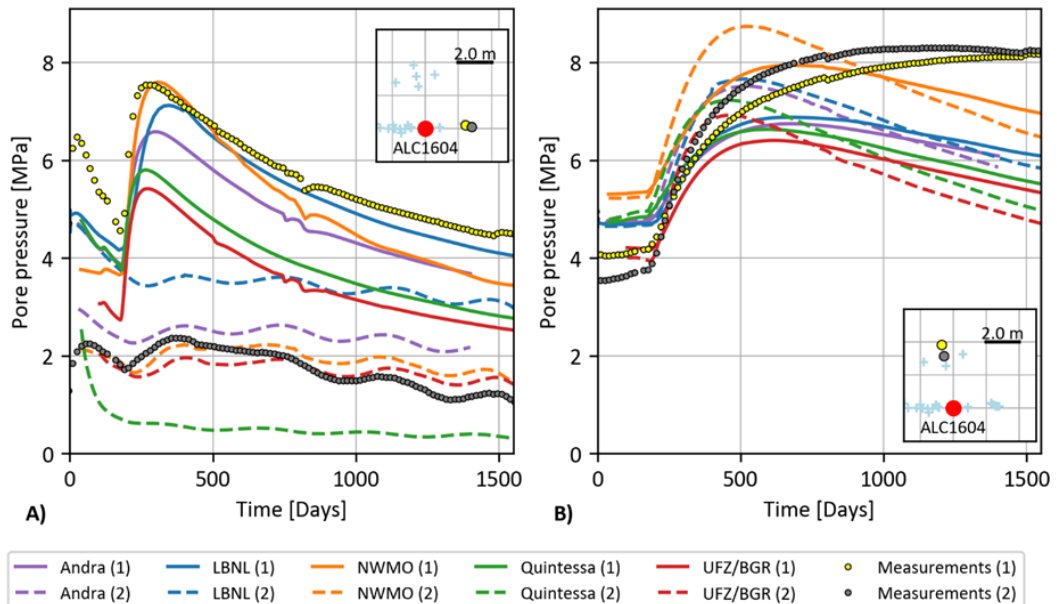


Figure 1.44: Comparison of numerical prediction and measurements of pore pressure for sensors: (A) ALC1616\_02 (1) and ALC1616\_05 (2), parallel to bedding and (B) ALC1617\_01 (1) and ALC1617\_02 (2), perpendicular to bedding [Seyedi *et al.*, 2021].

It is important to bear in mind that in the small-scale experiments the sensor locations were between 3 and 40 cell diameters away from the heating source. In particular, the sensors used for the calibration of the pore pressure were located at approximately 7 cell diameters away from the central borehole (TED1201), whereas, in the ALC experiment, the sensor locations used for the blind prediction were approximately 3 cell diameters away from ALC1604. This means that, unlike the TED experiment where the measurement points were located in the far field, the measurement points of the ALC experiment were in a transition zone between the near and far field in which modification of hydromechanical properties may possibly have some influence on the pore pressure. Therefore, it would have been interesting to study how the pore pressure would evolve at points located at the same proportional distance of the measuring points in the TED experiment to have a better understanding of the THM behavior of CO<sub>x</sub> at the far field.

### 1.6.3 Numerical modeling of THM response at repository scale

#### 1.6.3.1 General trends

As mentioned before, the current concept of HLW nuclear waste area consists in emplacement of waste packages in parallel cells drilled from access tunnels (Figures 1.8 and 1.9). A series of numerical simulations has been performed to highlight general trends of THM response of CO<sub>x</sub> to thermal loads at repository scale. Regarding the important number of parallel cells (tens of identical cells in each section) and their lengths (between 80 and 150 m), a plane strain model can be used to calculate the THM response of rock mass to temperature increase between two parallel HLW cells. The considered model consists in a vertical cut, perpendicular to cell axis at its middle length, from the surface down to 1000 m depth. The left side of the model passes through a cell center, while the right side goes over the mean distance between two cells (Figure 1.45). The considered thermal loading consists in a thermal flux in time applied on the cell wall. The model symmetry constrains the displacement, thermal flow and fluid flow to be nil on its left and right sides. These boundary conditions are also applied on the bottom of the model. Concerning the initial conditions, the temperature and pore pressure linearly change from the surface down to the lower side. HLW cells will be drilled parallel to the  $\sigma_H$  direction. The initial total stresses thus are quasi-isotropic in their section. The out of plane stress is considered to be equal 1.3 times the in plane stresses (i.e.,  $\sigma_x = \sigma_y = -12$  MPa,  $\sigma_z = -16$  MPa at 500 m depth).

A linear elastic behavior is considered to represent the mechanical behavior of all geological layers. A linear elastic model cannot represent the complex behavior of CO<sub>x</sub> claystone. However, it can be used to obtain a first estimate of its THM response to thermal loads in the far-field as shown through numerical simulation of some *in situ* experiments like TED especially in what concerns the pore pressure evolution. By far-field, we mean the area sufficiently far from the cell, which is not hydro-mechanically affected by the cell construction. It is worth reminding that the excavation diameter of the cell is smaller than one meter, while the distance between cells is about tens of meters. Investigation of the near-field THM response of CO<sub>x</sub> requires more complex constitutive models.

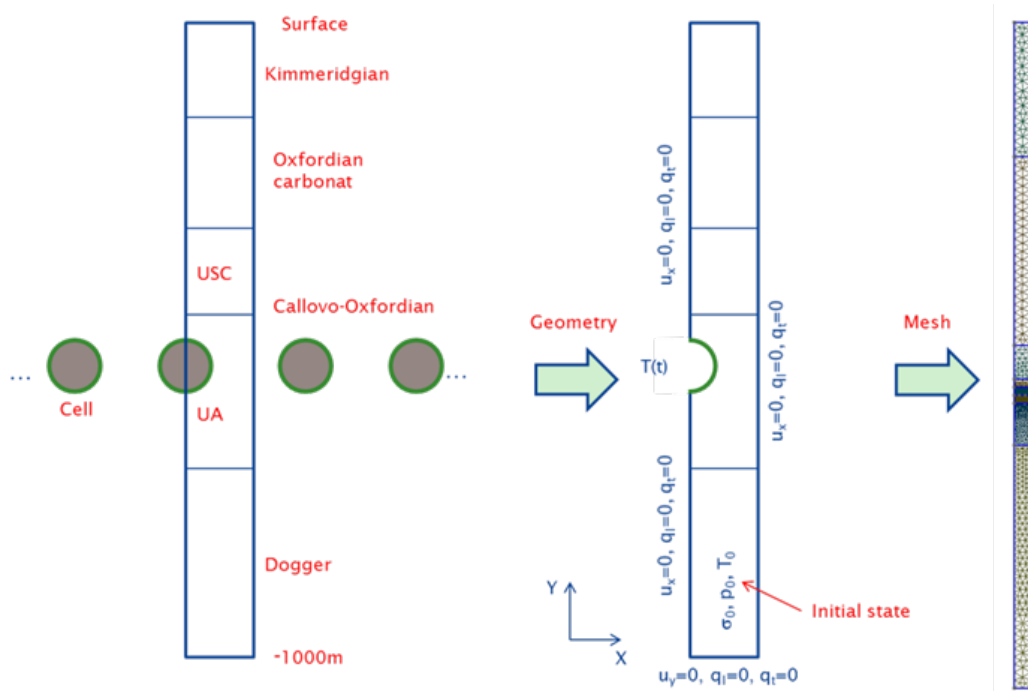


Figure 1.45: Schematic representation of HLW cells and deduced plan strain model and mesh.

Several research activities have been launched within the framework of the "GL Mouv", to take into account creep and plasticity effects (Andra/Ineris collaboration) and damage using the phase-field numerical framework (PhD thesis of Zhan YU - LaMcube laboratory). Finally, using linear elastic models makes it possible to perform statistical analysis using an important number of large-scale THM simulations.

Considering the periodic architecture of the HLW area, the zone located between two parallel cells is loaded by both cells. The THM lateral boundary conditions in this area and the interaction between cells provide high effective stresses in this zone. For a Representative Volume Element (RVE) of CO<sub>x</sub> located in this zone (Figure 1.46-top), the increase in temperature will result in (i) total stress changes mainly due to thermomechanical stresses, and (ii) an increase in pore pressure (Figure 1.46-bottom). This overpressure does not have an isotropic impact on the stress levels. In fact, the lateral symmetric conditions prevent horizontal expansion of the medium and horizontal dissipation of the pore pressure at midpoint of the centre-to-centre distance between cells. For this reason, the increase in temperature also results in a decrease in the total horizontal stresses (i.e., increasing compressive stress). In the vertical direction, the free surface condition at the top of the model enables "quasi-free" vertical expansion, resulting in only negligible changes in total stresses. This situation results in:

- a significant increase in the effective vertical stress (the tensile stress is considered to be positive) due to thermal pressurization that may cause effective tensile stresses;
- a decrease in total horizontal stresses due to thermo-mechanical compression stresses;
- an increase in the deviatoric stress (decrease in horizontal stresses and increase in vertical

stress).

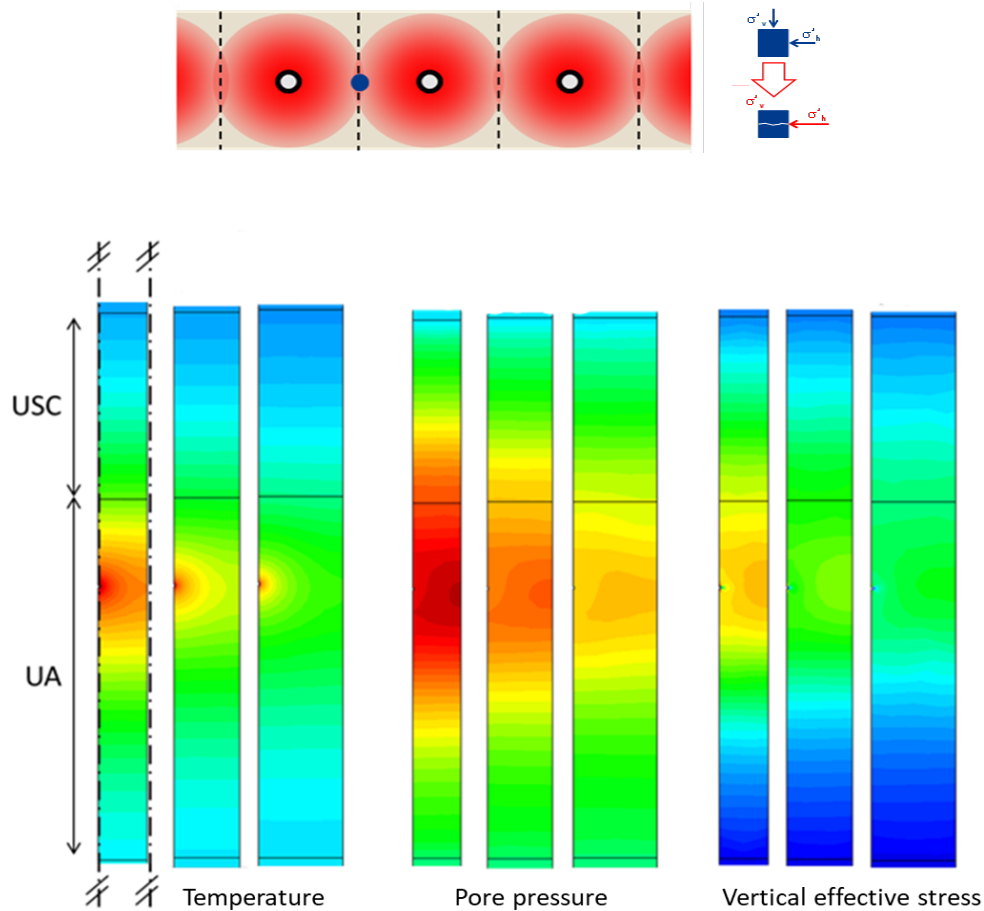


Figure 1.46: THM response of COx at the far field. (top) Schematic representation of the thermo-mechanical processes of an REV located at mid-distance between two cells. (bottom) Temperature, pressure and vertical effective stress field in COx between two parallel cells

This loading path may lead to fracture initiation/propagation. The fractures may be initiated in sub-horizontal direction in the case of appearance of vertical effective tensile stresses. In the case when the deviatoric stress is sufficiently high, shear fractures may appear in oblique direction.

To illustrate the THM pressurization at the repository scale, two different thermal loads are considered (Figure 1.47). The first one exhibits a fast increase of temperature during the first five years and then a rapid decrease of temperature. The second one presents also a fast temperature increase for the first twenty years but continued afterwards by a progressive decrease until 10,000 years. The results of numerical simulations have been studied at a small zone located at the middle distance between two parallel cells and at the level of the cell center. The THM modeling allows for the determination of the temperature and pore pressure evolutions with the host formation. A

thermomechanical pressurization coefficient  $\Lambda^*$  can be expressed as

$$\Lambda^* = \frac{\Delta p}{\Delta T} \quad (1.10)$$

The calculated evolution of this coefficient versus temperature is reported in Figure 1.47. Two different regimes are distinguished during the heating period. First, a linear relationship between pore pressure and temperature increase is observed when the temperature reaches about 32°C, i.e. a constant value of  $\Lambda^*$  as seen in Figure 1.47. This trend reveals that COx behaves as an undrained porous medium during this first period. However, the calculated pressurization coefficient is greater than the thermal pressurization measured during undrained heating tests on samples (Table 1.1). This difference is essentially attributed to thermomechanical effects. The increase of the absolute value of total mean stress at this area under undrained conditions induces additional pore pressure increase (Eq. 1.6). Second, a nonlinear relationship between these variables, translated by a progressive decrease of  $\Lambda^*$ , is obtained. This effect can be explained by the fact that when the pressure gradient between the considered zone and surrounding medium is sufficiently large, the dissipation of pore pressure begins. The hydraulic behavior is no longer undrained and pressurization coefficient decreases. Over the cooling time, the decrease of pore pressure versus temperature is observed.

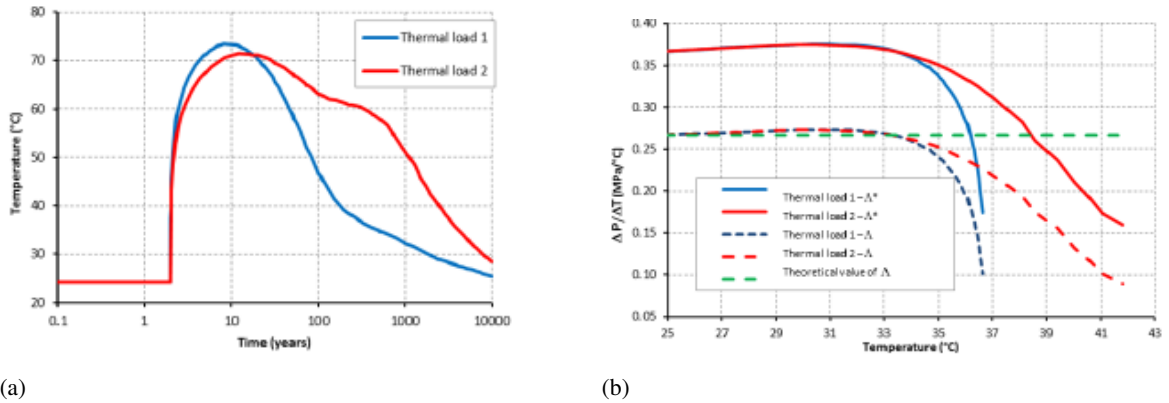


Figure 1.47: Thermal loads imposed on the cell wall (a), and evolution of thermos-mechanical pressurization coefficient  $\Lambda^*$  versus temperature during the heating period. Dashed green line corresponds to the value of thermal pressurization coefficient (b).

The thermomechanical pressurization coefficient  $\Lambda^*$  obtained in the first part of the heating period may be interpreted in the framework of poroelasticity. During the first heating period, the mean total stress variation is almost linear with the temperature at the considered zone stemming from the THM modeling. The pressure and mean total stress fields obtained by numerical simulation help us to determine the thermal pressurization coefficient

$$\Lambda = \frac{\Delta p - B \Delta \sigma_m}{\Delta T} \quad (1.11)$$

The coefficient of thermal pressurization calculated from Equation (1.11) based on numerical

simulations and theoretical derivations for undrained and constant total stress conditions as expressed in Equation (1.6) are presented in Figure 1.47. It is interesting to note that the thermal pressurization coefficient determined by THM modeling (Equation (1.11)) is very close to the theoretical value (Equation (1.6)). This result confirms that the low permeability COx behaves as an undrained porous medium at the beginning of heating period. Moreover, this analysis shows a way to evaluate the thermal pressurization coefficient  $\Lambda$  from the thermomechanical pressurization coefficient  $\Lambda^*$  measured by *in situ* heating tests. After the first heating period, this observation is no longer valid as the coefficient obtained by numerical simulation through Equation 1.11 decreases and becomes smaller than the undrained one. The competition between tow phenomena affects the pressure variation. Compressive total stresses induced due to the boundary conditions and the fluid flow when the pressure gradient becomes important affect the pressure field in two opposite ways. It can be stated that during the first phase, the behavior is total stress dominated and during the second one fluid flow dominated.

#### 1.6.4 Influence of different THM parameters

The HLW zone covers an area of around 8 km<sup>2</sup>. The 3D geological model of Callovo-Oxfordian has been developed progressively since the start of the 2000s as field investigations have progressed, based on analyses performed in deep boreholes and at the underground laboratory. The high-resolution 3D seismic survey of ZIRA (*an area of about 20 km<sup>2</sup>, which is the potential area to implement the underground facility of the industrial geological disposal called Cigeo*), performed in 2009-2010, provided a more detailed description, in particular concerning the vertical and horizontal mineralogical variability. Laterally, COx layer presents the same general organization over a zone of more than 350 km<sup>2</sup>, according to the results from boreholes drilled in a 15 km radius around Andra URL. All these investigations and results made it possible to build a 3D image of the variability of different THM parameters over the area of interest.

Different parameters may affect the THM response of rock to thermal loads. First, a “one factor at a time” sensitivity analysis (e.g., Rohmer and Seyedi [2010]) is conducted to evaluate the weight of each parameter on the THM response of COx claystone when a thermo-poroelastic behaviour is considered. It consists in varying each input parameter separately while, other parameters are fixed and to measure its effect on the output. The threshold values were defined based on observed variability in experimental results as a possible range of variation. The tested parameters were COx Young’s modulus [3 to 9 GPa], permeability [ $10^{-21}$  to  $2.0 \cdot 10^{-20} \text{m}^2$ ], thermal conductivity [0.95 to 1.25 W/m/K], Poisson’s ratio [0.2 to 0.4], Biot coefficient [0.6 to 1.0], thermal expansion coefficient of solid skeleton [ $10^{-5}$  to  $2.5 \cdot 10^{-5} \text{mathrm}K^{-1}$ ], and heat capacity [910 to 978  $\text{mathrm}J.kg^{-1}.K^{-1}$ ]. The obtained values of the vertical Terzaghi effective stress at the mid-distance between two parallel cells are reported in Figure 1.48. The performed analysis shows that the Young’s modulus and water permeability are the two parameters that affect most the THM response of the studied rock. Thermal conductivity, Poisson’s ratio and Biot coefficient constitute the second set of influencing parameters. It is worth noting that the weight of each parameter depends, among other factors, on the range of its

variability and the considered boundary conditions. Moreover, the present approach cannot account for the interactions between different parameters.

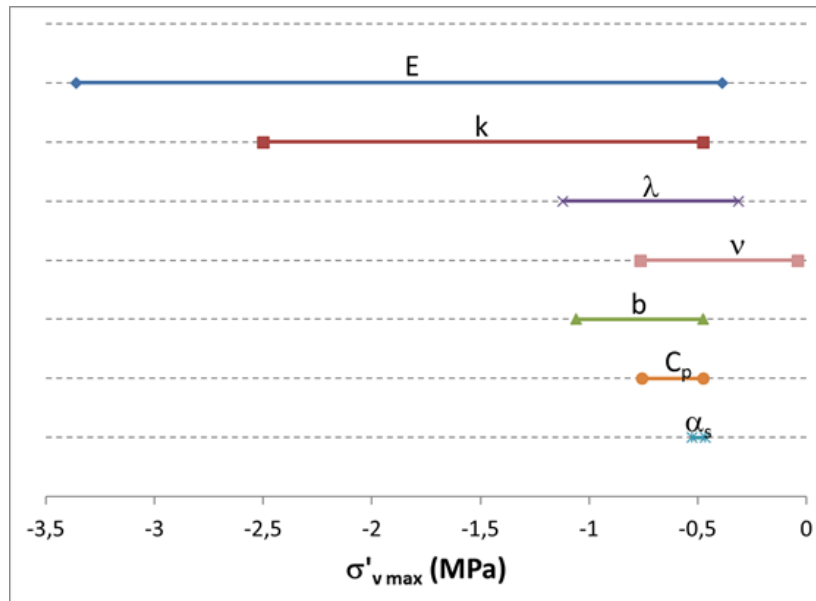


Figure 1.48: Effect of different parameters on the vertical effective stress at mid-distance between two parallel cells; E stands for Young's modulus,  $k$  permeability,  $\lambda$  thermal conductivity,  $\nu$  for Poisson's ratio,  $b$  Biot coefficient,  $\alpha_s$  thermal expansion coefficient of rock skeleton and  $C_p$  its heat capacity (the negative values correspond to compressive effective stresses) [Seyedi *et al.*, 2018].

The effects of the spatial variability of rock properties on the THM responses of the HLW repository can be estimated by using a stochastic approach. While the deterministic approach is useful and sufficient for many purposes, a stochastic approach is a useful tool in numerical analyses to assess the variability of rock properties. It accounts for fluctuations such as the spatial variability of rock properties and attempts to quantify them by calculating statistical quantities such as their mean and standard deviation.

In the following, a stochastic approach is used to investigate how the inherent spatial variability of COx properties may affect its THM response at HLW repository scale using a thermo-poro-elastic model. The most influential THM parameters of the model were used to generate the random fields. The selection of the most influential parameters was based on two parametric sensitivity analyses by calculating the Sobol indices, which determine the contribution of each input parameter to the overall model output variance [Sobol, 1993].

### 1.6.5 Sobol Indices

Traditional sensitivity analysis methods evaluate the response of a model to changes in individual parameters at a time. By contrast, the Global Sensitivity Analysis (GSA) summarizes the parameters importance over a range of values by identifying interactions between them, which could be significant in multiphysics models such as coupled THM ones. During the post-doc of C. Plúa and in the

framework of "DECOVALEX" international project, we aimed at providing new insights into the effect of spatial variability of CO<sub>x</sub> parameters on its THM response to thermal loading.

Sobol indices [Sobol, 1993] are a widely accepted measure in engineering fields. They are based on variance decomposition. First-order indices estimate the contribution of each input parameter to the overall model output variance on its own. Higher-order Sobol indices estimate the contribution due to the interactions of groups of input parameters at a time, thereby exposing interaction in a multiphysics model. Total indices account for the total contribution of each input parameter on its own plus all higher-order effects due to interactions. In this study, first-order and total indices were computed. If the total indices are substantially larger than the first-order ones, then higher-order interaction occur.

The Sensitivity Analysis Library (SALib, [Herman and Usher, 2017]) was used to sample and compute the Sobol indices. SALib is an open-source Python library for sensitivity analyses. It provides sampling and analysis modules, including the calculation of Sobol indices. In the following, the main steps are outlined: i) define the model parameters for the calculation of Sobol indices, ii) define bounds of the sampled parameter space, iii) generate a given number parameter sets using the Sobol sequence, called base sample iv) apply Saltelli method of cross-sampling [Saltelli *et al.*, 2008] to the base sample to obtain the total number of parameter sets, iv) run the total number of parameter sets through the THM model, and the output of all simulations is post-processed by SALib to calculate Sobol indices.

The parameters were sampled uniformly, except in cases in which the parameters vary some orders of magnitude. In these cases, an additional procedure to avoid bias from smaller or larger values is required. In CO<sub>x</sub>, the spatial variability of intrinsic permeability results in values ranging from  $5.0 \cdot 10^{-21} \text{ m}^2$  to  $5.0 \cdot 10^{-20} \text{ m}^2$ . On the contrary, material parameters such as Young's modulus, thermal conductivity and porosity show a lower degree of variation. Therefore, the permeability was sampled as follows: the exponents of the permeability values were uniformly sampled (e.g. lower and upper bounds [ $\log_{10}(5.0 \cdot 10^{-21})$ ,  $\log_{10}(5.0 \cdot 10^{-20})$ ]) and then the sample of the exponents were transformed back to real space. The sampling quality was evaluated by confidence intervals (i.e., interval estimate for Sobol indices) of the most sensitive parameters; if their confidence intervals are larger than 10 % of the value itself, the sample size needs to be increased.

### 1.6.6 Random Finite Element Method (RFEM)

Griffiths and Fenton [1993] introduced the so-called Random Finite Element Method (RFEM) that combines the random field theory with the finite element method and Monte Carlo Simulations in which the numerical analysis is repeated until the probabilities related to output quantities of interest become stable. The RFEM software was used for the generation of random fields.

The generation of random fields requires the definition of a probability distribution, usually given by the mean and the standard deviation, and a spatial correlation length,  $\theta$ . The RFEM software allows for different types of probability distributions: normal, log-normal, and bounded. The parameters follow a uniform distribution when the mean and the standard deviation are not provided. The Local

Average Subdivision Method proposed by [Fenton and Vanmarcke \[1990\]](#) was used for generating the random fields along with a Markovian correlation function in which the spatial correlation is assumed to decay exponentially with distance.

The rock properties that were assumed to have spatial variability were described as random variables. The spatial correlation lengths of each random variable were assumed to be equal in the different analyses. The spatial correlation length has units of length and it is possible to define different spatial variability in the vertical and horizontal directions, a common geological feature in sedimentary rocks such as claystone. It also requires the definition of a random field (RF) mesh, which is different from the finite element (FE) mesh. The size of the elements of the RF and FE meshes needs to be chosen following different criteria; the size of the elements of the FE mesh must be small enough to reproduce high gradients occurring in THM simulations to avoid numerical errors, while the size of the elements of the RF mesh must be selected to adequately capture the essential features of spatially variable properties. It thus depends on the spatial correlation length. In practice, the element size of the RF mesh should range between  $\theta/10$  and  $\theta/5$  for exponential correlation functions.

### 1.6.7 Benchmark exercise of an HLW repository

A hypothetical HLW repository was proposed as benchmark exercise based on the French concept for HLW disposal cells under the assumption of plane strain conditions. This assumption is more conservative than a 3D full model since the heat and pore-fluid dissipations in the axial direction of the micro-tunnels are ignored (see section 1.6.3.1). The simplified domain consists in a vertical cross-section of a quarter of the repository at mid-plane of HLW disposal cells. There are 28 parallel HLW disposal cells with a diameter of 0.8 m. The domain includes an access gallery in the symmetry axis that connects the gallery from which the HLW disposal cells are excavated with other access galleries. The access gallery has a diameter of 10.2 m. The HLW repository is located within the CO<sub>x</sub> formation at a depth of 560 m. The mid-distance between two parallel and consecutive cells is  $P_x = 52.3$  m. Note that these parameters do not reflect the final dimensions planned for the Cigéo project.

Based on Andra's database, a series of probability distributions are provided to represent the spatial variability of rock properties within Zira. Statistical distributions and cut-off limits are proposed based on the in situ and laboratory characterization data and 3D seismic survey. The initial and boundary conditions as well as the value of different THM parameters and their variability can be found in [[Plúa et al., In press](#)].

Given that the repository design consists of parallel, horizontal HLW disposal cells, the highest Terzaghi effective stresses in the far-field are expected at the mid-distance of two HLW disposal cells. The pore pressure around HLW disposal cells is lower due to its excavation, which is simulated by assuming atmospheric pressure on the cell walls during two years prior to the emplacement of HLW packages; this results in lower Terzaghi effective stress. Three types of analyses were performed: i) deterministic analysis assuming homogeneous parameters for each geological layer, ii) parametric sensitivity analyses by computing the Sobol indices (homogeneous parameters for each

geological layer), and iii) spatial variability analyses using random fields to represent the most sensitive parameters.

First, the case study was performed deterministically for three different sets of parameters of UA23 layer, where the cells will be built: i) mean values of parameters (reference case), ii) mean values except for permeability that was replaced with its minimum value, and iii) mean values except for permeability and Young’s modulus that were replaced with their minimum and maximum values respectively. The two most unfavorable values of permeability and Young’s modulus were analyzed since they are expected to be the most influential parameters on the THM response of the HLW repository [Seyedi *et al.*, 2018]. The deterministic calculations were performed using COMSOL and the model was a 2D simplification of the geometry shown in Figure 1.49; the 28 HLW cells were considered in the geometry.

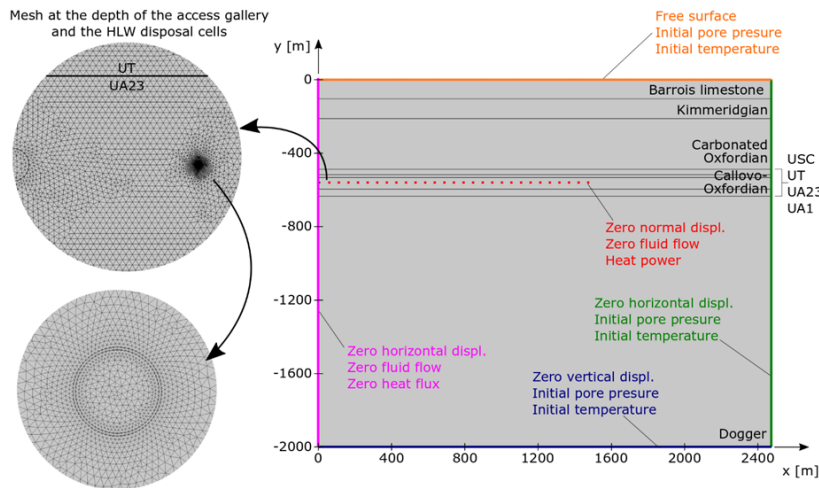


Figure 1.49: Simplified geometry and COMSOL mesh showing the access gallery and HLW cells: C1 and C2, [Plúa *et al.*, In press]

The Sobol indices were Saltelli 2008 computed to estimate the contribution of each THM parameter to the maximum values of temperature, pore pressure, and Terzaghi effective stress at Point P1. The first-order and total Sobol indices were calculated for two different analyses to study the contribution of i) the nine THM parameters of UA23, which are vertical component of young’s modulus ( $E_v$ ), Poisson ratio ( $\nu_{vh}$ ), Biot coefficient ( $b$ ), porosity ( $\phi$ ), vertical permeability ( $K_v$ ), density ( $\rho_{eq}$ ), vertical thermal conductivity ( $\lambda_v$ ), thermal expansion coefficient of solid phase ( $\alpha_s$ ), specific heat capacity ( $C_{p,eq}$ ) and ii) the permeability and Young’s modulus of all unit layers (i.e., USC, UT, UA23, and UA1).

The total cost for the Sobol indices is 11,000 and 10,000 model evaluations for the first and second analyses, respectively. These simulations were performed with *code – aster*. Since it involved a very large number of repeated calculations and, considering the large number of parallel cells, the analyses assumed lateral symmetry conditions on both sides of the repository. The geometry thus considered one half of a HLW cell and the width of the domain is  $Px/2$  (Figure 1.50).

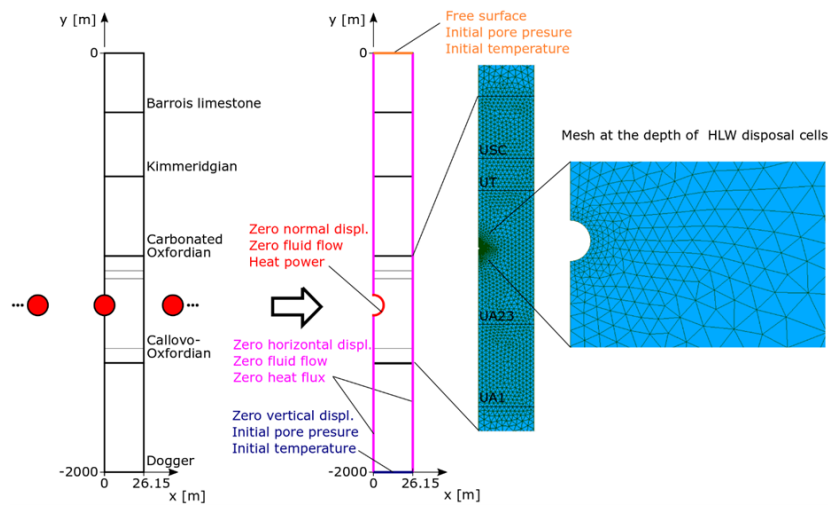


Figure 1.50: Simplified geometry with one HLW cell and *code – aster* mesh [Plúa *et al.*, In press]

Stochastic modelings have been then performed to investigate the influence of spatial variability in CO<sub>x</sub> on its THM responses with respect to the deterministic approach. The analyses were performed with four THM parameters of UA23 treated as random variables. It was decided to evaluate the influence of the spatial variability of the most influential parameters for each THM variable field: Young's modulus for the mechanical part, permeability for the hydraulic part, and thermal conductivity for the thermal part. Moreover, the Biot coefficient was also treated as a random variable and was negatively correlated to the Young's modulus. The selection of these parameters was based on results of the parametric sensitivity analyses, which are performed prior to the spatial variability analyses. The other three random variables are assumed to be uncorrelated. The other THM parameters are assumed to be homogeneous in all geological layers. In all cases, the anisotropy is kept constant.

The availability of field data related to the spatial correlation length is limited so it was decided to study three different spatial correlation lengths with the same ratio between the horizontal and vertical directions: 5 m x 3 m, 10 m x 6 m, and 20 m x 12 m. For each analysis, 2,000 sets of four random fields were generated with the RFEM software and then imported in COMSOL Multiphysics for the simulations. In order to reduce the computational time, only the eight central HLW cells were considered assuming lateral symmetry boundary conditions. The FE mesh has similar characteristics as the mesh of Figure 1.49 and the element size of the RF mesh is 1.0 m x 0.6 m for the three spatial correlation lengths. A set of random fields is shown in Figure 1.51 with a correlation length of 10 m x 6 m. The areas with the highest values of Young's modulus (in red) have the lowest values of Biot coefficient (in blue). For illustration purposes, the random field of the intrinsic permeability is shown in logarithm with base ten since the different values vary one order of magnitude.

Figure 1.52 shows the numerical results for three different parameter sets of UA23: i) mean values, ii) mean values except for permeability that is replaced with its minimum value, and iii) mean values except for permeability and Young's modulus that are replaced with their minimum and maximum values, respectively. The point location is at mid-distance of two HLW cells C14 and C15, i.e.,

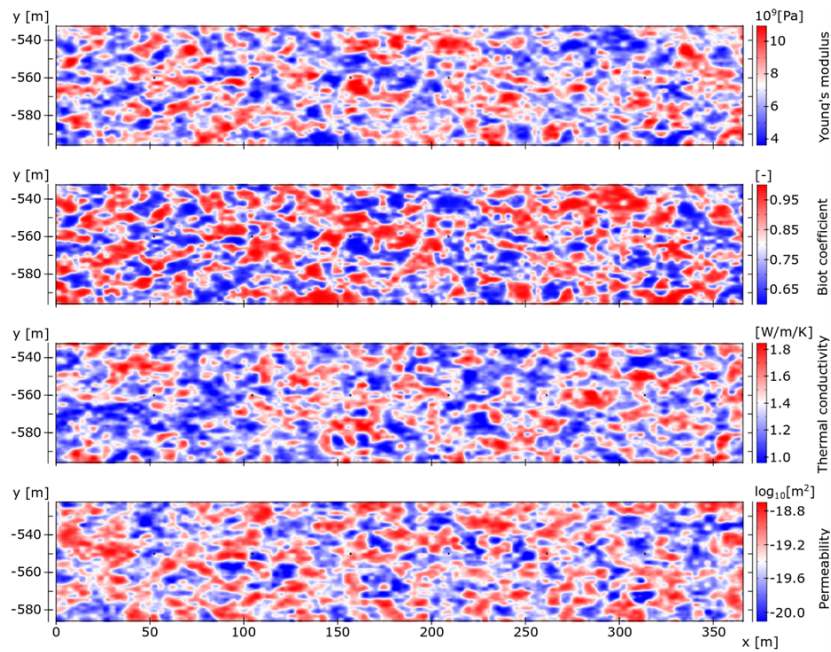


Figure 1.51: Set of random fields (Young's modulus, Biot coefficient, Thermal conductivity and Permeability) with a correlation length of 10 m x 6 m [Plúa *et al.*, In press]

Point P1. The combination of reduced permeability and the Young's modulus increases significantly the pore pressure and the Terzaghi effective stress about 4 MPa in both cases. The reduction in permeability affects the dissipation process of pore pressure whereas the Young's modulus induces a marked peak with respect to the reference case. In addition, the time occurrence of the maximum values happens earlier than in the reference case.

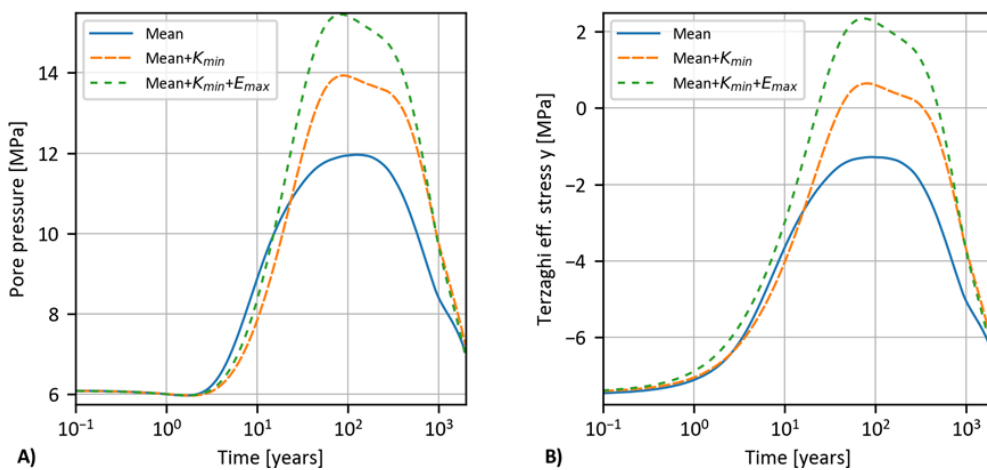


Figure 1.52: Deterministic analysis for three different parameter sets at Point P1. (A) pore pressure evolution and (B) vertical Terzaghi effective stress evolution. [Plúa *et al.*, In press]

### 1.6.7.1 Results and discussion

This analysis took into account the contribution of THM parameters in UA23 to the maximum values of the temperature, pore pressure, and Terzaghi effective stress at Point P1. In addition to the computed Sobol indices, the numerical results show the evolution of temperature, pore pressure, and Terzaghi effective stress represented by the mean of the total number of simulations, standard deviation, 68.26 % and 95.44 % prediction intervals. The latter two correspond to the standard deviation and twice the standard deviation at each side of the mean. The standard deviation is preferred over the variance to illustrate the amount of scatter in a variable since their units coincide and are easier to interpret.

The results of the parameter contribution to the maximum value of temperature at Point P1 are shown in Figure 1.53. Figure 1.53(A) shows that the highest variance in the results is given by the maximum standard deviation occurring 73 years after the waste emplacement whereas the variance of the temperature peak is lower and occurs 400 years later. The mean of the temperature evolution coincides with the numerical results obtained with the deterministic analysis using the mean of the THM parameters. The thermal conductivity is the most influential parameter with a first-order Sobol index of about 0.8 and a confidence interval of 8.0 % as shown in Figure 1.53(B). Similar values of the first-order and total Sobol indices indicate that there is no interaction between parameters.

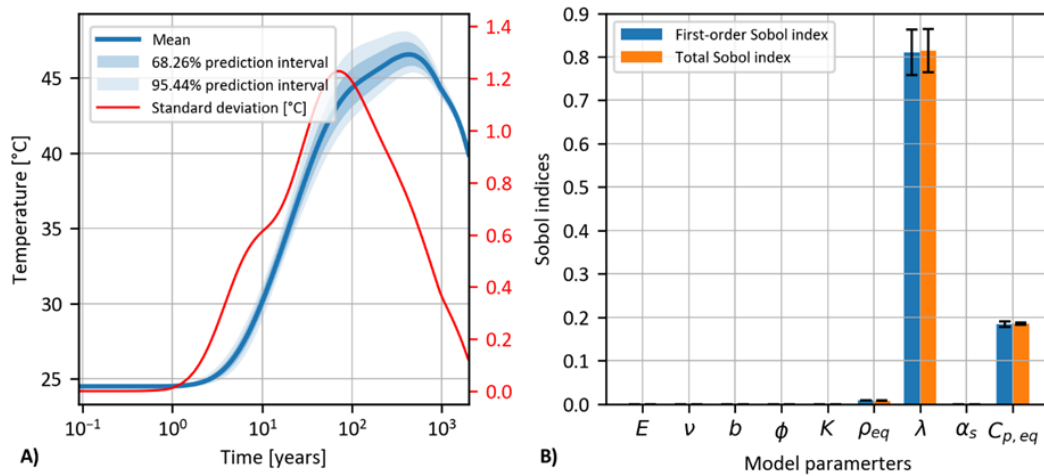


Figure 1.53: Parametric sensitivity analysis of layers UA23 at Point P1. (A) Temperature evolution. (B) Sobol indices contributing to the maximum temperature. [Plúa *et al.*, In press]

Figures 1.54 and 1.55 show the results of the parameter contribution to the maximum value of pore pressure and Terzaghi effective stress at Point P1, respectively. As observed in the deterministic analysis, Figure 1.54(A) and 1.55(A) show that a combination of the most unfavorable parameters has an influence on the time occurrence of the peaks of pore pressure and Terzaghi effective stress and they tend to occur earlier. Both means are slightly higher than the results obtained for the deterministic analysis with the mean of THM parameters. The main reason is the use of uniform distributions in which the mean and the median of some parameters do not coincide as it is the case of permeability and Young's modulus.

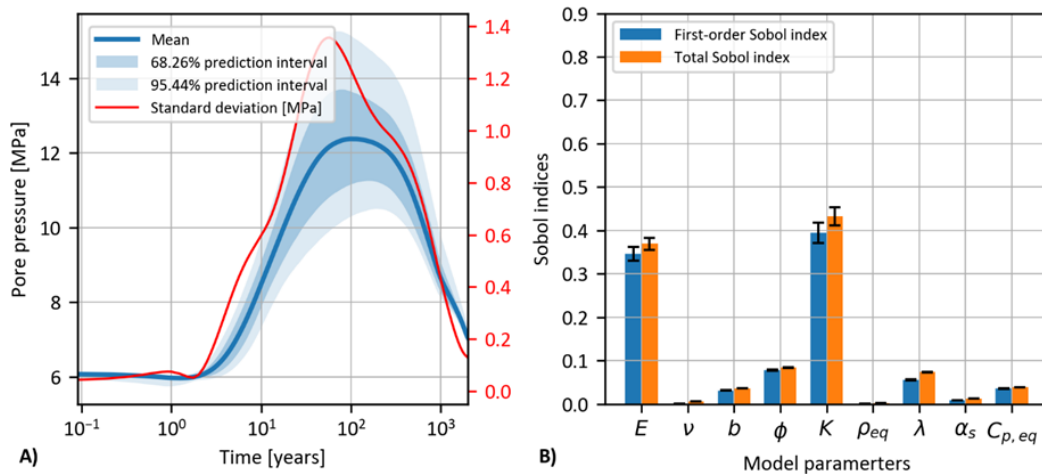


Figure 1.54: Parametric sensitivity analysis of layers UA23 at Point P1. (A) Pore pressure evolution and (B) Sobol indices contributing to the maximum pore pressure [Plúa *et al.*, In press].

Unlike temperature results, the highest variance coincides in time occurrence with the maximum values and are reached 55 years after the waste emplacement. The standard deviation is greater than 1.0 MPa in a range of 200 years; this high variance in the results is mainly due to the intrinsic permeability and Young’s modulus as shown in Figures 1.54(B) and 1.55(B). The intrinsic permeability and Young’s modulus are the most influential parameters in pore pressure and Terzaghi effective stress at Point P1, respectively. In both cases, the sum of first-order Sobol indices of permeability and Young’s modulus of UA23 are greater than 0.7. The difference between the first-order and total Sobol indices of these two parameters shows the existence of second-order interactions between them and possibly with other THM parameters, although the other parameters appear to have no higher-order effects. The confidence intervals of the first-order indices remain below 10 % in both cases, i.e., 6.0 % and 4.4 % for the permeability and the Young’s modulus, respectively, for the case of the pore pressure, and 4.6 % and 5.6 % for the case of Terzaghi effective stress.

A complementary analysis has been performed to investigate the influence of the surrounding layer parameters on the CO<sub>x</sub> response. This analysis only took into account the contribution of permeability and Young’s modulus of all unit layers to the maximum values of pore pressure and Terzaghi effective stress at Point P1. All other THM parameters have been set to their mean values. These results show that the parameter contribution of the surrounding unit layers is negligible and the permeability and Young’s modulus of UA23 are the most influential parameters [Plúa *et al.*, In press]

For the spatial variability analysis, the results of the Terzaghi effective stress are only presented. As an example, the evolution of effective stress is given in Figure 1.56(A) for the spatial correlations length 10 m x 6 m. As for the parametric sensitivity analyses, the evolution of the Terzaghi effective stress is represented by the mean of the total number of simulations, standard deviation, 68.26 % and 95.44 % prediction intervals. Figure 1.56(B) shows the theoretical probability and cumulative distribution curves obtained by the frequency histograms.

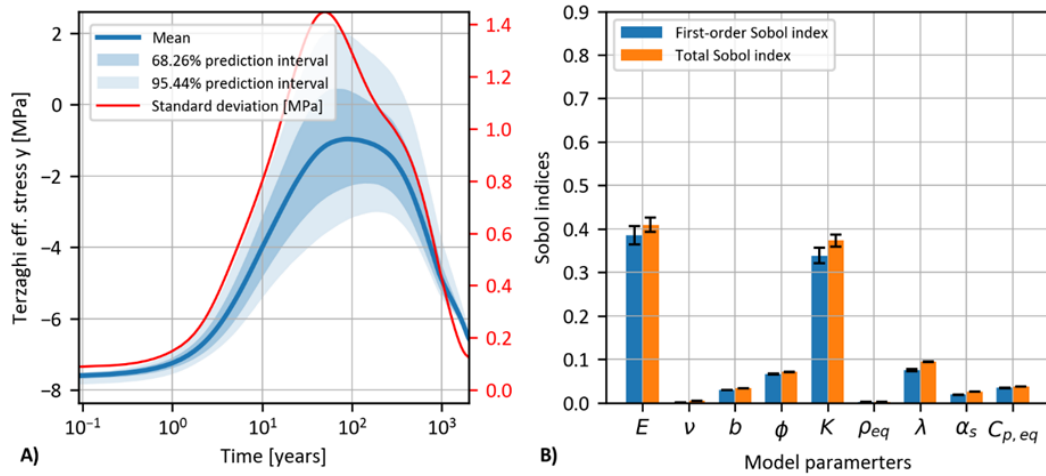


Figure 1.55: Parametric sensitivity analysis of layers UA23 at Point P1. (A) Vertical Terzaghi effective stress evolution and (B) Sobol indices contributing to the maximum vertical Terzaghi effective stress [Plúa *et al.*, In press].

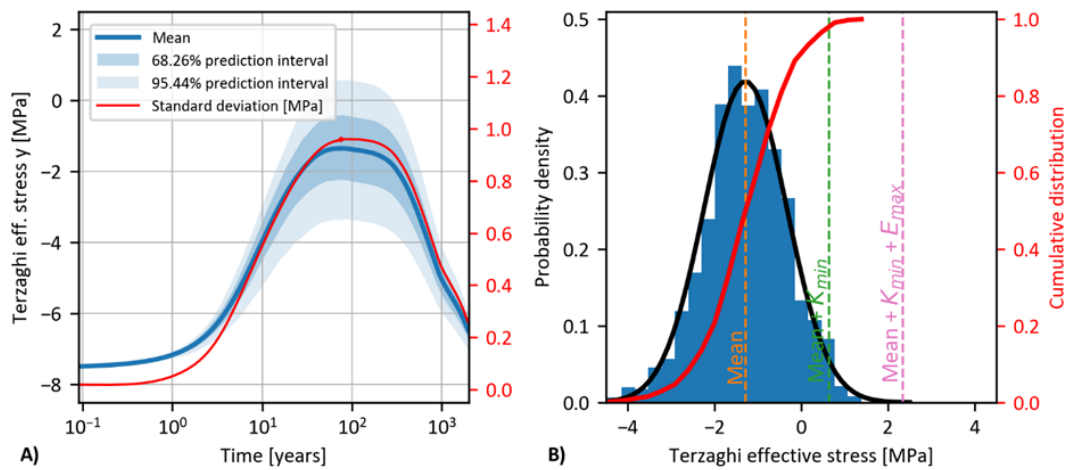


Figure 1.56: Spatial variability analysis for length scale 10 m x 6 m at Point P1. (A) Vertical Terzaghi effective stress evolution and (B) probability distribution of its maximum value. Vertical dashed lines indicate the maximum values obtained for the three cases studied in the deterministic analysis. [Plúa *et al.*, In press].

The numerical results for the three spatial correlation lengths yielded similar results. Both mean and standard deviation of Terzaghi effective stress do not show to be impacted by the studied spatial correlation lengths and they tend to the results of the deterministic analysis using the mean THM parameters. Due to the use of log-normal distributions, the standard deviation is reduced with respect to the values observed in the parametric sensitivity analyses that used uniform distributions for the studied THM parameters. Moreover, having a prediction interval that reaches tensile stresses at mid-distance of two HLW cells is not only a consequence of spatial variability of rock properties within Zira but also of the given  $P_x$  in this theoretical case study, which should be increased in real design.

It is also important to bear in mind that the numerical results in plane strain conditions overestimate the THM responses of an HLW repository.

Finally, the numerical result of a deterministic analysis with the mean THM parameters except for the permeability and the Young's modulus that are replaced with their most unfavorable values is only representative of at most 0.1% of the total cases in the stochastic analyses (3% if only the permeability is replaced).

### 1.6.8 Outlook

Even if the linear poroelastic behavior seems to reproduce in a satisfactory manner the CO<sub>x</sub> response to thermal loads at the far-field, the effect of different non-linearities must be investigated. Among other sources of non-linearity time-dependent behavior, plasticity and damage must be at least considered. Different challenges may arise. The first one concerns the realization of an important number of numerical simulations with non-linear mechanical constitutive laws.

A strategy to accelerate the non-linear computations may be considered based on the creation of a reduced order model. This can be done by means of an empirical reduced base (Incremental Proper Orthogonal Decomposition, POD), which replaces the complete FE model and then by reducing the computation domain (Discrete Empirical Interpolation method, DEIM). The reduced basis and domain can be computed after a full computation on the time history or can be adaptive, updating them following an error indicator. The same reduced base and domain can then be maintained for the next sets of parameters (e.g., permeability). These techniques may allow for a much faster exploration of the parametric space during the construction of statistical models.

To deal with the spatial variability a non-intrusive surrogate approach whose principle is to sample the input parametric domain (using sparse grids or Monte-Carlo sampling) and to compute the ensuing quantity of interest (such as maximum pressure value and location), may be used. A surrogate model (polynomial chaos or Gaussian process) could then be built by exploiting the input-output relationships. Once validated, the surrogate model can be used in lieu of THM simulators in order to derive the statistical information: moments, marginal and joint densities, sensitivity analysis, exceedance probabilities.

Another complexity is related to accurate estimations of parameters of such models and especially their variability over the studied area. The use of micro-macro non-linear models may provide some ways to overcome this difficulty. The parameters of the non-linear model would be obtained based on the mineralogy of the rock and their spatial variability.

## Chapter 2

# Damage and fracturing of quasi-brittle heterogeneous materials

This chapter presents parts of the research conducted while I was working at BRGM (2004-2012). The non-local damage model was developed during PhD of N. Guy (co-supervised with Dr F. Hild). The model was extended to account for hydro-mechanical coupling within a research collaboration with EDF R&D. The content of the chapter is a collection of excerpts from the following papers:

- Guy N., Seyedi D.M., Hild F. (2012) A probabilistic nonlocal model for crack initiation and propagation in heterogeneous brittle materials, *International Journal of Numerical Methods in Engineering*, **90**, pp. 1053-1072.
- Guy N., Seyedi D.M., Hild F. (2018) Characterizing fracturing of clay-rich Lower Watrous rock: From laboratory experiments to nonlocal damage-based simulations, *Rock Mechanics and Rock Engineering*, **51**, pp. 1777-87.
- Seyedi D.M., Guy N., Sy S., Granet S., Hild F. (2012) A non-local damage model for heterogeneous rocks – application to rock fracturing evaluation under gas injection conditions, in *Geomechanics in CO<sub>2</sub> Storage Facilities*, Pijaudier-Cabot G., Pereira J.M., Eds., pp. 59-73, John Wiley & Sons, Inc., Hoboken, NJ USA.

## 2.1 Introduction

Fracturing of rocks, when they are loaded under low confinement, is brittle in the sense that it occurs without any significant plastic strain. However, the material does not lose its entire load-carrying capacity at the onset of damage. A gradual degradation of the material integrity is observed, which is the result of debonding and cleavage fracture at the microscale rather than plastic slip. This behavior is commonly referred to as quasi-brittle fracture [Peerlings *et al.*, 1998]. Concrete, ceramics and some polymer matrix composites exhibit similar behavior.

The mechanical behavior of quasi-brittle materials is of great interest in a wide range of engineering applications. Among them, an increasing attention is paid to damage and fracturing of clay-rich rocks with their implication within environmental and energy applications. Beyond their applications as potential host formations for radioactive waste repository, which were discussed in Chapter 1, clay-rich rocks are of interest as potential caprock for geological storage of energy vectors (hydrogen, compressed air, mixture of  $H_2 - CH_4$ ) and  $CO_2$  and the extraction of shale oil and gas.

Quasi-brittle materials present important heterogeneity on their mechanical parameters because of their natural components. Their failure has usually a random character. The failure stress is scattered and the average level decreases with the volume of the sample. The effect of this scatter on the damage probability must be taken into account.

As discussed in section 1.5, the correct description of strain localization is another crucial condition for simulating a damaged region with continuum models. In numerical simulations with standard softening models the strain localizes in a band with the thickness of an element [Pietruszczak and Mróz, 1981]. Every mesh refinement will modify the global response of the structure. The obtained results exhibit thus a pathological dependence on the fineness of the mesh, the orientation of elements and in a more general form on the spatial discretization. As an extreme case, it can be shown that for a very fine discretization the predicted fracture energy approaches zero [Pietruszczak and Mróz, 1981, Bažant and Belytschko, 1985], which is unrealistic from a physical point of view. The corresponding mathematical problem has been identified as loss of ellipticity of the equilibrium equations [Triantafyllidis and Aifantis, 1986, Lasry and Belytschko, 1988, Borst *et al.*, 1998].

As early as 1976, Hillerborg proposed the Fictitious Crack Model [Hillerborg *et al.*, 1976], which provides a mesh-independent energy release upon crack propagation. This concept was adapted by Bažant and Oh [1983] to the so-called smeared crack formulation. In the crack band model, the fracture energy introduced by Hillerborg was smeared out over the area where the crack localizes.

Different regularization schemes were used to address the ill-posedness of the mathematical description at a certain level of accumulated damage. Non-local damage models [Pijaudier-Cabot and Bažant, 1987, Bažant and Pijaudier-Cabot, 1988] provide a suitable framework to have mesh objective results when one deals with the post-localized behavior. The main idea of non-local models is to consider that the behavior of each material point depends on the state of surrounding points. Let us assume that damage is governed by the strains. In a conventional local model, damage is usually related to a scalar measure of the local strain. In a non-local model, damage can be related to a

weighted volume average of this local strain through a regularization operator. The choice of such regularization operator does not rely on physical observations. The implicit gradient enhanced scheme proposed by [Peerlings \*et al.\* \[1998\]](#) provides a regularization of the strain by least squares method and reads for a domain  $\Omega$

$$R(\bar{\epsilon}) = \min_{\bar{\epsilon}} \int_{\Omega} \left( \frac{1}{2} (\bar{\epsilon} - \epsilon)^2 + \frac{1}{2} (l_c \nabla \bar{\epsilon})^2 \right) d\Omega \quad (2.1)$$

where  $\epsilon$  and  $\bar{\epsilon}$  are strain and regularized strain tensors respectively,  $l_c$  a characteristic length and  $\nabla$  the gradient operator. The gradient term introduces interactions between each material point and its surrounding. Minimizing the integral of Equation (2.1) is equivalent to solving the following differential equation

$$\bar{\epsilon} - l_c^2 \Delta \bar{\epsilon} = \epsilon \quad (2.2)$$

where  $\Delta$  denotes the Laplacian operator, considering the following boundary conditions

$$(\nabla \bar{\epsilon}) \cdot \mathbf{n} = \mathbf{0} \quad (2.3)$$

with  $\mathbf{n}$  a vector normal to the boundary. It can be noted that such regularization scheme will increase the strain in a point in the vicinity of the damaged zone and limits the strain gradient. This procedure will enlarge the localization band. Some modified versions include a projector canceling out the contribution of totally damaged elements to the regularization procedure to prevent a physically in-realistic enlargement of the localization band [[Godard, 2005](#)].

The effect of a statistical description of the continuum on the behavior of a nonlocal model at and after the onset of localization has already been studied [[Carmeliet and de Borst, 1995](#)]. The considered studies were performed using a nonlocal model based on a regularized strain. The material macro-scale heterogeneity was described based on the framework of the random field theory. It was shown that a stochastic description of the damage threshold does not solve the difficulties associated with strain localization and the use of a nonlocal scheme is necessary. Two internal lengths associated respectively with the internal length scale of the nonlocal continuum and the correlation length of the random field must be considered. The authors pointed out the proper modeling of the relationship between these internal lengths and their experimental identification as an important issue [[Carmeliet and de Borst, 1995](#)].

The statistical theory of strength proposed by [Weibull \[1939\]](#) is widely used to describe the random nature of the failure of quasi-brittle materials. However, it is shown that the classical Weibull theory cannot be used for situations where the failure of the structure is caused by the stable propagation of a macrocrack [[Bažant \*et al.\*, 1991](#)]. More specifically, the stress field used to calculate the failure probability at each point must take into account the stress redistribution due to the presence of macrocracks and reflect the localization of strains occurring prior to failure. A nonlocal Weibull theory was proposed by [Bažant and Xi \[1991\]](#) for improving this shortcoming. An average stress value was used in the fracture-process zone around the crack tip. The local (Cauchy's) stress was used elsewhere. An extension of the proposed analytical solution to a finite element nonlocal damage

model was also proposed. Considering the elastic analysis of fracture, the nonlocal strains were used to calculate the average stresses in the process zone as follows [Bažant *et al.*, 1991, Bažant and Xi, 1991]

$$P_f = \exp \left[ - \int_{\Omega} \sum_{i=1}^n \left( \frac{\langle E \bar{\varepsilon}_i(\mathbf{x}) - \sigma_u \rangle}{\sigma_0} \right)^m \frac{d\Omega(x)}{\Omega_r} \right] \quad (2.4)$$

where  $P_f$  denotes the failure probability,  $n$  number of dimension ( $n = 1, 2$  or  $3$ ),  $E$  Young's modulus,  $\bar{\varepsilon}(x)$  nonlocal strain,  $\sigma_u$ ,  $\sigma_0$  and  $m$  the Weibull parameters, and  $\Omega_r$  a reference volume. The product of  $E\bar{\varepsilon}(x)$  is considered as a nonlocal measure of the stress field in this setting.

It is worth noting that the aforementioned works are based on the failure probability defined as the crack initiation probability. Even though an example was presented by Bažant and Xi [1991] in which the asymptotic stress field around a crack tip was used to fit the averaging functions, no link was made to the stress intensity factor (SIF) calculation or crack propagation. Fracture mechanics provides powerful tools for describing the propagation of initiated cracks. The model presented at the next section aims at combining a damage-mechanics-based approach to model crack initiation with a fracture-mechanics-based one for modeling crack propagation.

## 2.2 A non-local damage framework

A double-threshold non-local damage model was developed during the PhD of N. Guy [2010]. The model aims at simulating crack initiation and propagation within a heterogeneous material. The inception of propagation on an existing defect is considered as crack initiation. Once a crack has initiated, its growth is governed by a regularized stress intensity factor. Crack initiation follows a Poisson-Weibull distribution. A simple brittle local damage model that provides the results following the weakest link hypothesis is introduced. The propagation of initiated cracks was then modeled through linear fracture mechanics principles. The stress intensity factor is considered as the governing parameter of the crack growth in this setting. It will be shown that the use of a simple local damage model with a non-local gradient enhanced regularization permits brittle failure of weakest link type and provides mesh-objective results for crack initiation. A new regularization scheme based on a stress regularization operator is proposed. The stress gradient regularization scheme is very close to the strain regularization proposed by Peerlings *et al.* [1998]. However, the proposed stress gradient regularization provides a more realistic modeling of strain localization as no regularization is performed on the strain field. Furthermore, it will be shown that with the stress gradient enhancement of a simple local damage model the stress intensity factor can be calculated without mesh refinement around crack tips in a crack network. A unique variable, i.e. the regularized stress is thus used for evaluating crack initiation and propagation.

The regularization is performed over a characteristic length  $\ell_c$  that must be long enough with respect to the size of the elements in the zone of interest. In the present case, it is proposed to choose the characteristic length equal to the largest defect size. This choice provides a crack initiation threshold greater than or equal to the crack growth threshold [Guy *et al.*, 2012]. The characteristic

length thus stands for a micro-structural parameter that is the size of the largest initial crack modeled as a defect. Larger cracks are modeled as a set of completely damaged elements. The regularization operator reads

$$\bar{\sigma} - \ell_c^2 \Delta \bar{\sigma} = \sigma, \quad (\nabla \bar{\sigma}) \cdot \mathbf{n} = \mathbf{0} \quad (2.5)$$

where  $\bar{\sigma}$  is the regularized stress tensor and  $\sigma$  the Cauchy stress tensor. The vector  $\mathbf{n}$  is normal to a surface where natural boundary conditions are considered.

### 2.2.1 Crack initiation

Let us consider the case of crack initiation under tensile stresses, in mode  $I$ , and that crack inception can only occur at initial defects represented by random locations and initiation stress levels. In this setting, the initiation of new macrocracks follows the weakest link assumption and a Weibull model can explain the scatter of the experimental results. An initiation probability  $P_i(el) \in [0; 1]$  calculated from a uniform distribution is assigned to each sub-domain (each element). An initiation stress is then calculated for each sub-domain from an inverse Weibull law

$$S_i(el) = \frac{\sigma_0}{(\lambda_0 V_{el})^{\frac{1}{m}}} [-\ln(1 - P_i(el))]^{\frac{1}{m}} \quad (2.6)$$

where  $V_{el}$  is the volume of the considered element,  $m$  the Weibull modulus, and  $\frac{\sigma_0^m}{\lambda_0}$  the scale parameter. A crack will initiate in the considered element if the regularized maximum principal stress reaches  $S_i(el)$ . The initiated macrocracks are assumed to be perpendicular to the regularized maximum principal stress direction. For a given characteristic length, a nominal stress is defined as

$$\sigma_{\ell_c} = \sigma_0 / (\lambda_0 \ell_c^3)^{1/m} \quad (2.7)$$

which is useful to obtain an estimation of the stress state associated with crack initiation. It corresponds to the necessary loading for initiating a crack in a loaded element of volume  $\ell_c^3$  with a probability of  $1 - 1/e \approx 0.63$ .

It is worth noting that the introduced crack initiation threshold leads to the same behavior for a domain independently to its spatial discretization. Let us consider a domain  $\Omega$  uniformly stressed, and a set of  $n$  independent sub-domains  $\Omega_i$  such that  $\cup_{i=1}^n \Omega_i = \Omega$ . For a given loading level, the probability for the first crack to initiate in the union of the  $n$  independent sub-domains  $\Omega_i$  and in the domain  $\Omega$  are equal. This equality is obtained by

$$P_i(|\cup_{i=1}^n \Omega_i|, \sigma_I) = 1 - \prod_{i=1}^n P_{N_d=0}(|\Omega_i|, \sigma_I) = 1 - \exp\left[-\sum_{i=1}^n |\Omega_i| \lambda_t(\sigma_I)\right] = P_i(|\Omega|, \sigma_I). \quad (2.8)$$

### 2.2.2 Crack propagation

Considering the two-dimensional case of a crack in an elastic medium submitted to a far field loading, the asymptotic Westergaard solution [Kanninen and Popelar, 1985] gives a good approximation of the stress field around the crack tip. Considering Equation (2.5) as a nonhomogeneous Helmholtz equation, the proposed operator provides a regularized stress field in the vicinity of the crack tip corresponding to Westergaard asymptotic solution. The present procedure allows the stress intensity factor to be calculated without any mesh refinement for a propagating crack. Therefore, a direct transition from a damage-mechanics-based model for crack initiation to a fracture-mechanics-based model for crack propagation is provided. In addition, both models use the same variable, the regularized stress. The crack propagation threshold reads

$$S_g(el) = \frac{6\Gamma^2 \left(\frac{3}{4}\right)}{5\pi} \frac{K_c}{\sqrt{\pi\ell_c}} \quad (2.9)$$

where  $K_c$  is the fracture toughness of the studied material. Furthermore, crack growth is assumed to occur at an existing crack tip and its direction is perpendicular to the regularized maximum eigen stress direction.

For a pure mode  $I$  loading case, the given threshold is equivalent to

$$K_c \leq K_I \quad (2.10)$$

when the characteristic length  $\ell_c$  is small compared to the crack length. It is to be noted that the introduced threshold is a mixed mode criterion because for a mixed mode loading the regularized maximal principal stress is

$$\bar{\sigma}_I = \frac{6\Gamma^2 \left(\frac{3}{4}\right)}{5\pi} \frac{1}{\sqrt{\pi\ell_c}} \frac{\left[5K_I + \sqrt{K_I^2 + 16K_{II}^2}\right]}{6}. \quad (2.11)$$

The introduced threshold is therefore equivalent to the following criterion

$$K_c \leq \frac{\left[5K_I + \sqrt{K_I^2 + 16K_{II}^2}\right]}{6} \approx K_I + \frac{2}{3}K_{II}. \quad (2.12)$$

where  $K_I$  and  $K_{II}$  stand for the mode  $I$  and  $II$  stress intensity factors respectively.

### 2.2.3 Threshold comparison

The initiation threshold was introduced by considering that a crack initiation stress is associated with each initial defects. In order to compare the initiation threshold with the crack growth threshold, let us consider that the most critical defect in a considered domain has a threshold stress corresponding to a crack of half length  $a$ , which is orientated perpendicular to the eigen stress direction. In that case,

the initiation threshold is expressed as

$$S_i = \frac{K_c}{\sqrt{\pi a}} \quad (2.13)$$

Assuming that the characteristic length is greater than  $a$  leads to

$$S_i = \frac{K_c}{\sqrt{\pi a}} \geq \frac{K_c}{\sqrt{\pi \ell_c}} > \frac{6\Gamma\left(\frac{3}{4}\right)}{5\pi} \frac{K_c}{\sqrt{\pi \ell_c}} = S_g \quad (2.14)$$

A characteristic length greater than the size of the largest initial crack (or defect) provides a crack initiation threshold greater than or equal to the crack growth threshold. It is worth noting that this condition is not initially satisfied because of the conservative nature of a two parameter Weibull law. Using a two-parameter Weibull law (without threshold) is equivalent to considering the possibility of having initial cracks (defects) of any size, even larger than the characteristic length. In the proposed setting, the characteristic length stands for a micro-structural parameter that is the size of the largest initial crack modeling as a defect. Initial cracks of size larger than  $2\ell_c$  can be modeled as a set of completely damaged elements.

#### 2.2.4 Local constitutive law

A simple damage law describing a perfectly brittle behavior of an isotropic material is used as a local damage law. It is derived by using Helmholtz' state potential [Lemaitre and Chaboche, 1990]

$$\rho\psi_e = \frac{1}{2} (1 - d) \boldsymbol{\varepsilon} : \boldsymbol{C} : \boldsymbol{\varepsilon} \quad (2.15)$$

where  $\boldsymbol{C}$  is the elasticity tensor of the virgin material,  $\rho$  the mass density, and  $d$  the damage variable. From the state potential, the elasticity law is obtained

$$\boldsymbol{\sigma} = \rho \frac{\partial \psi_e}{\partial \boldsymbol{\varepsilon}} = (1 - d) \boldsymbol{C} : \boldsymbol{\varepsilon}. \quad (2.16)$$

The thermodynamic force associated with the damage variable  $d$  is defined as

$$Y = -\rho \frac{\partial \psi_e}{\partial d} = \frac{1}{2} \boldsymbol{\varepsilon} : \boldsymbol{C} : \boldsymbol{\varepsilon}. \quad (2.17)$$

Damage growth is driven by

$$d = H(\langle \bar{\sigma}_I - S_i \rangle + \langle \bar{\sigma}_I - S_g \rangle) \quad \text{when } \dot{d} \geq 0 \quad (2.18)$$

where  $H$  denotes Heaviside step function,  $\bar{\sigma}_I$  the maximum principal regularized stress,  $S_i$  and  $S_g$  the initiation and crack growth thresholds.

### 2.2.5 Numerical implementation

The finite element method is used to solve the global problem. A Newton-Raphson scheme is chosen. The constitutive law is solved implicitly and the damage field is considered uniform in each element. The numerical model is introduced in code-aster. A specific finite element, initially developed for a strain gradient enhancement model [Galenne, 2009], is adapted for the spatial discretization [Guy *et al.*, 2012]. As shown in Figure 2.1 the regularized stress field is added as nodal degrees of freedom (DOFs). The introduced finite element is thus quadratic for the displacement field and linear for the regularized stress.  $P^2$  and  $P^1$  shape functions are used for displacement and regularized stress fields, respectively. Two types of unknowns are defined on the corner nodes and only displacements are calculated at middle nodes. A triangular element has thus 21 DOFs for a plane problem.

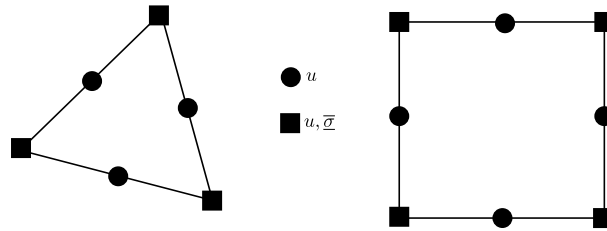


Figure 2.1: Nodal unknowns for two types of elements [Guy *et al.*, 2012].

Each undamaged element can be damaged in two different situations during the cracking process. An element may be located in the direct neighborhood of a crack tip. In that case, the element is marked and the crack propagation threshold will be considered for that element. Conversely, when there is no propagating crack in the direct neighborhood of the element, the initiation threshold is considered. Consequently, the geometrical position of crack tips and their corresponding elements are stored during the calculation.

In this method, a finite element is marked for propagation if and only if it is marked during previous Newton iterations. Each crack tip may thus induce the failure of one element during each iteration. The material behavior is implemented in an implicit manner to ensure the stability of converged states. During each time step, a crack tip may cause the failure of as much elements that is necessary for reaching equilibrium. The unstable propagation of the macrocracks thus can be simulated by the present model. A time step subdividing criterion based on the damage growth on the whole structure is also introduced. Applying this criterion does not allow for the initiation of more than one crack during each Newton iteration. This function enables us, for stable crack propagation conditions, to obtain results independent of the time step selected by the user.

### 2.2.6 Numerical validation

A set of numerical verification tests has been performed to investigate the accuracy and efficiency of the developed model [Guy *et al.*, 2012]. First considering a simple case of a beam of width  $2b$  and of infinite (very large) length that contains a central crack of length  $2a$  and is submitted to a horizontal

stress of  $\sigma_\infty$  for which an analytical approximation exists [Murikami, 1987]. The treated case is described in Figure 2.2.

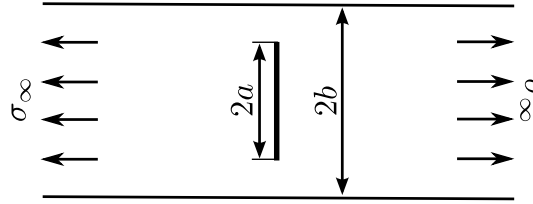


Figure 2.2: Schematic of the considered theoretical case [Guy *et al.*, 2012].

The analytical approximate for the stress intensity factor reads [Murikami, 1987]

$$K_{Ia} \approx \sigma_\infty \sqrt{\frac{\pi a}{\cos\left(\frac{\pi a}{2b}\right)}}. \quad (2.19)$$

For the numerical simulations, half of the domain was meshed. The half crack was modeled by a line of broken elements (elements where  $d \approx 1$ ). For a given characteristic length, a stress intensity factor was deduced from the nonlocal threshold

$$K_I(\ell_c) \approx \frac{5\pi}{6\Gamma^2\left(\frac{3}{4}\right)} \bar{\sigma}_I \sqrt{\pi \ell_c} \quad (2.20)$$

with  $\bar{\sigma}_I$  the maximum principal regularized stress at the crack tip. In order to compare the "nonlocal based" stress intensity factor to the usual one, the ratio  $R_I(\ell_c) = K_{Ia}/K_I(\ell_c)$  was introduced. The results of simulations performed for three characteristic lengths  $\ell_c$  of 20 mm, 40 mm and 80 mm are shown in Figure 2.3.

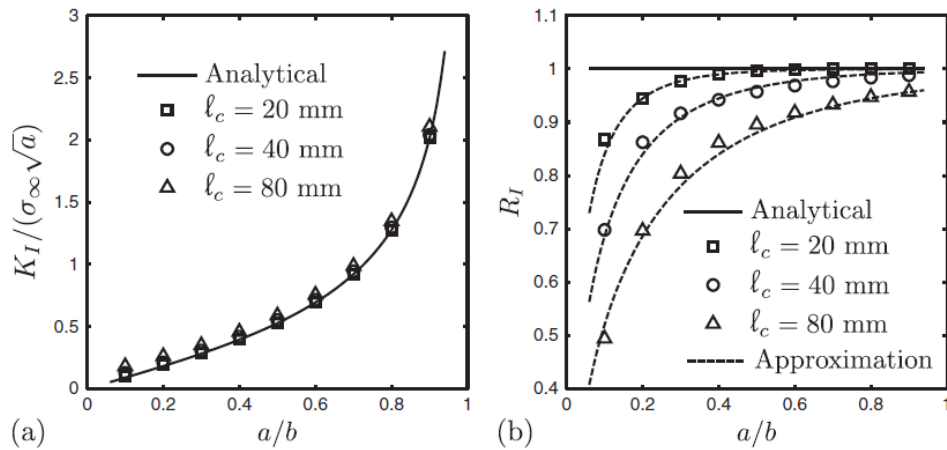


Figure 2.3: Stress intensity factors (a) and difference between analytical and nonlocal estimations (b) as functions of normalized crack lengths for different characteristic lengths [Guy *et al.*, 2012].

As shown in Figures 2.3(a) and 2.3(b) the nonlocal stress intensity factor tends to be equal to the usual stress intensity factor when the characteristic length decreases. The results obtained for

a characteristic length  $\ell_c = 20$  mm are close to the analytical solution. Furthermore, for each characteristic length the nonlocal stress intensity factor tends to be equal to the usual stress intensity factor when the crack length increases. It also appears that the value of the maximum principal regularized stress is larger for lower characteristic lengths. For each case, an approximation of  $R_I(\ell_c)$  is plotted in Figure 2.3(b). This approximation reads

$$R_I(\ell_c) = 1 - \exp \left[ - \left( \frac{a}{\ell_c} \right)^{\frac{2}{3}} \right] \quad (2.21)$$

and gives a good estimation of the characteristic length effect when  $a \geq \ell_c$ . Further, the nonlocal threshold associated with crack growth is such that

$$\lim_{a/\ell_c \rightarrow 0} K_I(\ell_c) = \frac{5\pi}{6\Gamma^2\left(\frac{3}{4}\right)} \sigma_\infty \sqrt{\pi \ell_c} \quad (2.22)$$

Considering the approximations (2.21) and (2.22) an estimation of the nonlocal threshold associated with crack growth is plotted in Figure 2.4. In order to compare different thresholds, the usual stress intensity factor threshold and some examples of Weibull-based threshold describing crack initiation are plotted in Figure 2.4. Micro and macro scales are defined in Figure 2.4. The proposed numerical strategy is such that the microcracks (cracks with  $a \leq \ell_c$ ) are not described by the damage field but associated with a Weibull threshold. The threshold of microcrack initiation is always greater than the minimum initiation threshold plotted in Figure 2.4 because the microcracks are assumed to be small ( $a \leq \ell_c$ ). Furthermore, in the developed numerical strategy, the macrocracks (cracks with  $a \geq \ell_c$ ) are represented by the damage field. When a crack initiates, the crack description changes and crack growth is then simulated by considering the nonlocal propagation threshold that tends to be equal to the usual stress intensity factor threshold as the crack grows.

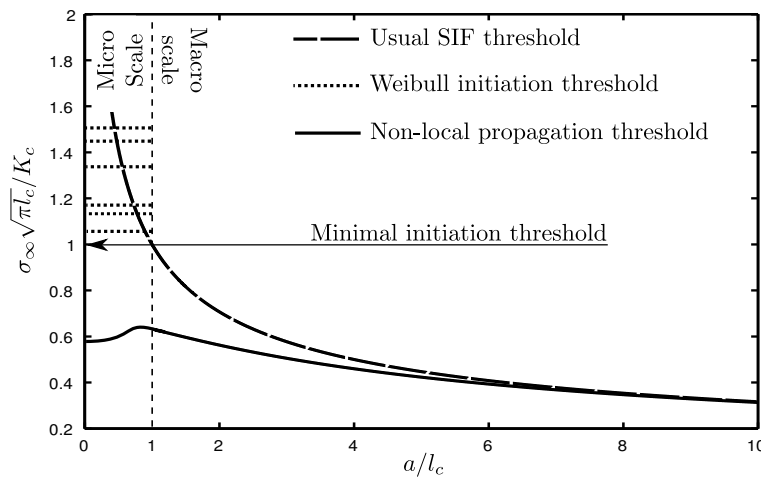


Figure 2.4: Change of the considered thresholds with normalized crack (or defect) size [Guy *et al.*, 2012].

The crack opening displacement is another parameter to be checked. If the crack of Figure 2.2 is located in an infinite plate, its opening displacement  $\Delta u_x$  is calculated by resorting to the analytical solution proposed by Muskhelishvili [Kanninen and Popelar, 1985]

$$\Delta u_x = \frac{4\sigma_\infty a}{E} \sqrt{1 - \left(\frac{a}{y}\right)^2} \quad (2.23)$$

where  $y$  denotes the coordinate of each point on the crack mouth from the crack center. The crack opening at its center can be also calculated as a function of the applied stress and crack geometry ( $a/b$  ratio) [Murikami, 1987]. The crack opening calculated by the model is compared to the two solutions for a large plate ( $a/b = 0.14$ ) in Figure 2.5. A very good agreement is observed between the model prediction and the analytical results. Such accurate results are important in view of coupling the developed model with an external flow simulator for coupled hydromechanical applications.

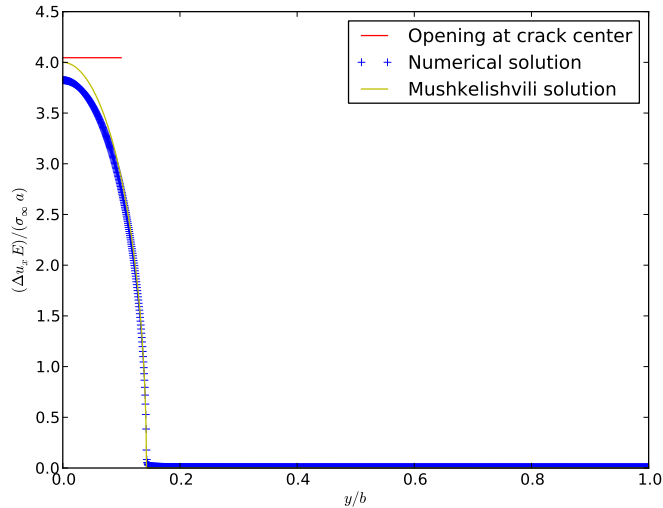
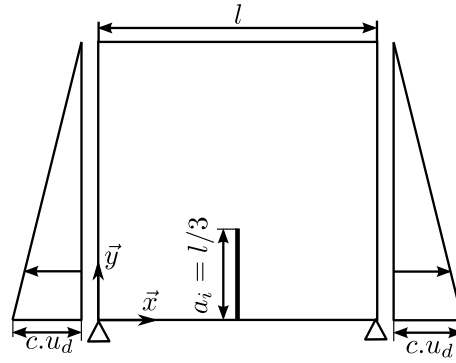


Figure 2.5: Comparison between the simulated and analytical crack opening displacement ( $a/b = 0.14$ ,  $\ell_c = 20$  mm) [Guy *et al.*, 2012].

The second tests devoted to validate the independence of the developed model to spatial discretizations. This property was studied with a particular attention as it has been the main reason for using a nonlocal formulation. The mesh-objective character of the crack initiation is assumed by using an inverse Weibull model and was demonstrated in [Guy *et al.*, 2012]. The propagation of a single crack was simulated using different spatial discretizations here. The chosen meshes allow to show that the results depend neither on the size nor on the shape and orientation of the the spatial discretization. However, the damage field depends on the spatial discretization because it is constant in each finite element. The studied case is shown in Figure 2.6.

The considered domain is a square with an edge length of  $l = 1$  m containing a vertical crack with an initial length of  $a_i = l/3$ . The initial crack is modeled by a set of broken elements (i.e.,

Figure 2.6: Schematic of the studied case [Guy *et al.*, 2012].

elements with  $d \approx 1$ ). The vertical displacements are set to zero on the lower boundary and the lateral boundaries were submitted to a horizontal displacement varying linearly with the height. On the left boundary, the horizontal displacement reads  $u_x(x=0, y) = -cu_d(1 - y/l)$  with  $c$  characterizing the loading level that is 0 at the initial state and 1 for the maximum loading. The horizontal displacement applied to the right boundary reads  $u_x(x=l, y) = -u_x(x=0, y)$ . We consider  $u_d = 0.2$  mm. The elastic parameters are  $E = 20$  GPa for Young's modulus, and  $\nu = 0,25$  for Poisson's ratio. The characteristic length is  $\ell_c = 0.1$  m and the material toughness  $K_c = 1 \text{ MPa}\sqrt{\text{m}}$ . The studied crack is submitted to a mode I loading because of the chosen boundary conditions. Crack growth is globally stable (the numerical sample failure is quasi-brittle). Figure 2.7 shows the simulation input and results for four different meshes, M1 to M4, the corresponding horizontal displacement and damage fields for a loading level such that  $c = 1$ .

The first three considered meshes (M1, M2 and M3) are of same shape but the element sizes are different. The length of an element edge is  $l/123$  for the coarsest mesh,  $l/165$  for the middle one and  $l/201$  for the finest. For the fourth mesh, the elements are tilted at  $45^\circ$  in the area, where the crack is assumed to grow; the length of the element edge in that area is  $l/165$ . The horizontal displacement and damage fields shown in Figure 2.7 are very close for all used meshes. For the first simulation, the length of the damaged area is equal to that of the crack, and the width of this area is equal to the element size. For the mesh containing tilted elements, the damaged area has a zigzagged shape that corresponds to the mesh shape. However the horizontal displacement field is very similar to the other ones.

To compare the results, the change of the crack length with the applied load is shown in Figure 2.8. The crack length  $a$  is deduced from the coordinate of the crack tip position given by the numerical model. The crack length appears to be independent of the spatial discretization. The observed differences are directly related to the time step of the calculation.

For the first three simulations and for every loading step, the abscissa of the crack tip is equal to 0.5 m with an uncertainty of  $1 \mu\text{m}$ . For the fourth case, the abscissa of the position of the crack tip ranges between  $0.5 \pm 8 \times 10^{-6}$  m for all steps. It is to be noted that the use of a tilted mesh does not significantly affect the direction of crack growth. For the simulation with the tilted mesh, the

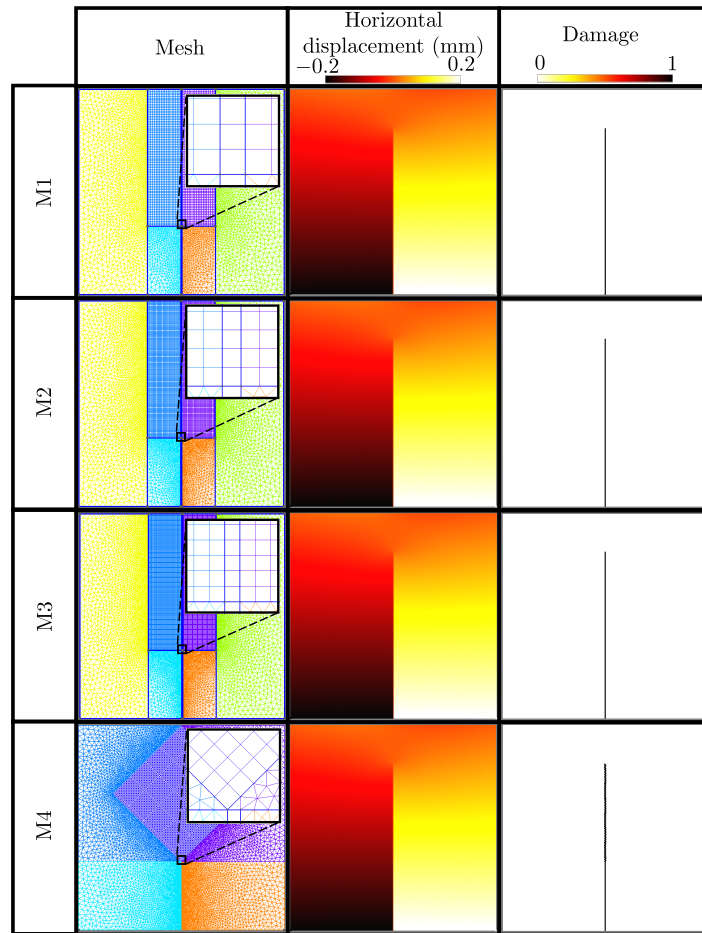


Figure 2.7: Meshes, horizontal displacement and damage fields for  $c = 1$  and for two of the simulations corresponding to the case shown in Figure 2.6 [Guy *et al.*, 2012]

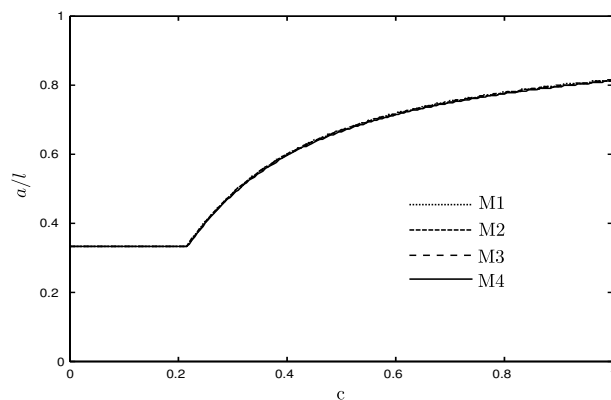


Figure 2.8: Crack growth with load  $c$  for the different meshes [Guy *et al.*, 2012].

maximum distance between the crack tip and the plane of symmetry is  $8 \mu\text{m}$ , which represents 1.3 % of the length of an element.

## 2.2.7 Experimental verification

In this section, the consistency of both experimental and numerical results provided by the model is checked. The initiation threshold is studied first through Brazilian test simulation. In order to validate the crack propagation threshold, crack propagation in a numerical sample is simulated with boundary conditions corresponding to a Sandwiched-Beam test. In each simulation, the characteristics used to describe the studied rock are issued from an experimental campaign.

The study is performed on rock samples from the Weyburn site (Canada). The latter is considered as a demonstration site for CO<sub>2</sub> storage [Preston *et al.*, 2005]. The International Energy Agency Green House Gas (IEAGHG) Weyburn-Midale CO<sub>2</sub> storage and monitoring project was designed to assess the technical feasibility of CO<sub>2</sub> geological storage at large scale. The Weyburn and Midale oil fields are located near Midale in Saskatchewan state. Various Enhanced Oil Recovery (EOR) techniques were used before the introduction of CO<sub>2</sub> for EOR in 2000. The rock samples were extracted from a depth of 1,300 m. They are located in a particular geological layer called Lower Watrous. Lower Watrous, as a clay-rich low-permeability rock is considered as a potential caprock for CO<sub>2</sub> storage in the Weyburn site.

### 2.2.7.1 Crack initiation

The Young's modulus and Poisson's ratio were identified via uniaxial compression tests [Guy *et al.*, 2018]. The identified Young's modulus is equal to 16 GPa and the Poisson's ratio is equal to 0.15. The experimental results show that the studied rock, as other geomaterials, exhibits a brittle behavior under unconfined compressive loading. The failure behavior in terms of crack initiation in mode *I* was first characterized considering a Weibull model. A two-parameter Weibull model was used to describe the behavior of the rock samples at failure. The Weibull parameters were determined using three-point flexural and Brazilian tests, thereby providing two different scales of effective volumes. Then, the ability of the numerical model to properly describe crack initiation was studied by modeling Brazilian tests.

The Weibull parameters were identified through an experimental campaign based on thirty three-point flexural and thirty-four Brazilian tests [Guy *et al.*, 2018]. The identification method [Silva *et al.*, 2004] allows results issued from the two types of tests to be considered at the same time. The Weibull diagram is shown in Figure 2.9. The identified Weibull modulus is  $m = 6.0$ , which corresponds to a clearly heterogeneous material; it is in the typical range of values for rocks ( $3 \leq m \leq 9$ ). As it can be seen in Figure 2.9, there is a good agreement between experimental data and the model. It is to be noted that the use of a two-parameter Weibull model leads to a conservative estimation of failure probability for the lowest stresses as no threshold is considered.

In order to validate the initiation threshold, numerical modeling of Brazilian tests was performed. The rock samples were modeled in a 2D setting under plane strain hypothesis by disks that have a radius of  $R = 43$  mm. The rock parameters are those identified previously. The Weibull modulus is  $m = 6.0$  and the scale parameter is  $\sigma_0^m / \lambda_0 = 7.3 \times 10^{35} \text{ Pa}^m \text{ m}^3$ . The characteristic length is

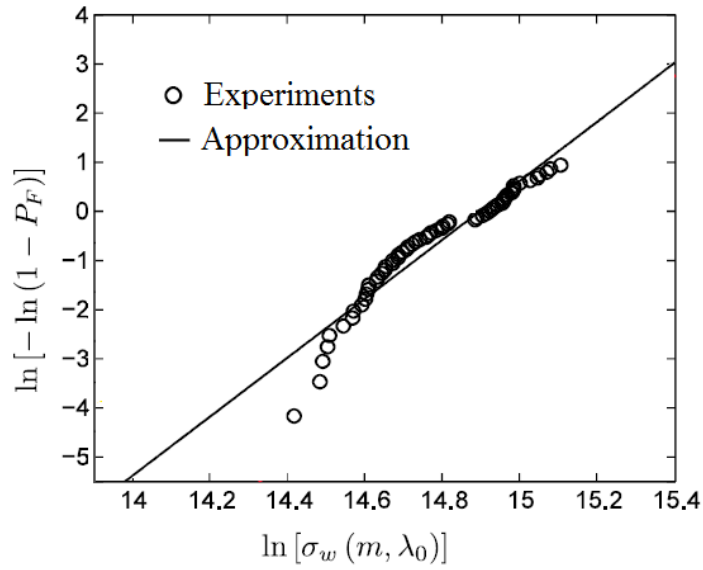


Figure 2.9: Modified Weibull diagram for the identification of parameters based on three-point bending and Brazilian tests [Guy *et al.*, 2018].

considered as  $\ell_c = 2$  mm to be small enough to allow for a relevant description of the stress state in the numerical specimen with the regularized stress. A characteristic length of  $\ell_c = 2$  mm implies that initial cracks (initial defects) are smaller than 4 mm, which is a reasonable hypothesis. The nominal initiation stress is  $\sigma_{\ell_c} = \sigma_0 / (\lambda_0 \ell_c^3)^{1/m} = 21.2$  MPa. The numerical model is shown in Figure 2.10.

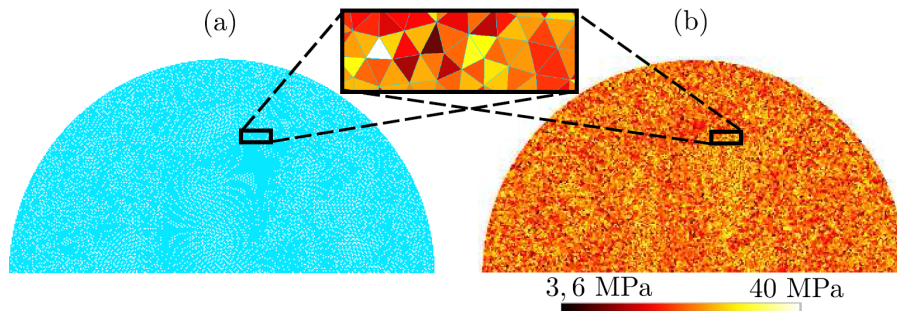


Figure 2.10: Mesh (a) and crack initiation threshold (b) for the upper half of the model used to simulate Brazilian tests [Guy *et al.*, 2018].

In Figure 2.10(b) the initiation thresholds obtained for each element of one numerical sample are mapped. The initiation threshold for each element was obtained considering its size and following a random selection of an initiation probability from a uniform distribution using Equation (2.6). This procedure results in a scattered map ranging from 3.6 MPa to 40 MPa. Only the lowest initiation thresholds have an influence on the results as the potential initiation sites. In the numerical simulations, the regularized stress field tends to lead to crack initiation in the middle of the specimen, which is consistent with experimental observations.

The theoretical failure probability reads

$$P_F = 1 - \exp \left[ - \left( \frac{\sigma_w}{\sigma_0} \right)^m \right]. \quad (2.24)$$

One hundred simulations were performed to obtain one hundred Weibull stresses  $\sigma_{wi}$ . For each Weibull stress  $i$  a failure probability was defined  $P_{Fi} = i/(n + 1)$ . The results of numerical simulations, analytical model (Eq. (2.24)) and experiments are plotted in Figure 2.11.

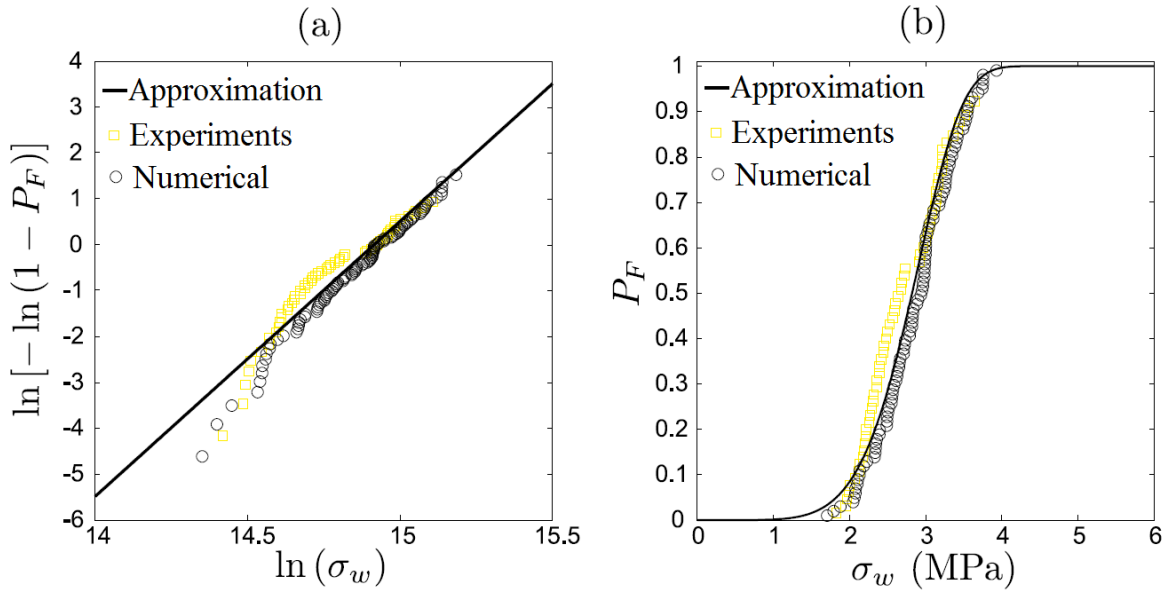


Figure 2.11: Modified Weibull diagram (a) and failure probability  $P_F$  as functions of the Weibull stress  $\sigma_w$  (b) for the numerical, analytical and experimental approaches [Guy *et al.*, 2018].

The results provided by the three approaches are consistent. Only small differences are observed for low probabilities. This difference is due to the cut-off of the lowest part of the Weibull distribution associated with initial defects due to the consistency condition (Eq. (2.14)) of two thresholds. In the present case, the consistency condition leads to the hypothesis that initial cracks are smaller than 4 mm. It appears that for low probabilities the numerical model is closer to the experimental results than the analytical model.

### 2.2.7.2 Crack propagation

In linear elastic fracture mechanics, the fracture toughness is usually compared to stress intensity factors to predict crack propagation. The material toughness can be identified from three-point bending tests performed on notched specimens even if in this context crack propagation is unstable for brittle materials. Pre-cracking can be performed with Sandwiched-Beam tests that allow for stable crack propagation [Srawley, 1976]. Specific DIC features have been already developed in order to calculate stress intensity factors [Forquin *et al.*, 2004, Roux and Hild, 2006]. They have been used hereafter. The material toughness was measured with a two-step experimental campaign consisting of

first pre-cracking the sample (here with an SB configuration) and then loading the pre-cracked sample in three-point bending up to failure.

The failure of a brittle material tends to be very sudden because it commonly results from unstable crack propagation. Pre-cracking of brittle sample is one of the concerns of their toughness measurement. One solution is to load the specimen in such a way that crack initiation and stable propagation are possible (Sandwiched-Beam (SB) test [Pancheri *et al.*, 1998]). The SB test uses three beams: a central beam to be pre-cracked and two other identical beams made of a more rigid material as shown in Figure 2.12.

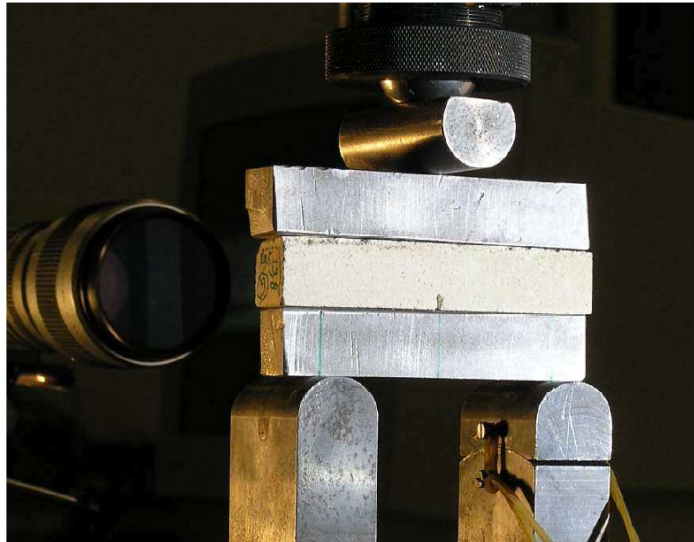


Figure 2.12: Sandwiched-Beam test in which the rock sample is loaded with the two aluminum alloy beams [Guy *et al.*, 2018].

In the present study, the lower and upper beams are made of aluminium alloy and have a Young's modulus of 70 GPa. Crack initiation and location can be detected with the use of DIC (Figure 2.13). From the measured displacement field, the mean infinitesimal strains per element were computed. The maximum eigen strain field exhibits a very localized region corresponding to the presence of a crack. At this stage of the experimental process, the material arrest toughness can be deduced from the observed displacement fields [Roux and Hild, 2006] under the assumption that the crack is propagating.

After sample pre-cracking, three-point bending tests have been performed for toughness identification with the use of DIC. Figure 2.14 shows the results for sample no. 2 in three-point bending for an applied load of  $F = 350$  N. The horizontal displacement field is shown after rigid body translation removal. The crack tip location used for the post-processing step is plotted in white. The area in black is used for the post-processing based on a comparison between identified displacement field and Williams' series of the displacement field close to the singularity [Roux and Hild, 2006]. The stress intensity factor was estimated for different loading levels in order to obtain a better estimation of the fracture toughness. Knowing the failure load for each sample, the fracture toughness was

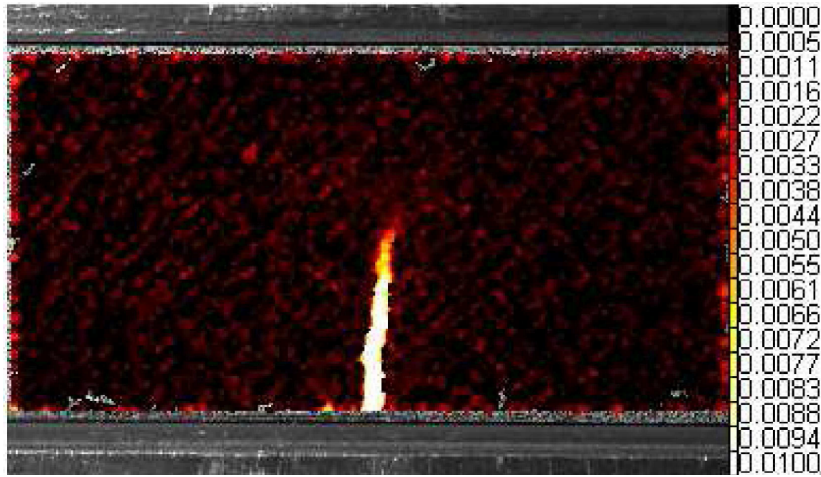


Figure 2.13: Maximum eigen strain field in sample no. 2 when pre-cracked. The physical size of 1 pixel is  $\approx 20.7 \mu\text{m}$  [Guy *et al.*, 2018].

estimated by linearly extrapolating the stress intensity factor with the applied load. Five samples have led to fracture toughness identification for both steps of the experimental campaign. The mode  $I$  stress intensity factors are scattered from  $K_I(a) = 0.11 \text{ MPa}\sqrt{\text{m}}$  to  $K_I(a) = 0.32 \text{ MPa}\sqrt{\text{m}}$  for the pre-cracking phase, and between  $K_I(b) = 0.16 \text{ MPa}\sqrt{\text{m}}$  and  $K_I(b) = 1.04 \text{ MPa}\sqrt{\text{m}}$  for the subsequent three-point flexural tests. The observed scatter again reflects the material heterogeneity.

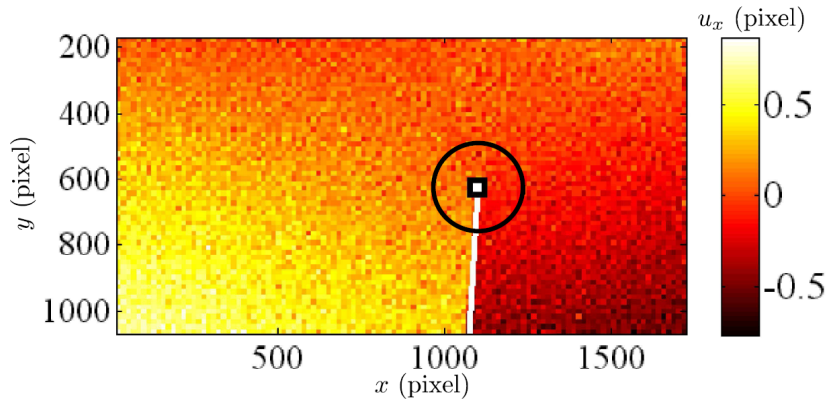


Figure 2.14: Measured horizontal displacement field (expressed in pixels) when rigid body translations have been removed. Pre-cracked sample (no. 2) submitted to a load  $F = 350 \text{ N}$  in three-point flexural test. The physical size of 1 pixel is  $\approx 20.3 \mu\text{m}$  [Guy *et al.*, 2018].

Despite scattered results, two clear tendencies can be pointed out. First, the mode  $II$  stress intensity factors are significantly lower than mode  $I$  levels. The mode  $II$  stress intensity factors are relatively higher for the SB tests as shown by the values  $r_K = K_{II}/K_I$ . It means that the cracking mode is mode  $I$  dominant for the three-point bending tests. This result can be explained by the confinement induced by the use of the metallic beams. Second, the stress intensity factors estimated for both tests are different with averages of  $K_I(a) = 0.21 \text{ MPa}\sqrt{\text{m}}$  and  $K_I(b) = 0.55 \text{ MPa}\sqrt{\text{m}}$ .

This tendency (of finding lower values for the pre-cracking tests) is observed for each sample. It can be explained by the fact that the stress intensity factors identified in three-point bending tests are associated with crack propagation inception whereas those determined with SB (pre-cracking) tests correspond to crack arrest. Given the experimental scatter, it is chosen to select a single value  $K_c = 0.21 \text{ MPa}\sqrt{\text{m}}$  as a conservative estimate.

In order to validate the crack propagation threshold, the results obtained with DIC were compared with those issued from numerical simulations. First, an SB test was modeled. The DIC results were based on a spatial discretization of  $8 \times 8$  pixel elements (1 pixel  $\approx 20.7 \mu\text{m}$ ). The measured displacements on the external boundary of the analyzed area were used as (Dirichlet) boundary conditions of the numerical model. In the present case, the external boundary is a rectangle and the finite element models used in the numerical computations are based on the same mesh used for DIC purposes. With such setting there is no need to model friction between the different beams of the SB test, and realistic boundary conditions are prescribed as measured via DIC. The crack initiation threshold is uniform and considered high enough in the modeled domain,  $S_i = 10 \text{ MPa}$  to ensure that crack initiation appears at the right location, which is induced by the displacement loading on the bottom face. The high horizontal displacement gradient due to the initiated crack leads to a loading that induces a very significant local increase of the regularized stress, thereby initiating the crack in the numerical model.

The horizontal displacement fields measured from an experiment and simulated are shown in Figure 2.15 together with the damage field at the end of the numerical computation. The results of the numerical computation are in good agreement with the experimental observations. In both cases the crack length is of the same order. A difference is observed concerning the crack orientation. For the numerical computation, the crack orientation has an angle of  $3^\circ$  with the vertical axis at initiation. After initiation, the crack propagation direction changes and tends to be inclined by  $30^\circ$ . For the experimental results, the crack orientation is of  $7^\circ$  for most of the propagation and tends to turn at the end of the experiments. This difference in terms of orientation is not surprising considering the applied load on the lower boundary. The displacement field used as a boundary condition in the computation does not only exhibit a significant gradient at the crack base for the horizontal value but also for the vertical one leading to a mode *II* loading of the crack in the 2D simulation. Therefore it is relevant that the crack tends to be inclined in the simulation.

A major difference between the experiment and the simulation is that the experiment is performed on a 3D sample and that the crack propagation during the experiment is indeed related to a 3D displacement field. The displacement estimated through DIC at the surface could be only partially representative of the 3D displacement field. Therefore, the observed gradient of vertical displacement at the crack base could only concern the vicinity of the surface of the observed specimen, leading to a less inclined crack in the experiment than in the simulation. Moreover, Lower Watrous presents a slight elastic anisotropy as most sedimentary rocks. This stiffness anisotropy may also affect the crack propagation orientation.

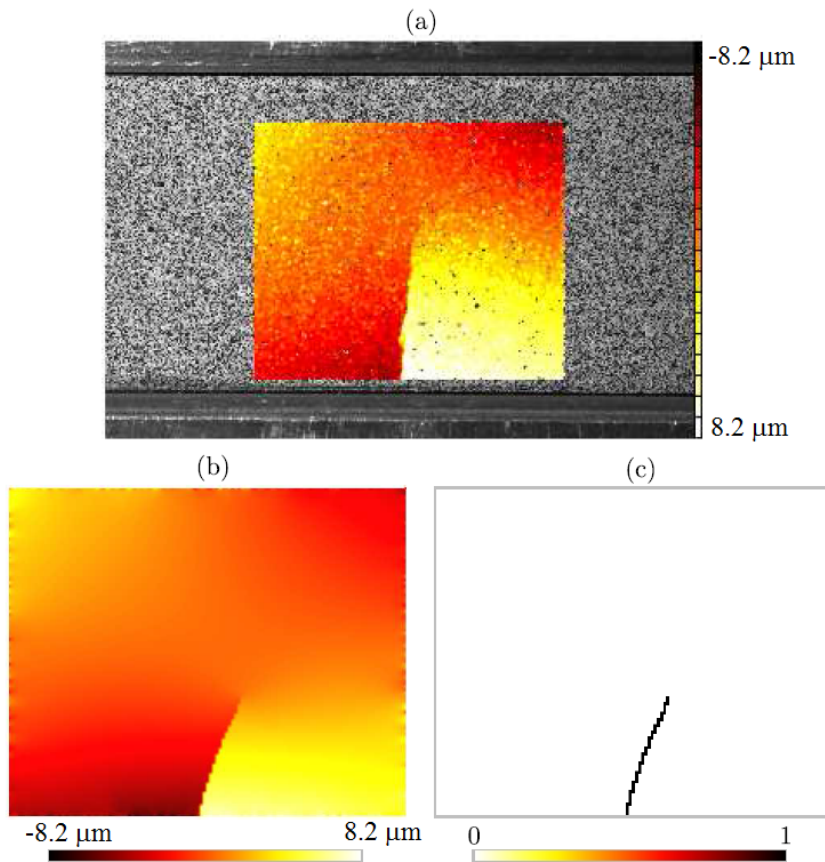


Figure 2.15: (a) Horizontal measured displacement field. (b) Simulated displacement field. (c) Damage field for sample no. 2 in the Sandwiched-Beam test [Guy *et al.*, 2018].

### 2.3 Towards a hydromechanical fracturing model

Carbon capture and storage (CCS) has been suggested as a potential method to reduce the emission of greenhouse gases into the atmosphere. Deep saline aquifers are of main interest for geological storage as they may provide important storage capacities. Evaluation of the sustainable injection pressure is one of the main parts of the safety study of a  $CO_2$  storage site. Deep well injection changes the stress state in geological formations. A change in the stress field may affect the hydraulic response of the medium through induced damage in the rock mass. The main goal of the present work is to introduce a hydromechanical damage model that takes into account the effect of mechanical heterogeneities on the fracturing probability due to gas injection operations.

It is now well-established that the behavior of porous media is governed by coupling of different phases [Coussy, 2004]. As an example, any fluid injection within an underground reservoir induces a pore pressure build-up in the geological reservoir and changes the total and effective stresses in the reservoir and adjacent geological formations. Different modeling strategies can be used to simulate these couplings. These strategies can be split into two major classes:

1. Fully coupled approach: governing equations of flow and solid mechanics are solved simulta-

neously during each time step. An iterative scheme, typically a Newton-Raphson method, is used to obtain the converged solution.

2. Sequential scheme: flow and mechanical problems are solved sequentially. Intermediate information from the first solved problem, i.e., flow or mechanical, is linked to the second one. An iterative scheme is used to obtain a converged solution.

Sequential schemes are developed and used as fully coupled schemes could be very expensive from a computational point of view, especially when very large spatial scales are considered. In addition, in a sequential scheme two separate simulators, each specific to the problem of interest, can be used.

Numerical modeling of  $CO_2$  injection integrity and performance must consider couplings of various phenomena, namely, geochemistry, geomechanics, fluid and heat flow, and transport. Sequential coupling of specified codes is always used to this end. Rutqvist *et al.* [2002] developed a sequential approach coupling THOUGH2 (a THC code) and FLAC3D (mechanical analysis) for the analysis of coupled multiphase fluid flow, heat transfer, and deformation in porous rocks. Rutqvist and Tsang [2002] then applied this simulator to study the caprock hydromechanical changes associated with  $CO_2$  injection into an aquifer. Vidal-Gilbert *et al.* [2009] used a “one way” coupling of reservoir and geomechanical analysis, where pressures obtained from reservoir simulations were integrated as input for a geomechanical model. Rohmer and Seyedi [2010] developed a sequential coupling of THOUGH2 and code-aster for large-scale hydromechanical models of a storage complex using sequential execution and data transfer.

### 2.3.1 Hydromechanical coupling scheme

The developed damage model was integrated within a specific hydromechanical coupling scheme to evaluate damage initiation in the caprock during  $CO_2$  injection operations. Hydraulic and mechanical calculations were performed sequentially using different modules of code-aster. Figure 2.16 gives a schematic view of the developed approach. At step  $n$ , the pore pressure  $p$  in the whole geological medium is calculated by the hydraulic simulator. The pressure is then transferred to the mechanical code as a body force. In this manner, the effect of pressure change on the effective stresses is obtained considering Biot’s coefficient. Only the over-pressure induced by gas injection was considered. The whole domain was considered as saturated. Classical governing equations following Biot’s poroelasticity were considered to describe the hydromechanical behavior of the whole domain before damage initiation.

The mechanical problem follows the resolution of the flow problem using an appropriate time discretization scheme. In this setting, the volumetric strain term of porosity change (Equation 2.27) is evaluated explicitly. The flow problem is solved while the strain remains constant in the whole model. In the same manner, the pressure is prescribed during the solution of the mechanical problem at  $t_{n+1}$  determined from the previous flow problem. The pressure corrections are considered as “loads” for

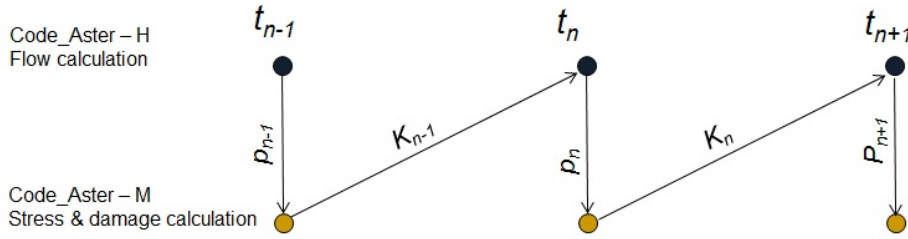


Figure 2.16: Schematic representation of sequentially linking hydraulic and mechanical calculations with  $p_n$  pressure,  $K_n$  permeability and  $t_n$  time at the end of the  $n^{th}$  time step [Seyedi *et al.*, 2013].

solving the mechanical problem [Settari and Mourits, 1998]. The momentum equation thus reads

$$\text{div} \boldsymbol{\sigma}' - b(\nabla \cdot p) + r\mathbf{g} = 0 \quad (2.25)$$

where  $\boldsymbol{\sigma}'$  is the effective stress tensor,  $b$  Biot's coefficient, and  $p$  the pressure. For an elastic behavior, the porosity  $\varphi$  is updated using the following expression

$$d\varphi = (b - \varphi) \left( d\varepsilon_v + \frac{dp}{K_s} \right) \quad (2.26)$$

where  $\varepsilon_v$  is the volumetric strain, and  $K_s$  the compressibility of the solid phase. Effective stress changes are thus calculated everywhere at each time step.

### 2.3.2 Application example and results

The developed model was used to evaluate the damage probability of a hypothetical caprock. It was shown that the reservoir-caprock interface constitutes a critical part of the storage complex where damage may occur due to pressure build-up in the reservoir for high values of the injection pressure (e.g., Rohmer and Seyedi [2010]). A part of caprock of 1000 m in length, and located between 900 m and 1000 m depth was considered. An extensional stress regime, i.e.,  $|\sigma_h| < |\sigma_v|$  was considered, a situation where vertical fractures may be initiated in the caprock [Guy *et al.*, 2010]. The effect of the injection procedure is idealized by a gradual increase of the pore pressure on the caprock-reservoir interface. Three zones were considered. In the middle zone (a segment of 100 m) of the bottom line of caprock (Figure 2.17) the pressure increases from the initial hydrostatic pressure  $p_0$  to  $3p_0$  during five years. On two 200-m long segments on both sides of the middle part, the pressure increases from  $p_0$  to  $2p_0$  during the same period. Finally, the pressure remains constant elsewhere on the bottom boundary of caprock. It was assumed that the pressure remains constant on the upper boundary of caprock. Lateral boundaries of caprock were considered as impermeable (i.e., flux set to zero). Vertical displacements on the bottom and horizontal displacements on the lateral boundaries were set to zero. Table 2.1 summarizes the main hydromechanical parameters used in the calculation. No coupling from the mechanical calculation on the flow problem was considered.

When the maximum pressure reaches 2.1 times the initial pressure ( $p_0$ ), tensile horizontal stresses

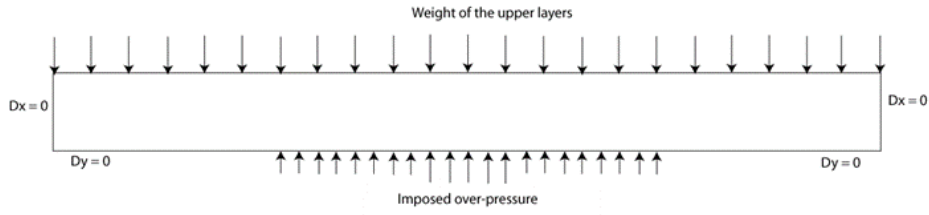


Figure 2.17: Studied caprock and considered boundary conditions [Seyedi *et al.*, 2013].

Table 2.1: Main hydromechanical parameters of the caprock [Seyedi *et al.*, 2013].

$E$ (GPa)	$\nu$	$K_{int}$ ( $m^2$ )	$\varphi$ (%)	$\rho$ ( $kg/m^3$ )	$K_{IC}$ ( $MPa.m^{0.5}$ )	$m$
16	0.28	$10^{-17}$	5	2700	1.0	6

appear on a part of the reservoir-caprock interface. the first cracks initiates when the prescribed pressure on the middle part of the model reaches  $2.4 p_0$ . Figure 2.18 shows the corresponding pore pressure distribution in caprock and the formed crack network. A zoom of the initiated crack network is presented in Figure 2.19. In this figure, the elements where the cracks are initiated are depicted in dark gray, propagation paths are black and finally the crack tips are in light gray. As it can be seen, all cracks are not initiated on the reservoir-caprock interface, where the horizontal stress is highest, due to caprock heterogeneity.

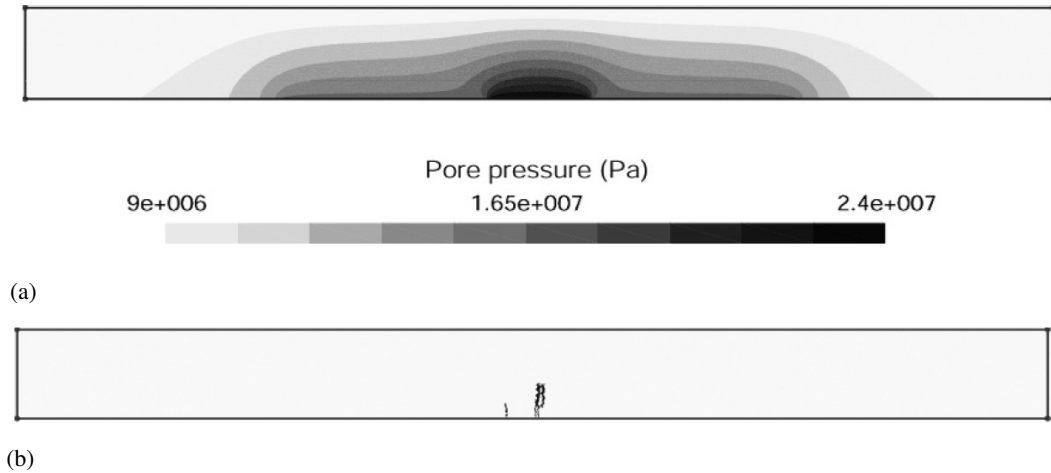


Figure 2.18: Pore pressure distribution (a) in Pa, and initiated crack network (b) in the caprock, when  $p_i = 2.4p_0$  [Seyedi *et al.*, 2013].

The Weibull modulus  $m$  describes the heterogeneity of the studied material. A higher value of  $m$  corresponds to a less heterogeneous material. The effect of  $m$  on the fracturing pressure of the studied caprock is investigated through a set of parametric calculations. Four typical values for  $m$  are considered, namely,  $m = 3, 6, 9$  and  $12$ . Figure 2.20 shows different crack networks obtained for four calculations. The results show that cracks can be initiated in a larger zone for more heterogeneous



Figure 2.19: Zoom on the formed crack network, dark gray elements show the initiation points, black elements propagation line and light gray elements crack tips [Seyedi *et al.*, 2013].

caprocks (i.e., small values of  $m$ ). Furthermore, the sustainable over-pressure decreases slightly for more heterogeneous rocks as the first cracks are initiated earlier. It seems that in this particular case, the heterogeneity of the effective stress field attenuates the effects of material heterogeneity. It is worth noting that the parametric study is performed for different values of  $m$  while  $\sigma_0$  and  $\lambda_0$  remained constant.

All presented simulations were stopped when the first crack network was formed as the main goal was to estimate the sustainable injection pressure for a given site. No damage–permeability relationship was used. However, the non-local model calculates correctly crack openings, which can be then used to estimate the crack hydraulic conductivity and so to calculate the equivalent permeability of the damaged elements.

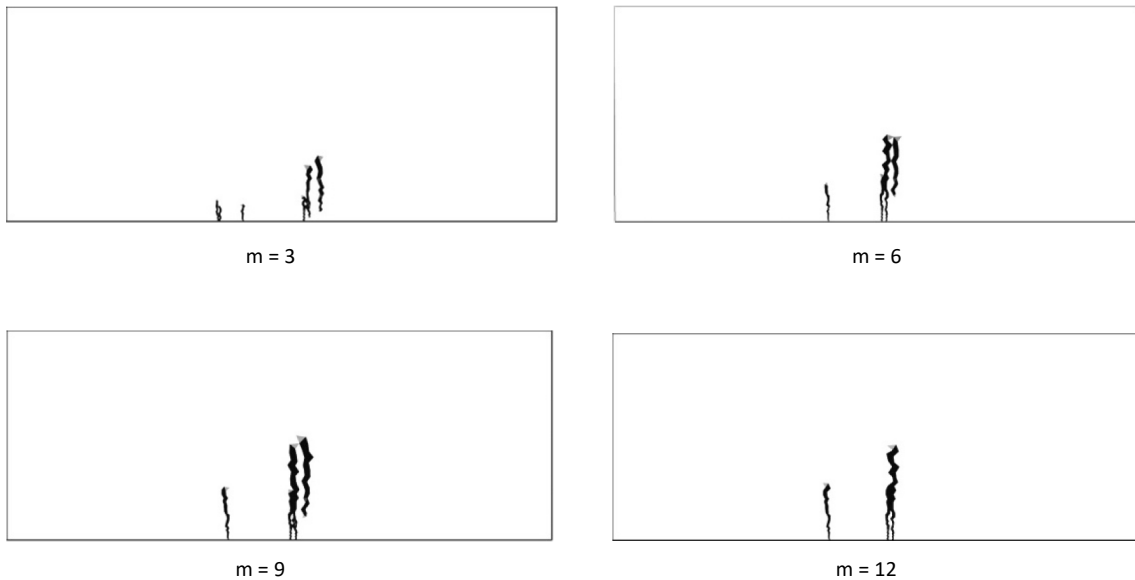


Figure 2.20: Patterns of induced crack network for different values of  $m$  [Seyedi *et al.*, 2013].

## 2.4 Outlook

The presented fracturing model can be extended to account for more features. For instance three major perspectives can be mentioned. The first one concerns the thermal effects. The second one is about the hydromechanical couplings by accounting for permeability change due to fracturing. The last one is extending the model to anisotropic media.

It is generally accepted that thermal effects may be decoupled from hydraulics and mechanical processes especially when dealing with low-permeable porous media. Heat transfer is essentially controlled by conduction and the role of convection is negligible in such media. The extension of the developed HM scheme to account for thermal effects is thus rather straightforward and may be handled via external coupling schemes. In cases where convection must be taken into account, well-established thermo-hydraulic simulators (e.g., TH modules of code-aster) can be used without any particular effort.

Concerning the hydromechanical coupling, the developed non-local model calculates crack openings [Guy *et al.*, 2012]. Only one macro-crack initiates and propagates through each element. Knowing the crack opening in each element, additional permeability due to the presence of a crack can be calculated for each damaged element by using a cubic law [Olivella and Alonso, 2008]

$$K_D \cong K_{int} + \frac{b_f^3}{12a_f} \quad (2.27)$$

where  $K_D$  is the equivalent permeability of a damaged element,  $K_{int}$  the reference intrinsic permeability of the rock matrix,  $b_f$  the crack opening displacement, and  $a_f$  the width associated with each fracture (i.e., the element width). It is worth noting that taking into account mechanical effects on flow simulation and the use of a damage-permeability relationship may influence the results in terms of sustainable pressure and the pattern of crack network.

The third point concerns accounting for mechanical anisotropy on crack initiation and propagation. A first step may be considering the elastic (stiffness) anisotropy. One may expect this effect to influence the direction of crack propagation.

The model can be also extend to account for fracture toughness anisotropy or even a heterogeneous fracture toughness field. Rigorous experimental investigations are necessary to identify the fracture toughness of the material in different directions. SB tests seem to be good candidates in this view. However, regarding the scatter of experimental results, and knowing that initial flaws and material heterogeneities control the fracture toughness of brittle materials, using a heterogeneous toughness field combined with elastic anisotropy seems to be a more appropriate way.



## Chapter 3

# Seismic fragility of structures

This chapter presents parts of my research activities during my time at BRGM (2004-2012) within 2 ANR-funded (VEDA and EVSIM) and 2 EU-funded (PER-PETUATE and MATRIX) collaborative projects. The content of the chapter is a collection of excerpts from the following papers:

- Seyedi D.M., Gehl P., Douglas J., Davenne L., Mezher N., Ghavamian S. (2010) Development of seismic fragility surfaces for reinforced concrete buildings by means of nonlinear time-history analysis, *Earthquake Engineering and Structural Dynamics*, **39**, pp. 91-108.
- Gehl P., Seyedi D.M., Douglas J. (2013) Vector-valued fragility functions for seismic risk evaluation, *Bulletin of Earthquake Engineering*, **11**, pp. 365-384.
- Negulescu C., Ulrich T., Baills A., Seyedi D.M. (2014) Fragility curves for masonry structures submitted to permanent ground displacements and earthquakes, *Natural Hazards*, **74**, pp. 1461-1474.
- Réveillère A., Gehl P., Seyedi D., Modaressi H. (2012) Development of seismic fragility curves for mainshock-damaged reinforced-concrete structures. 15<sup>th</sup> World Conference on Earthquake Engineering, Lisbon, Portugal, p. 999 hal-00742861.

## List of abbreviations

DLS	Damage Limite State
EDP	Engineering Demand Parameter
GMPE	Ground-Motion Prediction Equations
HCF	High Cycle Fatigue
IM	Intensity Measure
ISDR	Inter-Story Drift Ratio
LS	Least squares
MDF	Multi-Degree-of-Freedom
MLE	Maximum-Likelihood
PGA	Peak Ground Acceleration
PGD	Peak Ground Displacement
PGV	Peak Ground Velocity
ROC	Receiver Operating Characteristics
RVE	Representative Volume Element
SD	Spectral Displacement
SSE	Sum-of-Squared Errors
ULS	Ultimate Limit-State
VPSHA	Vector-Valued Probabilistic Seismic Hazard Analysis
URM	Unreinforced Masonry

### 3.1 Introduction

Accurate earthquake risk evaluation requires a correct estimation of seismic hazard and a good evaluation of seismic vulnerability of structures through appropriate earthquake damage models. The earthquake shaking should be expressed in terms of a number of accessible and relevant parameters for use in vulnerability analyses.

Extensive studies in the USA (e.g. HAZUS framework [FEMA, 1999]) and in Europe (e.g. RISK-UE [Mouroux and Brun, 2006]) have produced efficient approaches for vulnerability assessments. Such procedures consist in finding the expected damage level induced in each kind of element at risk for a given hazard level. Depending on the size of the considered area and the importance of the element at risk the method may be statistical (semi-empirical vulnerability functions), based on simplified structural models or methods of analysis/assessment, or through direct time-history nonlinear computations.

Analytical vulnerability curves adopt damage distributions simulated from the analysis of structural models under increasing earthquake loads [Rossetto and Elnashai, 2005]. A variety of procedures have been followed, ranging from elastic analyses of equivalent single-degree-of-freedom systems, adaptive pushover analyses of multistory models to nonlinear time-history analyses of 3D models of structures. The choices made for the analysis method, structural idealization, seismic hazard characterization

and damage models strongly influence the derived curves and have been seen to induce significant discrepancies in seismic risk assessments made by different groups for the same location, structure type and seismicity [Strasser *et al.*, 2008].

Seismic fragility analyses are inherently probabilistic as each of their constituents (e.g. hazard level, material properties, structural model and limit-state definition) is uncertain. The uncertainties can be split into two categories: aleatory (variability), which are inherently random, and epistemic, which are consequences of lack of knowledge. Most engineering applications are affected by both types of uncertainties. Although some researchers suggest that a clear distinction must be made between them [e.g. Paté-Cornell, 1996], it is often difficult to determine whether an uncertainty is random or epistemic from a modeling point of view [Kiureghian and Ditlevsen, 2009]. Practically speaking, this distinction is rather a choice of the modeler. Separating the uncertainties into these two categories helps to determine which ones can be reduced [Kiureghian and Ditlevsen, 2009].

Two main sources of uncertainty, namely the variability in the ground motion and mechanical properties of the target building are considered in the following. A literature review shows several attempts at taking into account this random character on seismic response. Among others, Kwon and Elnashai [2006] investigated the effects of strong-motion variability and random structural parameters on vulnerability curves of a reinforced concrete (RC) building and they concluded that the effect of strong-motion variability is much more important than the randomness in material parameters. Masonry constructions exhibit more variability in their mechanical properties compared to RC and steel frame structures. It is thus expected that such ranking obtained for RC or steel structures cannot be directly applied to masonry constructions.

On the other hand, a considerable source of epistemic uncertainty in seismic risk analyses occurs in the construction of fragility curves. A fragility curve, by definition, represents the conditional probability of reaching a given damage state for a given hazard level characterized by one intensity measure (IM, also known as ground-motion parameter). The standard method to develop fragility curves neglects the uncertainty in the estimated damage caused by the use of a single IM, which cannot represent all characteristics of a ground motion. Some efforts have been made to model the effect of several IMs on structural damage. Baker and Cornell [2005] proposed a vector-based IM made of two parameters: spectral acceleration (SA) and epsilon, which is defined as the difference between the logarithms of observed SA and predicted SA at a given period. They showed that considering two IMs instead of one can improve the collapse probability calculation for a multi-degree-of-freedom (MDF) structure. Kafali and Grigoriu [2007] used an alternative IM expressed by two parameters: earthquake magnitude and source-to-site distance. Rajeev *et al.* [2007] used SA at the first ( $T_1$ ) and second eigenperiods ( $T_2$ ) of the structure as IMs. With reference to an RC-frame structure, the accuracy of prediction of the seismic risk using the considered vector IM versus a conventional scalar IM is presented. The authors showed that an effective choice of  $T_2$  leads to a better estimate of the seismic risk than that obtained employing a scalar IM consisting of SA at  $T_1$  only, while reducing the associated dispersion in the estimate. However, for the studied structure, the reduction is negligible in light of the effort required in switching from a scalar to a vector IM. Koutsourelakis [2010] introduced

a Bayesian framework to derive vector-valued fragility functions from limited available data. The author used a statistical-learning model based on logistic regression to assess the relative importance of different IMs: peak ground acceleration (PGA), root-mean-squared (RMS) intensity, Arias intensity and the power of the excitation spectrum at a period close to that of the structure.

Although previous researchers have shown that using more than one strong-motion intensity parameter may lead to a better prediction of damage, very few have gone the extra step to develop fragility functions for various damage states explicitly involving more than one parameter and those studies that have, are limited due to their use of simplistic structural models (e.g. single-degree-of-freedom systems), ground motions (e.g. stochastic time-histories) and/or damage levels (e.g. collapse or non-collapse).

Within the framework of two ANR<sup>1</sup> funded projects (VEDA ANR-CATTEL-2005 and EVSIM ANR-PGCU-2008), we developed a methodology based on non-linear numerical analyses and statistical techniques to build fragility surfaces and vector-valued fragility functions. This methodology was then extended to account for multi-hazard risks (permanent settlement and seismic hazard for historical monuments during FP7 PERPETUATE project) and after-shock damages (FP7 MATRIX project).

A complete framework is proposed in the present chapter to develop multi-parameter fragility functions characterizing the physical vulnerability of buildings against earthquakes. These functions may be presented as fragility surfaces or vector-valued fragility curves. Stochastic approaches based on the results of several hundred nonlinear time-history analyses are proposed.

## 3.2 Fragility surfaces

The main goal is to reduce the uncertainty of seismic risk estimations by representing the seismic hazard by two IMs. The fragility curves thus become fragility surfaces. First, the representation of the strong ground motion was improved by introducing the fragility surface concept in risk assessments for current reinforced concrete structures through nonlinear time-history analysis of MDF systems. The selected IMs should be poorly correlated for efficient characterization of the shaking. On the contrary, structural damage must be correlated to the selected parameters. The damage level of a typical reinforced concrete structure was evaluated via nonlinear numerical calculations. By considering the parts of the structure that would suffer significant damage during strong ground motions (plastic hinges), an adequate 3D nonlinear robust-yet-simplified finite element model is created to allow for numerous computations. The maximum inter-story drift ratio was used to define the damage level of the studied structure. The relationships between various IMs and the computed damage were compared. Such a study can help to find a small number of ground-motion parameters that lead to, when used together to characterize the shaking, the smallest scatter in the estimated damage. Fragility surfaces were then proposed for the studied structure.

---

<sup>1</sup>The French National Research Agency

### 3.2.1 Structural model and analysis

The model structure was defined based on an existing building constructed in the 1970s. This is an eight-story regular frame reinforced concrete (RC) structure as shown in Figure 3.1. The structural system of the building mainly consists of parallel shear walls in the  $Y$  direction, and RC beam-columns frames in the  $X$  direction. The main purpose of the structural model developed for this study was not to account in detail for all mechanisms of degradation that the structure could suffer during severe ground motions but rather to develop a realistic model to be able to conduct many nonlinear calculations to demonstrate the fragility surface concept. Therefore, the modeled structure was simplified based on several considerations. Induced damage was assumed to be concentrated at the ends of beams and columns. The failure mode is of a plastic-hinge type [e.g. Marante and Flórez-López, 2003]. The used model does not account for phenomena such as concrete crushing or steel rebar buckling. Once the concept of fragility surfaces is demonstrated and methods for their construction are refined, the structural model may be enriched to account for degradation mechanisms such as shear failure, rebar buckling, concrete cover spalling, axial force-moment interaction, cyclic fatigue and steel rebar debonding.

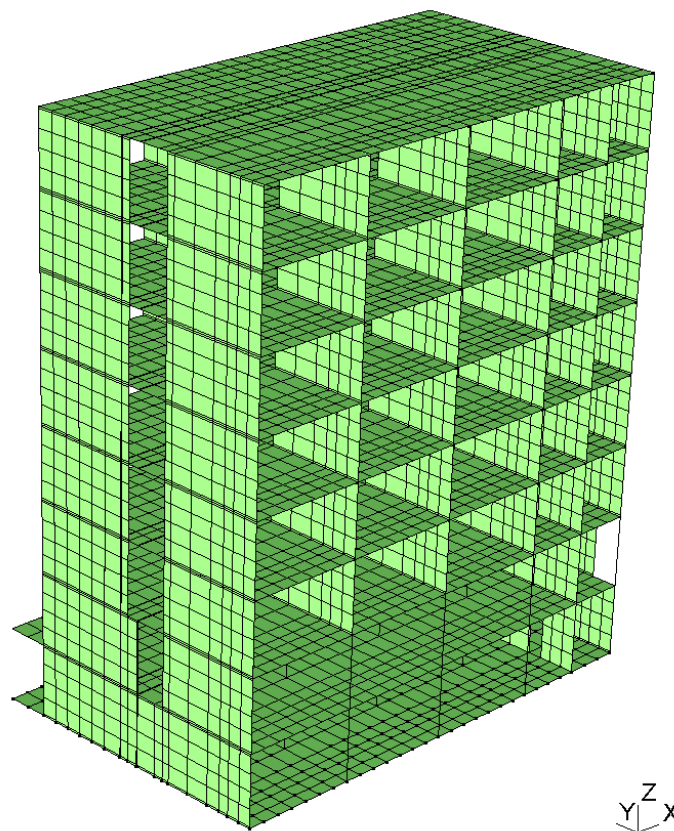


Figure 3.1: Finite element mesh of the studied building [Seyedi *et al.*, 2010]

Observations made of buildings that have suffered damage during past earthquakes show that

well-designed frame structures exhibit nonlinearities mainly through the creation of plastic hinges at the ends of beams and columns. Assuming that the chosen building would behave similarly, and seeking an efficient model, discrete finite elements were placed at the ends of all beams and columns to allow for the creation of plastic hinges. The main features of the material model used to describe the behavior of these plastic hinges are: maximum moment capacity, isotropic strain hardening and inelastic rotation (energy dissipation) [Seyedi *et al.*, 2010]. The response of the model to cyclic loading is shown in Figure 3.2.

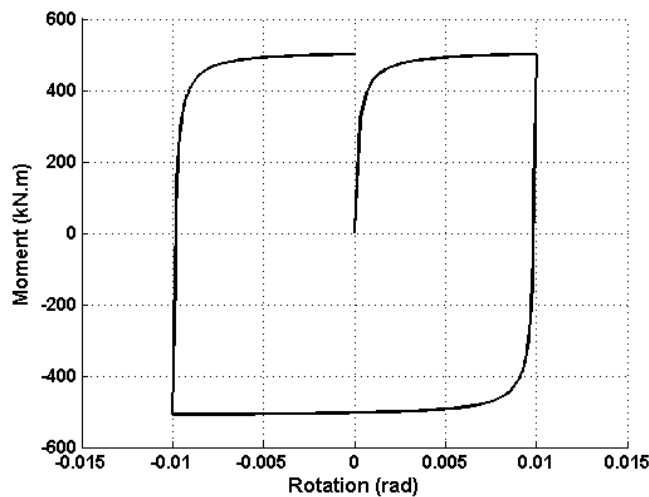


Figure 3.2: Nonlinear behavior of the discrete models used to represent the formation of plastic hinges [Seyedi *et al.*, 2010]

### 3.2.2 Selection of input time-histories

For the study summarized herein we have paid attention to the selection of time-histories that are appropriate for the seismic hazard of the region of interest and also provide an appropriate range of motions so that the possible variation in structural response is not underestimated. It is assumed that the analyzed structure is located in the French Antilles (Guadeloupe and Martinique), which is a region affected by both crustal and subduction (interface: shallow-dipping thrust events, and intraslab: deep, generally normal-faulting, events) earthquakes. Therefore, a set of strong-motion records were compiled that is consistent with the seismicity of this region. A magnitude-distance-earthquake-type filter was applied to a large database of strong-motion records from various regions of the world (mainly the Mediterranean region, the Middle East, western North America, central America, Japan and Taiwan) to exclude records from magnitudes and distances that were not possible for the French Antilles. This led to a preliminary selection of many hundreds of strong-motion records.

Due to the long run times of the finite element analyses of the structural response it was necessary to optimize the number of selected accelerograms. A minimum number of accelerograms covering the range of ground motions that could be experienced in the region of interest had to be selected. Only

those natural accelerograms with ground-motion characteristics that covered useful ranges of possible motions were selected. The input time-history dataset was augmented with records simulated using non-stationary stochastic method [Pousse *et al.*, 2006] to cover the whole range of possible motions. In total, 571 synthetic accelerograms were used in addition to the 169 natural records previously selected. An advantage of using these simulated ground motions over natural accelerograms is that the structural modeling was faster due to the generally shorter length of the records.

### 3.2.3 Selection of strong-motion parameters

A small number of ground-motion parameters must be chosen that lead to, when used together to characterize the shaking, the smallest scatter in estimated damage, computed using the structural model. Orthogonal parameters are sought that characterize different aspects of the shaking, e.g. amplitude, frequency content and duration, so that the fewest number of parameters is needed. A trade off needs to be found between introducing more parameters, thereby leading to a reduction in scatter in the fragility curve, and the uncertainty in the estimation of these parameters for given earthquake scenarios. The parameter chosen to represent ground motion in the construction of vulnerability curves must be both representative of damage potential of earthquakes and easily quantifiable from knowledge of the earthquake characteristics. In this study, we selected several strong-motion intensity parameters that can be well estimated through ground-motion prediction equations (GMPEs) and that are likely to have a strong influence on the building response. The plastic hinge model used in this study does not take into account any phenomena like fatigue that depend on the number of cycles. Therefore, it is more suitable to evaluate the damage level by measuring peak displacements of structural elements during the simulation. The inter-story drift ratio (ISDR), i.e. the relative peak displacement between two consecutive floors, is a widely-used indicator to measure the behavior of structures. ISDR was evaluated at each story and the highest value was kept to give an overall idea of the building damage level. The 740 selected accelerograms discussed in the previous section were used to run nonlinear structural analyses.

A statistical analysis was performed to measure the correlation between the structural response and selected IMs. As expected, the parameters related to the relative duration of the signal or the number of cycles did not have any influence on the building response. Conversely, spectral displacements at the natural structural periods are strongly correlated with the ISDR as shown in Figure 3.3. The choice of the periods at which the spectral displacements (SD) were examined was guided by eigenvalue analysis of the modeled building. The two main eigenperiods along the  $X$  direction (the direction where the seismic input was applied) were found to be 1.26 and 0.41 s and, hence, SDs at these two periods were considered as IMs.

Many input time-histories are required to construct reliable fragility surfaces. Considering a graph with the two selected strong-motion IMs on the two axes, the chosen time-histories should cover in a homogeneous manner the dataspace of possible motions. This is not really true for the two selected parameters (Figure 3.4). Yet these two parameters are sufficiently uncorrelated to be used to build a

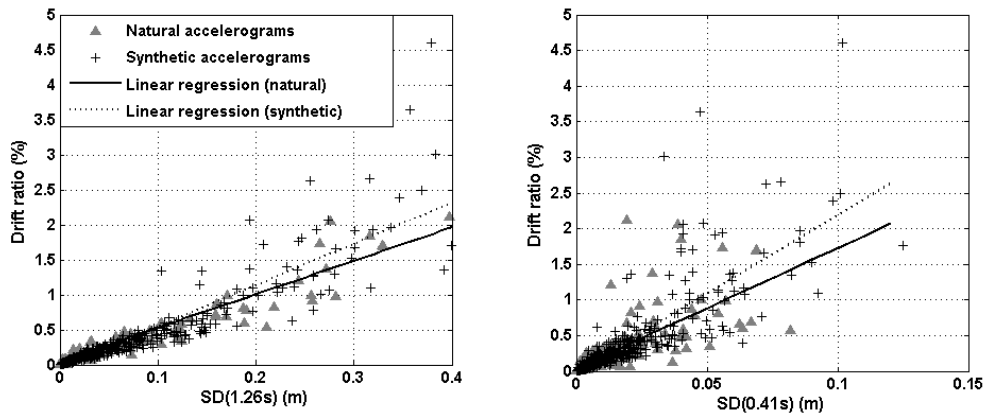


Figure 3.3: Linear regression between spectral displacements at the first two natural structural periods and inter-storey drift ratio. Black squares (and solid lines) refer to natural accelerograms whereas gray triangles (and dashed lines) are from synthetic records [Seyedi *et al.*, 2010]

fragility surface, e.g. for an SD(1.26s) of 0.01m, Figure 3.4 shows that SD(0.41s) ranged between roughly  $6 \cdot 10^{-6}$ m and 0.02m. Only some extreme situations (i.e. low SD(1.26s) and very high SD(0.41s) and vice versa) are not represented. These situations are not, in fact, realistic for earthquake shaking.

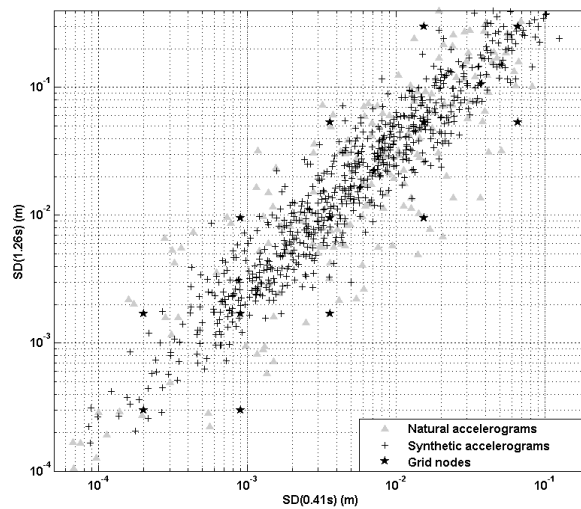


Figure 3.4: Distribution of selected time-histories in SD(0.41s)- SD(1.26s) space. The crosses (and the gray triangles) represent synthetic (and natural) accelerograms respectively. The stars denote the nodes of the grid (i.e. the points in the neighborhood of which the damage probability was evaluated) [Seyedi *et al.*, 2010]

### 3.2.4 Construction of fragility surfaces

The first step for constructing fragility functions is to define target damage states. Based on thousands of observations Rossetto and Elnashai [2003] developed empirical functions that correlate ISDR and

damage level for different types of European RC buildings. Depending on the type of RC structure, relations convert ISDR into a homogenized reinforced concrete damage index ( $DI_{HRC}$ ), which can then be linked to the EMS-98 [Grunthal, 1998] damage scale. Table 3.1 represents the relationships proposed by Rossetto and Elnashai [2003]. The correlation between  $DI_{HRC}$  and the EMS-98 damage level is shown in Table 3.2 [Rossetto and Elnashai, 2003]. Given the model of the studied structure the relationship for non-ductile moment-resisting frames was used to estimate the damage level of the structure based on the ISDR.

Table 3.1: Relationships between inter-story drift ratio (ISDR) and  $DI_{HRC}$  [Rossetto and Elnashai, 2003]

Structural system	Proposed relationship	$R^2$
Non-ductile moment-resisting frames	$DI_{HRC} = 34.89 \ln(\text{ISDR}) + 39.39$	0.991
In-filled frames	$DI_{HRC} = 22.49 \ln(\text{ISDR}) + 66.88$	0.822
Shear-wall systems	$DI_{HRC} = 39.31 \ln(\text{ISDR}) + 52.98$	0.985
General structures	$DI_{HRC} = 27.89 \ln(\text{ISDR}) + 56.36$	0.760

Table 3.2: Correlation between damage index  $DI_{HRC}$  and EMS 98 damage level [Rossetto and Elnashai, 2003]

$DI_{HRC}$ value	EMS 98 damage level	Description
DI < 0	D0	No damage
0 < DI < 30	D1	Negligible to slight damage
30 < DI < 50	D2	Moderate damage
50 < DI < 70	D3	Extensive damage
70 < DI < 100	D4	Very heavy damage
DI > 100	D5	Collapse

For the two chosen strong-motion intensity parameters (here, SD(T1) and SD(T2), T1 and T2 being the first (1.26s) and second (0.41s) natural periods of the building) 25 couples (nodes) of coordinates  $(x_i, y_i)$  have been selected so as to cover the space defined by the parameters  $x$  and  $y$ , where  $x$  and  $y$  are SD(0.41s) and SD(1.26s), respectively (see Figure 3.4). For each of the 740 accelerograms used in the simulations, the closest nodes  $(x_i, y_i)$  were sought on the grid. To avoid bias due to differently-scaled parameters the distances between recorded SDs and the nodes were first normalized. For each node, the probability of exceeding the damage level  $D_k$  was evaluated using as follows

$$P(d > D_k | (x_i, y_i)) = N(D_k, (x_i, y_i)) / N_{tot}(x_i, y_i) \quad (3.1)$$

where  $N_{tot}(x_i, y_i)$  is the number of points that are closest to the node  $(x_i, y_i)$ .

This approach enabled us to obtain 25 probability values for each damage level  $D_k$  and then the fragility surfaces was built using an appropriate interpolation technique. Figure 3.5 shows the calculated fragility surfaces for four different damage levels: D1 to D4. Each surface represents

the conditional probability of reaching or exceeding  $D_k$  damage state "k" for each given value of parameters SD(1.26s) and SD(0.41s).

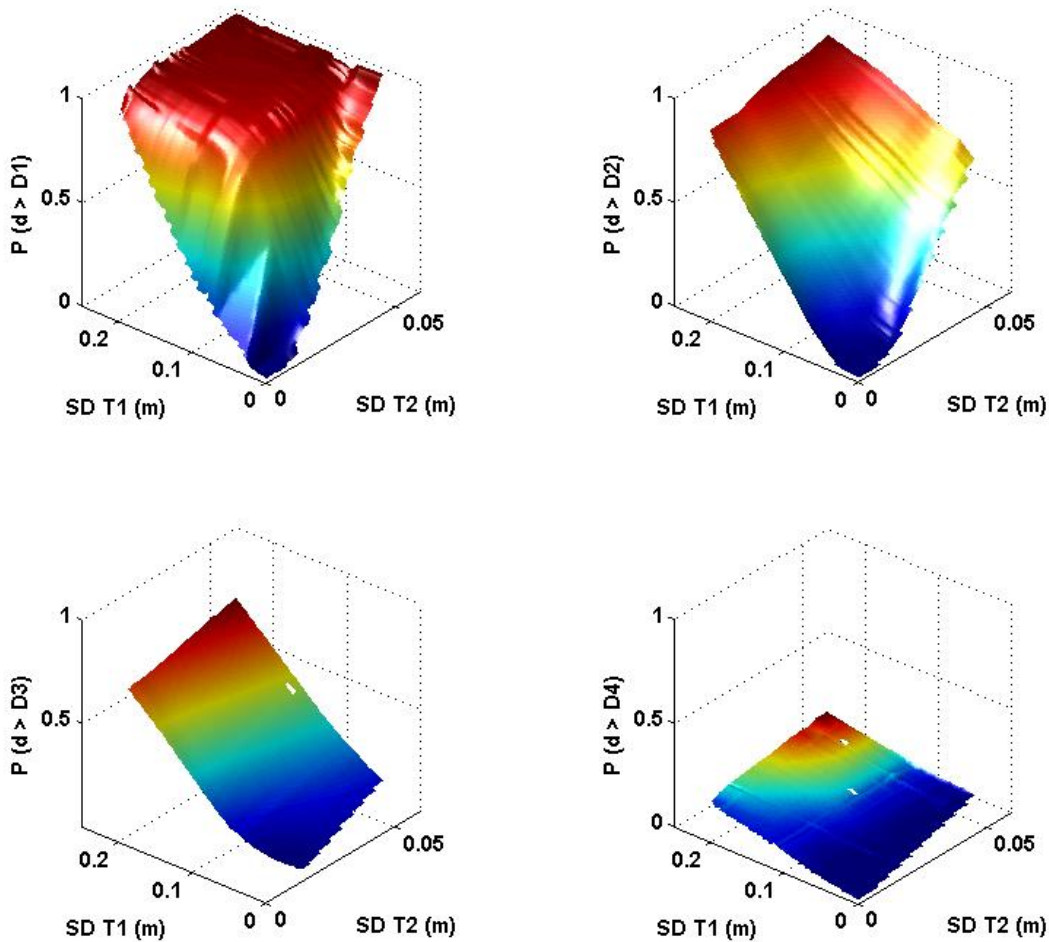


Figure 3.5: Fragility surfaces of the studied building for four damage levels (based on EMS 98). The parameters are spectral displacements at T1 and T2, the periods corresponding to the main eigenmodes of the building in the X direction [Seyedi *et al.*, 2010].

These surfaces can be visualized as fragility curves by projecting the surfaces onto the SD(1.26s) or SD(0.41s) planes (Figure 3.6). These figures demonstrate the wide variation that may exist between fragility curves based on only one strong-motion intensity parameter. Considering only one intensity measure parameter, e.g. SD(T1), an average curve was built, which does not incorporate the variability in ground motions as measured by another parameter, e.g. SD(T2). It is seen (Figure 3.6) that there is a discrepancy of up to 50% between two curves (probability of 30% for SD(T2)=0.015 m and 80% for SD(T2)=0.05 m for an SD(T1) of 0.05m).

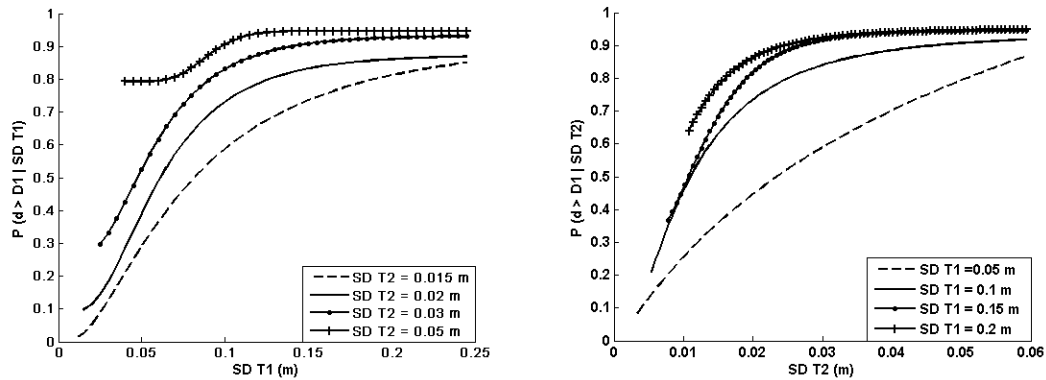


Figure 3.6: Fragility curves with spectral displacement at period T1 (left) and T2 (right). The curves are plotted as “slices” of the fragility surface for different values of SD(T2) (left) and SD(T1) (right). Note that the slices were slightly smoothed and they are only plotted where they are sufficiently constrained by the analysis [Seyedi *et al.*, 2010].

### 3.3 Vector-valued fragility functions

Vector-valued fragility functions were developed to overcome some shortcomings of the fragility surfaces [Gehl *et al.*, 2013]. Presenting multi-variable fragility functions in the form of vector-valued curves renders their use easier than fragility surfaces as the resulting curves are presented in the same format as the standard fragility curves. Moreover, the previous study did not account for uncertainties due to the variability of mechanical properties of structural elements. To overcome this shortcoming, several variants of the structural model were also considered in order to account for variability in its mechanical properties. The developed method mainly relies on the exploitation of numerous nonlinear dynamic analyses because their use, as opposed to pushover curves and response spectra, allows for the study of the influence of many IMs. The developed methodology is presented in the following through its application to an unreinforced masonry building. First, a structural model of the studied building was considered and characterized. Modal analysis was performed to identify dynamic properties of the model. Damage limit states were determined through pushover analysis. Then the model was subjected to many accelerograms that were selected based on the seismotectonic context of the region of interest.

The results enable the study of the effects of many ground-motion characteristics on the building response, using various data mining techniques, such as the variable clustering method, comparison of standard deviations and ROC (Receiver Operating Characteristics) analysis. The performance of single IMs was then compared to combinations of two (or more) IMs, with respect to their ability to reduce the dispersion in fragility functions. Fragility curves, commonly based on a lognormal distribution and a hybrid parameter, were finally represented as a fragility function (or surface) with respect to two IMs. The proposed method is applied here, as an example, to a two-story Unreinforced Masonry (URM) building.

### 3.3.1 Test structure and numerical model

A numerical model was developed based on the results of an experiment at the University of Pavia [Magenes *et al.*, 1995] on a real-scale building. The exact geometry of the real building was considered, while the mechanical properties were either taken from [Magenes *et al.*, 1995] (i.e. shear and compressive strength) or selected from common features of brick masonry and calibrated using the experimental pushover curve. The structure is 6.4 m high, with plan dimensions of  $6 \times 4.4$  m. The mock-up consists in a single-cell building, without any internal walls. The numerical model was built using the TREMURI code [Lagomarsino *et al.*, 2006], which allows a masonry wall to be discretized into several components (vertical elements, named "piers", horizontal ones, named "spandrels", and rigid zones), through an equivalent-frame approach (Figure 3.7). The behavior of the masonry panel was represented by a macroelement developed by Gambarotta and Lagomarsino [1996], and later improved by Penna [2006]. This nonlinear macromodel takes into account the common in-plane damage mechanisms of masonry panels, namely: shear failure (sliding or diagonal cracking) and bending failure (tensile and compressive cracking). The out-of-plane failure mechanism of walls is not taken into account. Even though out-of-plane behavior may play an important role in local damage, this mechanism is commonly neglected when the overall behavior of a structure is being considered [Calderini *et al.*, 2009].

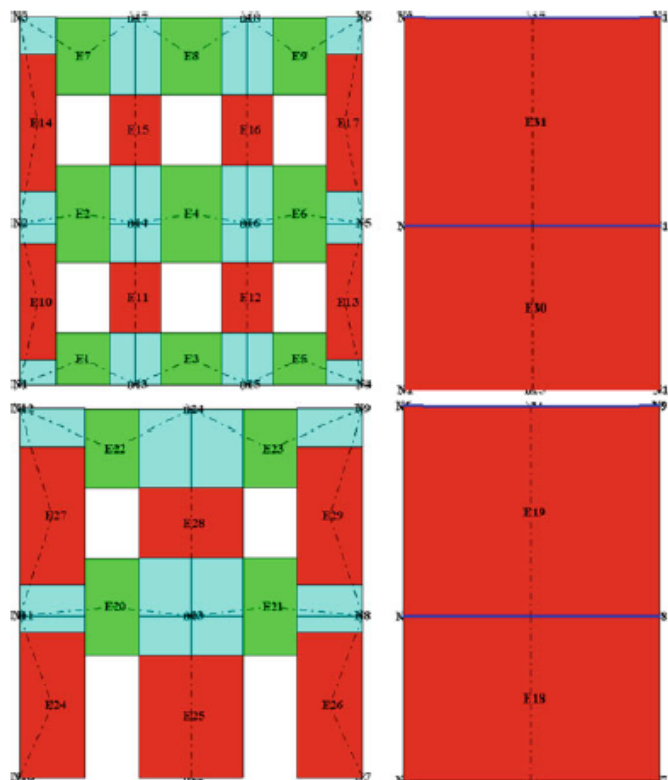


Figure 3.7: Numerical model of the test building [Gehl *et al.*, 2013].

The building tested by Magenes *et al.* [1995] was subjected to cyclic lateral loading on each of the

two façade walls. The façade with the door (referred as "door wall", see Figure 3.7) was disconnected from the transverse walls in the experiment, thus allowing focus on the in-plane mechanism of a masonry panel. The model was therefore calibrated based on the pushover analysis of the same façade (see Figure 3.8(a)). The actual pushover curve for the whole building was also computed using the results from a single wall analysis (Figure 3.8(b)).

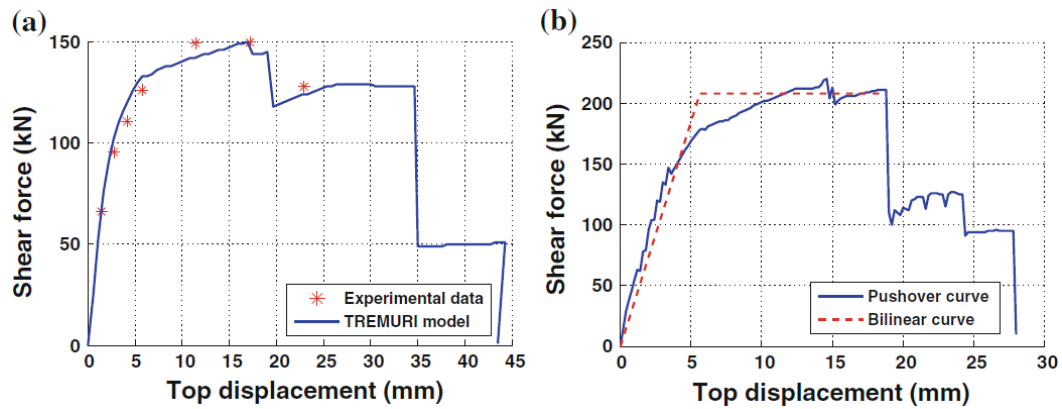


Figure 3.8: (a) Pushover results for a façade wall and comparison between the TREMURI model and experimental data by [Magenes \*et al.\* \[1995\]](#). (b) Modal pushover of the whole building model and corresponding bilinear idealization [[Gehl \*et al.\*, 2013](#)].

Modal analysis of the 3D model gives the first mode along the façade of the building (referred to as the  $X$ -direction), with a period  $T = 0.149$  s. Higher modes along the  $X$ -axis (torsion and opposite-floor displacements) are observed with periods around 0.05 s. Pushover analysis of the building in the  $X$ -direction enabled estimation of the ultimate displacement ( $d_u = 18.8$ ) mm as well as the elastic-limit point ( $d_y = 5.6$  mm for a shear force of 210 kN), using an idealized bilinear curve that was fitted to the actual pushover curve (see Figure 3.8(b)). The bilinear curve was calculated based on Eurocode-8 criteria for the computation of ULS (ultimate limit-state) and DLS (damage limit-state).

The evaluation of damage states for the complete building was not trivial, as the criteria used to define the local damage level of a macroelement could not simply be extrapolated to the global level. Numerous damage indicators are available in the literature. The maximum transient displacement at the top of the structure was used in the following because its evaluation is straightforward and many correlations between floor displacement and damage states were available. [Milutinovic and Trendafiloski \[2003\]](#) proposed relations to link top displacements  $d_y$  and  $d_u$  to the EMS-98 [[Grunthal, 1998](#)] damage scale (Table 3.3). The studied structure has a predominant first mode, which corresponds to a uniform distribution of displacement along the building height. The pushover analysis was carried out with an adaptive scheme based on the first modal shape, thus ensuring that the damage thresholds estimated from the static analysis and based on top displacement were adequate proxies for the floor drifts and a relevant indicator for both local and global damage. Still, it is noted that the choice of a given damage indicator may affect the results (e.g. identification of optimal IMs), as displacement-

based damage measures are strongly correlated with "peak" IMs (e.g. PGA and PGV (Peak Ground Velocity)), whereas energy-based indexes are more influenced by IMs representing the energy content of the signal (e.g. Arias intensity or cyclic damage parameters).

Table 3.3: Correlation between EMS-98 damage states and transient top displacement, for URM buildings, according to Milutinovic and Trendafiloski [2003].

Damage state	Limit-displacement equation	Limit for $d$ (mm)
Slight	$d = 0.7d_y$	3.94
Moderate	$d = 0.7d_y + 0.05(0.9d_u - 0.7d_y)$	4.59
Extensive	$d = 0.7d_y + 0.2(0.9d_u - 0.7d_y)$	6.54
Very heavy	$d = 0.7d_y + 0.5(0.9d_u - 0.7d_y)$	10.43
Collapse	$d = 0.9d_u$	16.92

Once the reference building model was developed, uncertainties in mechanical properties of brick masonry was taken into account by deriving a set of variants with respect to the basic model. These variants were developed by randomly sampling material properties, which were assumed to follow a normal distribution. Twenty variant models were generated out of the parametric distribution. A Latin hypercube sampling scheme was used to capture the possible combinations with a reduced number of models. Thus, with 20 models, intervals of 5% were defined and, for each parameter, an aleatory interval picked to sample the value for a given model. This procedure resulted in a total of 21 structures (one basic model plus 20 variants). For each of them, a pushover analysis was performed to identify the boundaries of the EMS-98 damage states, which are specific to each variant.

### 3.3.2 Nonlinear dynamic analyses

Dynamic analyses of the models required a large set of strong-motion records to build robust fragility functions. A dataset of 777 accelerograms was assembled, using both a sample of records from the European Strong-Motion Database [Ambraseys *et al.*, 2004] and synthetic signals generated using the non-stationary stochastic procedure proposed by Pousse *et al.* [2006]. The records correspond to shallow crustal earthquakes of magnitude ( $M_w$ ) between 4.5 and 6.5 and epicentral distances between 10 and 100 km. The signals also sampled the five Eurocode-8 soil classes to account for local site variability.

The selected accelerograms were then applied at the base of the structure, along the  $X$ -direction. The number of simulations was optimized and the dataset of 777 accelerograms divided into 37 groups of 21 records each. Thus, within each group, it was possible to randomly assign each accelerogram to one of the 21 models. It is worth noting that the 37 groups were selected by ranking all accelerograms with respect to PGA (IM selected *a priori* to represent the "damage potential" of the signal). This ensured that each group contained comparable signals, and as a result it was assumed that all 21 models were subjected to accelerograms with similar intensity levels.

Finally, all nonlinear dynamic analyses were carried out and the maximum transient displacement at the top of the building was used to identify the different damage states, based on Table 3.3. The results showed that EMS-98 intermediate damage states are too narrow. The five damage states were thus merged into only two. Damage states from "slight" to "extensive" were considered as "yield"; the damage states "very heavy" and "collapse" were also merged into one (near-collapse/collapse), as the numerical simulations near the ultimate deformation limits of the macroelements are usually less accurate and there is no benefit in setting a clear boundary between these damage states.

### 3.3.3 Studied IMs

For each of the accelerograms used in the simulations, 50 IMs were calculated, ranging from PGA to cyclic and duration parameters and elastic response spectral ordinates. A variable clustering technique was then performed to rank them according to their cross-correlation [Gehl *et al.*, 2013]. It consists of a succession of principal component analyses and the merging of the parameters with strong correlation into distinct class-variables, called "clusters" reducing many IMs to only three or four less-correlated parameters that are representative of the range of studied IMs.

The efficiency of each IM for the prediction of the damage state (none, yielding or collapse) of the structure must be evaluated. A convenient way of measuring the accuracy of a "predictor" is to perform a Receiver Operating Characteristic (ROC) analysis of the data [e.g. Fawcett, 2003]. For a given IM, a set of data for "model training" (e.g. development of a fragility model based on the chosen IM, which will then be compared to a second dataset in the "validation" phase) was used. The first data set was used to build a fragility curve for a given damage state, based on a lognormal distribution, using the procedure proposed by Shinozuka *et al.* [2000]. Then, using a second set of (validation) data, a confusion matrix was built for different thresholds of damage probabilities. First, for each point  $x_i$ , the damage probability (for instance, yielding or collapse) was evaluated using the previously defined lognormal distribution:  $p_i = P(d_i \geq DS|x_i)$ . Then, for a range of probability thresholds  $p_0$  varying from 0 to 1,  $p_0$  and  $p_i$  were compared: if  $p_i \geq p_0$ , then the predicted damage  $d_i$  was 1, and  $-1$  otherwise. The predicted  $d_i$  were compared to their actual value to assess whether the damage state was accurately estimated or not. Thus, for each value of the threshold  $p_0$ , all data points were classified into four possible combinations, which form the so-called confusion matrix:

- predicted  $d = 1$  and actual  $d = 1$ : true positive or "hits",
- predicted  $d = 1$  and actual  $d = -1$ : false positive or "false alarms",
- predicted  $d = -1$  and actual  $d = 1$ : false negative or "misses",
- predicted  $d = -1$  and actual  $d = -1$ : true negative or "correct rejections".

It can be observed that the most efficient IM will be the one that minimizes both "misses" and "false alarms". Two measures that assess the quality of a prediction model are: sensitivity, which is the ratio of the number of hits to hits and misses, and specificity, which is the ratio of the number of correct rejections to correct rejections plus false alarms. The ROC curve was then constructed by plotting the different values of these ratios obtained for all thresholds  $p_0$ , the vertical axis being the

sensitivity and the horizontal one the complement of specificity (Figure 3.9).

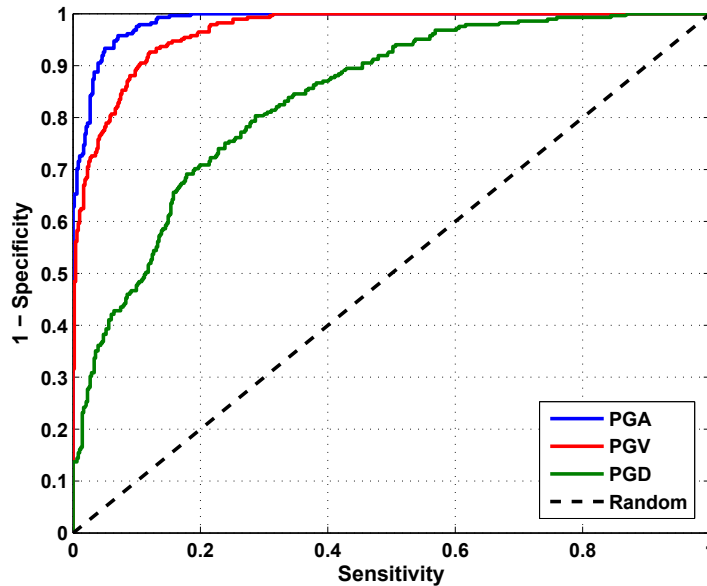


Figure 3.9: Example of ROC curves for three ground-motion parameters for the yield damage state [Gehl *et al.*, 2013].

One way to read these ROC curves is to check if they are close to the  $(0, 1)$  corner, which is the indicator of a satisfactory model. In contrast, the  $45^\circ$  line represents a perfectly random predictor and any ROC curve near that region implies a mediocre prediction model. As a result, whereas the shape of a curve cannot be easily exploited, a commonly-used indicator is the area under the ROC curve (AUC). AUC close to unity denotes an efficient model, whereas values close to 0.5 indicate little advantage over chance. However, it must be kept in mind that AUC is useful in evaluating the global performance of a parameter but two ROC curves may overlap locally.

AUC values were computed for each of the 50 IMs regressed over a lognormal distribution, and for each of the two considered damage states (yielding and collapse), to assess which ones were the most useful in predicting the effect of earthquake shaking for this structure. The results of analysis show that one IM that is the best for both damage states cannot be found. Acceleration-related parameters (e.g. PGA, A95, ARMS, ASI and cyclic damage parameters) and response spectral accelerations at short periods (up to 0.25) were efficient in predicting yielding, whereas, parameters like PGV, PGD (Peak Ground Displacement), absolute durations and spectral accelerations at longer periods were more efficient for the prediction of collapse. It is also worth noting that the two groups of IMs that are emerging from the ROC analysis are more or less the same as the two first clusters identified by the variable clustering analysis performed above. This observation reinforces the idea that a combination of two IMs may improve the prediction of damage, as the first could be useful in predicting slight damage, and the second more efficient for higher damage states.

### 3.3.4 Vector-valued fragility functions

In the previous section, ROC analyses showed that two IMs may lead to more accurate assessment of both yield and collapse. A hybrid IM was, therefore, proposed using a linear combination of IM1 and IM2

$$\log X_i = \frac{\alpha_1}{\alpha_1 + \alpha_2} \log \text{IM1}_i + \frac{\alpha_2}{\alpha_1 + \alpha_2} \log \text{IM2}_i \quad (3.2)$$

where  $\alpha_1$  and  $\alpha_2$  are regression coefficients. This new parameter was considered as a single variable and the probability of reaching or exceeding a given damage state given  $X$  was then expressed via the usual lognormal distribution [Shinozuka *et al.*, 2000]

$$P(\text{damage} \geq DS|X) = \frac{1}{2} \left[ 1 + \operatorname{erf} \left( \frac{\log X - \mu}{\sigma\sqrt{2}} \right) \right] \quad (3.3)$$

where  $\mu$  is the mean,  $\sigma$  the standard deviation,  $DS$  damage state and  $\operatorname{erf}$  is the error function. Then, by expressing  $X$  as a function of IM1 and IM2 and by introducing  $\beta_1 = \frac{\alpha_1}{(\alpha_1 + \alpha_2)\sigma\sqrt{2}}$ ,  $\beta_2 = \frac{\alpha_2}{(\alpha_1 + \alpha_2)\sigma\sqrt{2}}$  and  $\beta_0 = \frac{\mu}{\sigma\sqrt{2}}$ , the following relationship was obtained

$$P(\text{damage} \geq DS|\text{IM1}, \text{IM2}) = \frac{1}{2} [1 + \operatorname{erf}(\beta_1 \log \text{IM1} + \beta_2 \log \text{IM2} - \beta_0)] \quad (3.4)$$

Finally, the coefficients  $\beta_i$  were evaluated through the maximization of the following likelihood function

$$L = \prod_{i=1}^n P_i^{y_i} (1 - P_i)^{1-y_i} \quad (3.5)$$

where  $y_i$  is the so-called binomially distributed variable and equals unity when the damage state is reached, and null otherwise and  $P_i$  is the probability of reaching or exceeding the damage state given  $(\text{IM1}_i, \text{IM2}_i)$ .

Using the relationships presented above, several combinations of IMs were tested and these new fragility models were evaluated through an ROC analysis. Comparing the AUC found for two IMs with those obtained for single-parameter fragility functions shows a general improvement in the prediction of damage states. Also, the standard deviations were reduced for both damage states in comparison to single IM models, thus showing the performance of multivariate fragility functions in terms of uncertainty reduction. It is now possible to accurately predict both damage states (yield and collapse) at the same time, by using a combination of IMs from two clusters. Nonetheless, it is not strictly correct to speak of "hybrid" parameters (e.g. a function of two IMs) because the coefficients in the linear combination are specific to each damage state, depending on the relative influence of each parameter. It is thus preferable to refer to them as vector-valued parameters, whose scalar components can be linearly combined in a regression model.

### 3.3.5 Bivariate fragility functions

The ROC analysis showed that there was a wide choice of adequate couples of IMs to use as variables in fragility functions. Since the couple (PGV, PGA/PGV) was efficient and these two parameters are almost orthogonal (correlation coefficient equal to  $-0.15$ ), they were chosen for the first example fragility surface (see Figure 3.10), using Equation (3.4).

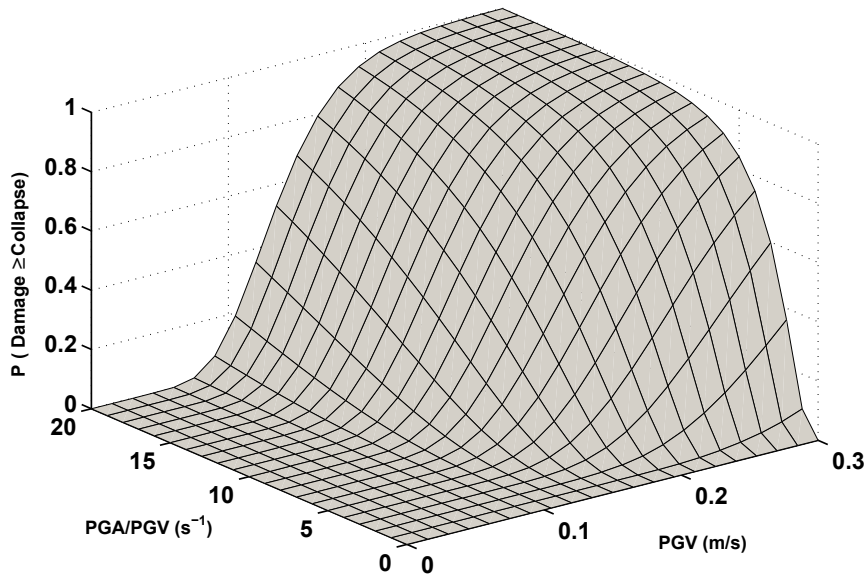


Figure 3.10: Example of a fragility surface for the "Collapse" state, using the couple (PGV, PGA/PGV) as earthquake descriptors [Gehl *et al.*, 2013].

The choice of two parameters that are uncorrelated or almost orthogonal is convenient, as it allows evaluation of the vulnerability on the whole 2D space defined by PGV and PGA/PGV, even in the corners that contain high values of one parameter and low values of the second. To study the effect of the second parameter, single-variable fragility curves were plotted by keeping the second IM constant, and then compared with a fragility curve built by considering only the first parameter (Figure 3.11).

First, it is noticed that the use of a second parameter (here the ratio PGA/PGV) induces a steady increase in the damage probability. For instance, in the case of small PGVs (PGV around 0.05), the single-variable curve shows almost zero probability of damage. However, the fragility surface indicates that if this signal is accompanied by high accelerations (e.g. high PGA/PGV ratios around 20 or 30), then there is actually a non-negligible probability of damage (around 0.25). A crucial observation is that the single-variable curve is flatter than those extracted from surfaces. This confirms that fragility models built with a single IM have a greater scatter than surfaces, and they are associated with higher epistemic uncertainty because earthquake signals are only characterized by a single number.

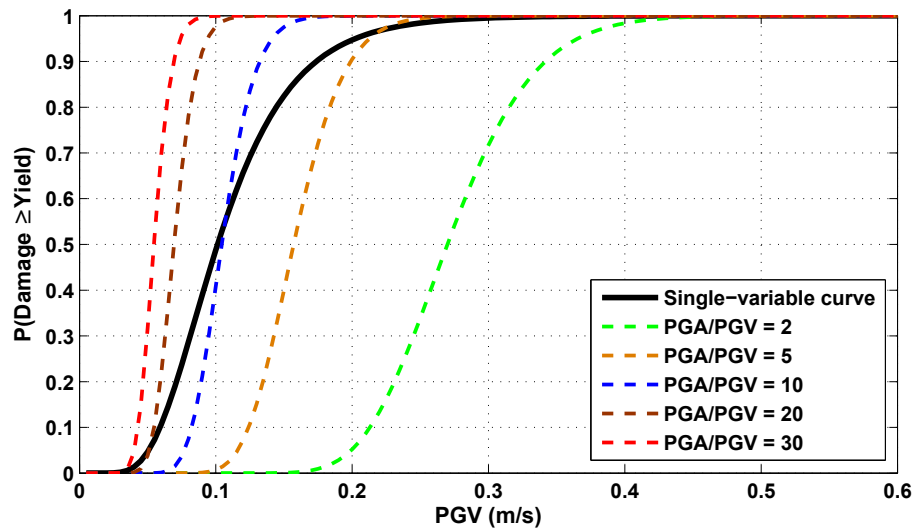


Figure 3.11: Single-variable fragility curve (solid black line) compared to slices of a fragility surface [Gehl *et al.*, 2013].

### 3.4 Extension of the method to multi-hazard risk assessment and damaged structures

Introduction of vector-valued fragility functions or fragility surfaces opens new insights into the multi-hazard vulnerability estimation. In such perspective, the impact of several hazards, i.g., earthquake and fire, permanent settlement and earthquake or the influence of aging or previous damage on the physical vulnerability of structures may be addressed.

#### 3.4.1 Fragility curves for masonry structures subjected to permanent ground displacements and earthquakes

The fragility functions for masonry structures subjected to permanent ground displacements and earthquakes were developed within the FP7-funded PERPETUATE project [Lagomarsino and Cattari, 2015]. Historical structures and old town centers represent an important fragment of existing buildings and a valuable and irreplaceable part of the urban heritage. Many of these old structures present damage due to previous earthquakes or due to changes in the soil conditions. The analysis must be based on the structure as is. Geometrical irregularities, as well as damaged or even missing structural elements must be considered.

A prototype building was first damaged by differential settlements and then subjected to a set of earthquakes with different intensities. When subjected to differential settlements, the deformed shape of structures is no longer symmetrical. Consequently the structure will presumably be more vulnerable to earthquakes. In fact, this geometrical asymmetry will probably have a significant effect

on the distribution and dissipation of seismic loads (EC8 4.2.1.1).

The structure considered in this study was a fictitious 3 stories masonry building reinforced by tie-rods. It was 9 m high and its ground dimensions were  $10 \times 14$  m. The thickness of masonry exterior walls was 60 cm for the two first stories and 40 cm for the third one. The interior walls were thinner: 36 cm for the two first stories and 24 cm for the third one. Floors were modeled by 5 cm thick elastic membrane element. Tie-rods were reinforcing the structure at every floor level. Since differential settlements were applied, the whole soil-foundation-structure system had to be modeled. A conventional impedance function model taking into consideration the frequency-dependent stiffness and damping of soil was considered. As for the masonry structure presented in the previous section the building was modeled using Tremuri finite element code [Lagomarsino *et al.*, 2006]. Figure 3.12 shows a 2D view of the four exterior walls of the structure. In the planar view of the walls, the red rectangles are masonry elements with pier behavior, the green ones are masonry elements with spandrel behavior and the blue ones are rigid links between the masonry macro-elements.

To obtain a differential settlement pattern, it was assumed that two external walls were subjected to a variable settlement on their length while a zero settlement was considered for the other walls (Figure 3.13). The prescribed differential settlement presented its maximum magnitude in the corner formed by the wall P4 and P1 (Figure 3.13). It is worth noting that in this framework it was assumed that a homogeneous settlement does not induce any damage to the structure. A similar settlement configuration was considered for 5 studied structures with 5 different settlement maximum magnitudes, ranging from 5 to 25 cm, with a constant step of 5 cm. A zero displacement condition was prescribed on the wall P2 and P3. Finally, the settlements for others points of the base of structure were calculated by a bilinear interpolation, as illustrated in Figure 3.13.

A first dataset of ground motion time-histories was gathered by selecting records corresponding to shallow crustal earthquakes (magnitude  $M_w < 7.5$ , focal depth  $h < 30$  km) from the European Strong-Motion Database [Ambraseys *et al.*, 2004] and from the PEER NGA database (Next Generation Attenuations Relationships for Western US project). A further selection was then carried out to reduce the number of records presenting low PGA, which were predominant in the dataset, but were not very useful for quantifying the non-linear dynamic response of the structure. Finally, a dataset of 152 ground motion time-histories was assembled, which were used to carry out the dynamic analysis.

#### 3.4.1.1 Combined static (imposed settlements) and dynamic (time-histories) analyses

The main idea here is to estimate the seismic vulnerability of buildings already suffered from differential settlements, which is quite frequent for historical monuments. By neglecting the effects of differential settlements, the fragility curves obtained for undamaged structures may underestimate the structure vulnerability.

First, the structure was subjected to differential settlements. As an example, damage initiation and growth in wall P4 for a maximum settlement magnitude of 25 cm in the corner of the buildings is represented in Figure 3.14. Once the building was affected by differential settlements, the dynamic

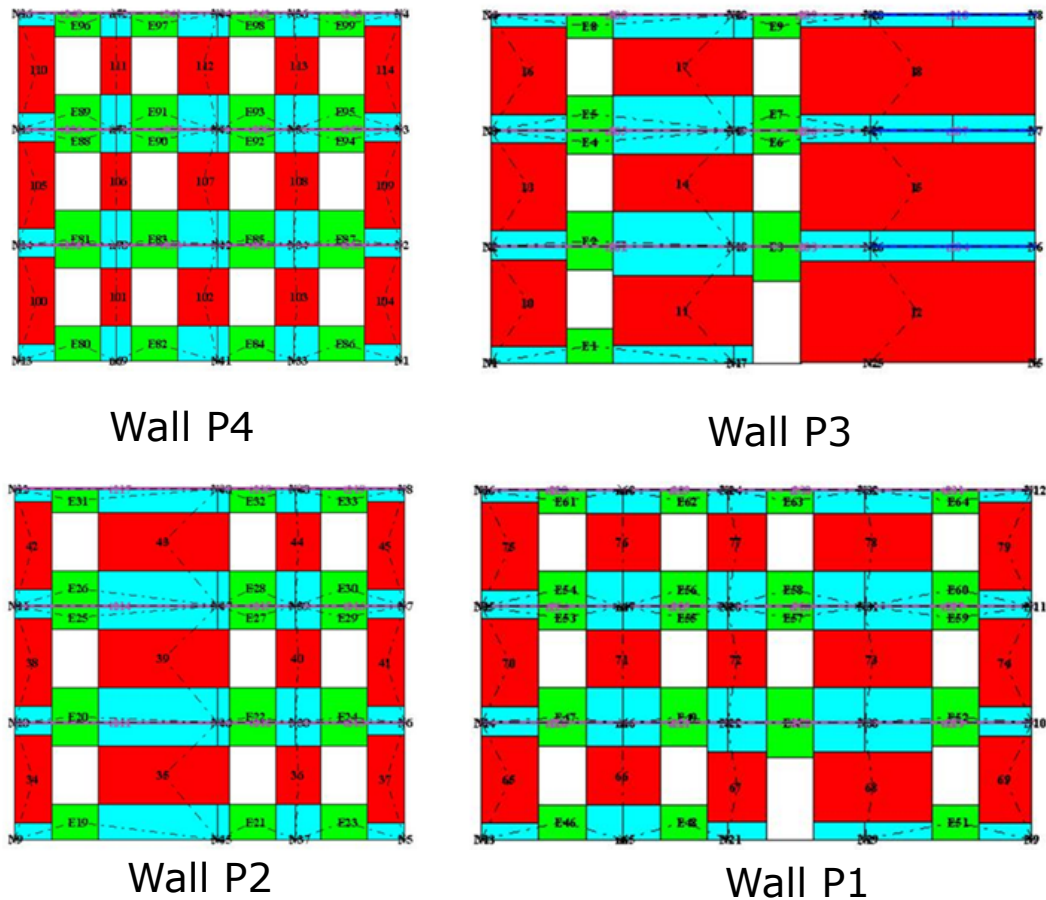


Figure 3.12: Blueprints of the exterior walls of the numerical model. Wall P1 is the façade of the structure. The red rectangles are masonry elements with pier behavior, the green ones are masonry elements with spandrel behavior and the blue ones are rigid links between the masonry macro-elements [Negulescu *et al.*, 2014].

analyses are performed.

The fragility functions were calculated successively for the undamaged structure (without differential settlements) and for the structure already damaged by differential settlements ranging from 5 to 25 cm in the corner of the structure. To obtain these curves, the same set of ground motion records was used, so that the influence of the prescribed settlements could be precisely assessed [Negulescu *et al.*, 2014]. The fragility curves (for damage states 1 and 5) obtained for the intact structure and for the structures previously damaged by settlements are presented in Figure 3.15. At first glance, the curves are relatively similar. Nevertheless, it is observed that the curves corresponding to pre-damaged structures are right shifted compared to those of the intact building. It means that, as expected, pre-damaged structures were more vulnerable to further solicitations.

The results also show that the median of the curves are progressively decreasing when magnitude of differential displacement increases. It is also interesting to note the increase in the standard

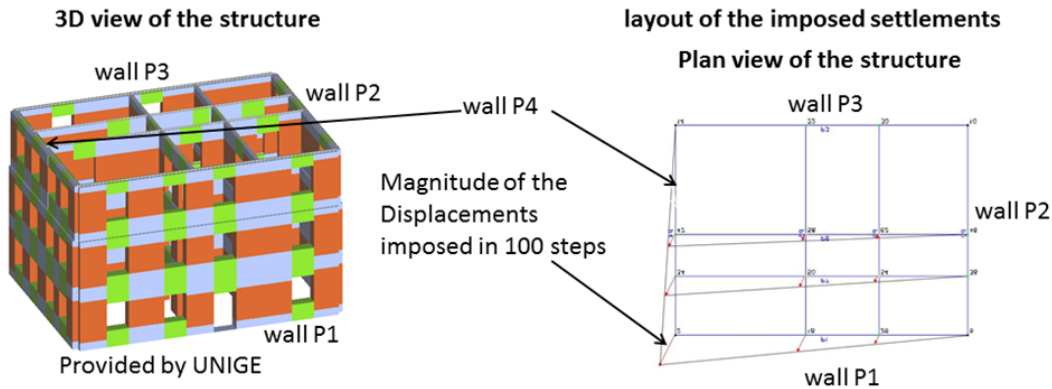


Figure 3.13: 3D view of the structure (left) and layout of the prescribed settlements at the foundation level (right) [Negulescu *et al.*, 2014].

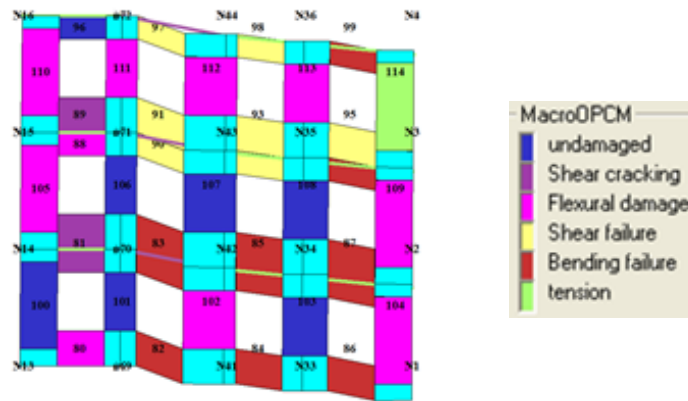


Figure 3.14: Damage initiation and growth in wall P4 for a maximum amplitude of 25 cm. A scaling factor equal to 4 is used [Negulescu *et al.*, 2014].

deviation of curves with the amplitude of prescribed differential settlements. Pre-damaged structures were showing more strongly non-linear responses, subject to larger variability [Negulescu *et al.*, 2014]. It is worth noticing that the structure is well withstanding the differential settlements, the difference between the curves being not as significant as could be anticipated. The resilience of masonry structures to differential settlement is known to be important, particularly because of larger dissipation areas compared with other structures like for example reinforced concrete ones. However, it is observed that the probability of exceeding a given damage state increases with the settlement magnitude.

Considering the initial differential settlement as a second hazard, the obtained results were recast in the form of fragility surfaces [Seyedi *et al.*, 2010], where the probability of exceeding a damage level is calculated as a function of two hazard intensity, namely, PGA and settlement amplitude. In Figure 3.16, the fragility surfaces for LS1 and LS5 are displayed as functions of the two intensity

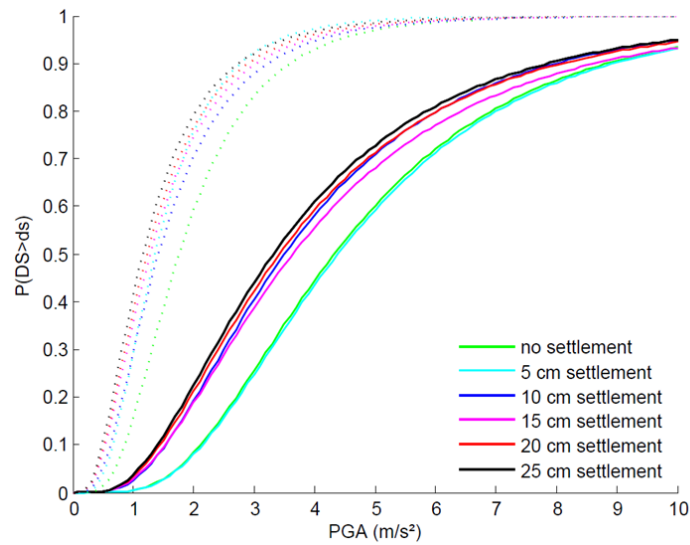


Figure 3.15: Comparison of fragility functions obtained for damage states 1 (dotted lines) and 5 (solid lines). The magnitude of the settlement is represented by the color of the curve [Negulescu *et al.*, 2014].

parameters PGA (in  $m/s^2$ ) and settlements (in cm). Once again, it is observed that the increase in vulnerability of structures with differential settlements is not linear and some threshold effects occur.

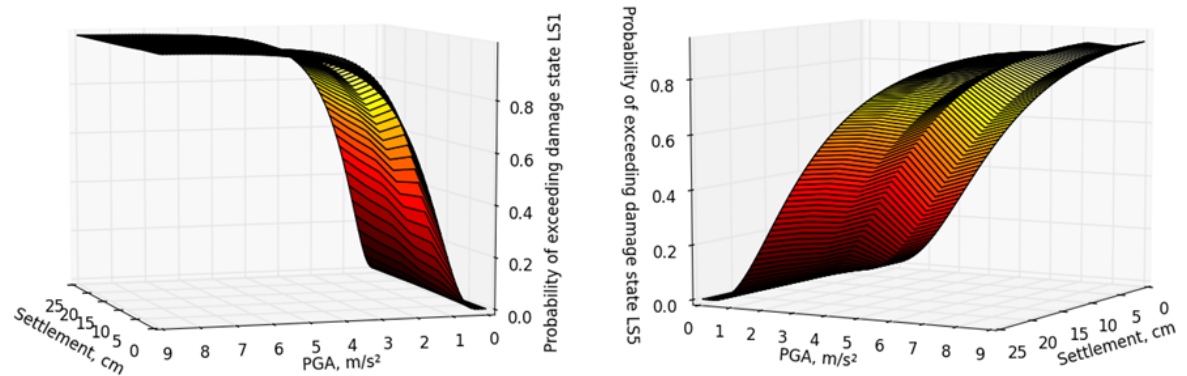


Figure 3.16: Probability of exceeding LS1 (left) and LS5 (right), as functions of the amplitude of differential settlement and of PGA [Negulescu *et al.*, 2014].

### 3.4.2 Fragility curves for damaged structures

Most of the seismic risk assessment tools only consider an initially undamaged structure undergoing one mainshock event. However, structures may be initially damaged from past earthquakes or due to other hazards during their service life. A seismic sequence is commonly made of a mainshock followed

by series of aftershocks. In the post-mainshock context, during which the structure is not repaired, the rate of earthquake occurrence is significantly increased (due to the presence of aftershocks) and the physical vulnerability of possibly mainshock-damaged buildings may also increase. In this context, updated knowledge of the vulnerability of the damaged buildings is of critical importance to accurately assess the associated risk and guide building-occupancy policies after a main seismic event.

### 3.4.2.1 State-dependent fragility functions

A methodology to derive fragility curves for structures that are initially in a given damage state was developed within the European FP7-funded Matrix project [Reveillere *et al.*, 2012]. Contrary to the widely used incremental dynamic analysis, successive dynamic analyses with a set of unscaled natural ground-motion records were performed. Several samples of structures in each damage state, which may differ by their local damage configuration, were generated. The current condition of the structure was represented by its residual drift ratio and the additional transient drift obtained from the next dynamic simulation was used to assess whether the structure reaches another damage state or not.

The performance of the building at time  $t_0$  is by itself a combination of its current Damage State (DS) and of its capacity to withstand future seismic actions. The actual state of the building at  $t_0$  is characterized by the probability of being in one of the  $n$  damage states (defined by an appropriate damage scale):  $P(DS_{t_0} = i; i \in [0, n])$ . For each of these possible initial damages states  $DS_{t_0}$ , the capacity of the building needs to be estimated through state-dependent fragility curves, which give the probability for a structure in state  $DS_{t_0}$  to reach or exceed a given damage state with respect to an IM of a given level  $a$ :  $P(DS \geq k | DS_{t_0} = i, IM = a); k \in [1, n]$ .

Once these components were defined, the initial state of the structural system was described and its fragility to future earthquakes was quantified as follows [Luco *et al.*, 2011]

$$P(DS \geq k | IM = a) = \sum_{i=0}^n P(DS_{t_0} = i) \cdot P(DS \geq k | DS_{t_0} = i, IM = a) \quad (3.6)$$

A methodology for developing DS-dependent fragility functions was proposed using a set of unscaled natural records [Reveillere *et al.*, 2012]. Ground-motions from this set were applied to the structure until each DS was populated with enough outcomes, which may have different local damage configurations. Damaged structures were then used to compute the response to the next ground shaking. The Engineering Demand Parameter (EDP) used in this framework was  $\Delta_{t,max}$  the maximum transient inter-story drift ratio (ISDR), which can be linked to damage state thresholds [Rossetto and Elnashai, 2003]. Moreover, the estimation of ISDR in the dynamic simulations gave access to residual drift. This quantity is noted  $\Delta_{r,t_0} = |\Delta_r(t_0)|$  since it is the value of IDSDR evaluated at time  $t_0$ . In the time-dependent framework, the residual drift is of paramount importance as it represents the updated initial conditions of the structure at  $t_0$ .

The starting point of the study was a single structure in intact state, which was subjected to a set of  $N$  time-histories. This first set of analyses then yielded  $N$  new structures, which were distributed along different DS classes, depending on the recorded value of  $\Delta_{t,max}$ . For each initial damage state,

20 combinations of structures / ground-motion records were sampled based on a Latin Hypercube Sampling procedure. This sampling methodology was applied to the structures ranked based on their initial residual drift, and on the ground-motions ranked according to the intensity measure (IM) of interest (e.g. SA or PGA), in order to optimize the number of simulations required for testing the range of possible combinations of initial drifts and ground motions with no bias. This step was repeated 25 times in order to populate each damage states with enough structures and to obtain a satisfying statistical significance (see Figure 3.17).

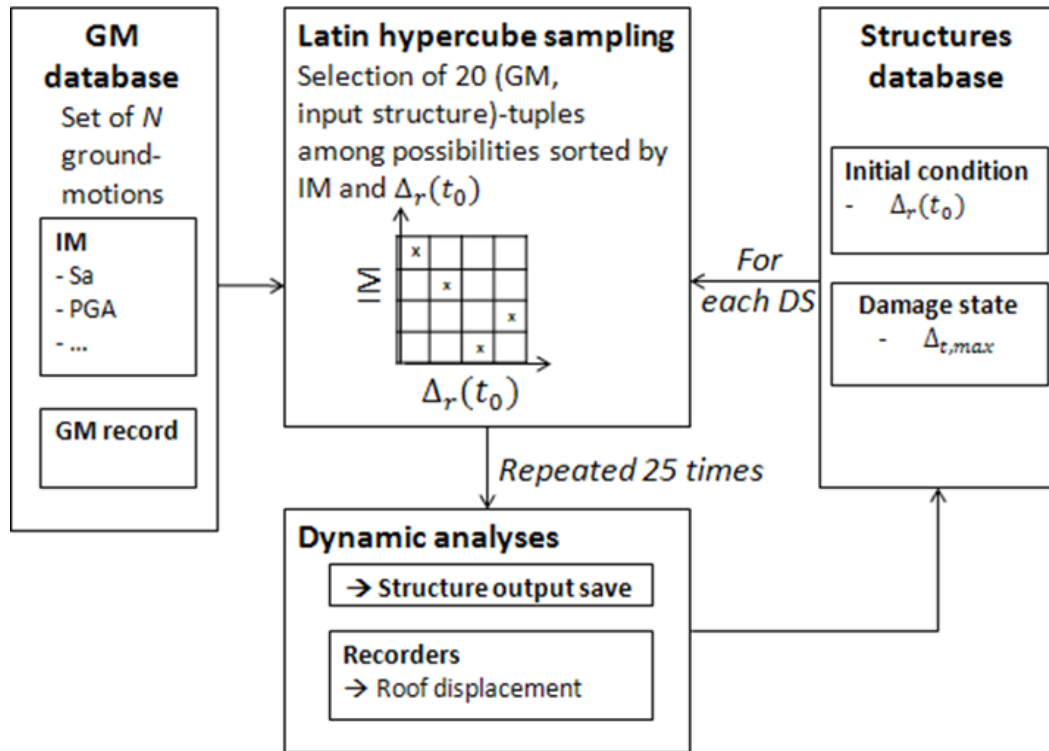


Figure 3.17: General simulation scheme for the dynamic analyses [Reveillere *et al.*, 2012].

This approach enables to get a full representation of the possible outcomes in the different damage states. Therefore it has the advantage of accounting for variability of damaged structures when building DS-dependent fragility curves. Different combinations of local damage mechanisms were translated into the residual drifts, whose distribution was used to estimate the variability in initial conditions.

### 3.4.2.2 Dynamic analysis and results

To illustrate the developed methodology, a single-story single-bay reinforced-concrete frame (3 m high and 4 m wide) was considered. The beams and columns were considered linear elastic and the damage mechanism was concentrated at the extremities, with the formation of plastic hinges. The main parameters (e.g. yield and capping moment) used for this study corresponded to beams and columns elements from a previous work presented in section 3.2.1.  $SA(T1)$  was chosen as the  $IM$

of interest for this structure,  $T_1 = 0.195$  s being the period of the fundamental mode. The drift thresholds to identify the damage states were those proposed by Rossetto and Elnashai [2003] for the EMS-98 damage scale (D1 – Slight, D2 – Moderate, D3 – Heavy, D4 – Very heavy).

The structure was submitted to successive ground-motions. A set of 175 time-histories was used indifferently as mainshocks or aftershocks. Dynamic simulations were carried out using the OpenSees software [McKenna *et al.*, 2010]. A specific regression technique, accounting for the distribution of residual drift due to the loading history prior to  $t_0$  was followed to build fragility curves for previously damaged buildings [Reveillere *et al.*, 2012].

The results showed, as expected, the capacity reduction of the frame, as previously damaged structures tend to have higher probabilities (i.e. lower median values of IM) of reaching further damage states due to an aftershock. The standard deviation was higher for initially damaged structures. This is explained by the distribution of initial residual drift, which is the source of additional scatter, as opposed to the initial undamaged structure, whose state is well defined. Using the estimated fragility parameters, DS-dependent fragility curves are displayed in Figure 3.18. This figure clearly shows the effect of successive ground shakings on the stability of the frame, and the translation of the curves (from solid black to light grey) from the right to the left is also observed. These fragility curves express the transition probability for one damage state to another and they may therefore be referred to as state-dependent fragility curves.

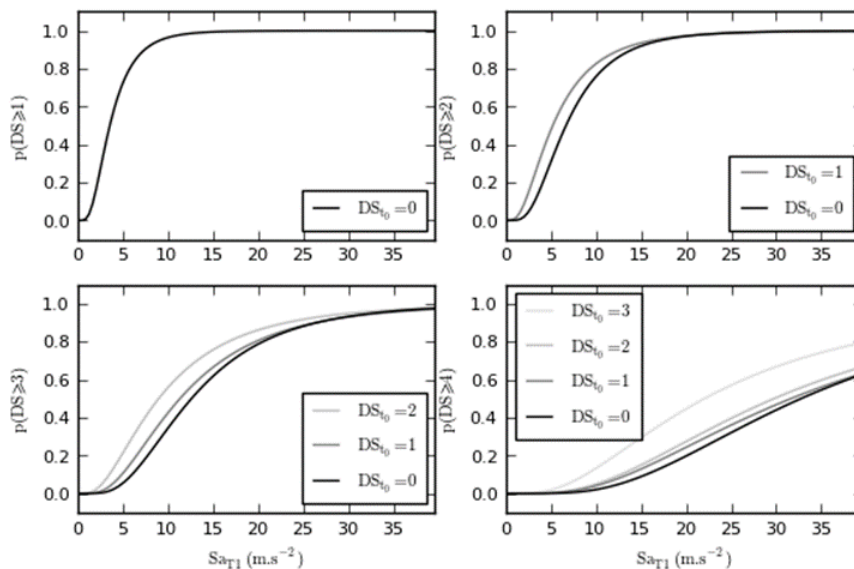


Figure 3.18: State-dependent fragility curves [Reveillere *et al.*, 2012].

### 3.5 Outlook

Current methods used to evaluate seismic risk are based on fragility curves representing the ground motion by a single IM (e.g. PGA). Different types of uncertainty affect the results of such evaluations. Three sources of aleatory and epistemic uncertainty are addressed in the work presented in this chapter. The variability of the ground motion and randomness of the material properties of the buildings have been taken into account through a large number of nonlinear time-history calculations. Moreover, representing earthquake shaking by a single IM introduces epistemic uncertainties in the risk evaluation as such approach cannot fully represent the effect of an earthquake on the response of structures. It was shown that an increase from one to two IMs leads to a significant reduction in the scatter in the fragility function and consequently a potential reduction in the uncertainty in evaluated earthquake risk.

The development of efficient numerical models capable of reproducing the main mechanisms of degradation under seismic loading is an essential element for the deployment of this approach. Concerning URM buildings, it would be useful to investigate the effect of the out-of-plane failure on fragility curves. In large-scale seismic risk assessments, the behavior of a typology of buildings is generally studied. The effect of geometrical variability on the vulnerability of a given typology must be taken into account by introducing a population of different buildings belonging to the same typology.

Construction of fragility functions using non-linear dynamic simulations are very time-consuming. Currently there is little guidance in the literature on how many dynamic runs (time-histories) need to be used to obtain robust fragility curves. Among other factors, the regression technique used for constructing fragility functions affects their accuracy and precision [Gehl *et al.*, 2015]. Fragility curves were derived from randomly-generated clouds of structural-response results using least-squares (LS), sum-of-squared errors (SSE) and maximum-likelihood estimation (MLE) to investigate the influence of number of dynamic analyses on the accuracy of structural response estimates using each technique [Gehl *et al.*, 2015].

Different statistical measures were used to estimate the quality of fragility functions derived by considering varying numbers of ground motions. The effectiveness of the results was demonstrated by their application to a single-degree-of-freedom structural model. The results showed that the LS regression method for the derivation of fragility curves is to be preferred since it requires far fewer time-histories to obtain an accurate fragility curve than the MLE and the SSE approaches [Gehl *et al.*, 2015]. However, MLE is recommended when drifts are unknown or inaccurate (e.g. observations following earthquakes of damaged/undamaged buildings or for deriving collapse probabilities). More analyses are necessary to optimize the number of non-linear analyses for different purposes using appropriate regression techniques.

Using model reduction and High-performance computing (HPC) techniques is one promising solution to improve efficiency of the approach. Data mining and artificial intelligence techniques have also been used recently to decrease the number of necessary numerical calculations for the

construction of fragility functions [e.g. [Saint et al., 2020](#)].

To make use of the vector-valued fragility functions like those proposed in this section within risk evaluations, it would be necessary to conduct a Vector-valued probabilistic seismic hazard analysis (VPSHA) [[Bazzurro and Cornell, 2002](#)] so that the joint probability of surpassing thresholds for two (or more) IMs was correctly estimated. VPSHA has yet to become a standard procedure in risk evaluations but it is likely to become more widespread.

Starting from the fragility surface concept, the presented methodology can be used to account for multi-hazard risk analyses. As demonstrated in section 3.4.2 the initial damage of structures can also be taken into account. It can thus be extended to account for different ageing phenomena, which may induce damage in structures.

## Chapter 4

# Perspectives

### 4.1 Concluding statement

Modeling the mechanical behavior of solid materials is inherently affected by various uncertainties at different scales. These uncertainties are due, on the one hand, to the variability of material parameters, and, on the other hand, to the heterogeneous character of materials. Another source of variability comes from the randomness of loads applied to structures. In engineering approaches, safety factors account for this randomness of nature and variable characteristics.

Providing new energy resources, promoting new technologies in view of environmental protection, and mitigation of natural risks are some of the most promising research areas, in which engineers play a significant role. Cutting-edge technologies must be developed to mitigate undesirable effects of climate change. Furthermore, growth of the world population and population concentration in urban areas encourages the deployment of efficient natural risk mitigation programs.

Taking into account the effects of material heterogeneities and variability of the applied loading has been the principal subject of my research activities during the last twenty years. These applications have often been linked to energy and environmental issues. Working at CEA Energy Division is an opportunity to continue working on various subjects related to different areas of energy and the environment. Estimation of the lifetime of industrial structures, design and study of energy storage systems are some of the application areas.

### 4.2 Some research perspectives

In the near future, I will continue my research on lifetime studies and risk analyses of structures. In Mechanical and Thermal Studies Section (SEMT), we are fortunate to benefit from exceptional experimental equipment and, at the same time, to be involved in the numerical modeling of structures. Strengthening the dialogue between modeling and experiment is a research area that I would like to pursue.

In the following, I briefly present the research themes that I wish to pursue. I address two topics

in particular: numerical modeling of ductile tearing and seismic fragility of structures.

#### 4.2.1 Numerical modeling of ductile tearing

Since the pioneering work of Griffith [1921], linear elastic fracture mechanics has proven its ability to predict the failure of cracked structures whose behavior can be described as brittle, i.e., when an abrupt failure occurs without any significant plastic strain being observed. This approach is called "global", in the sense that only one parameter (typically the energy release rate or stress intensity factor) is needed to establish a propagation criterion for cracks. For ductile materials, it is possible to use this theory as long as the plastic zone remains small compared to that of the structure, and the J-integral introduced by Rice [1968] is widely used today in this precise framework. However, this approach suffers from a number of well-known problems. It does not allow crack initiation to be treated, the critical value of  $J_c$  depends on the geometry of the structure, the loading conditions in the ductile regime, and is thus not a material property.

The so-called "local approach" gave rise to important research in the 1980s because it opened the possibility of overcoming certain shortcomings of the global approach. Several models of this type exist, in particular those of Gurson [1977] (and its modified version GTN [Tvergaard and Needleman, 1984]) and Rousselier [1987]. They have the merit of taking into account the effect of triaxiality of stresses in the mechanical response of ductile materials.

The use of these models gives rise to other problems. Among them, important computation times and strain localization and mesh dependency can be cited. Recent works have explored the possibility of regularizing such models thanks to "non-local" formalisms in which the behavior of the material at a given point depends also on that of its neighborhood over a certain distance.

A number of experimental studies have been conducted at different scales at CEA to investigate ductile tearing. An experimental program has been conducted recently to investigate ductile tearing of aged austenitic stainless welds within the EU-funded Atlas+ project. An experimental campaign on laboratory specimens was run to have a fine characterization of the weld. Tensile specimens were taken across the weld junction so that the changes of tensile properties within the different zones of the weld could be investigated. CT specimens were used to investigate ductile crack propagation within the weld. Then, a large-scale 4-point bending test was performed on the aged pipe (Figure 4.1) to challenge the issues of transferability of laboratory data to component scale. A stereo-correlation technique was used for full-field deformation measurements and follow ductile crack propagation during the pipe-bending test. This experimental campaign provided valuable data on crack initiation and propagation at industrial scale in the plastic regime. However, accurate modeling of such test remains a challenging topic. For instance, two improvement paths may be explored for numerical modeling of ductile tearing. The first one consist in developing a deletion criterion for completely "damaged" elements. When modeling ductile tearing with a local approach, the elements at the crack tip deform a lot leading to numerical problems (e.g., negative Jacobian). Different criteria can be considered to remove damaged elements. A first choice could be a threshold value of the porosity in

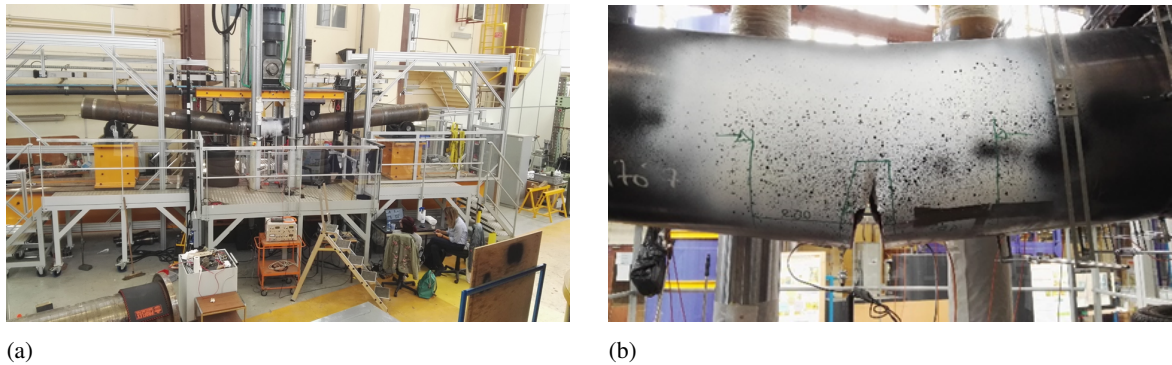


Figure 4.1: Four point bending test on Atlas+ mock-up (a), and zoom on the ductile tearing after the test (b).

each element. Another interesting way to explore is to define an energy based criterion. Therefore, a link between local approach modeling and nonlinear fracture mechanics quantities (e.g.,  $J$  integral) can be built.

The second improvement consist in the development of a non-local version of these types of models. In particular, it will be necessary to choose the variable(s) to be regularized, as well as a suitable regularization scheme. Different possibilities have already been examined. For example, [Leblond \*et al.\* \[1994\]](#) developed a non-local evolution law for porosity or in a more recent work the cumulative plastic strain has been regularized [[Zhang \*et al.\*, 2018](#)].

When dealing with ductile tearing in industrial components, predicting unstable crack propagation is a crucial issue. A bifurcation theory based approach may be followed in this view. Concerning the numerical approach, the phase field method seems to be an interesting candidate [e.g. [Miehe \*et al.\*, 2016](#)]. The developed framework may be later extended to account for other issues such as ductile to brittle transition.

## 4.2.2 Seismic fragility of structures

Since 1<sup>st</sup> March 2021, I started a new position as the head of the laboratory of seismic mechanics studies (EMSI). An important part of my future research activities will naturally be in the field of seismic mechanics.

Accounting for the current state of structures and components in seismic risk assessment is an important and not sufficiently developed topic. Most of risk assessment approaches consider a free-of-damage state for the structures. In spite of accurate construction and manufacturing technologies, all engineering structures contain defects and cracks that may grow due to service loads leading to damage inception in the structure. The updated knowledge of the vulnerability of damaged structures is of critical importance to accurately assess the associated risk and guide structure operability policies.

Based on the developments presented in Chapter 3, a general framework can be proposed to account for previous damage. As a first attempt, let us consider initial damage due to thermal fatigue.

Some components in nuclear power plants are subjected to thermomechanical loadings. Thermal fatigue cracking (striping) was observed in the mixing zones of the auxiliary cooling systems in nuclear power plants. This is not troublesome as long as a fracture analysis indicates that the cracks will not grow notably during the remaining service life. However, one may expect that the presence of this initial damage affect the vulnerability of the studied structure against a seismic event.

A particular issue will be to find a consistent damage definition between thermal fatigue and seismic loading. Thermal fatigue can be considered as High Cycle Fatigue (HCF). HCF occurs in an elastic regime at the RVE scale and fatigue damage is localized at the microscopic scale. In contrary, seismic loading may induce plastic strains at the RVE scale.

Concerning the construction of fragility functions, the use of artificial intelligence techniques is a promising perspective. The purpose is to reduce the number of numerical calculations by avoiding parametric models such as the lognormal model to estimate fragility curves. Moreover, these techniques may help addressing the question of the best seismic IM indicator [e.g. [Hariri-Ardebili and Saouma, 2016](#)]. The methodology consists in building a metamodel (different techniques can be used) that expresses the statistical relationship between seismic inputs and structural outputs.

The EMSI Lab benefits from remarkable experimental facilities such as the Azalée shaking table with 6 degrees of freedom, 6 m x 6 m surface, and a payload of 1000 kN. We would like to improve our experimental investigations in two main area. The first one concerns the use of Digital Image Correlation (DIC) techniques during experimental campaigns. DIC is currently used at EMSI. The purpose is to make progress toward a two-scale approach. At the mock-up scale, the main goal is a more accurate identification of the global kinematics of tested structures. The desired result is thus a better definition of boundary conditions and their history during tests. Accurate definition of boundary conditions is a challenging issue in such large-scale tests. At a smaller scale, DIC provides full-field data on a area of interest (displacement and strain field, damage, cracking density...). Such results provide valuable data for model verification and validation.

The second one consists in a more interactive dialogue between experiments and numerical simulations. This goal can be achieved by developing appropriate test control tools and modern monitoring techniques (e.g. DIC) on the one hand, and developing High-Performance Computing (HPC) techniques on the other hand. In a second step, these developments should make it possible to carry out hybrid tests.

# References

- Abdulmajid, M.**, 2020. Determination of the in-situ fracture properties of the Callovo-Oxfordian claystone: application to the prediction of fractures around tunnels. PhD Dissertation, Sorbone Université. 49, 145
- Ambraseys, N., Douglas, J., Sigbjörnsson, R., Berge-Thierry, C., P, P.S., Costa, G. and Smit, P.**, 2004. Dissemination of European Strong-Motion Data, vol. 2 using Strong-Motion Datascape Navigator. Technical report, CD-ROM collection, Engineering and Physical Sciences Research Council, United Kingdom. 112, 118
- Armand, G., Bumbieler, F., Conil, N., de La Vaissiere, R., Bosgiraud, J.M. and Vu, M.**, 2017b. Main outcomes from in situ thermo-hydro-mechanical experiments programme to demonstrate feasibility of radioactive high-level waste disposal in the Callovo-Oxfordian claystone. *Journal of Rock Mechanics and Geotechnical Engineering*, 9:415–427. 12, 20, 26
- Armand, G., Conil, N., Talandier, J. and Seyedi, D.M.**, 2017. Fundamental aspects of the hydromechanical behaviour of Callovo-Oxfordian claystone: From experimental studies to model calibration and validation. *Computers and Geotechnics*, 85:277–286. 7, 8, 9, 10, 11, 18, 29, 32, 38, 143
- Armand, G., Leveau, F., Nussbaum, C., de La Vaissiere, R., Noiret, A., Jaeggi, D., Landrein, P. and Righini, C.**, 2014. Geometry and properties of the excavation induced fractures at the Meuse/Haute-Marne URL drifts. *Rock Mechanics and Rock Engineering*, 47:21–41. 20, 21, 22, 51, 143
- Armand, G., Noiret, A., Cruchaudet, M. and Conil, N.**, 2011. Mine by experiment performed in the Callovo-Oxfordian claystone at the Meuse Haute Marne Underground Research Laboratory (France). In *ISRM 12<sup>th</sup> International Congress on Rock Mechanics*. Beijin. 24
- Armand, G., Noiret, A., Morel, J. and Seyedi, D.**, 2015. Pore pressure change during the excavation of deep tunnels in the Callovo Oxfordian claystone. In *ISRM 13<sup>th</sup> International Congress on Rock Mechanics*. Montreal. 12
- Armand, G., Noiret, A., Zedgondi, J. and Seyedi, D.M.**, 2013. Short- and long-term behaviors of drifts in the Callovo-Oxfordian claystone at the Meuse/Haute-Marne Underground Research Laboratory. *Journal of Rock Mechanics and Geotechnical Engineering*, 5:221–230. 25, 27, 144
- Aubry, D. and Modaressi, A.**, 1992. Strain localization in multipotential elastoplasticity. *International Journal for Numerical Methods in Engineering*, 34:349–363. 40
- Bažant, Z. and Belytschko, T.**, 1985. Wave propagation in strain-softening bar: exact solution. *Journal of Engineering Mechanics*, 111:381–389. 74

- Baker, J.W. and Cornell, A.C.**, 2005. A vector-valued ground motion intensity measure consisting of spectral acceleration and epsilon. *Earthquake Engineering & Structural Dynamics*, 34(10):1193–1217. 101
- Bažant, Z. and Xi, Y.**, 1991. Statistical size effect in quasi-brittle structures: II. Nonlocal theory. *Journal of Engineering Mechanics - ASCE*, 117(11):2623–2640. 75, 76
- Bažant, Z., Xi, Y. and Reid, S.**, 1991. Statistical size effect in quasi-brittle structures: I. Is weibull theory applicable? *Journal of Engineering Mechanics - ASCE*, 117(11):2609–2622. 75, 76
- Bazzurro, P. and Cornell, C.**, 2002. Vector-valued probabilistic seismic hazard analysis (VPSHA). In 7<sup>th</sup> U.S. national conference on earthquake engineering. paper No. 61. 126
- Belmokhtar, M., Delage, P., Ghabezloo, S., Tang, A.M., Menaceur, H. and Conil, N.**, 2017. Poroe-lasticity of the Callovo–Oxfordian Claystone. *Rock Mechanics and Rock Engineering*, 50(4):871–889. 15
- Berryman, J.**, 1992. Effective stress for transport properties of inhomogeneous porous rock. *Journal of Geophysical Research*, 97:251–265. 32
- Biot, M.**, 1941. General theory of of threediemnsional consolidation. *Journal of Applied Physics*, 12:155–164. 12
- Bonnet-Eymard, T., Ceccaldi, F. and Richard, L.**, 2011. Extension of the Andra underground laboratory: methods and equipment used for dry, dust-free works. In *World Tunnel Congres.* Helsinki. 23
- Borst, R.D., Sluys, L., Muhlaus, H. and Pamin, J.**, 1998. Fundamental issues in finite element analysis of localization of deformation. *Engineering Computations*, 10:99–121. 74
- Braun, P., Ghabezloo, S., Delage, P., Sulem, J. and Conil, N.**, 2019. Determination of Multiple Thermo-Hydro-Mechanical Rock Properties in a Single Transient Experiment: Application to Shales. *Rock Mechanics and Rock Engineering*, 52(7):2023–2038. 15, 18, 19, 143
- Bésuelle, P. and Hall, S.**, 2011. Characterization of the strain localization in a porous rock in plane strain condition using a new true-triaxial apparatus, p. 345–352. Springer. 47
- Băzant, Z. and Oh, B.**, 1983. Crack band theory for fracture of concrete. *RILEM Materials Structures*, 16:155–177. 74
- Băzant, Z.P. and Pijaudier-Cabot, G.**, 1988. Nonlocal Continuum Damage, Localization Instability and Convergence. *Journal of Applied Mechanics*, 55(2):287–293. 74
- Bumbieler, F., Plúa, C., Tourchi, S., Vu, M.N., Vaunat, J., Gens, A. and Armand, G.**, 2021. Feasibility of constructing a full-scale radioactive high-level waste disposal cell and characterization of its thermo-hydro-mechanical behavior. *International Journal of Rock Mechanics and Mining Sciences*, 137:104 555. 55, 56, 145
- Calderini, C., Cattari, S. and Lagomarsinol, S.**, 2009. In-plane strength of unreinforced masonry piers. *Earthquake Engineering and Structural Dynamics*, 38(2):243–267. 110
- Campanella, R. and Mitchell, J.**, 1968. Influence of temperature variations on soil behavior. *J Soil Mech. Fdn Div., Am. Soc. Civ. Engrs*, 94:709–734. 18

- Cariou, S., Duban, Z., Davy, C., Skoczylas, F. and Dormieux, L.**, 2012. Poromechanics of partially saturated COx argillite. *Appl Clay Sci.*, 56:36–47. 14
- Carloz, T.**, 2017. Nucléation et propagation de fissures en conditions anisotropes. PhD Dissertation, Université Paris-Est. 49
- Carmeliet, J. and de Borst, R.**, 1995. Stochastic approaches for damage evolution in standard and non-standard continua. *International Journal of Solids and Structures*, 32:1149–1160. 75
- Chambon, R., Cailherie, D. and Hassan, N.**, 1998. One-dimensional localisation studied with a second grade model. *Eur J Mech A-Solid*, 17:637–656. 40
- Conil, N., Talandier, J., Djizanne, H., de la Vaissiere, R., Righini-Waz, C., Auvray, C., Morlot, C. and Armand, G.**, 2018. How rock samples can be representative of in situ condition: A case study of Callovo-Oxfordian claystones. *Journal of Rock Mechanics and Geotechnical Engineering*, 10:613–623. 9, 18
- Conil, N., Vittel, M., Plúa, C., Vu, M.N., Seyedi, D. and Armand, G.**, 2020. In situ investigation of the THM behavior of the Callovo Oxfordian claystone. *Rock Mechanics and Rock Engineering*, 53:2747–2769. 26, 29, 30, 31, 144
- Coussy, O.**, 2004. Poromechanics. J. Wiley & sons, Chichester, 2<sup>nd</sup> edition. 52, 92
- Cuvillieza, S., Djouadib, I., Raude, S. and Fernandes, R.**, 2017. An elastoviscoplastic constitutive model for geomaterials: application to hydromechanical modelling of claystone response to drift excavation. *Computers and Geotechnics*, 85:321–40. 40
- Diñç, O. and Scholtès, L.**, 2018. Discrete Analysis of Damage and Shear Banding in Argillaceous Rocks. *Rock Mechanics and Rock Engineering*, 51:1521–1538. 47, 48, 145
- Distinguin, M. and Lavanchy, J.**, 2007. Determination of hydraulic properties of the Callovo-Oxfordian argillite at the bure site: Synthesis of the results obtained in deep boreholes using several in situ investigation techniques. *Physics and Chemistry of the Earth*, 32:379–392. 6, 12
- van den Eijnden, B., Bésuelle, P. and Collin, F.**, 2017. Modeling the strain localization around an underground gallery with a hydro-mechanical double scale model; effect of anisotropy. *Computers and Geotechnics*, 85:384–400. 41
- Ewy, R.T.**, 2015. Shale/claystone response to air and liquid exposure, and implications for handling, sampling and testing. *International Journal of Rock Mechanics and Mining Sciences*, 80:388–401. 9
- Fairhurst, C.**, 1964. On the validity of the “Brazilian” test for brittle materials. *Int. J. Rock Mech. Min. Sci. Geomech. Abstr.*, 1:535–546. 35
- Fawcett, T.**, 2003. ROCgraphs: notes and practical considerations for data mining researchers, HPL-2003-4. Technical report, HP Laboratories, Palo Alto (CA, USA). 113
- FEMA**, 1999. AHAZUS earthquake loss estimation methodology: User’s manual. Technical report, Federal Emergency Management Agency. 100
- Fenton, G. and Vanmarcke, E.**, 1990. Simulation of random fields via local average subdivision. *J Eng Mech*, 116:1733–1749. 65

- Forquin, P., Rota, L., Charles, Y. and Hild, F.**, 2004. A method to determine the macroscopic toughness scatter of brittle materials. *Int. J. Frac.*, 125:171–187. 88
- Galenne, E.**, 2009. Modélisation non locale à gradient de déformation. Technical report, Documentation code-aster, EDF R&D. 80
- Gambarotta, K. and Lagomarsino, S.**, 1996. On dynamic response of masonry panels. In *National conference on Masonry mechanics between theory and practice*. Messina. 110
- Gaucher, E., Tournassat, C., Pearson, F., Blanc, P., Crouzet, C., Lerouge, C. and Altmann, S.**, 2009. A robust model for pore-water chemistry of clayrock. *Geochimica et Cosmochimica Acta*, 73:6470–6487. 6
- Gehl, P., Douglas, J. and Seyed, D.M.**, 2015. Influence of the Number of Dynamic Analyses on the Accuracy of Structural Response Estimates. *Earthquake Spectra*, 31(1):97–113. 125
- Gehl, P., Seyed, D.M. and Douglas, J.**, 2013. Vector-valued fragility functions for seismic risk evaluation. *Bulletin of Earthquake Engineering*, 11:365–384. 109, 110, 111, 113, 114, 116, 117, 147
- Ghabezloo, S. and Sulem, J.**, 2008. Stress dependent thermal pressurization of a fluid-saturated rock. *Rock Mechanics and Rock Engineering*, 42(1):1. 18
- Godard, V.**, 2005. Modélisation de l'endommagement anisotrope du béton avec prise en compte de l'effet unilatéral : Application à la simulation des enceintes de confinement nucléaires. PhD Dissertation, Université Paris 6. 75
- Griffith, A.**, 1921. The phenomena of rupture and flow in solids. *The Philosophical Transactions of the Royal Society London (Series A)*, 221:163–198. 35, 128
- Griffiths, D. and Fenton, G.**, 1993. Seepage beneath water retaining structures founded on spatially random soil. *Géotechnique*, 43:577–587. 64
- Grunthal, G.**, 1998. European macroseismic scale 1998 (EMS-98). Chaier du Centre Européen de Géodynamique et de Séismologie. Technical report, Conseil de l'Europe. 107, 111
- Guayacan-Carrillo, L.M., Ghabezloo, S., Sulem, J., Seyed, D.M. and Armand, G.**, 2017. Effect of anisotropy and hydro-mechanical couplings on pore pressure evolution during tunnel excavation in low-permeability ground. *International Journal of Rock Mechanics and Mining Sciences*, 97:1–14. 12, 33, 34, 36, 37, 42, 144, 149
- Guayacan-Carrillo, L.M., Sulem, J., Seyed, D.M., Ghabezloo, S., Noiret, A. and Armand, G.**, 2016. Analysis of Long-Term Anisotropic Convergence in Drifts Excavated in Callovo-Oxfordian Claystone. *Rock Mechanics and Rock Engineering*, 49:97–114. 23, 24, 25, 143
- Gurson, A.**, 1977. Continuum theory of ductile rupture by void nucleation and growth: Part I— Yield criteria and flow rules for porous ductile media. *Journal of Engineering Materials and Technology*, 99:2–15. 128
- Guéry, A.A.C., Cormery, F., Shao, J.F. and Kondo, D.**, 2009. A multiscale modeling of damage and time-dependent behavior of cohesive rocks. *Int. J. Numer. Anal. Meth. Geomech.*, 33:567–589. 46

- Guy, N.**, 2010. Modélisation probabiliste de l'endommagement des roches : application au stockage géologique du  $CO_2$ . PhD Dissertation, Ecole Normale Supérieure de Cachan. 76
- Guy, N., Seyedi, D. and Hild, F.**, 2010. Hydro-mechanical modelling of geological  $CO_2$  storage and the study of possible caprock fracture mechanisms. *Georisk*, 4:110–117. 94
- Guy, N., Seyedi, D.M. and Hild, F.**, 2012. A probabilistic nonlocal model for crack initiation and propagation in heterogeneous brittle materials. *International Journal for Numerical Methods in Engineering*, 90(8):1053–1072. 76, 80, 81, 82, 83, 84, 85, 97, 146
- Guy, N., Seyedi, D.M. and Hild, F.**, 2018. Characterizing Fracturing of Clay-Rich Lower Watrous Rock: From Laboratory Experiments to Nonlocal Damage-Based Simulations. *Rock Mechanics Rock Engineering*, 51:1777–1787. 86, 87, 88, 89, 90, 92, 146, 147
- Hariri-Ardebili, M. and Saouma, V.**, 2016. Probabilistic seismic demand model and optimal intensity measure for concrete dams. *Structural Safety*, 59:67–85. 130
- Hauseux, P., Roubinb, E., Seyedi, D.M. and Colliata, J.**, 2016. FE modelling with strong discontinuities for 3D tensile and shear fractures: Application to underground excavation. *Computer Methods in Applied Mechanics and Engineering*, 309:269–287. 48
- Hecht, F.**, 2012. New development in FreeFem++. *Journal of Numerical Mathematics*, 20:17 409–24. 32
- Herman, J. and Usher, W.**, 2017. SALib: An open-source Python library for sensitivity analysis. *Journal of Open Source Software*, 2(9). 64
- Hill, R.**, 1965. Continuum micro-mechanics of elastoplastic polycrystals. *Journal of the Mechanics and Physics of Solids*, 13:89–101. 46
- Hillerborg, A., Modéer, M. and Petersson, P.E.**, 1976. Analysis of crack formation and crack growth in concrete by means of fracture mechanics and finite elements. *Cement and Concrete Research*, 6(6):773 – 781. 74
- Horseman, S.T., Higgo, J., Alexander, J. and Harrington, J.**, 1996. Water, gas and solute movement through argillaceous media. Technical report, Report for the NEA Working Group on Measurement and Physical Understanding of Groundwater Flow through Argillaceous Media (“Clay Club”), a Sub-group of the NEA Coordinating Group on Site Evaluation and Design of Experiments for Radioactive Waste Disposal (SEDE). DNEA/OECD Report CC-96/1. 12
- Kafali, C. and Grigoriu, M.**, 2007. Seismic fragility analysis: Application to simple linear and nonlinear systems. *Earthquake Engineering & Structural Dynamics*, 36(13):1885–1900. 101
- Kanninen, M. and Popelar, C.**, 1985. *Advanced Fracture Mechanics*. University Press: Oxford. 78, 83
- Kiureghian, A.D. and Ditlevsen, O.**, 2009. Aleatory or epistemic? Does it matter? *Structural Safety*, 31(2):105 – 112. 101
- Koutsourelakis, P.**, 2010. Assessing structural vulnerability against earthquakes using multi-dimensional fragility surfaces: a bayesian framework. *Probab Eng Mech*, 25:49–60. 101

- Kwon, O.S. and Elnashai, A.**, 2006. The effect of material and ground motion uncertainty on the seismic vulnerability curves of RC structure. *Engineering Structures*, 28(2):289 – 303. 101
- Lachenbruch, A.H.**, 1980. Frictional heating, fluid pressure, and the resistance to fault motion. *Journal of Geophysical Research: Solid Earth*, 85(B11):6097–6112. 18
- Lagomarsino, S. and Cattari, S.**, 2015. PERPETUATE guidelines for seismic performance-based assessment of cultural heritage masonry structures. *Bulletin of Earthquake Engineering*, 13:13–47. 117
- Lagomarsino, S., Penna, A. and Galasco, A.**, 2006. TREMURI program: Seismic analysis program for 3D masonry buildings. University of Genoa. 110, 118
- Lasry, D. and Belytschko, T.**, 1988. Localization limiters in transient problems. *International Journal of Solids and Structures*, 24(6):581 – 597. 74
- Leblond, J.B., Perrin, G. and Devaux, J.**, 1994. Bifurcation effects in ductile metals with nonlocal damage. *Journal of Applied Mechanics*, 61:236–242. 129
- Lebon, P. and Ghoreychi, M.**, 2000. French underground research laboratory of Meuse/ Haute Marne THM aspect of argillite formation. In *Eurock 2000 symposium, Aachen, Germany*. 6
- Lemaitre, J. and Chaboche, J.L.**, 1990. Mechanics of solide materials. Cambridge university press. 79
- Levard, P.C., Mekki, S., Launeau, F. and Landais, P.**, 2017. Physical protection specificities of a deep geological disposal: The case of the French project Cigéo. In *International Conference on Physical Protection of Nuclear Material and Nuclear Facilities*. Vienna, Austria. 17, 143
- Luco, N., Gerstenberger, M., Uma, S., Ryu, H., Liel, A. and Raghunandan, M.**, 2011. A methodology for post-mainshock probabilistic assessment of building collapse risk. In *9 Pacific Conference on Earthquake Engineering*. Auckland, New Zealand. 122
- Magenes, G., Kingsley, G. and Calvi, G.**, 1995. Static testing of a full scale, two-story masonry building: test procedure and measured experimental response, in experimental and numerical investigation on a brick masonry building prototype. Tech. Rep. Report 3.0 Numerical Prediction of the experiment: 1.1-1.41. Technical report, CNR-GNDT. 110, 111, 147
- Manica, M., Gens, A., Vaunat, J. and D.F., R.**, 2017. Time-dependent anisotropic model for argillaceous rocks. Application to an underground excavation in Callovo-Oxfordian claystone. *Computers and Geotechnics*, 85:156–162. 42, 44, 145
- Marante, M.E. and Flórez-López, J.**, 2003. Three-dimensional analysis of reinforced concrete frames based on lumped damage mechanics. *International Journal of Solids and Structures*, 40(19):5109–5123. 103
- Martin, C., Lanyon, G., Blumling, P. and Mayor, J.**, 2002. The excavation disturbed zone around a test tunnel in the Opalinus Clay. In *NARMS/TAC 2002*, p. 1581–1588. Toronto. 24
- McKenna, F., Scott, M.H. and Fenves, G.L.**, 2010. Nonlinear Finite-Element Analysis Software Architecture Using Object Composition. *Journal of Computing in Civil Engineering*, 24(1):95–107. 124

- Michot, L., Villieras, F., François, M., Bihannic, I., Pelletier, M. and Cases, J.M.**, 2002. Water organisation at the solid-aqueous solution interface. *Comptes-rendus Geoscience*, 334:611–631. 12
- Miehe, C., Aldakheel, F. and Raina, A.**, 2016. Phase field modeling of ductile fracture at finite strains: A variational gradient-extended plasticity-damage theory. *International Journal of Plasticity*, 84:1–32. 129
- Milutinovic, Z. and Trendafiloski, G.**, 2003. WP4 vulnerability of current buildings. Tech rep, Risk-UE: An advanced approach to earthquake risk scenarios with applications to different European towns. Technical report, FP6 Rsk-UE project. 111, 112, 149
- Mohajerani, M., Delage, P., Sulem, J., Monfared, M., Tang, A. and Gatmiri, B.**, 2012. A laboratory investigation of thermally induced pore pressures in the Callovo-Oxfordian claystone. *International Journal of Rock Mechanics and Mining Sciences*, 52:112 – 121. 18, 19, 143
- Monfared, M., Sulem, J., Delage, P. and Mohajerani, M.**, 2011. A Laboratory Investigation on Thermal Properties of the Opalinus Claystone. *Rock Mechanics and Rock Engineering*, 44(6):735. 18
- Mouroux, P. and Brun, B.L.**, 2006. Presentation of RISK-UE project. *Bull. Earthquake Eng.*, 58(4):319–321. 100
- Murikami, Y.**, 1987. Stress Intensity Factor Handbook. Pergamon Press: Oxford. 81, 83
- Negulescu, C., Ulrich, T., Baills, A. and Seyed, D.M.**, 2014. Fragility curves for masonry structures submitted to permanent ground displacements and earthquakes. *Natural Hazards*, 74:1461–1474. 119, 120, 121, 148
- Olivella, S. and Alonso, E.E.**, 2008. Gas flow through clay barriers. *Géotechnique*, 58(3):157–176. 97
- Palciauskas, V.V. and Domenico, P.A.**, 1982. Characterization of drained and undrained response of thermally loaded repository rocks. *Water Resources Research*. 18
- Pancheri, P., Bosetti, P., Maschio, R.D. and Sglavo, V.**, 1998. Production of sharp cracks in ceramic materials by three-point bending of sandwiched specimens. *Eng. Frac. Mech.*, 59:447–456. 89
- Panet, M.**, 1995. Le calcul des tunnels par la méthode de converge-confinement. Presse de l'ENPC. 39
- Pardoën, B. and Collin, F.**, 2017. Modelling the influence of strain localisation and viscosity on the behaviour of underground drifts drilled in claystone. *Computers and Geotechnics*, 85:351–67. 40, 41, 144
- Paté-Cornell, M.**, 1996. Uncertainties in risk analysis: Six levels of treatment. *Reliability Engineering and System Safety*, 54:54–95. 101
- Peerlings, R.H.J., de Borst, R., Brekelmans, W.A.M. and Geers, M.G.D.**, 1998. Gradient-enhanced damage modelling of concrete fracture. *Mechanics of Cohesive-frictional Materials*, 3(4):323–342. 74, 75, 76
- Penna, A.**, 2006. A macro-element procedure for the non-linear dynamic analysis of masonry buildings. PhD Dissertation, Politecnico de Milano. 110

- Perrier, L., Pijaudier-Cabot, G. and Grégoire, D.**, 2018. Extended poromechanics for adsorption-induced swelling prediction in double porosity media: Modeling and experimental validation on activated carbon. *International Journal of Solids and Structures*, 146:192 – 202. 13
- Pietruszczak, S. and Mróz, Z.**, 1981. Finite element analysis of deformation of strain-softening materials. *International Journal for Numerical Methods in Engineering*, 17:327–334. 74
- Pijaudier-Cabot, G. and Băzant, Z.P.**, 1987. Nonlocal Damage Theory. *Journal of Engineering Mechanics*, 113:1512–1533. 74
- Pijaudier-Cabot, G., Vermorel, R., Miqueu, C. and Mendiboure, B.**, 2011. Revisiting poromechanics in the context of microporous materials. *Comptes Rendus Mécanique*, 339(12):770 – 778. 13
- Plúa, C., Vu, M.N., Seyedi, D.M. and Armand, G.**, In press. Effects of inherent spatial variability of rock properties on the thermo-hydro-mechanical responses of a high-level radioactive waste repository. *Int. J. Rock Mech. Mining Sciences*. 65, 66, 67, 68, 69, 70, 71, 146
- Pousse, G., Bonilla, L., Cotton, F. and Margerin, L.**, 2006. Non stationary stochastic simulation of strong ground motion time histories including natural variability: Application to the K-net Japanese database. *Bulletin of Seismological Society of America*, 96:2103–2117. 105, 112
- Preston, C., Monea, M., Jazrawi, W., Brown, K., Whittaker, S., White, D., Law, D., Chalaturnyk, R. and Rostron, B.**, 2005. IEA GHG Weyburn CO<sub>2</sub> monitoring and storage project. *Fuel Processing Technology*, 86(14):1547 – 1568. 86
- Rajeev, P., Franchin, P. and Pinto, P.**, 2007. Increased accuracy of vector-IM-based seismic risk assessment? *Journal of Earthquake Engineering*, 12:111–124. 101
- Reveillere, A., Gehl, P., Seyedi, D. and Modaressi, H.**, 2012. Development of seismic fragility curves for damaged reinforced concrete structures mainshock-damaged reinforced-concrete structures. In *15 World Congress of Earthquake Engineering*. Lisbon. 122, 123, 124, 148
- Rice, J.**, 1968. A path independent integral and the approximate analysis of strain concentration by notches and cracks. *Journal of Applied Mechanics*, 35:379–386. 128
- Rice, J.R.**, 2006. Heating and weakening of faults during earthquake slip. *Journal of Geophysical Research: Solid Earth*, 111(B5). 16
- Robinet, J.C., Sardini, P., Coelho, D., Parneix, J.C., Prêt, D., Sammartino, S., Boller, E. and Altmann, S.**, 2012. Effects of mineral distribution at mesoscopic scale on solute diffusion in a clay-rich rock: example of the Callovo-Oxfordian mudstone (Bure, France). *Water Resources Research*, 48:1–10. 8, 32, 143
- Robinet, J.C., Sardini, P., Siitari-Kauppi, M., Prêt, D. and Yven, B.**, 2015. Upscaling the porosity of the Callovo-Oxfordian mudstone from the pore scale to the formation scale; insights from the 3H-PMMA autoradiography technique and SEM BSE imaging. *Sedimentary Geology*, 321:1–10. 7
- Rohmer, J. and Seyedi, D.M.**, 2010. Coupled Large Scale Hydromechanical Modelling for Caprock Failure Risk Assessment of CO<sub>2</sub> Storage in Deep Saline Aquifers. *Oil Gas Sci. Technol. - Rev. IFP*, 65:503–517. 62, 93, 94

- Rossetto, T. and Elnashai, A.**, 2003. Derivation of vulnerability functions for European-type RC structures based on observational data. *Engineering Structures*, 25(10):1241 – 1263. 106, 107, 122, 124, 149
- Rossetto, T. and Elnashai, A.**, 2005. A new analytical procedure for the derivation of displacement-based vulnerability curves for populations of RC structures. *Engineering Structures*, 27(3):397 – 409. 100
- Rousselier, G.**, 1987. Ductile fracture models and their potential in local approach of fracture. *Nuclear Engineering and Design*, 105:97–111. 128
- Roux, S. and Hild, F.**, 2006. Stress intensity factor measurements from digital image correlation: post-processing and integrated approaches. *Int. J Frac*, 140:141–157. 88, 89
- Rutqvist, J. and Tsang, C.F.**, 2002. A study of caprock hydromechanical changes associated with CO<sub>2</sub> injection into a brine aquifer. *Environmental Geology*, 42:296–305. 93
- Rutqvist, J., Wu, Y.S., Tsang, C.F. and Bodvarsson, G.**, 2002. A modeling approach for analysis of coupled multiphase fluid flow, heat transfer, and deformation in fractured porous rock. *International Journal of Rock Mechanics and Mining Sciences*, 39(4):429 – 442. 93
- Saint, R., Feau, C., Martinez, J.M. and Garnier, J.**, 2020. Efficient methodology for seismic fragility curves estimation by active learning on Support Vector Machines. *Structural Safety*, 86:101–117. 126
- Saltelli, A., Ratto, M., Andres, T., Campolongo, F., Cariboni, J., Gatelli, D., Saisana, M. and Tarantola, S.**, 2008. Global sensitivity analysis. The primer. John Wiley & Sons. 64
- Settari, A. and Mourits, F.**, 1998. A coupled reservoir and geomechanical simulation system. *SPE J*, 3:219–226. 94
- Seyedi, D., Vitel, M., Vu, M. and Armand, G.**, 2018. Key parameters controlling thermo-hydro-mechanical pressurization in Callovo-Oxfordian claystone. In *International Symposium on Energy Geotechnics (SEG-2018)*. Lausanne, Switzerland. 63, 66, 146
- Seyedi, D.M., Armand, G. and Noiret, A.**, 2017. “Transverse Action” – A model benchmark exercise for numerical analysis of the Callovo-Oxfordian claystone hydromechanical response to excavation operations. *Computers and Geotechnics*, 85:287–305. 20, 25, 28, 37, 38, 39, 40, 43, 143, 144, 145
- Seyedi, D.M., Gehl, P., Douglas, J., Davenne, L., Mezher, N. and Ghavamian, S.**, 2010. Development of seismic fragility surfaces for reinforced concrete buildings by means of nonlinear time-history analysis. *Earthquake Engineering & Structural Dynamics*, 39(1):91–108. 103, 104, 106, 108, 109, 120, 147
- Seyedi, D.M. and Gens, A.**, 2017. Numerical analysis of the hydromechanical response of Callovo-Oxfordian claystone to deep excavations. *Computers and Geotechnics*, 85:275–277. 37
- Seyedi, D.M., Guy, N., Sy, S., Granet, S. and Hild, F.**, 2013. A Non-Local Damage Model for Heterogeneous Rocks – Application to Rock Fracturing Evaluation Under Gas Injection Conditions, chapitre 4, p. 59–74. John Wiley Sons, Ltd. 94, 95, 96, 147, 149

- Seyedi, D.M., Plúa, C., Vitel, M., Armand, G., Rutqvist, J., Birkholzer, J., Xu, H., Guo, R., Thatcher, K., Bond, A., Wang, W., Nagel, T., Shao, H. and Kolditz, O.**, 2021. A numerical benchmark exercise for thermo-hydro-mechanical modeling of an in situ heating test in the Callovo-Oxfordian claystone. *International Journal of Rock Mechanics Mining Engineering*, 144:104–582. 17, 52, 53, 54, 57, 143, 145
- Shen, W., Kondo, D., Dormieux, L. and Shao, J.**, 2013. A closed-form three scale model for ductile rocks with a plastically compressible porous matrix. *Mechanics of Materials*, 59:73–86. 45, 46, 145
- Shinozuka, M., Feng, M., Lee, J. and Naganuma, T.**, 2000. Statistical analysis of fragility curves. *Journal of Engineering Mechanics*, 126(12):1124–1131. 113, 115
- Silva, A.D., Proença, S., Billardon, R. and Hild, F.**, 2004. Probabilistic approach to predict cracking in lightly reinforced microconcrete panels. *J Eng Mech*, 130:931–941. 86
- Sobol, I.**, 1993. Sensitivity analysis for non-linear mathematical models. *Mathematical Modelling and Computer Experiments*, 1:407–414. 63, 64
- Song, Y., Davy, C., Troadec, D., Blanchenet, A.M., Skoczylas, F., Talandier, J. and Robinet, J.C.**, 2015. Multi-scale pore structure of CO<sub>x</sub> claystone: Towards the prediction of fluid transport. *Marine and Petroleum Geology*, 65:63–82. 7, 8, 143
- Souley, M., Armand, G. and Kazmierczak, J.**, 2017. Hydro-elasto-viscoplastic modeling of a drift at the Meuse/Haute-Marne URL. *Computers and Geotechnics*, 85:306–20. 40
- Srawley, J.**, 1976. Wide range stress intensity factor expressions for ASTM E 399 standard fracture toughness specimens. *Int. J Frac*, 12:475–476. 88
- Strasser, F.O., Bommer, J.J., Şeşetyan, K., Erdik, M., Çağnan, Z., Irizarry, J., Goula, X., Lucantoni, A., Sabetta, F., Bal, I.E., Crowley, H. and Lindholm, C.**, 2008. A Comparative Study of European Earthquake Loss Estimation Tools for a Scenario in Istanbul. *Journal of Earthquake Engineering*, 12(sup2):246–256. 101
- Sulem, J., Lazar, P. and Vardoulakis, I.**, 2007. Thermo-poro-mechanical properties of clayey gouge and application to rapid fault shearing. *International Journal for Numerical and Analytical Methods in Geomechanics*, 31(3):523–540. 16, 18
- Sulem, J., Panet, M. and Guenet, A.**, 1987. Closure analysis in deep tunnels. *Int J Rock Mech Min Sci Geomech Abstr*, 24:145–154. 24
- Triantafyllidis, N. and Aifantis, E.C.**, 1986. A gradient approach to localization of deformation. I. Hyperelastic materials. *Journal of Elasticity*, 16(3):225–237. 74
- Tvergaard, V. and Needleman, A.**, 1984. Analysis of the cup-cone fracture in a round tensile bar. *Acta Metall*, 32:157–169. 128
- Vardoulakis, I.**, 2002. Dynamic thermo-poro-mechanical analysis of catastrophic landslides. *Géotechnique*, 52(3):157–171. 18
- Vidal-Gilbert, S., Nauroy, J.F. and Brosse, E.**, 2009. 3D geomechanical modelling for CO<sub>2</sub> geologic storage in the Dogger carbonates of the Paris Basin. *International Journal of Greenhouse Gas Control*, 3(3):288 – 299. 93

- Vu, T., Sulem, J., Subrin, D., Monin, N. and Lascols, J.**, 2013. Anisotropic closure in squeezing rocks: the example of Saint-Martin-la-Porte access gallery. *Rock Mechanics & Rock Engineering*, 46:231–246. 24
- Weibull, W.**, 1939. A Statistical theory of the strength of materials. *Royal Swedish Institute for Engineering Research*, 151. 75
- Wenk, H.R., Voltolini, M., Mazurek, M., Loon, L.R.V. and Vinsot, A.**, 2008. Preferred orientations and anisotropy in shales: Callovo-Oxfordian shale (France) and Opalinus Clay (Switzerland). *Clays and clay minerals*, 56:285–306. 8
- Wileveau, Y., Cornet, F., Desroches, J. and Blumling, P.**, 2007. Complete in situ stress determination in an argillite sedimentary formation. *Phys. Chem. Earth*, 32:866–878. 19
- Yao, C., Shao, J., Jiang, Q. and Zhou, C.**, 2017. Numerical study of excavation induced fractures using an extended rigid block spring method. *Computers and Geotechnics*, 85:368–83. 40, 42, 144
- Yuan, H., Agostini, F., Duan, Z., Skoczylas, F. and Talandier, J.**, 2017. Measurement of Biot's coefficient for CO<sub>x</sub> argillite using gas pressure technique. *International Journal of Rock Mechanics and Mining Sciences*, 92:72 – 80. 14, 143
- Zhang, C., Czaikowski, O. and Rothfuchs, T.**, 2010. Thermo-Hydro-Mechanical behaviour of the Callovo-Oxfordian clay rock. *GRS*, 266. 10, 11, 12, 143
- Zhang, Y., Lorentz, E. and Besson, J.**, 2018. Ductile damage modelling with locking-free regularised GTN model. *International Journal for Numerical Methods in Engineering*, 113:1871–1903. 129



# List of Figures

1.1	Pore size distribution curves for COx claystone [Armand <i>et al.</i> , 2017] (a) and, Spatial distribution of mineral content visualized by SEM BSEi after image segmentation (b) [Robinet <i>et al.</i> , 2012] (Clay matrix shown in Yellow). . . . .	8
1.2	COx claystone microstructure at different scales: (right) Clay matrix with carbonate and quartz inclusions, viewed using synchrotron X-ray microtomography [Robinet <i>et al.</i> , 2012], (left) 3D reconstruction of pore network from segmented images obtained by FIB/SEM [Song <i>et al.</i> , 2015]) . . . . .	8
1.3	Stress-strain curves of triaxial compression tests under different confining pressures on COx claystone [Armand <i>et al.</i> , 2017] . . . . .	10
1.4	Stress-strain curves of triaxial extension tests at two different mean pressures, with HR = 90% [Armand <i>et al.</i> , 2017] . . . . .	11
1.5	Strain evolution with time during uniaxial creep tests [Zhang <i>et al.</i> , 2010] . . . . .	12
1.6	Biot's tensor components obtained by gas test using argon and helium (modified from [Yuan <i>et al.</i> , 2017]) . . . . .	14
1.7	Three-stage loading protocol and schematic volumetric response for mechanical or thermal tests [Braun <i>et al.</i> , 2019] . . . . .	15
1.8	Schematic representation of the Cigéo facilities [Levard <i>et al.</i> , 2017] . . . . .	17
1.9	Schematic representation of HLW micro-tunnels [Seyedi <i>et al.</i> , 2021] . . . . .	17
1.10	Measured thermal pressurization coefficient on two COx samples (modified from [Mohajerani <i>et al.</i> , 2012]). . . . .	19
1.11	Meuse/Haute-Marne URL layout and principal stress directions. [Seyedi <i>et al.</i> , 2017].	20
1.12	Conceptual model of induced fracture networks around drifts parallel to $\sigma_H$ . Dark and light brown surfaces show shear fractures and green ones extension fractures [Armand <i>et al.</i> , 2014]. . . . .	21
1.13	Conceptual model of induced fracture networks around drifts parallel to $\sigma_h$ [Armand <i>et al.</i> , 2014]. . . . .	22
1.14	Convergence measurement sections for two different drift geometries [Guayacan-Carrillo <i>et al.</i> , 2016] . . . . .	23
1.15	Horizontal and vertical convergences measured at GCS (a) and GED (b) drift [Guayacan-Carrillo <i>et al.</i> , 2016]. . . . .	24
1.16	Comparison between predicted convergence (solid lines) and measurements (points) as a function of time for a drift parallel $\sigma_H$ (GCR). Model parameters are fitted on the 40 first days of data [Guayacan-Carrillo <i>et al.</i> , 2016]. . . . .	25
1.17	Concept of the mine-by test at GCS drift [Seyedi <i>et al.</i> , 2017] . . . . .	25

1.18	Rock mass displacement measured in the mine-by test: (a) Total response; (b) instantaneous response; and (c) time-dependent response of the extensometer OHZ1501. "PM" values represent the face advancement, "d" values show the distance of each point from the drift wall. Green dashed line shows the instance when the face reaches the extensometer location. Purple dashed line represents the instance beyond which, there is no face advancement effect on the section [Armand <i>et al.</i> , 2013]. . . . .	27
1.19	Pore pressure evolution during the digging in horizontal (a) and vertical (b) direction. "PM" values represent the face advancement, "d" values show the distance of each point from drift wall. Dashed vertical lines show the instance when the face reaches the measurement points [Seyedi <i>et al.</i> , 2017]. . . . .	28
1.20	Three-dimensional layout of the TED experiment [Conil <i>et al.</i> , 2020]. . . . .	29
1.21	Plan view of the temperature (green diamonds), pressure (cyan triangles for monopackers and purple triangles for multipackers) and displacement (orange crosses) measurement boreholes and sensors in rock mass (top) and cross-section view at the 14 m plane of the temperature and pressure sensors (bottom) [Conil <i>et al.</i> , 2020]. . . . .	30
1.22	Temperature history in boreholes TED1210 (perpendicular to the bedding plane) and TED1219 (in the bedding plane) at three distances from the drift [Conil <i>et al.</i> , 2020].	31
1.23	Temperature and pore pressure evolution at borehole TED1253. Modified from [Conil <i>et al.</i> , 2020]. . . . .	31
1.24	Initial conditions for two-dimensional numerical model ( $\sigma_{x,0}$ and $\sigma_{y,0}$ are the initial stress state in horizontal and vertical direction of the drift cross section; and $p_0$ the initial pore pressure) [Guayacan-Carrillo <i>et al.</i> , 2017]. . . . .	33
1.25	Instantaneous pore pressure change induced by instantaneous excavation with drained boundary conditions: (a) Drift following the direction of $\sigma_H$ . (b) Drift following the direction of $\sigma_h$ . Left: horizontal pore pressure evolution, right: vertical pore pressure evolution [Guayacan-Carrillo <i>et al.</i> , 2017]. . . . .	34
1.26	Major and minor principal effective stresses ( $\sigma'_1$ and $\sigma'_3$ ) in the horizontal, vertical and diagonal directions of drift cross-section for a drift following the orientation of $\sigma_H$ (top) and $\sigma_h$ (bottom) for Case 6 ( $E_x/E_y = 1.6$ ). Fairhurst's criterion is represented with solid lines and Mohr-Coulomb criterion with dashed lines [Guayacan-Carrillo <i>et al.</i> , 2017]. . . . .	36
1.27	Extension of the failure zone around a drift parallel to $\sigma_H$ . (a) Case 8, (b) Case 7, (c) Case 6 [Guayacan-Carrillo <i>et al.</i> , 2017]. . . . .	36
1.28	Extension of the failure zone around a drift parallel to $\sigma_h$ . (a) Case 8, (b) Case 7, (c) Case 6 [Guayacan-Carrillo <i>et al.</i> , 2017]. . . . .	37
1.29	Geometry and boundary conditions, drift parallel to $\sigma_h$ (left), drifts parallel $\sigma_H$ (right) [Seyedi <i>et al.</i> , 2017]. . . . .	39
1.30	Mechanical (left) and hydraulic (right) deconfinement curves. [Seyedi <i>et al.</i> , 2017] .	40
1.31	Shear banding around a drift parallel to $\sigma_H$ (test case 2.3) representing the overall extent of the fractured zone [Pardoen and Collin, 2017]. . . . .	41
1.32	Fracture patterns for test case 2.1 ( $//\sigma_h$ ) (a) Displacement magnified by 5; (b) blue color for tensile cracks and pink for shear cracks. Test case 2.3 ( $//\sigma_H$ ). (c) Displacement magnified by 5; (d) blue color for tensile cracks and pink for shear cracks [Yao <i>et al.</i> , 2017] . . . . .	42

1.33	Computed convergence. (a) Test case 2.1: drift parallel $\sigma_h$ with a soft support system. (b) Test case 2.2: drift parallel $\sigma_h$ with a soft support system. (c) Test case 2.3: drift parallel $\sigma_h$ with a soft support system and hydromechanical coupling [Seyedi <i>et al.</i> , 2017]	43
1.34	Calculated (dashed lines) and measured (solid lines) pore pressure evolution in measurement points of borehole OHZ1521 (horizontal response) (a), and in measurement points of borehole OHZ1522 (vertical response) (b) [Manica <i>et al.</i> , 2017].	44
1.35	Representative volume element (RVE) of COx modeled as a matrix-inclusion system at meso-scale and an assembly of clay particles and inter-particle pores at micro-scale [Shen <i>et al.</i> , 2013].	46
1.36	Influence of the direction of loading with respect to the material orientation on the uniaxial compressive strength (UCS) and axial elastic modulus (E) of the calibrated anisotropic DEM model [Dinç and Scholtès, 2018]	47
1.37	Micromechanical description of damage and failure during a biaxial compression test ( $\sigma_3 = 2$ MPa). (a) Stress–strain response and cumulative number of microcracks, (b) spatiotemporal distribution of microcracks [tensile cracks are classified as type 1 (blue), whereas shear cracks are classified as type 2 (red)], and (c) deviatoric strain fields [Dinç and Scholtès, 2018]	48
1.38	Experimental test setup used to perform quasi-static fracture tests. The electromechanical machine is equipped with a load cell sensor of 10kN, and a clip gauge with 5 mm maximum opening to measure the applied force and the crack opening displacement, respectively [Abdulmajid, 2020].	49
1.39	Temperature evolution at sensors: (A) TED1219_05, located parallel to bedding and (B) TED1210_05, located perpendicular to bedding. The heat power history is plotted in light blue [Seyedi <i>et al.</i> , 2021].	53
1.40	Pressure evolution at sensors: (A) TED1258_01, located parallel to bedding, (B) TED1258_01, located perpendicular to bedding. The heat power history is plotted in light blue [Seyedi <i>et al.</i> , 2021].	54
1.41	Pressure evolution at sensors (A) TED1240_01 and (B) TED1240_02. The heat power history is plotted in light blue [Seyedi <i>et al.</i> , 2021].	54
1.42	Three-dimensional layout of the ALC experiment [Bumbieler <i>et al.</i> , 2021].	56
1.43	Comparison of numerical prediction and measurements of temperature for sensors (A) ALC1616_02 (1) and ALC1616_05 (2), parallel to bedding and (B) ALC1617_01 (1) and ALC1617_02 (2), perpendicular to bedding [Seyedi <i>et al.</i> , 2021].	57
1.44	Comparison of numerical prediction and measurements of temperature for sensors: (A) ALC1616_02 (1) and ALC1616_05 (2), parallel to bedding and (B) ALC1617_01 (1) and ALC1617_02 (2), perpendicular to bedding [Seyedi <i>et al.</i> , 2021].	57
1.45	Schematic representation of HLW cells and deduced plan strain model and mesh.	59
1.46	THM response of COx at the far field. (top) Schematic representation of the thermo-mechanical processes of an REV located at mid-distance between two cells. (bottom) Temperature, pressure and vertical effective stress field in COx between two parallel cells	60
1.47	Thermal loads imposed on the cell wall (a), and evolution of thermos-mechanical pressurization coefficient $\Lambda^*$ versus temperature during the heating period. Dashed green line corresponds to the value of thermal pressurization coefficient (b).	61

1.48	Effect of different parameters on the vertical effective stress at mid-distance between two parallel cells; E stands for Young's modulus, $k$ permeability, $\lambda$ thermal conductivity, $\nu$ for Poisson's ratio, b Biot coefficient, $\alpha_s$ thermal expansion coefficient of rock skeleton and $C_p$ its heat capacity (the negative values correspond to compressive effective stresses) [Seyedi <i>et al.</i> , 2018]. . . . .	63
1.49	Simplified geometry and COMSOL mesh showing the access gallery and HLW cells: C1 and C2, [Plúa <i>et al.</i> , In press] . . . . .	66
1.50	Simplified geometry with one HLW cell and <i>code – aster</i> mesh [Plúa <i>et al.</i> , In press] . . . . .	67
1.51	Set of random fields (Young's modulus, Biot coefficient, Thermal conductivity and Permeability) with a correlation length of 10 m x 6 m [Plúa <i>et al.</i> , In press] . . . . .	68
1.52	Deterministic analysis for three different parameter sets at Point P1. (A) pore pressure evolution and (B) vertical Terzaghi effective stress evolution. [Plúa <i>et al.</i> , In press] . . . . .	68
1.53	Parametric sensitivity analysis of layers UA23 at Point P1. (A) Temperature evolution. (B) Sobol indices contributing to the maximum temperature. [Plúa <i>et al.</i> , In press] . . . . .	69
1.54	Parametric sensitivity analysis of layers UA23 at Point P1. (A) Pore pressure evolution and (B) Sobol indices contributing to the maximum pore pressure [Plúa <i>et al.</i> , In press]. . . . .	70
1.55	Parametric sensitivity analysis of layers UA23 at Point P1. (A) Vertical Terzaghi effective stress evolution and (B) Sobol indices contributing to the maximum vertical Terzaghi effective stress [Plúa <i>et al.</i> , In press]. . . . .	71
1.56	Spatial variability analysis for length scale 10 m x 6 m at Point P1. (A) Vertical Terzaghi effective stress evolution and (B) probability distribution of its maximum value. Vertical dashed lines indicate the maximum values obtained for the three cases studied in the deterministic analysis. [Plúa <i>et al.</i> , In press]. . . . .	71
2.1	Nodal unknowns for two types of elements [Guy <i>et al.</i> , 2012]. . . . .	80
2.2	Schematic of the considered theoretical case [Guy <i>et al.</i> , 2012]. . . . .	81
2.3	Stress intensity factors (a) and difference between analytical and nonlocal estimations (b) as functions of normalized crack lengths for different characteristic lengths [Guy <i>et al.</i> , 2012]. . . . .	81
2.4	Change of the considered thresholds with normalized crack (or defect) size [Guy <i>et al.</i> , 2012]. . . . .	82
2.5	Comparison between the simulated and analytical crack opening displacement ( $a/b = 0.14$ , $\ell_c = 20$ mm) [Guy <i>et al.</i> , 2012]. . . . .	83
2.6	Schematic of the studied case [Guy <i>et al.</i> , 2012]. . . . .	84
2.7	Meshes, horizontal displacement and damage fields for $c = 1$ and for two of the simulations corresponding to the case shown in Figure 2.6 [Guy <i>et al.</i> , 2012] . . . . .	85
2.8	Crack growth with load $c$ for the different meshes [Guy <i>et al.</i> , 2012]. . . . .	85
2.9	Modified Weibull diagram for the identification of parameters based on three-point bending and Brazilian tests [Guy <i>et al.</i> , 2018]. . . . .	87
2.10	Mesh (a) and crack initiation threshold (b) for the upper half of the model used to simulate Brazilian tests [Guy <i>et al.</i> , 2018]. . . . .	87
2.11	Modified Weibull diagram (a) and failure probability $P_F$ as functions of the Weibull stress $\sigma_w$ (b) for the numerical, analytical and experimental approaches [Guy <i>et al.</i> , 2018]. . . . .	88
2.12	Sandwiched-Beam test in which the rock sample is loaded with the two aluminum alloy beams [Guy <i>et al.</i> , 2018]. . . . .	89

2.13	Maximum eigen strain field in sample no. 2 when pre-cracked. The physical size of 1 pixel is $\approx 20.7 \mu\text{m}$ [Guy <i>et al.</i> , 2018]. . . . .	90
2.14	Measured horizontal displacement field (expressed in pixels) when rigid body translations have been removed. Pre-cracked sample (no. 2) submitted to a load $F = 350 \text{ N}$ in three-point flexural test. The physical size of 1 pixel is $\approx 20.3 \mu\text{m}$ [Guy <i>et al.</i> , 2018]. 90	
2.15	(a) Horizontal measured displacement field. (b) Simulated displacement field. (c) Damage field for sample no. 2 in the Sandwiched-Beam test [Guy <i>et al.</i> , 2018]. . . . .	92
2.16	Schematic representation of sequentially linking hydraulic and mechanical calculations with $p_n$ pressure, $K_n$ permeability and $t_n$ time at the end of the $n^{\text{th}}$ time step [Seyedi <i>et al.</i> , 2013]. . . . .	94
2.17	Studied caprock and considered boundary conditions [Seyedi <i>et al.</i> , 2013]. . . . .	95
2.18	Pore pressure distribution (a) in Pa, and initiated crack network (b) in the caprock, when $p_i = 2.4p_0$ [Seyedi <i>et al.</i> , 2013]. . . . .	95
2.19	Zoom on the formed crack network, dark gray elements show the initiation points, black elements propagation line and light gray elements crack tips [Seyedi <i>et al.</i> , 2013].	96
2.20	Patterns of induced crack network for different values of $m$ [Seyedi <i>et al.</i> , 2013]. . . . .	96
3.1	Finite element mesh of the studied building [Seyedi <i>et al.</i> , 2010] . . . . .	103
3.2	Nonlinear behavior of the discrete models used to represent the formation of plastic hinges [Seyedi <i>et al.</i> , 2010] . . . . .	104
3.3	Linear regression between spectral displacements at the first two natural structural periods and inter-storey drift ratio. Black squares (and solid lines) refer to natural accelerograms whereas gray triangles (and dashed lines) are from synthetic records [Seyedi <i>et al.</i> , 2010] . . . . .	106
3.4	Distribution of selected time-histories in SD(0.41s)- SD(1.26s) space. The crosses (and the gray triangles) represent synthetic (and natural) accelerograms respectively. The stars denote the nodes of the grid (i.e. the points in the neighborhood of which the damage probability was evaluated) [Seyedi <i>et al.</i> , 2010] . . . . .	106
3.5	Fragility surfaces of the studied building for four damage levels (based on EMS 98). The parameters are spectral displacements at T1 and T2, the periods corresponding to the main eigenmodes of the building in the X direction [Seyedi <i>et al.</i> , 2010]. . . . .	108
3.6	Fragility curves with spectral displacement at period T1 (left) and T2 (right). The curves are plotted as "slices" of the fragility surface for different values of SD(T2) (left) and SD(T1) (right). Note that the slices were slightly smoothed and they are only plotted where they are sufficiently constrained by the analysis [Seyedi <i>et al.</i> , 2010].	109
3.7	Numerical model of the test building [Gehl <i>et al.</i> , 2013]. . . . .	110
3.8	(a) Pushover results for a façade wall and comparison between the TREMURI model and experimental data by Magenes <i>et al.</i> [1995]. (b) Modal pushover of the whole building model and corresponding bilinear idealization [Gehl <i>et al.</i> , 2013]. . . . .	111
3.9	Example of ROC curves for three ground-motion parameters for the yield damage state [Gehl <i>et al.</i> , 2013]. . . . .	114
3.10	Example of a fragility surface for the "Collapse" state, using the couple (PGV, PGA/PGV) as earthquake descriptors [Gehl <i>et al.</i> , 2013]. . . . .	116
3.11	Single-variable fragility curve (solid black line) compared to slices of a fragility surface [Gehl <i>et al.</i> , 2013]. . . . .	117

3.12	Blueprints of the exterior walls of the numerical model. Wall P1 is the façade of the structure. The red rectangles are masonry elements with pier behavior, the green ones are masonry elements with spandrel behavior and the blue ones are rigid links between the masonry macro-elements [Negulescu <i>et al.</i> , 2014]. . . . .	119
3.13	3D view of the structure (left) and layout of the prescribed settlements at the foundation level (right) [Negulescu <i>et al.</i> , 2014]. . . . .	120
3.14	Damage initiation and growth in wall P4 for a maximum amplitude of 25 cm. A scaling factor equal to 4 is used [Negulescu <i>et al.</i> , 2014]. . . . .	120
3.15	Comparison of fragility functions obtained for damage states 1 (dotted lines) and 5 (solid lines). The magnitude of the settlement is represented by the color of the curve [Negulescu <i>et al.</i> , 2014]. . . . .	121
3.16	Probability of exceeding LS1 (left) and LS5 (right), as functions of the amplitude of differential settlement and of PGA [Negulescu <i>et al.</i> , 2014]. . . . .	121
3.17	General simulation scheme for the dynamic analyses [Reveillere <i>et al.</i> , 2012]. . . . .	123
3.18	State-dependent fragility curves [Reveillere <i>et al.</i> , 2012]. . . . .	124
4.1	Four point bending test on Atlas+ mock-up (a), and zoom on the ductile tearing after the test (b). . . . .	129

# List of Tables

1.1	Typical values of thermal pressurization coefficient of some geomaterials . . . . .	18
1.2	Material and stress state parameters for various studied cases in a 2D model for the excavation effect [Guayacan-Carrillo <i>et al.</i> , 2017]. . . . .	33
2.1	Main hydromechanical parameters of the caprock [Seyedi <i>et al.</i> , 2013]. . . . .	95
3.1	Relationships between inter-story drift ratio (ISDR) and $DI_{HRC}$ [Rossetto and Elnashai, 2003] . . . . .	107
3.2	Correlation between damage index $DI_{HRC}$ and EMS 98 damage level [Rossetto and Elnashai, 2003] . . . . .	107
3.3	Correlation between EMS-98 damage states and transient top displacement, for URM buildings, according to Milutinovic and Trendafiloski [2003]. . . . .	112